Doctorate of National Interest

on

Space Science and Technology

The Active Phases of a Galaxy in the JWST and Euclid Era: From Radio Jets and Multiphase Outflows to Mergers

Lorenzo Ulivi

Supervisors: Prof. Alessandro Marconi, Dott. Giovanni Cresci

Year 2024/2025

Look again at that dot. That's here. That's home. That's us. On it everyone you love, everyone you know, everyone you ever heard of, every human being who ever was, lived out their lives. The aggregate of our joy and suffering, thousands of confident religions, ideologies, and economic doctrines, every hunter and forager, every hero and coward, every creator and destroyer of civilization, every king and peasant, every young couple in love, every mother and father, hopeful child, inventor and explorer, every teacher of morals, every corrupt politician, every "superstar," every "supreme leader," every saint and sinner in the history of our species lived there–on a mote of dust suspended in a sunbeam. ...

It has been said that astronomy is a humbling and character-building experience. There is perhaps no better demonstration of the folly of human conceits than this distant image of our tiny world. To me, it underscores our responsibility to deal more kindly with one another, and to preserve and cherish the pale blue dot, the only home we've ever known.

Carl Sagan, Pale Blue Dot, 1994

Abstract

The objective of this thesis is to study the key processes that regulate the growth and evolution of galaxies, focusing on the role of active galactic nuclei (AGNs). AGN feedback, in the form of energy flows and radio jets, is a fundamental mechanism that regulates star formation, redistributes gas and dust, and shapes the structure of the host galaxy. Another phenomenon that affects galactic evolution is galaxy mergers, as these provide fresh gas, triggering starbursts and fueling black hole activity, sometimes leading to the formation of multiple AGNs within the same system.

We first provide an overview of these phenomena, discussing AGN physics, feedback mechanisms, and the impact of galaxy mergers. We also include a brief chapter on the emerging role of machine learning in analyzing astronomical data that will be useful for the last chapter of this thesis.

This thesis is based on four original articles published or in the process of publication, which form the basis of the following three chapters.

In the first one, we analyzed four bright type 2 AGNs using Multi Unit Spectroscopic Explorer (MUSE) integral field spectroscopy, Very Large Array (VLA) and e-MERLIN radio observations with the goal of studying the interplay between radio jets, outflows, and the properties of the interstellar medium (ISM). We detected extended ionized gas outflows (up to 15 kpc, with velocities up to 1000 km/s) and identified a strong increase in the widths of emission lines perpendicular to the jets, consistent with interactions between the jets and the ISM. Even low-power jets were found to be capable of injecting significant amounts of energy into the interstellar medium.

The second one focuses on the study of two Ultra Luminous InfraRed Galaxies (ULIRGs), Arp 220 and Mrk231, observed with JWST/NIRSpec. We spatially resolved the ionized and hot molecular gas in the nuclear region and identified multiple high-velocity multiphase outflows originating from both nuclei of Arp220. Combined NIRSpec and ALMA observations reveal that most of the outflowing mass resides in cold molecular gas. The multidirectional outflows in Arp 220 may affect the interstellar medium more uniformly than the collimated outflows typically seen in isolated galaxies. In Mrk231, we performed a kinematic study of the gas in both the infrared (IR) and optical bands using MEGARA IFU data. We identified clumps at velocity up to 1000 km/s and an outflow as traced by [OII] with velocity up to 2000 km/s. Moreover, we proposed a new binary black hole model (BBH) that can potentially explain multiple multi-band observational features of Mrk231, building on the hypothesis first suggested by Yan et al. (2015).

Finally, in the last chapter, we identified dual or gravitationally lensed AGNs using the first Quick Release (Q1) of Euclid data. We developed a convolutional neural network (CNN) trained on realistic simulations, capable of detecting pairs of AGNs at sub-arcsecond separations. Once we learned the potential of the CNN from simulations and its outperformance compared to standard methods, we applied this method to

approximately 6,000 quasars (QSO). We estimated a fraction of dual AGNs to be approximately 0.25%, and identified promising candidates, highlighting the potential of machine learning (ML) to discover these rare systems in future Euclid image release. This thesis explored different phenomena at work in galaxies that are fundamental for understanding their evolution and for constraining models, providing new insights into the roles of these processes.

List of Publications

First author publications

- **2025** — *Unveiling the gas structure in the nuclear region of the binary black hole candidate Mrk 231.* Ulivi, L. et al., in prep.
- **2025** — *Euclid: A machine-learning search for dual and lensed AGN at sub-arcsec separations.* Ulivi, L. et al., submitted to *Astronomy & Astrophysics*.
- **2025** — *JWST/NIRSpec insights into the circumnuclear region of Arp 220: A detailed kinematic study.* Ulivi, L. et al., *Astronomy & Astrophysics*, Volume 693, id.A36.
- **2024** — *Feedback and ionized gas outflows in four low-radio power AGN at $z \sim 0.15$.* Ulivi, L. et al., *Astronomy & Astrophysics*, Volume 685, id.A122.

Other Publications

- **2025** — *Evidence of the fast acceleration of AGN-driven winds at kiloparsec scales.* Marconcini, C. et al., *Nature Astronomy*, Volume 9, p. 907–915.
- **2025** — *MIRACLE II: Unveiling the multi-phase gas interplay in the circumnuclear region of NGC 1365 via multi-cloud modeling.* Ceci, M. et al., eprint arXiv:2507.08077, submitted to *A&A*.
- **2025** — *MIRACLE I: Unveiling the Multi-Phase, Multi-Scale physical properties of the Active Galaxy NGC 424 with MIRI, MUSE, and ALMA.* Marconcini, C. et al., eprint arXiv:2503.21921.
- **2025** — *Classifying spectra of emission-line regions with neural networks: An application to integral field spectroscopic data of M33.* Bracci, C. et al., *Astronomy & Astrophysics*, Volume 697, id.A148.
- **2025** — *The JWST/NIRSpec view of the nuclear region in the prototypical merging galaxy NGC 6240.* Ceci, M. et al., *Astronomy & Astrophysics*, Volume 695, id.A116.
- **2025** — *Euclid: I. Overview of the Euclid mission.* Euclid Collaboration, Mellier, Y. et al., *Astronomy & Astrophysics*, Volume 697, id.A1.
- **2025** — *MARTA: Temperature–temperature relationships and strong-line metallicity calibrations from multiple auroral lines detections at cosmic noon.* Cataldi, E. et al., eprint arXiv:2504.03839.

- **2025** — *Euclid Quick Data Release (Q1): The Strong Lensing Discovery Engine A – System overview and lens catalogue.* Euclid Collaboration, Walmsley, M. et al., eprint arXiv:2503.15324.
- **2025** — *Euclid Quick Data Release (Q1): The Strong Lensing Discovery Engine C – Finding lenses with machine learning.* Euclid Collaboration, Lines, N. E. P. et al., eprint arXiv:2503.15326, accepted to *A&A*.
- **2025** — *Euclid Quick Data Release (Q1): The Strong Lensing Discovery Engine E – Ensemble classification of strong gravitational lenses: lessons for Data Release 1.* Euclid Collaboration, Holloway, P. et al., eprint arXiv:2503.15328.
- **2025** — *Euclid: Finding strong gravitational lenses in the Early Release Observations using convolutional neural networks.* Nagam, B. C. et al., eprint arXiv:2502.09802.
- **2025** — *Euclid: Searches for strong gravitational lenses using convolutional neural nets in Early Release Observations of the Perseus field.* Pearce-Casey, R. et al., *Astronomy & Astrophysics*, Volume 696, id.A214.
- **2024** — *Euclid: Early Release Observations – Overview of the Perseus cluster and analysis of its luminosity and stellar mass functions.* Cuillandre, J. et al., *Astronomy & Astrophysics*, Volume 697, id.A11.
- **2024** — *Growing a nuclear star cluster from star formation and cluster mergers: The JWST NIRSpec view of NGC 4654.* Fahrion, K. et al., *Astronomy & Astrophysics*, Volume 687, id.A83.
- **2024** — *No evidence of active galactic nucleus features in the nuclei of Arp 220 from JWST/NIRSpec IFS.* Perna, M. et al., *Astronomy & Astrophysics*, Volume 690, id.A171.
- **2024** — *HOMERUN: A new approach to photoionization modeling: I. Reproducing observed emission lines with percent accuracy and obtaining accurate physical properties of the ionized gas.* Marconi, A. et al., *Astronomy & Astrophysics*, Volume 689, id.A78.
- **2024** — *MUSE adaptive-optics spectroscopy confirms dual active galactic nuclei and strongly lensed systems at sub-arcsec separation.* Scialpi, M. et al., *Astronomy & Astrophysics*, Volume 690, id.A57.
- **2023** — *GMP-selected dual and lensed AGNs: Selection function and classification based on near-IR colors and resolved spectra from VLT/ERIS, Keck/OSIRIS, and LBT/LUCI.* Mannucci, F. et al., *Astronomy & Astrophysics*, Volume 680, id.A53.
- **2023** — *MOKA3D: An innovative approach to 3D gas kinematic modelling. I. Application to AGN ionized outflows.* Marconcini, C. et al., *Astronomy & Astrophysics*, Volume 677, id.A58.
- **2023** — *Bubbles and outflows: The novel JWST/NIRSpec view of the $z = 1.59$ obscured quasar XID2028.* Cresci, G. et al., *Astronomy & Astrophysics*, Volume 672, id.A128.

List of Figures

List of Figures

Contents

Chapter 1

Introduction

1.1 Outline of the thesis

In this thesis, we address the various feedback processes that shape galaxy evolution, ranging from gas accretion through galaxy interactions to the impact of radio jets and AGN-driven outflows on the interstellar medium (ISM). Each chapter focuses on a specific aspect of this broad theme. The first two chapters serve as an introduction to clarify the concepts that we will revisit in the following three chapters. These three chapters present the original results from four articles written over the past three years: two published in A&A, one submitted to A&A after the review of the Euclid Consortium and another one in preparation.

In **Chapter 1**, we provide an overview of the main feedback phenomena that influence galaxy evolution. We introduce the Active Galactic Nucleus (AGN) phase, describing how radio jets, feedback processes such as outflows, and galaxy mergers contribute to shaping the overall structure and evolution of galaxies.

In **Chapter 2**, we describe the observational instrumentation used in this work, including integral field unit (IFU) spectrographs such as NIRSpec on JWST and MUSE on the VLT and the space survey telescope Euclid. Moreover, we present a brief introduction to Machine Learning (ML) and deep learning techniques, with particular focus on their applications in astrophysics. We will return to this chapter in Chapter 5 when we use a particular type of machine learning technique, such as CNN, to select dual AGNs from Euclid's images.

In **Chapter 3**, we investigate radio jets in Seyfert 2 galaxies, a class traditionally considered radio-quiet, in order to explore their role in driving feedback.

In **Chapter 4**, we present a kinematic analysis of the nuclear regions of Arp 220 and Mrk 231. Both are prototypical ultra-luminous infrared galaxies (ULIRGs) with merger-driven activity, and we focus on characterizing the properties of their ISM and outflows. Moreover, we propose a new binary black hole model for Mrk231.

In **Chapter 5**, we turn to the study of dual AGN systems using the first observations from the *Euclid* mission. This work introduces a novel methodology for identifying dual AGN candidates and provides a statistical analysis of their frequency. Such systems are particularly relevant as they represent prime progenitors of supermassive black hole (SMBH) binaries, which are expected to be key sources for future gravitational wave detections with the *LISA* observatory.

In **Chapter 6**, we draw our conclusions and discuss future perspectives.

Throughout all the thesis, we will assume $\Omega_{\rm m} = 0.286$ and $H_0 = 69.9$ km s^{-1}Mpc^{-1}

[Bennett et al., 2014].

1.2 The standard picture of galaxy evolution

Everything evolves with time. People grow and change. When I first thought about embarking on this journey into astrophysics, I was a child, younger and shorter, and I had much less knowledge and experience than I have now at the end of this PhD. Similarly, but over timescales far longer than a human lifetime, galaxies also evolve. The structure of a galaxy in the early Universe was very different from what we observe today. At the highest redshifts, distant in time and space, galaxies appear small, clumpy, irregular, growing rapidly through high burst of star formation and mergers. In the local Universe they tend to be more massive, well-structured with large bulges and extended disk, and many are now quiescent, with no available gas to form new stars. How does this evolution occur? The scientific consensus obtained through both observations and simulations was that in the early Universe, galaxies grow and evolve through hierarchical mergers (e.g., Conselice [2003], Rodriguez-Gomez et al. [2015], Duncan et al. [2019], Ferreira et al. [2020]) and although observational studies of extremely high-redshift galaxies were previously limited, the fraction of peculiar galaxies increased with redshift. However, the first JWST observations challenged this picture. In fact, Ferreira et al. [2023], Nelson et al. [2023], and Robertson et al. [2023] found a higher fraction of high-redshift massive disks and a lower fraction of peculiar galaxies than expected. This could create several tensions with galactic formation models, but the overall picture of galaxy evolution remains unchanged, and given that the low-mass galaxies are mostly seen merging, this still points toward mass assembly via mergers. One of the main question is: how do galaxies grow? How does the gas accrete onto the center of the galaxy, from kilo-parsec to sub-parsec scales?

1.2.1 The growth of galaxies and the role of merging

One of the main problems hindering the feeding of SMBHs is the loss of angular momentum: in fact, the gas must lose several orders of magnitude of specific angular momentum to move from kiloparsec scales to sub-parsec accretion disks [Frank and Rees, 1976, Bournaud and Combes, 2002, Combes et al., 2025]. This loss is primarily driven by gravitational torques produced by non-axisymmetric structures such as stellar bars, spiral arms, and tidal interactions, which redistribute angular momentum between stars and gas, enabling the latter to flow inward. On smaller scales, clumpy instabilities and turbulence can induce gas inflows toward the central regions.

Another mechanism that has long been predicted to play a significant role in the evolution and overall mass build-up of the galaxy is galaxy mergers [White and Rees, 1978]. They are quite common, given that the typical separation between galaxies is only about a hundred times their own size, much less than the separation (relatively to their size) between stars in star clusters. The duration of the mergers, from the first encounter to the final relaxed single object stage, is very long and can last 10-20% of the age of the universe. The final stage of the mergers are instead shorter ($\sim$100-200 Myr) and more violent and also involves the interaction of the two BHs.

Major mergers provide another way to get rid of the initial angular momentum of the gas in the colliding systems. During this phase gas is funnelled towards their centres which can trigger starburst events, i.e., high rates of star formation [Patton

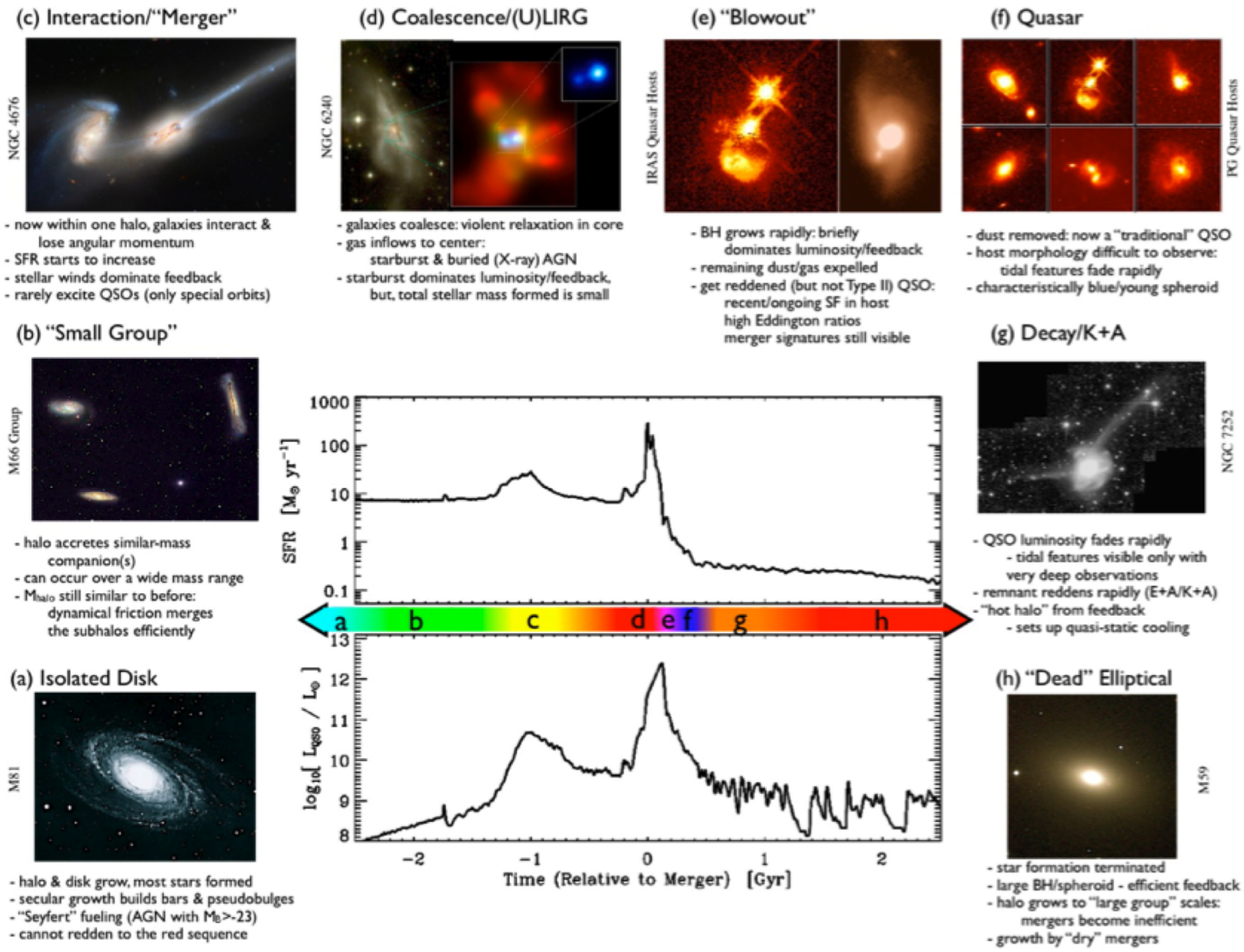

Figure 1.1: Schematic outline of mass accumulation histories of both stellar contents and SMBHs through gas-rich major mergers suggested by hydrodynamical simulations (top and bottom plots in the central panel, respectively). Galaxy mergers induce mass accretion toward the central region of the merged galaxy, causing prominent starburst and triggering (buried) AGN activity. Once SMBH grows rapidly, its violent radiative feedback blows out the surrounding gas, which makes the AGN a luminous quasar visible/recognizable at the optical wavelength. This AGN feedback terminates the star formation. After the gas is consumed, the galaxy will become red and dead (elliptical galaxies). This figure is reproduced from Hopkins et al. [2008]

et al., 2011, Torrey et al., 2012, Patton et al., 2013, Lanz et al., 2013, Moreno et al., 2015, Pearson et al., 2019, Moreno et al., 2019, Patton et al., 2020, Ellison et al., 2022, Thorp et al., 2022, Duan et al., 2024, Yuan et al., 2024, Reeves and Hudson, 2024] or can also trigger AGN activity [Silk and Rees, 1998, Hopkins et al., 2008, Ellison et al., 2011, Gao et al., Sharma et al., 2024, Duan et al., 2024]. These events can generate powerful stellar winds or AGN-driven outflows that may suppress accretion, leading to a phase of self-regulated growth. This represents the most rapid and active stage in a galaxy's evolution, potentially culminating in a blowout event that expels most of its gas and dust, quenching star formation, and leaving behind a red, quiescent galaxy. As inferred from Fig. 1.1, the blowout phase occurs over a short timescale ($\sim$100–200 Myr), followed by a rapid decline in the star formation rate by up to a factor of $\sim$1000.

The interplay between gas inflow, angular momentum transport, star formation, and feedback is therefore central to understanding the co-evolution of galaxies and their central black holes during the active phase [Combes et al., 2025].

However, despite this general picture, the quantitative impact of mergers on star-formation rates remains debated, with studies showing conflicting results. Some suggest that mergers have minimal effects on the SFR [Pearson et al., 2019, Renaud et al., 2022] while others report a significant enhancement of star formation as a result of these mergers [Ellison et al., 2010, Scudder et al., 2012, Patton et al., 2013, Davis et al., 2015, Patton et al., 2020].

1.3 Active Galactic Nuclei

Given the pivotal role of AGNs in galaxy evolution, this section provides a detailed description of their main characteristics. The main feature that distinguishes AGNs from normal or inactive galaxies is the presence of a SMBH at the center, accreting material (hence "active"). The first hint of the existence of AGNs was found by Edward A. Fath in 1908, who detected bright emission lines in the nuclear spectrum of the galaxy NGC 1068 [Fath, 1908]. Edwin Hubble, in 1926, recorded the presence of emission lines in other sources, and in the late 1940s, Carl K. Seyfert observed a few luminous objects showing broad emission lines produced by atoms in a wide range of ionization states [Seyfert, 1943]. The unknown nature of these objects led astronomers to describe them as Quasi-Stellar Objects (QSOs), shortened to quasars, reflecting the fact that they appeared as luminous point-like sources.

Detailed studies of large samples of AGNs began in the late 1970s, thanks in part to developments in radio astronomy. A peculiar feature of these objects is their emission over a wide range of frequencies (approximately 10 orders of magnitude), from radio to X-ray, unlike normal galaxies, which show spectra mainly limited in the optical/NIR wavelengths.

Unlike the spectra of stars or normal galaxies, AGN spectra cannot be described solely in terms of blackbody emission; non-thermal processes, such as synchrotron radiation, must also be invoked.

1.3.1 The engine of AGN

AGNs are among the brightest extragalactic sources. The nature of their "central engine" was long debated, but the most widely accepted model involves a hot accretion

disk surrounding a SMBH [Shakura and Sunyaev, 1973]. This represents the most efficient accretion process known in astrophysics. Accretion disks in galactic centers naturally form from infalling gas, which settles into the central plane of the galaxy while retaining most of its angular momentum. Viscosity within the disk provides a mechanism to transport angular momentum outward, allowing gas to spiral inward and release a significant fraction of its gravitational energy. This energy can be converted into electromagnetic radiation with high efficiency, or into kinetic energy carried away by outflows.

The fundamental process at work in an active nucleus is the conversion of mass into energy with an efficiency η_r. The luminosity, i.e., the rate at which energy is emitted by the nucleus, is given by

$$L_{\mathrm{AGN}} = \frac{\eta_r}{1-\eta_r}\,\dot{M}_{\mathrm{BH}}c^2, \tag{1.1}$$

where $\dot{M}_{\mathrm{BH}} = dM/dt$ is the mass accretion rate onto the black hole, and $(1-\eta_r)$ accounts for radiative losses.

The gravitational potential energy of a mass m at a distance r from a central mass M is

$$U = \frac{GMm}{r}. \tag{1.2}$$

Thus, the rate at which the potential energy of infalling material is converted into radiation is

$$L \sim \frac{dU}{dt} = \frac{GM}{r}\frac{dm}{dt} = \frac{GM\dot{m}}{r}, \tag{1.3}$$

where $\dot{m} = dm/dt$ is the mass crossing radius r per unit time.

By combining Eqs. 1.1 and 1.3, one finds that the mass-to-energy conversion efficiency is proportional to M/r, which reaches its maximum when the central object is a black hole, as in AGNs and when the material is accreting at the Schwarzschild radius. Simplified estimates suggest $\eta_r \sim 0.1$, i.e., more than an order of magnitude higher than the efficiency of nuclear fusion. Such a high efficiency, combined with SMBH masses of millions to billions of solar masses, implies that the total energy output can exceed the binding energy of the AGN host galaxy. Consequently, AGNs can strongly influence galaxy evolution by heating gas in and around galaxies. All processes involving the interaction between black hole-released energy (radiative or mechanical) and the host galaxy are collectively referred to as AGN feedback and will be discussed later in this chapter.

1.3.2 The structure of an AGN

The detailed structure of AGNs is not yet fully determined, but all proposed models and geometries converge on the presence of the following components. These include a central SMBH surrounded by an accretion disk, a hot corona of relativistic electrons, broad and narrow line regions, a dusty torus and, in some cases, relativistic jets. A schematic illustration of these components is shown in Figure 1.2.

- **Accretion Disk:** The physical properties of accretion in AGN are still a subject of active research. The standard model assumes an optically thick, geometrically thin accretion disk (Shakura and Sunyaev [1973]). The emission from such a disk can be approximated as a sum of black bodies, arising from the local dissipation of the gravitational energy of the infalling gas. In this picture, the disk is treated

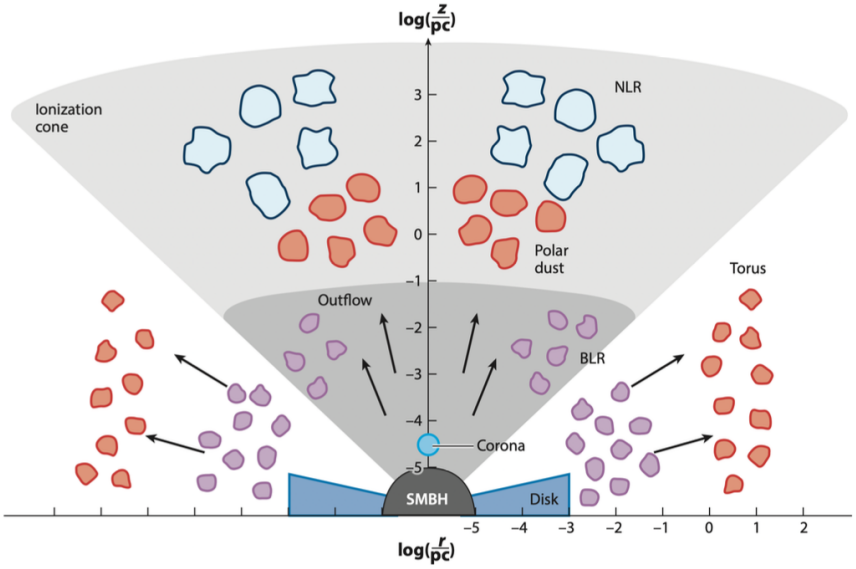

Figure 1.2: Cartoon showing the predicted structure of an AGN. Credit: Hickox and Alexander [2018].

as a series of concentric annuli, each radiating approximately as a black body with a temperature that depends on the radius. The total disk emission is obtained by summing the contributions from all annuli.

Assuming that half of the gravitational energy released is radiated away and the other half heats the disk, the radial temperature profile can be estimated. The rate at which gravitational energy is dissipated at a radius r is

$$\frac{dU}{dt} = \frac{GM\dot{m}}{r},$$

and the corresponding luminosity is

$$L = \frac{GM\dot{m}}{2r}. \tag{1.4}$$

Applying the Stefan-Boltzmann law to the disk surface, one finds

$$L = 2\pi r^2 \sigma_{\rm SB} T^4, \tag{1.5}$$

from which the temperature as a function of radius can be expressed as

$$T(r) = \left(\frac{GM\dot{m}}{4\pi\sigma_{\rm SB} r^3}\right)^{1/4}. \tag{1.6}$$

A more accurate physical treatment (e.g., King et al. [2008]) gives the surface temperature profile as

$$T(r) = \left[\frac{3GM\dot{m}}{8\pi\sigma_{\rm SB} r^3}\left(1 - \sqrt{\frac{R_{\rm in}}{r}}\right)\right]^{1/4}, \tag{1.7}$$

where $R_{\rm in}$ is the inner radius of the accretion disk. As these equations predict, the disk temperature increases toward the center, causing the peak frequency of the emission from each annulus to shift to higher energies. Typical temperatures range between 10^5 and 10^6 K, producing a multi-color black body spectrum that primarily covers the optical/UV band and, in some cases, extending into the soft X-ray range in case of low massive central SMBH.

- **Corona:** The accretion disk is thought to be surrounded by a hot corona of relativistic electrons, although its exact properties and location remain uncertain. In the simplest models, this component serves as the primary source of X-ray emission (two-phase model; Haardt & Maraschi 1991) and is described as a hot ($T \sim 10^8$–10^9 K), tenuous ($n \sim 10^8\,{\rm cm}^{-3}$), optically thin plasma. The corona is likely located above or within the inner regions of the accretion disk, at distances of roughly 3–10 $r_{\rm g}$ from the central black hole [Fabian et al., 2015].

- **Broad-Line Region (BLR):** At sub-parsec scales from the nucleus lies the BLR, a system of dense gas clouds orbiting the central SMBH and partially covering the ionizing source. The high density in the BLR suppress all the optical forbidden emission but not the semiforbidden. The strongest predicted emission are Hα, Lyα, MgII, CIVλ1549, OVIλ1035. The dynamics of these clouds are dominated by the gravitational potential of the SMBH, making the kinematic properties of the BLR a crucial tool to constrain the mass and structure of the central engine. Analysis of the emission line intensities indicates a characteristic gas temperature of approximately 10^4 K. The observed line widths are dominated by Doppler broadening caused by the high velocities of the BLR clouds, ranging from ~ 1000 to $> 10^4\,{\rm km\,s}^{-1}$, with a typical full width at half maximum (FWHM) of $\Delta v \sim 5000\,{\rm km\,s}^{-1}$.

- **Narrow-Line Region (NLR):** The NLR extends from tens to thousands of parsecs from the central SMBH. Given its distance, it is the only AGN component that can be spatially resolved in the optical. The NLR is of great importance, as it represents the largest spatial scale where the ionizing radiation from the central source dominates over other processes, such as star formation or shocks. The intensity of the emission lines observed in NLR spectra provides direct information on the physical conditions of the ionized gas. Unlike the BLR, the electron densities in the NLR are low enough to allow the detection of many forbidden transitions that at higher densities would be collisionally suppressed. The ratios of specific forbidden lines can therefore be used to estimate both the electron density and the temperature of the gas. Optical and UV spectra of numerous sources reveal a wide variety of emission lines, covering a broad range of ionization states: from low-ionization lines such as [O I] λ6300, to intermediate-ionization lines like [O III] $\lambda\lambda 4959, 5007$, and in some cases even very highly ionized species such as [Fe VII] λ6087, [Fe X] λ6375, and coronal lines.

  The emission line profiles in the NLR are often asymmetric, frequently showing an excess of flux on the blue side. This is generally interpreted as evidence for a net outflow (or inflow) of NLR clouds through a dusty medium, which preferentially obscures the redshifted emission. Modern IFU instruments enable two-dimensional spatial and velocity mapping of the NLR, revealing that its morphology is usually asymmetric rather than spherically symmetric. In addi-

tion to photoionization, collisional ionization and shock heating are thought to contribute significantly to the ionization balance of the NLR gas. In AGN with high radio power, the NLR axis typically aligns with the radio axis, suggesting a physical connection between the thermal narrow-line gas and the non-thermal plasma responsible for radio emission. In several cases, the radio morphology shows evidence of shocks at the interface between the radio jets and the interstellar medium of the host galaxy. These shocks can compress and accelerate the gas, generating bow shocks and producing post-shock material that is subsequently photoionized by the central source.

One of the most distinctive morphological features of the NLR, particularly in type II AGN, is the presence of "ionization cones": wedge-shaped structures extending over kiloparsec scales and characterized by a high [O III] $\lambda5007/\mathrm{H}\beta$ ratio. These cones can appear either as single-sided or bi-conical structures, and their axes are not necessarily aligned with the symmetry axis of the host galaxy. The presence of ionization cones demonstrates that the NLR gas is illuminated anisotropically, consistent with the scenario in which the central source of ionizing radiation is obscured by a dusty torus. However, it remains unclear whether the torus itself collimates the radiation, or whether the radiation is already anisotropic at smaller radii and simply carves out the observed openings in the torus.

- **Dusty Torus:**

  The region between ~ 0.1 to ~ 10 pc from the central SMBH is commonly referred to as the molecular torus. Its properties, inferred by interpolation between BLR and the NLR, include typical densities of $n \sim 10^4$–10^7 cm^{-3} and velocity dispersions of $\Delta v \sim 1000$ km s^{-1} [e.g., Jaffe et al., 2004]. Located at a sufficient distance from the ionizing radiation, this region contains both dust and molecular gas. Its detailed geometry remains debated, with models ranging from smooth to clumpy distributions, a combination of the two or, in some cases, including an extended component of dusty material along the polar axis often observed in outflow [e.g., Stalevski et al., 2012, 2016, Lopez-Rodriguez et al., 2025, Isbell et al., 2025]. However the main role of the torus is that absorbs the optical and UV emission from the accretion disk and reprocesses it into IR radiation.

- **Jets:** Ejected material from an accreting SMBH can manifest as highly collimated and powerful relativistic jets [Begelman et al., 1984]. These structures extend from parsec to megaparsec scales and emit synchrotron radiation as well. Also high-energy emission in the X-ray and γ-ray bands can arise from inverse Compton processes. Relativistic outflows are typically launched along the polar axis, radiating across the entire electromagnetic spectrum. Jets are most commonly observed in these directions, where dusty outflows are also detected. Usually the radio spectra from very compact sources are flat or slightly inverted, and indicate the base of a jet. High-resolution radio observations further reveal that many Seyfert galaxies host compact, sub-parsec scale nuclear emission with brightness temperatures exceeding 10^7 K, and in some cases display misaligned parsec-scale jets, possibly indicative of jet precession or binary AGN (Middelberg et al. [2004], Giroletti and Panessa [2009], Panessa and Giroletti [2013]).

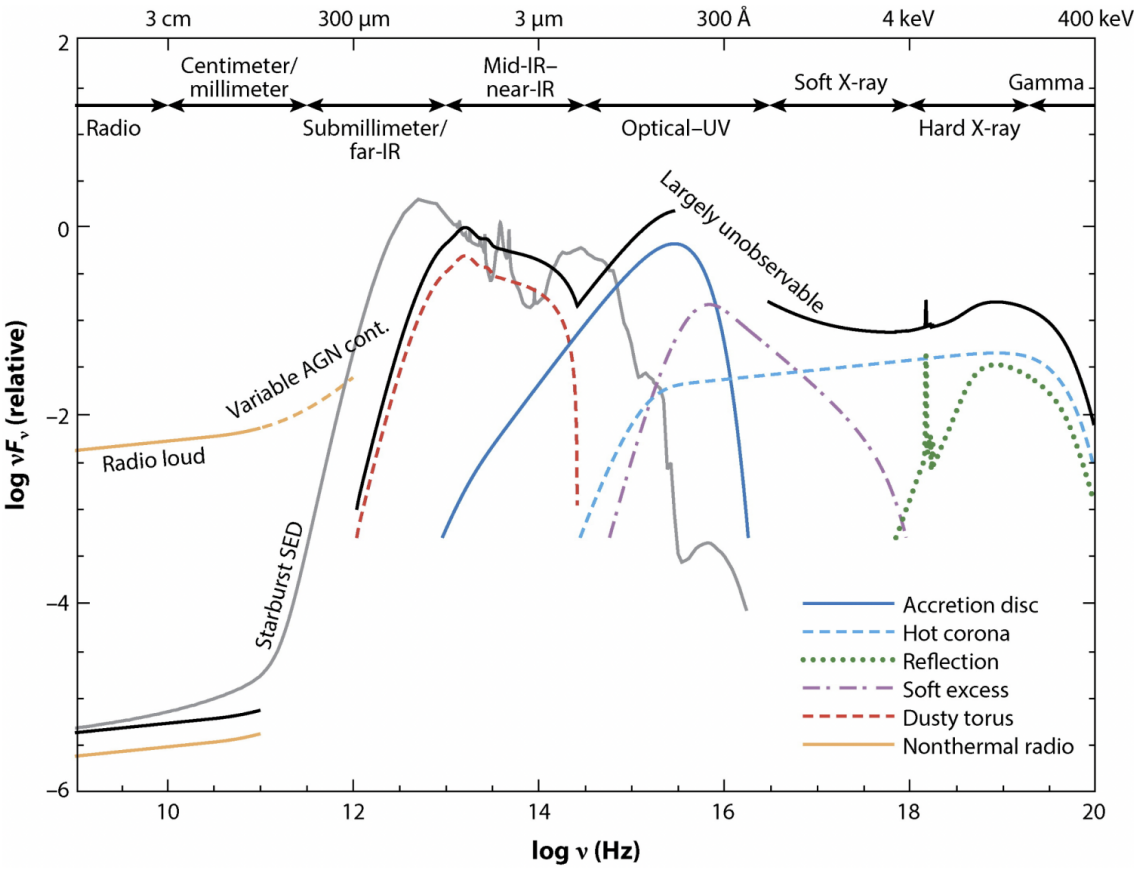

Figure 1.3: Broad-band SED of an unobscured AGN (black curve) across the broad gamma ray–radio waveband: the frequency and wavelength ranges for individual wavebands are highlighted. Individual continuum-emitting components are coloured and labelled including emission from a star-forming component (grey curve) and the brighter radio emission from a radio-loud AGN (labelled yellow curve, Hickox and Alexander [2018]).

1.3.3 The Spectral Energy Distribution

AGN are unlike any other class of astronomical object. They cannot be described by a single, dominating process. Instead, AGN radiate energy over the entire electromagnetic spectrum, and are the sites of pair-production, cosmic rays, and gravitational waves. Radiation is created through multiple processes, including blackbody, synchrotron, Comptonisation, bremsstrahlung, and line emission. Gravity attracts material inward toward the black hole, but mass and energy can also be ejected into the host galaxy and beyond. Gas can be viewed in absorption and emission, and it exists in various physical states that can be optically thick and thin, as well as neutral and completely ionized. Ionisation can occur through collisional and radiative excitation. Moreover, all these physical processes are subject to extreme gravity and magnetic fields, often invoking special and general relativity and relativistic magnetohydrodynamics (MHD). In this section, we will present the spectral energy distribution (SED) of AGNs from X-rays to radio. In Fig.1.3 a typical AGN SED over all the electromagnetic spectrum is shown, with the most relevant components labeled.

X-ray

AGN emission in the X-ray band ($\sim 0.1 - 100$ keV; see Fig. 1.3) provides a powerful probe of the innermost regions of these systems. The X-ray radiation emerging from within a few tens of gravitational radii ($R_{\rm G} = GM/c^2$) is primarily produced in the hot corona through thermal Comptonization in an optically thin plasma of relativistic electrons. This primary X-ray continuum illuminates the inner accretion disc, giving rise to a reflection spectrum that is subsequently blurred by relativistic effects near the black hole.

In type I AGN, the soft X-ray spectrum is typically characterized by several narrow absorption lines superimposed on a strong continuum. In contrast, type II AGN display narrow emission lines more prominently, since the central continuum is strongly attenuated by obscuration. A spectral feature common to both classes is the iron Kα emission line at 6.4 keV. In type I AGN, this line is relatively weak and broad, with an equivalent width (EW) of $\lesssim 100$ eV. In type II AGN, where the central engine is obscured at 6.4 keV, the iron Kα line is much stronger (EW $\sim 1 - 2$ keV) and remains narrow.

A useful diagnostic to connect the X-ray and ultraviolet (UV) properties of AGN is the optical-to-X-ray spectral index, $\alpha_{\rm ox}$. It is defined as

$$\alpha_{\rm ox} = \frac{\log\left(L_{2\,\rm keV}/L_{2500\ \text{Å}}\right)}{\log\left(\nu_{2\,\rm keV}/\nu_{2500\ \text{Å}}\right)}, \tag{1.8}$$

where $L_{2\,\rm keV}$ and $L_{2500\ \text{Å}}$ are the monochromatic luminosities at 2 keV (X-rays) and 2500 Å (UV), respectively. This parameter effectively quantifies the relative strength of the X-ray emission compared to the UV continuum and provides insights into the coupling between the accretion disc and corona. Studies show that Lx/LUV is luminosity dependent such that increases with $L_{\nu(\,2500)}$ It was generally found that $\alpha_{\rm ox}$ is anti-correlated with the UV luminosity (see e.g. Lusso et al. [2012]). This observed anticorrelation between $\alpha_{\rm ox}$ and UV luminosity suggests that in more UV-luminous AGN the corona is relatively less efficient at producing X-rays, leading to a weaker X-ray compared to the stronger disc emission.

UV and optical band

The UV and optical band is dominated by the emission of the accretion disk and the stellar continuum. In luminous type I AGNs, the observed emission has a predominantly nonstellar origin, as indicated by the absence of strong stellar absorption features. The luminosity of this nuclear, nonstellar component relative to the host galaxy can vary by several orders of magnitude. However, many AGN in local Universe are much fainter than their host galaxy and stellar emission dominated their total light. The AGN luminosity increases with decreasing wavelength, meaning that the stellar light contaminates less at UV wavelengths.

In the UV and optical ranges, AGN spectra exhibit a rich set of broad and narrow emission lines originating from photoionized gas in the BLR and NLR, respectively. The most prominent features in the optical band include the hydrogen Balmer lines (especially Hα and Hβ), [OIII]λ5007, [NII]$\lambda\lambda$6548, 6583, and [SII]$\lambda\lambda$6716, 6731. In the UV, strong emission lines such as Lyα, CIVλ1549, CIII]λ1909, SiIVλ1397, and MgIIλ2798 dominate the spectrum. Among these, FeII is particularly complex: its nu-

merous transitions blend into broad, irregular features, making it challenging to model or empirically determine the relative line intensities.

- **Type I and Type II AGN**

  Nowadays, the classification of AGNs is mainly based on the features observed in the optical spectra.
  Khachikian and Weedman [1974] were the first that distinguished two types of AGNs: Type 1 and Type 2. Type 1 galaxies show strong and very broad emission lines (2000-10000 km/s if interpreted as Doppler broadening) that include both permitted and forbidden lines whereas Type 2 galaxies have both permitted and forbidden lines, but showing a very narrow emission line profile with widths that don't exceed 1200 km/s. The comparison of the two spectra is shown in Fig.1.4. Another difference between Seyfert 1 and Seyfert 2 is about the optical-UV continuum of the observed spectrum, in fact Type 1 are dominated by a bright featureless continuum coming from the center of AGN which often overwhelms the continuum produced by stars while in Type 2 the continuum is significantly less luminous. Quasar spectra are similar to those of Seyfert except for the fact that narrow lines are weaker relative to the dominant broad lines.
  We will refer to galaxies with broad lines as 'type I AGNs' or Seyfert 1 and to galaxies with only narrow lines as 'type II AGNs' or Seyfert 2 galaxies.

- **LINER**

  Heckman [1980] identified a very low nuclear-luminosity class of 'Low Ionization Nuclear Emission-line Region' galaxies called LINERs. The spectra is similar to Seyfert 2 galaxies, but they show a very strong low-ionization lines, e.g [OI]λ6300 and [NII]λ λ6548,6583. The [OI]λ6300 line is strong in partly neutral gas ionized by AGN because the X-ray radiation can penetrate beyond HII into the region where most of oxygen is neutral, excite OI and produce [OI]λ6300. Since [OIII]5007/Hβ is not always a good indicator to distinguish ionized regions since the ratio depends also on metallicity, Baldwin et al. [1981b] combined various emission lines intensity ratio to distinguish LINERs from Seyfert galaxies and HII regions.
  Fig.1.5 is an example of BPT diagram (for Baldwin, Phillips and Terlevich) which demonstrate how LINERs can be distinguished from normal AGNs (Seyfert and QSO) and HII regions on the basis of [OIII]/Hβ vs [SII]/Hα and [OIII]/Hβ vs [NII]/Hα. The LINERs can be distinguished from type 2 AGN by their low values of [OIII]/Hβ relative to [NII]/Hα and from HII regions by their larger values of NII/Hα.
  It is not yet fully clear the relationship between LINERs and AGNs but a LINER-type spectra can also be produced in cooling flows, starbust-driven winds and in shock-heated gas (Heckman [1980]).

- **Little Red Dots**

  Recent spectroscopic observations with the James Webb Space Telescope (JWST) have revealed a population of red, compact galaxies at redshifts $z > 3$ [Akins et al., 2023, Kocevski et al., 2023, Labbe et al., 2025, Barro et al., 2024]. These so-called "little red dots" (LRDs) exhibit red rest-frame optical colors but blue rest-frame UV colors, forming a characteristic "V-shape" in their spectral energy

distributions (SEDs). LRDs are likely to host obscured AGNs, as suggested by their SEDs and the frequent detection of broad-line emission in the sample [Greene et al., 2024, Kocevski et al., 2023]. Conversely, some AGNs identified via broad Hα emission are found to correspond to LRDs [Matthee et al., 2024]. While the red optical colors are generally attributed to significant dust attenuation in the AGN, the origin of their blue UV emission remains uncertain; it may arise from scattered light from an obscured AGN or from a young stellar population [Greene et al., 2024].

Although many LRDs display the main feature that characterizes AGNs, the BLR, they also show notable differences compared to typical AGNs. For instance, they do not appear to emit X-rays, have a flattened rather than steeply rising infrared spectrum, and display very little variability among themselves. Furthermore, these high-redshift (high-z, $4 < z < 7$) broad-line AGNs are found to host overmassive black holes (BHs) relative to the relation commonly observed in the local Universe between the mass of the black hole and the stellar mass $M_{\rm BH}$–M_* relation [Harikane et al., 2023, Kokorev et al., 2023, Maiolino et al., 2024a,b, Pacucci et al., 2023, Stone et al., 2023, Chen et al., 2024, Furtak et al., 2024, Yue et al., 2024].

Near, Mid and Far- IR

Near-infrared (NIR; 1–5 μm) observations are sensitive to hot dust at temperatures of $\sim$400–1500 K, which traces the inner edge of the dusty structure at the sublimation radius of dust grains (0.1-1 pc), heated directly by ultraviolet and optical radiation from the accretion disk [e.g., Kishimoto et al., 2009, Hönig, 2019, Kishimoto et al., 2022]. This hot component is often associated with graphite grains, which can survive at higher temperatures than silicates.

Mid-infrared (MIR) emission in AGN is commonly attributed to thermal radiation from dust on parsec scales around the central SMBH. However, high-resolution observations of nearby Seyfert galaxies have revealed that a significant fraction of the MIR output (in some cases $\gtrsim 50\%$) arises from extended emission in the polar region on scales of up to $\sim$100 pc [e.g., Bock et al., 2000, Packham et al., 2005, Hönig and Kishimoto, 2010, Reunanen et al., 2010, Isbell et al., 2025]. In this framework, the innermost, hot part of the dusty structure may be geometrically thick and provide the obscuration associated with the classical torus at sub-parsec scales, while a dusty wind extends along the polar axis over several to tens of parsecs, contributing substantially to the observed MIR emission.

At longer wavelengths, the far-infrared (FIR; $\gtrsim 30\,\mu$m) emission generally traces cooler dust ($T \sim$ 20–60 K) distributed on scales of hundreds of parsecs to kiloparsecs. In many AGN hosts this component is dominated by starburst in the circumnuclear and galactic disk regions, rather than the AGN itself.

- **ULIRG** Ultraluminous infrared galaxies (ULIRGs) with IR luminosities $L_{IR} > 10^{12}$ $L_\odot$ are among the most luminous objects in the local Universe. Their extreme IR luminosity is due to the combination of high SFR and AGN activity, coupled with a high dust content, which intercepts the UV photons emitted from either hot young stars or AGN and reemits them at longer wavelengths [Soifer et al., 1984, Sanders and Mirabel, 1996, Lonsdale et al., 2006, U et al., 2012].

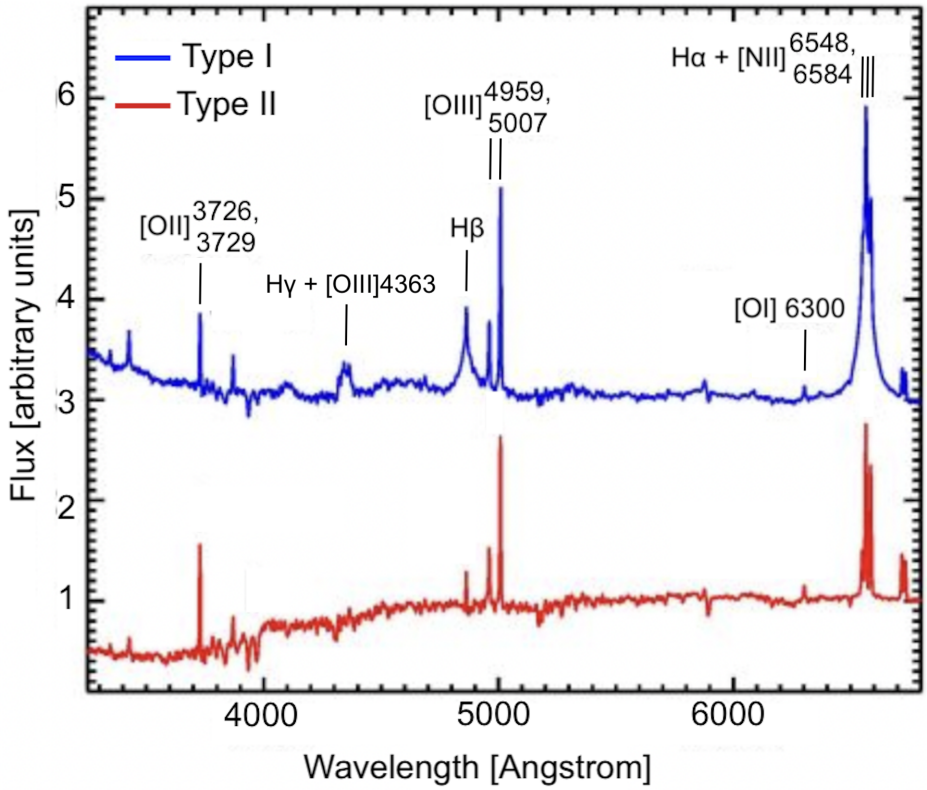

Figure 1.4: Comparison of type 1 (blue) and type 2 (red) AGN spectra. Type 1 AGNs show both broad permitted emission lines (originating from the broad-line region, BLR) and narrow forbidden emission lines (from the narrow-line region, NLR). In contrast, type 2 AGNs exhibit only narrow emission lines, both permitted and forbidden, due to the obscuration of the BLR. In addition, the blue–UV continuum emission at wavelengths shorter than 4500 Å is significantly weaker in type 2 AGNs compared to type 1, as the direct view of the accretion disk is blocked by circumnuclear dust. The figure is adapted from DiPompeo et al. [2018]. The main emission lines are labeled.

In the starburst-quasar evolutionary scenario [Sanders et al., 1988, Hopkins et al., 2008], ULIRGs are thought to represent a rapidly growing phase of massive galaxies. Within this framework, the merger of gas-rich galaxies triggers a phase of vigorous star formation (SF), fueling the growth of SMBHs and the eventual onset of AGN activity. As the merger progresses, powerful outflows generated by both starburst and AGN winds shape the galactic environment, influencing subsequent SF and black hole accretion with feedback mechanisms [Di Matteo et al., 2005, Silk, 2013].

Local ULIRGs may represent scaled-down analogs of the dusty, star-forming mergers observed at $z > 2$ [e.g., Casey et al., 2014]. As such, they provide excellent laboratories for investigating in detail the physical processes that drive the potentially diverse evolutionary pathways of gas-rich galaxy mergers, which played a major role in shaping the high-redshift universe.

Radio

The main mechanism producing radio emission in AGN is the synchrotron radiation, arising from relativistic electrons spiraling around magnetic field lines in the jets and

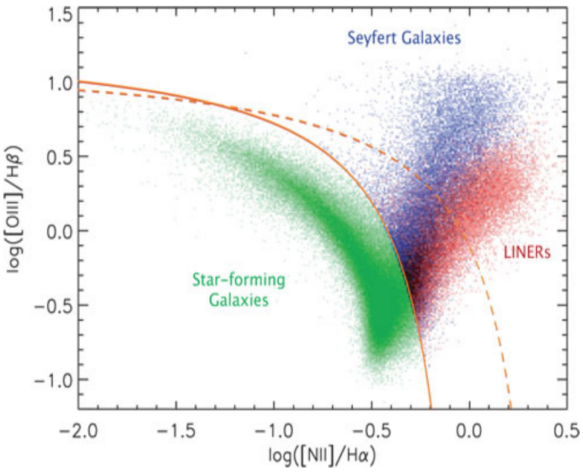

Figure 1.5: An example of a BPT (Baldwin et al. [1981b]) diagram. On x-axis the emission-line flux ratio [OIII]/Hβ and on y-axis the ratio [NII/Hα for 55757 objects detected with SDSS with S/N$>$ 3. The yellow dashed curve shows the demarcation between starburst galaxies and AGN defined by Kewley et al. [2001] while the yellow curve identifies the demarcation by Kauffmann et al. [2003]. Green, blue and red dots stand for star-forming galaxies, AGNs and LINERs, respectively.

lobes. The observed radio spectrum depends strongly on the region from which the emission originates. The compact nuclear core typically shows a flat spectrum ($S_\nu \propto \nu^{-\alpha}$, with $\alpha \sim 0-0.5$) due to self-absorbed synchrotron radiation in the dense, compact plasma. This core emission is often variable on short timescales. In contrast, the extended jets and radio lobes exhibit a steep spectrum ($\alpha \sim 0.7 - 1$), characteristic of optically thin synchrotron emission, and are generally stable over long timescales. High-resolution radio observations allow the distinction between core-dominated and lobe-dominated sources.

- **Radio-quiet and radio-loud AGNs**

  The term quasar was initially associated only with powerful radio sources (radio-loud), but very quickly astronomers realized the existence of AGNs with lower radio emission, called radio-quiet AGNs. The first difference is about the SED of the two classes of objects reported in Fig. 1.3. Whereas the thermal emissions from the AGN (continua and lines from X-ray to infrared wavelengths) are quite similar in the two classes, the radio emission of radio-loud sources is typically 100 times higher than radio-quiet sources. The radio-loud objects show central radio cores or radio jets at large scales, and the kinetic power associated with the jets represents a significant fraction of the total bolometric luminosity. On the other hand, the weak radio emissions from the radio-quiet objects are energetically less significant. Moreover, the radio-quiet objects turn out to be 10–20 times more numerous than radio-loud, representing about 90% of the AGNs. Another difference is about the morphology of the host galaxies of radio-quiet and radio-loud AGNs. In fact, radio-loud objects are usually associated with elliptical galaxies which have undergone recent mergers, while the radio-quiets prefer spiral hosts [Wilson and Colbert, 1995]. It is necessary to distinguish carefully between radio-loud and radio-quiet quasars. A useful criterion appears to be the radio-optical ratio of specific flux at 5 GHz and at 4400 Å. Due to the relation-

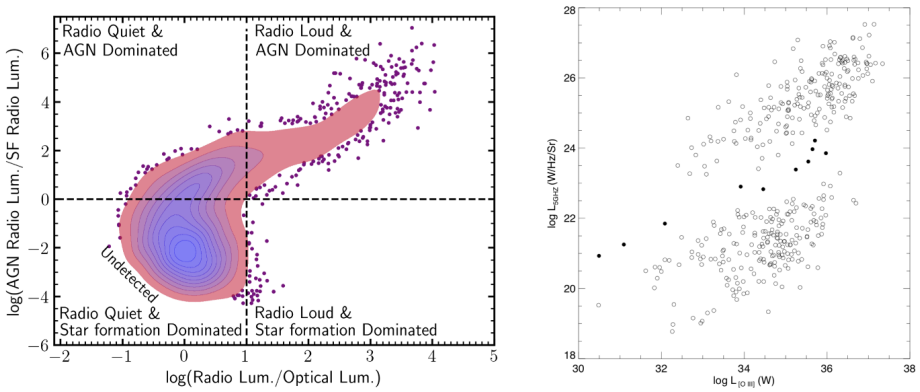

Figure 1.6: Left: comparison between the 'radio-loud' criterion for quasars (x-axis) (i.e., $R = L_{5,\mathrm{GHz}}/L_{4400,\text{Å}}$, with a cut-off value at $R = 10$) and the ratio of radio luminosity attributed to AGN to that attributed to star formation (y-axis). Right: Bimodal distribution of radio-quiet and radio-loud galaxies. Total 5 GHz luminosity vs. [OIII] line luminosity for the sample of 409 AGNs of Xu et al. [1999]. The filled circles represent the intermediate sources.

ship between SFR and the associated radio luminosity in star-forming galaxies, it is possible to estimate the expected contribution of star formation to the total observed radio luminosity [e.g. Helou et al., 1985, Ivison et al., 2010]. Therefore, any galaxy with significant radio emission above this is expected to have radio emission associated with an AGN, and is sometimes labelled as a 'radio AGN' [e.g. Best and Heckman, 2012, Macfarlane et al., 2021, Del Moro et al., 2013]. Historically, radio galaxies are considered loud when $L_{5,\mathrm{GHz}}/L_{4400,\text{Å}}$ is above 10 and quiet when the ratio is below 10 [Kellermann et al., 1989], see Fig. 1.6 (left). Another feature of radio galaxies (both radio-quiet and radio-loud) is that they obey a linear $\log L_{5,\mathrm{GHz}}$–$\log L_{[OIII]}$ relation (see right panel in Fig. 1.6), with a nearly identical slope but with a shift toward higher radio power for the radio-loud sources, by a factor of $\sim 10^3 - 10^4$. The criterion to distinguish radio-loud and radio-quiet is to consider the position of the AGN in the $\log L_{5,\mathrm{GHz}}$–$\log L_{[OIII]}$ relation Xu et al. [1999]. Alternative definitions of radio loudness have been proposed relying on the ratio between radio at GHz and the X-ray luminosities, $R_{\mathrm{X}} = \nu L_{\nu}(5\,\mathrm{GHz})/L_{2-10\,\mathrm{keV}}$ [Terashima et al., 2002]. This approach is particularly well suited for low-luminosity AGN, where optical emission may be strongly contaminated by the host galaxy or affected by extinction, while hard X-rays provide a more direct tracer of the accretion power.

1.4 AGN Unification Model

Once described the main features of the types of AGNs, we introduce the Unified Model of AGNs. This model postulates that all the observed differences between the types of AGN are due to orientation effects with respect to the line of sight to the observer.
As we see in Fig.1.7 the model includes a supermassive black hole, a rotating disk of infalling material surrounding the black hole, a jet speeding outward from the poles of the disk and in order to explain why the same type of object looks different when viewed

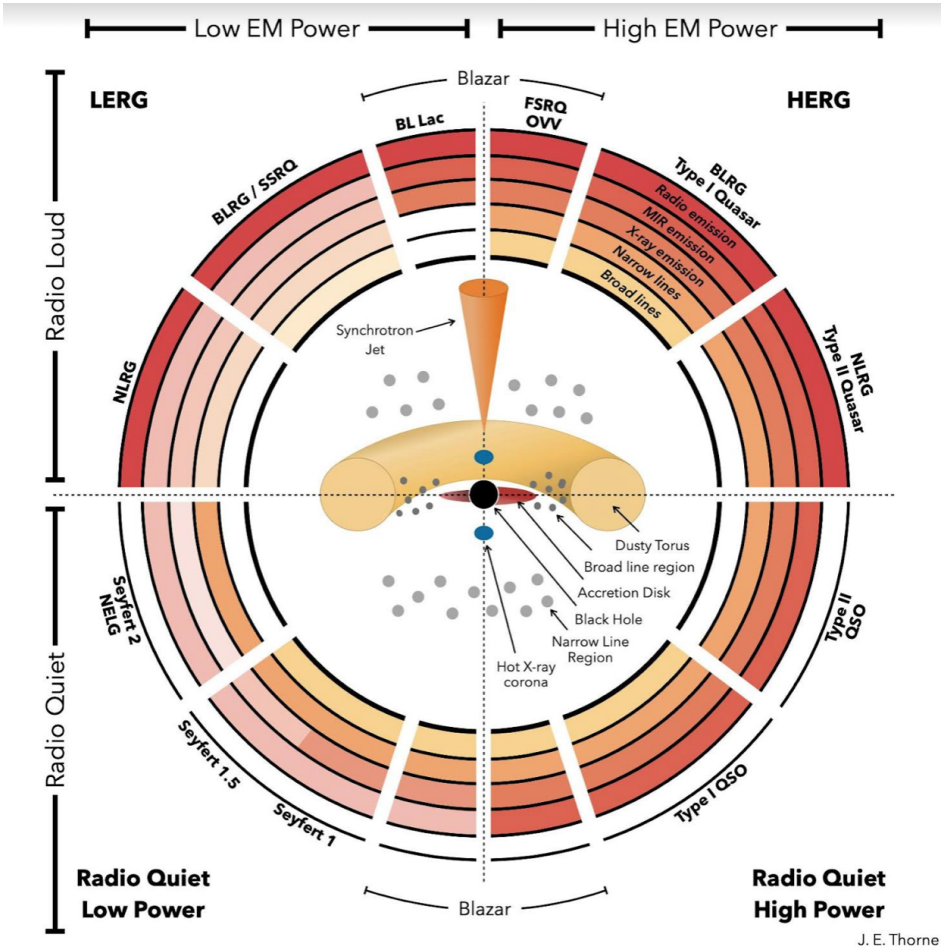

Figure 1.7: AGN unification diagram illustrating the main components of the unification model. The observed type of AGN depends primarily on the orientation of the system with respect to the observer's line of sight (excluding LINERs). The diagram is divided into two main classes: radio-loud AGNs (upper part) and radio-quiet AGNs (lower part). The intensity of each concentric shell represents the relative strength of different emission components, moving outward from the center: broad emission lines, narrow emission lines, X-ray emission, mid-infrared (MIR) emission, and radio emission. Blazars correspond to sources in which the jet is aligned with the observer's line of sight. Type I AGNs and broad-line radio galaxies (BLRGs) are observed when the line of sight is at an intermediate angle to the jet axis, while type II AGNs and narrow-line radio galaxies (NLRGs) appear when the view of the nucleus is obscured by the dusty torus.

from different angles, a thick, dusty, doughnut-shaped 'torus' is included. An estimation of the size of the toroidal structure is in the order of parsec scale, large enough to obscurate the center of AGN where broad lines are emitted and small enough not to obscure the lower-density gas surrounding the center where narrow lines are produced. A strong observational evidence of Unified Model between type 1 and type 2 AGNs was obtained by Antonucci and Miller [1985] when they discovered broad optical lines in the polarized spectrum of NGC 1068 (classified as Seyfert 2). This discovery revealed the presence of a BLR in Seyfert 2 nucleus, which is hidden to our line of sight, but whose light is scattered in our direction.
Another piece of evidence is the direct correlation between the luminosity of Hα, $L_{H\alpha}$, and the luminosities of featureless continuum at wavelength near $L_{4400,\text{Å}}$ in different types of AGNs. This evidence suggests that the hydrogen emission lines produced via the photoionization of H atoms by the continuum radiation and the subsequent recombination in type I and type II AGNs has a common origin.
Osterbrock [1977] suggested that type 1 and type 2 are physically the same objects, but in Seyfert 2s the BLR is obscured from our view by a dust torus surrounding the central source. The differences is due to the position of the observer, in fact, in case of Seyfert 1 the observer is looking at the central source along the torus axis and the obtained spectra will show broad lines, while in Seyfert 2s the central source is covered and only the narrow line region can be observed.
This model is independent of the radio emission of the source. In fact, also radio galaxies are classified by their optical properties into broad-line radio galaxies (BLRGs) and narrow-line radio galaxies (NLRGs) and the Unified model suggests that this difference is due to the position of the observer. The optical-UV spectrum of BLRGs is very similar to the spectrum of type I AGNs with some indication for an additional nonthermal contribution to the optical continuum. The optical emission-line spectrum of NLRGs show features sometimes similar to type II AGNs and sometimes similar to LINERs.

1.5 Interacting AGN

The formation and growth of SMBHs are closely linked to the evolution of their host galaxies. When two galaxies merge, the SMBHs in their nuclei become part of the same post-merger galaxy, and eventually merge together, typically on timescales of the order of Gyr [e.g. Khan et al., 2012]. In the final stages of a merger, both SMBHs may be simultaneously active, forming a dual AGN system (i.e. two accreting SMBHs within a single merged galaxy). These systems provide a unique laboratory for studying SMBH growth, AGN triggering, and the interplay between galaxy evolution processes and nuclear activity. Simulations predict that dual AGN can form in both major and minor galaxy mergers [e.g., Capelo et al., 2015, 2017, Chen et al., 2023], with longer observable dual-AGN lifetimes expected in major mergers. Conversely, the highest SMBH mass ratios are predicted to arise in minor mergers, which may dominate the observed population at lower luminosities ($< 10^{44}\,\text{erg}\,\text{s}^{-1}$). One of the major challenges in theoretical studies of galaxy evolution concerns the predicted frequency of these interacting AGN. The expected occurrence of dual and binary AGNs, in particular, depends on several key factors, such as the galaxy merger rate, the characteristic timescales over which mergers take place, and the probability of AGN triggering after a merger. Because these parameters are highly uncertain, different works and cosmological simulations predict divergent predictions ranging between a dual AGN fraction

(defined as the number of AGNs in pair divided by the total number of AGNs) of 10^{-4} in the EAGLE simulation to 0.1 in Romulus (see Fig. 1.8) [Rosas-Guevara et al., 2019, Volonteri et al., 2022].

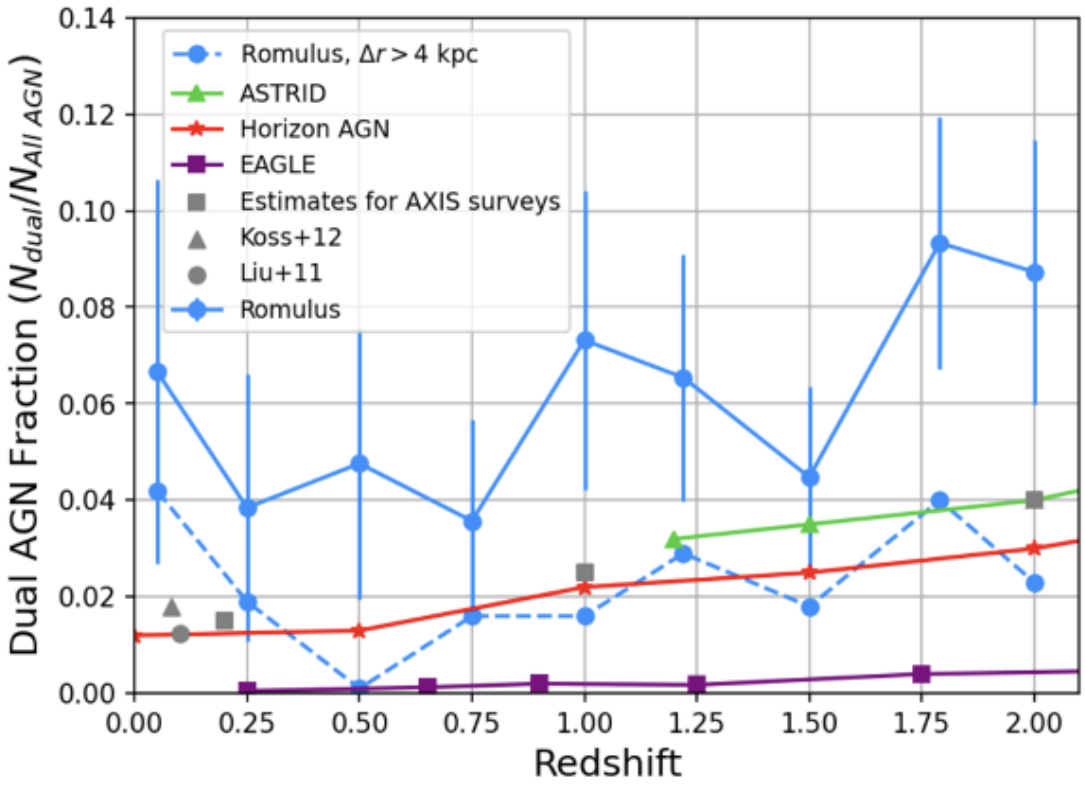

Figure 1.8: Predictions of the DAGN fraction as a function of redshift from different cosmological simulations: Romulus Saeedzadeh et al. [2024] ASTRID (Chen et al. [2023], green), Horizon-AGN (Volonteri et al. [2022], red), EAGLE (Rosas-Guevara et al. [2019], purple). Observational estimates are shown with grey triangle (Koss et al. [2012]) and grey circle (Liu et al. [2010]), while the grey square shows observational predictions for upcoming AXIS surveys (Foord et al. [2024])

While theoretical models predict that dual AGN should be relatively common, especially at separations below several kpc [e.g. Rosas-Guevara et al., 2019, Volonteri et al., 2022, Chen et al., 2023], observational studies have found mixed results, with reported dual AGN fractions ranging from a few percent to about 25% depending on selection method and sample properties [e.g. Koss et al., 2012, Perna et al., 2025]. However, these estimates are possibly affected by several biases, including reliance on visual classification which can miss obscured or compact systems, as well as luminosity cuts, maximum separation, and the selection of the sample considered. Quantifying the frequency and properties of dual AGN as a function of separation, redshift, and host galaxy properties (e.g. extinction, star formation, black hole mass) is essential for constraining models of SMBH formation and co-evolution with galaxies. In particular, galactic scales ranging from tens of kiloparsecs to tens of parsecs represent a key regime, corresponding to the late stages of mergers when SMBHs are on the path to forming bound binaries.

On the observational side, there is still a lack of robust statistical samples of kpc-

scale dual AGN systems at $z > 1$. Identifying such systems poses significant challenges, primarily due to the stringent requirements on spatial resolution and reliable AGN diagnostics. For instance, detecting dual AGN at kpc separations requires sub-arcsec resolution, while their intrinsic rarity demands wide-area searches.

Below we list the methods used in the literature to detect interacting AGNs such as dual AGNs and binary AGNs. In these works a distinction is often made between dual AGN and binary AGN based on their spatial separation. Systems in which the two AGNs are gravitationally bound with separations less than 30 pc are classified as binary AGN, whereas systems with larger separations are referred to as dual AGN.

1.5.1 Dual AGN

Over the past decades, several systematic approaches have been developed to identify dual AGNs. One of the most widely used methods focuses on detecting double-peaked AGNs (DPAGNs), where the presence of two velocity components in emission lines may indicate dual or binary SMBHs with projected separations ranging from ∼30 pc to 10 kpc [e.g. Wang et al., 2009]. Thanks to large spectroscopic surveys such as the Sloan Digital Sky Survey (SDSS) and the DEEP2 Galaxy Survey, hundreds of DPAGN candidates have been identified [e.g. Wang et al., 2009, Liu et al., 2010, Smith et al., 2010, Rosario et al., 2011, Ge et al., 2012, Barrows et al., 2013, McGurk et al., 2015]. However, follow-up observations using spatially resolved long-slit, integral-field spectroscopy [e.g. McGurk et al., 2011, Shen et al., 2011, Comerford et al., 2012] and high-resolution imaging [e.g. Liu et al., 2013, Comerford et al., 2015, Müller-Sánchez et al., 2015] have revealed that only about 2–5% of DPAGNs are dual AGNs. In most cases, the observed double peaks arise instead from complex gas kinematics around a single AGN—such as rotating disks or biconical outflows within the narrow-line region [e.g. Comerford et al., 2012, Smith et al., 2010, Shen et al., 2011, Fu et al., 2011, 2012, Nevin et al., 2016]. More recently, alternative systematic searches based on radio imaging [Fu et al., 2015] and mid-infrared color selection [Satyapal et al., 2014, 2017] have been proposed, although the number of confirmed dual AGNs remains very limited.

One of the methods that has proven to be most efficient is the Gaia Multi-Peak (GMP) technique (Mannucci et al. [2022], Scialpi et al. [2023]), which leverages Gaia's high spatial resolution (FWHM ≈ 0.11") to detect multiple peaks in the one-dimensional light profiles of sources. The method uses the parameter `ipd_frac_multi_peak`, introduced in EDR3, to select objects with a high fraction of transits exhibiting multiple peaks-signaling systems with multiple compact optical components. As shown in Fig. 1.9a, this technique has made it possible to find dual AGNs up to redshift 3 with separations of less than 0.8", representing a significant improvement over other methods such as vastrometry or double peak AGN. However, this approach is limited to optically bright quasars due to Gaia's magnitude limit of $G \sim 21$, corresponding to $L_{\rm bol} \gtrsim 10^{46}$ erg s^{-1} at $z \gtrsim 0.5$. Consequently, Gaia-selected samples probe only the most luminous AGN population, introducing a significant bias against more typical, moderate-luminosity AGN and limiting the completeness of these surveys. The *Euclid* telescope, thanks to its high spatial resolution (FWHM∼0.15"), extensive sky coverage, stable PSF, and multi-band photometric capabilities, allows for a selection of candidates up to 4 magnitudes fainter than Gaia and with a much larger luminosity ratio (see Fig. 1.9b) gathering a representative sample of QSO with $L_{\rm bol} \sim 10^{44}$ erg s^{-1}

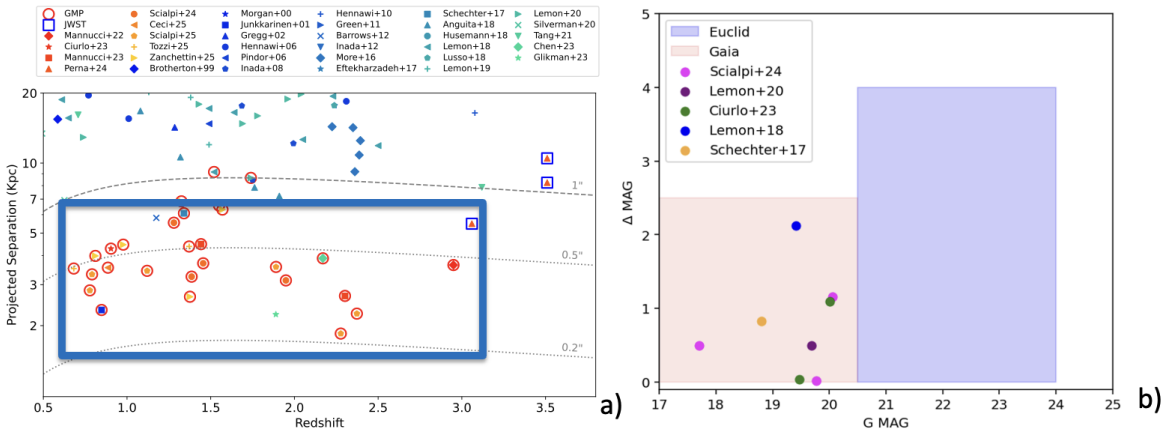

Figure 1.9: a) Projected separation vs. redshift of all confirmed dual AGN at $z > 0.5$ from the literature and from the GMP method (updated compilation not yet published). Blue square represents the region probed by *Euclid*, b) Magnitude difference between the primary and secondary source as a function of the mean G-band magnitude for *Gaia* (red shaded area) and *Euclid* (blue shaded area). Literature systems are overplotted with different colors according to the reference. As shown, *Euclid* selected sample will cover an unexplored parameter space.

1.5.2 Binary AGN

Once the host galaxies have merged into a single spheroid, the SMBHs previously residing at the centers of the progenitor galaxies, are expected to undergo subsequent phases of growth [Blecha, 2017] as they sink toward the center of the post-merger remnant galaxy. This migration occurs from kiloparsec scales down to tens of parsecs through dynamical friction [Blecha, 2017, Capelo et al., 2015, Van Wassenhove et al., 2012]. At parsec to few tens of parsec scales (depending on the SMBH masses), the SMBHs form a gravitationally bound binary system [e.g., Begelman et al., 1980, Rodriguez et al., 2006]. The binary then continues to harden through several processes: dynamical friction, stellar scattering, viscous drag within a circumbinary disk, and ultimately, gravitational wave (GW) emission [e.g., Begelman et al., 1980, Volonteri et al., 2003, Kelley et al., 2017]. These mechanisms are expected to dominate the binary hardening on scales of $\gtrsim$1 pc, $\sim$0.01–1 pc, 10^{-5}–0.01 pc, and $< 10^{-5}$ pc, respectively, based on results from the Illustris simulations [Kelley et al., 2017]. The coalescence of inspiraling SMBH binaries not only results in a single, more massive SMBH but also generates strong gravitational waves. Inspiraling SMBHs are considered the most plausible source of the recently detected low-frequency GW background reported by the NANOGrav 15-year PTA collaboration [Agazie et al., 2023]. Future space-based GW observatories, such as the Laser Interferometer Space Antenna (LISA; Amaro-Seoane et al. 2023), will be capable of detecting GW signals from inspiraling intermediate-mass black hole binaries over the next few decades.

To date, only a two binary AGN have been unambiguously confirmed in the literature: J0402+379, discovered by Rodriguez et al. [2006], which exhibits two distinct compact radio cores separated by $\sim$7 pc, spatially resolved via Very Long Baseline Interferometry (VLBI). These dual, flat-spectrum radio cores provide direct evidence of two actively accreting SMBHs within a single galactic nucleus. The other case of binary system is OJ 287 whose 136 yr long optical light curve has been explained by

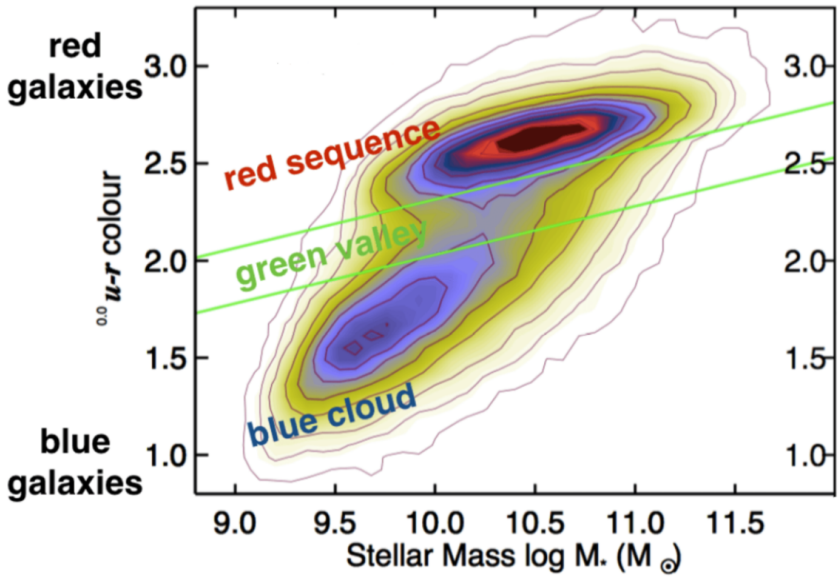

Figure 1.10: Colour–mass diagram from Schawinski et al. [2014], based on a local sample of approximately 47,700 galaxies. Galaxies are distributed in two main regions of the diagram: the diffuse, blue "blue cloud," populated by star-forming galaxies, and the narrow "red sequence," where quiescent galaxies reside. For the more massive galaxies, AGN feedback is believed to play a key role in driving their evolution from star-forming to quiescent systems, with galaxies transitioning through the intermediate "green valley" region.

a binary black hole model where the secondary is in a 12 yr orbit around the primary Valtonen et al. [2025] at a distance of 0.09 pc from the central SMBH. Beyond these confirmed systems, numerous studies have searched for additional candidates using a range of techniques: periodic variability in light curves [e.g., Graham et al., 2015a,b, Charisi et al., 2016, Liu et al., 2016, 2019]; double-peaked or velocity-offset spectroscopic emission lines and/or radial velocity shifts over time [e.g., Eracleous et al., 2012, Shen, 2013, Ju et al., 2013, Liu et al., 2014, Runnoe et al., 2015]; or the identification of multiple milliarcsecond-scale radio cores [e.g., Gitti et al., 2013, Liu et al., 2014, Kharb et al., 2017] and X-shaped radio morphologies [e.g., Lal and Rao, 2007]. While these searches have yielded extensive samples of binary AGN candidates, no further systems have yet been conclusively confirmed.

1.6 AGN Feedback

Growing AGN release energy with the potential to alter their host galaxies and larger-scale environment; a process named "AGN feedback". AGN feedback is widely recognized as the main driver for the transition of galaxies from the so-called blue cloud region, characterized by large rate of SF and blue colors, and the red sequence, characterized instead by quenched galaxies, through the so-called 'green valley' region (see Fig.1.10).

Nowadays, the AGN feedback is a key ingredient in semianalytic models and hydrodynamic simulations of galaxy evolution to explain many observed properties of the galaxies that would not be possible to explain without invoking the AGN feedback.

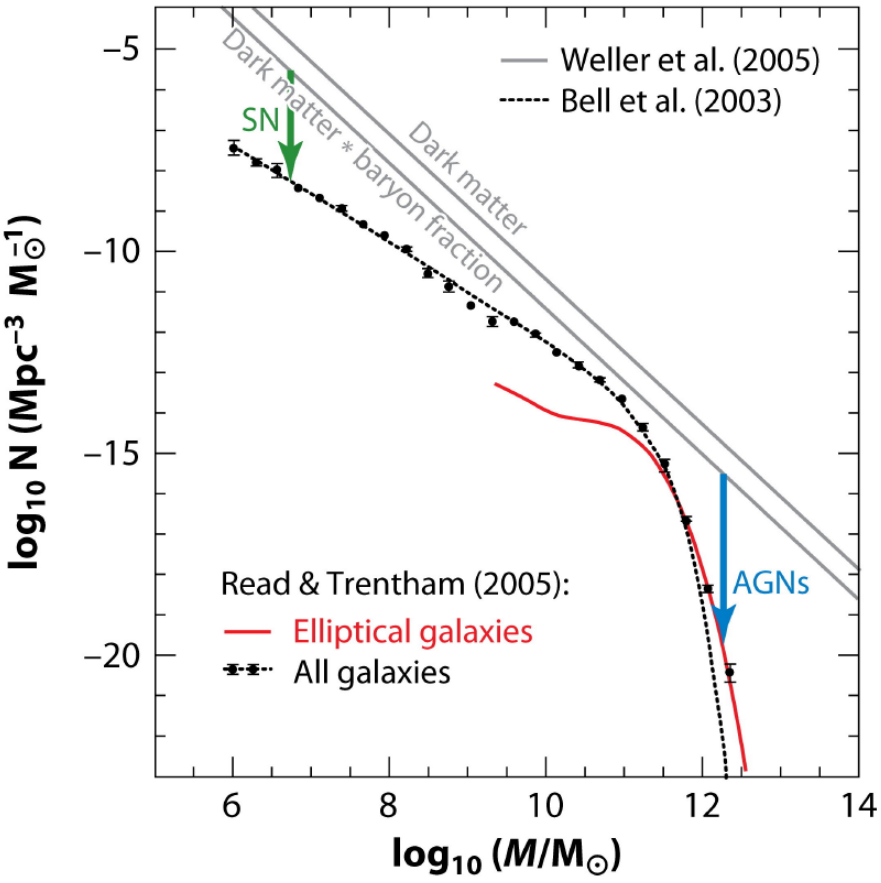

Figure 1.11: Galaxy baryonic mass function (black points for all galaxies, red curve for ellipticals only) from Read and Trentham [2005] fitted with a Schechter [1976] function [Bell et al., 2003, Hinshaw et al., 2013]. The observed mass function is compared with the mass function of cold dark matter halos from numerical simulations, and with the same dark matter mass function scaled by the universal baryon fraction of 0.163. Green and blue arrows indicate the effects of stellar (SN) and AGN feedback, respectively, which are required for semi-analytic models to reproduce the observed stellar mass function. Figure from Kormendy and Ho [2013].

Here we will present three observational evidence that suggest a relevant role of AGN feedback.
These are:
i) the observed discrepancy in the luminosity function of galaxies between observations and models without considering feedback both at low and high masses,
ii) the scaling relations observed between the mass of the BHs and the properties of the bulge of the host galaxies,
iii) the similarity between the BH accretion history and the star formation history throughout cosmic time.

1.6.1 Luminosity function

In the absence of AGN feedback, theoretical models fail to reproduce the observed number of massive spheroidal galaxies. Figure 1.11 shows the comparison between

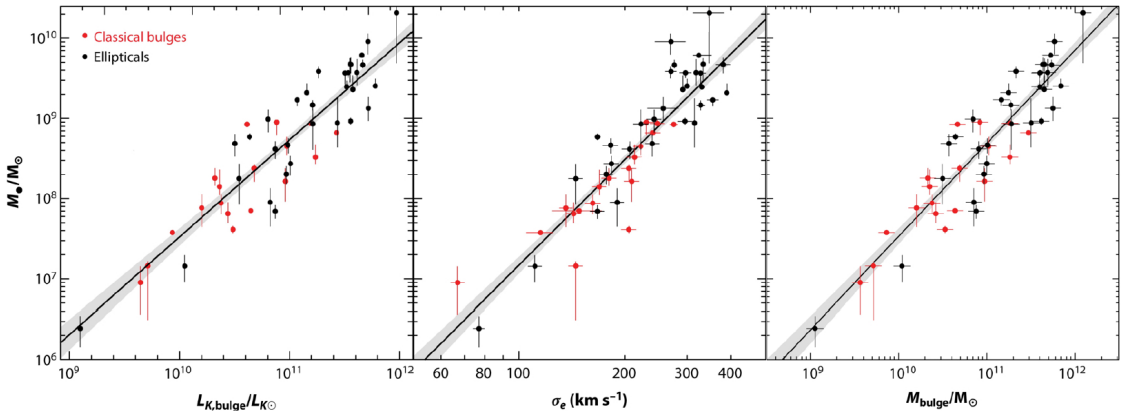

Figure 1.12: From left to right: black hole mass versus host galaxy bulge K-band luminosity, stellar velocity dispersion, and bulge mass, respectively. Red and black points indicate classical bulges and elliptical galaxies. The black line is the best fit, with its 1σ range shown as grey shading. Figure from Kormendy and Ho [2013].

the observed stellar mass function of galaxies (i.e. the number density of galaxies as a function of stellar mass) and that predicted by ΛCDM models of galaxy evolution. A significant discrepancy emerges both at low and high masses. A better agreement between models and observations can be achieved by including feedback processes.

At the low-mass end, the discrepancy can be resolved by incorporating stellar feedback from supernovae (SNe; Dekel and Silk 1986), which are powered by young, massive stars in star-forming regions. These explosions produce intense ionizing radiation that can slow down or even halt star formation (SF) and the accretion of cold gas from the halo. This mechanism appears to be effective up to $M \sim 3 \times 10^{10}\, M_\odot$, where the difference between the observed and predicted stellar mass functions reaches a minimum. At higher masses, the discrepancy increases again and is generally attributed to AGN feedback: radiation, outflows, or radio jets from the AGN can interact with the cold star-forming gas in the galaxy, suppressing star formation in a similar manner.

1.6.2 BH–host galaxy scaling relations

AGN feedback has also been invoked in simulations to explain the observed correlations between the mass of the central black hole and various properties of the host galaxy bulge, such as luminosity [Kormendy and Richstone, 1995], mass [Häring and Rix, 2004], and stellar velocity dispersion [Ferrarese and Merritt, 2000, Gebhardt et al., 2000]. These relations have been verified over large samples of both spiral and elliptical galaxies. For elliptical galaxies, the bulge corresponds to the entire system, whereas for spirals it refers only to the central component.

The correlations span several orders of magnitude in black hole mass, luminosity, and velocity dispersion, and are now commonly used to estimate black hole masses when direct measurements are not feasible. These relations suggest a strong link between black hole growth, galaxy formation, and AGN activity. Since the gravitational influence of the black hole is negligible compared to the size of the galactic bulge, the physical mechanism behind these correlations must have a non-gravitational origin—hence the relevance of AGN feedback.

The M–σ relation can be derived from basic considerations [King, 2003, 2005, King

and Pounds, 2015a, Fabian, 2012, Costa et al., 2014]. A key quantity is the Eddington luminosity, $L_{\rm Edd}$.

Assuming a central source of mass M (in our case, the SMBH) and luminosity L, and a fully ionized gas at distance r, the radiation pressure force per particle is:

$$f_{\rm rad} = \frac{N_e \sigma_T}{4\pi r^2 c} \int_0^\infty L_\nu \, d\nu = \frac{N_e \sigma_T L}{4\pi r^2 c}, \tag{1.9}$$

where N_e is the electron density and σ_T the Thomson cross-section.

The gravitational force per particle is:

$$f_g = \frac{GM\mu m_p N_e}{r^2}, \tag{1.10}$$

where G is the gravitational constant, m_p the proton mass, and μ the mean molecular weight.

Equating $f_{\rm rad} = f_g$ defines the Eddington luminosity:

$$L_{\rm Edd} = \frac{4\pi c G M \mu m_p}{\sigma_T}, \tag{1.11}$$

which represents the maximum luminosity beyond which radiation pressure prevents further accretion.

To compare accretion rates across a wide range of black hole masses, we introduce the Eddington ratio, defined as the ratio of the observed accretion luminosity to the Eddington luminosity, $\lambda_{\rm Edd} = L_{\rm acc}/L_{\rm Edd}$. High values of $\lambda_{\rm Edd}$ (typically $\gtrsim 0.1$) indicate systems accreting at a relatively high rate. Nevertheless, the Eddington ratio does not represent an absolute limit: supermassive black holes can experience episodic phases of super-Eddington accretion ($\lambda_{\rm Edd} \gtrsim 1$).

1.6.3 BH and star formation history

Another observational evidences which point to the need of AGN (and SN) feedback is the similarity between the BH accretion history and the star formation history throughout cosmic time suggesting broad co-evolution of black holes and their host galaxies [e.g. Marconi et al., 2004, Shankar et al., 2009, Aird et al., 2015]. In Fig. 1.13, a comparison between the total star formation rate (SFR) density from Madau and Dickinson [2014], with estimates of SMBH accretion density from Aird et al. [2015] is shown. Both the SFR density and the SMBH accretion density peak at $z \sim 2$. At higher redshifts, the SMBH accretion density declines more steeply than the SFR density, implying that galaxies may assemble their stellar mass before their central SMBHs grow, or that the efficiency of SMBH formation and growth is lower in the early Universe. Although it is unlikely that the parallel evolution of these two histories is a coincidence, discrepancies among published accretion histories indicate that this comparison should still be treated with caution.

1.6.4 AGN Feedback mode

There is no general consensus on which outflow mechanism is the most significant, whether radiation pressure on dusty gas, accretion disc winds, radio jets or cosmic rays (e.g., Fabian [2012], Zakamska et al. [2016], Venturi et al. [2021]). Consequently,

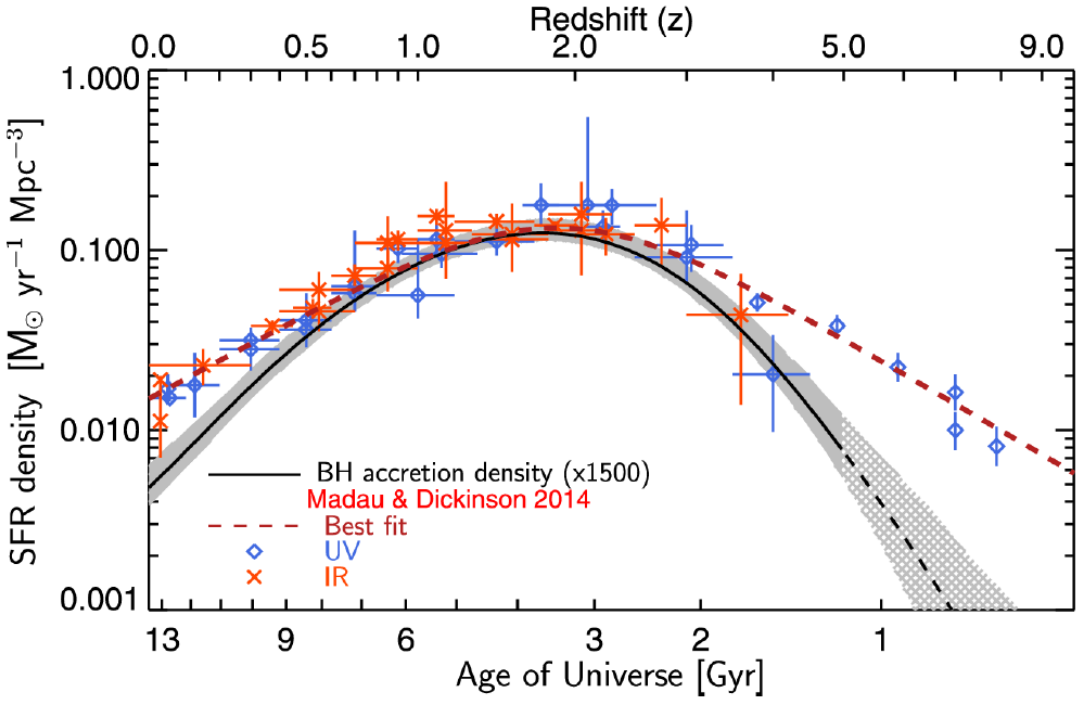

Figure 1.13: Star formation rate (SFR) density compared to the black hole mass accretion density as a function of redshift (or cosmic time). Points represent SFR measurements from Madau and Dickinson [2014] based on rest-frame UV (blue diamonds) and IR (orange crosses) observations, with the best-fit relation shown as a dashed red curve. The black curve shows the BH accretion rate density from Aird et al. [2015], scaled by a factor of 1500, with uncertainties indicated by the shaded grey area. The dashed black line and hatched region mark the model extrapolation beyond data coverage. Figure from Aird et al. [2015].

the literature is full of observational studies exploring these topics. They range from multi-wavelength, highly detailed, observations of individual targets through to statistical tests on large galaxy samples. Due to the diversity of these studies, it may be challenging to interpret the results within the context of one another, and within the context of the theoretical studies around AGN feedback. The literature presents a variety of observational approaches to probe AGN feedback, each highlighting different gas phases and spatial scales. However, it remains an open question to what extent these methods trace complementary aspects of the same phenomenon, and how consistently they can be connected to theoretical predictions.

1.6.5 Radio Jet Feedback

Relativistic jets from AGN are commonly observed to influence gas on the scales of the host galaxy, heat ISM and suppress cooling flows. The clearest observational evidence of feedback through jets is found in the local Universe in the most massive galaxies ($>10^{11} M_{\odot}$), as the brightest cluster galaxies (BCGs) in the cool core clusters of galaxies. In these objects, AGN jets interact most strongly with the gas by inflating bubbles of relativistic plasma that can directly heat the ISM by producing shocks or by mechanical energy in the form of pdV [Bîrzan et al., 2004, 2008, Cavagnolo et al., 2010]. The

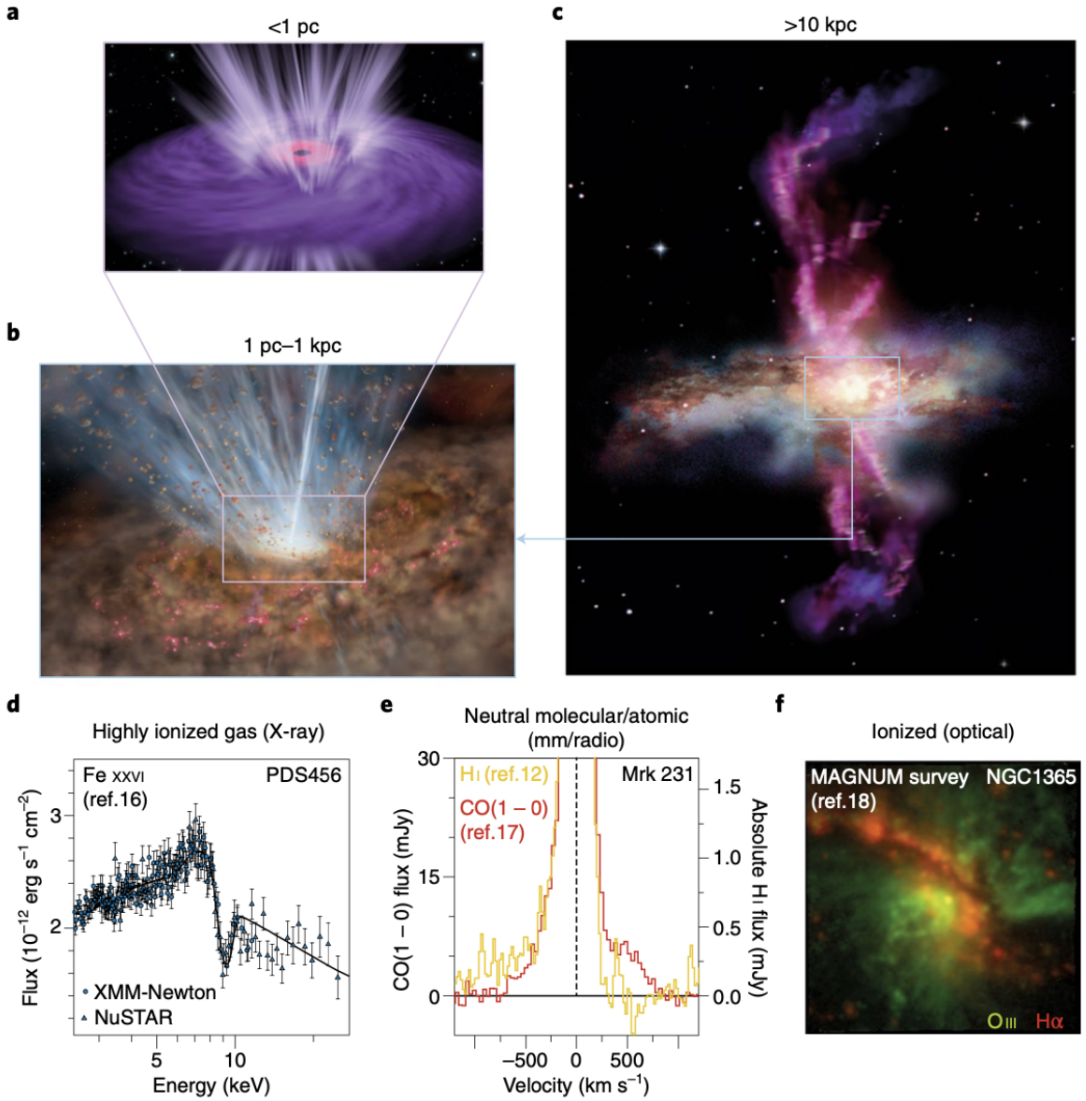

Figure 1.14: Artistic view and observational evidence of multi-phase AGN outflows, accelerated by the central engine (1 pc; a), and then propagating through the surrounding ISM (1–1000 pc; b), out to galaxy edge (10 kpc; c). Lower panels show AGN outflows detected in different gas phases in three well studied nearby AGN: the highly ionized, X-ray ultrafast outflow in PDS 456 (Nardini et al. [2015]; d); the neutral outflow in both atomic and molecular phases, observed in Mrk 231 (Cicone et al. [2012], Morganti et al. [2016]; e); the ionized outflow in NGC 1356, extending over kpc-scales (Venturi et al. [2018]; f). Image from Cicone et al. [2018].

bubbles are observed to carve out cavities in the hot gas and by the analysis of the cavities it is possible to estimate the mechanical energy injected in the ISM by the jets. The injected energy allows to balance the energy loss through cooling; in fact, without a source of energy keeping the gas in the halo hot, the gas would radiatively cool in a short time, resulting in intense star formation in the galaxy [e.g. Gabor et al., 2011, Bower et al., 2012]. This suggests a cycle in which the interstellar medium cools and condenses into molecular clouds that form stars and feed the supermassive black hole; then nuclear accretion and black hole spin produce mechanically powerful radio AGN that heat the cooling atmosphere, slowing the rate of cooling, and the cycle repeats. For this reason kinetic mode is also called 'maintenance mode'. While most systems are roughly consistent with obeying such a cycle, there are some examples in which the radio jets relay more power than the necessary power to simply reheat the gas and may be sufficient to unbind much of the hot atmosphere [e.g. McNamara et al., 2005, 2009]. There is increasing evidence that, in radio-loud AGN, the interaction between the radio jets and the interstellar medium (ISM) of the host galaxy can also be responsible for large-scale outflows. Integral field unit (IFU) observations of powerful ($P_{1.4,\mathrm{GHz}} > 10^{26}, \mathrm{W}, \mathrm{Hz}^{-1}$) radio-loud quasars have revealed [O III] outflows aligned with the radio jet axis over scales of ~ 10 kpc, with velocities of $v \sim 1000$ km s^{-1} and FWHM ~ 1000 km s^{-1}. [e.g. Nesvadba et al., 2006, 2007, 2008]. These results suggest that radio jets could be able to transport huge amounts of matter and energies from sub-parsec central regions to Mpc-scale lobes, with a kinetic power comparable to that of the host galaxy and the AGN. Massive and fast outflows of neutral or molecular gas driven by the radio jets have been observed in a growing number of objects [Morganti et al., 2015, Cicone et al., 2014, McNamara et al., 2009]. Some recent studies have pointed out that this mechanism of feedback could be relevant for relatively weak radio sources, with low-power radio jets which are typically classified as radio-quiet [Combes et al., 2013, Alatalo et al., 2015, Venturi et al., 2021]. Simulations of low-power jets show that in the central region (r $\sim$500pc) the jets are able to launch an outflow of ionized gas with speeds $\sim$200 km/s in the same direction of the radio jet, as in the massive radio-loud galaxy found by Nesvadba et al. [2008]. In the simulations of Mukherjee et al. [2018a], the relativistic jets create a cavity and beyond it the jets interact with the clouds and they quickly decelerate, launching a sub-relativistic outflow ($v \sim 0.01$–0.1c) of non-thermal plasma. But this is not the only effect the radio jet can have on the host galaxy. In recent years, attention has been paid to a very peculiar phenomenon observed in nearby Seyfert galaxies, which I discuss in the next paragraph and in the continuation of my thesis.

1.6.6 Width Enhancement Perpendicular to the Radio Jet

Evidence of the interaction between low-power radio jets and ISM was found by Venturi et al. [2021] in Seyfert galaxies. They detected a peculiar enhancement of velocity dispersion perpendicularly to the direction of propagation of the jets (Fig. 1.15). This phenomenon was previously observed in other local Seyfert galaxies. For example, Finlez et al. [2018] observed the enhancement of the velocity dispersion in [OIII] emission line in NGC 3393, interpreting it as equatorial outflow from the accretion disc and perpendicular to the radio jet axis (in black line in Fig. 1.16). Couto et al. [2013] and Shimizu et al. [2019] reported the phenomenon in Arp102B and in IC5063, interpreting it as small-scale bipolar outflow. Freitas et al. [2018] observed it in Mrk 79, interpreting

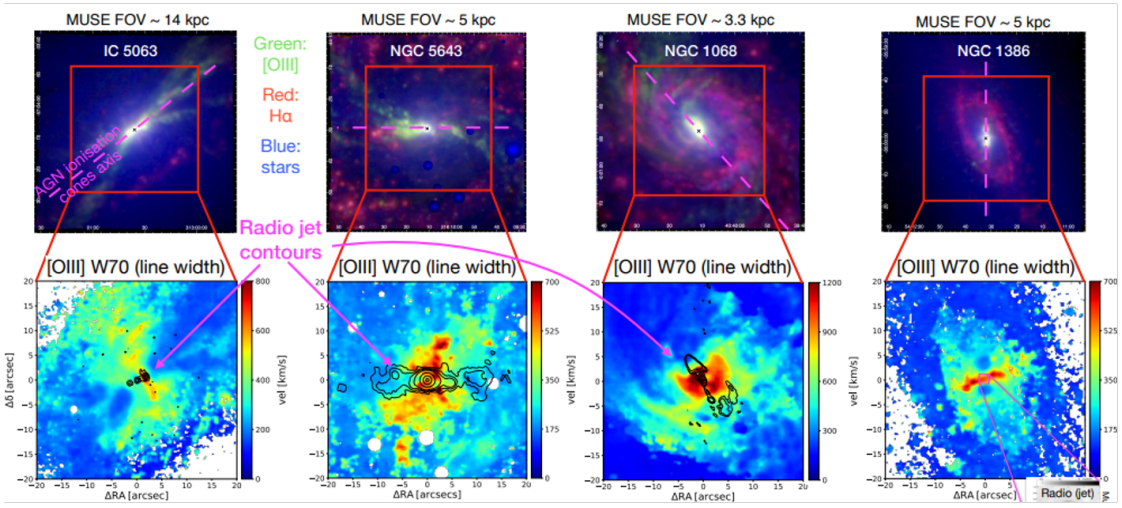

Figure 1.15: Enhancement of velocity dispersion perpendicularly to the direction of propagation of the jets in nearby Seyfert galaxies of the MAGNUM survey. Upper panels: Three-color image from MUSE, [OIII] in green, Hα in red, stellar continuum collapsed in the spectral range 5100–5800 Å in blue. Dashed purple lines mark the direction of the radio jet. Lower panels: Velocity dispersion of [OIII] emission line. Contours in black show the contours of the radio jets. Adapted from Venturi et al. [2021]

it as lateral expansion of the gas due to the passage of the radio jet (green contours). This phenomenon is observed not only in [OIII] but also in [FeII] emission line as shown in Riffel et al. [2014] (radio jet in green line of left panel). The connection between this feature and the jet was not recognized, as they gave different interpretations like beam smearing, equatorial outflows from the accretion disc, or multidirectional outflows (see Fig. 1.16). Venturi et al. [2021] favored the interpretation that this phenomenon was due to the interaction between the jet and the ISM. In fact, the perpendicular extended line velocity width enhancement is observed exclusively in galaxies hosting a (low-power) jet whose inclination happens to be low enough over the galaxy disc to have significant interaction with its ISM.

1.6.7 The multi-scale and multi-phase nature of outflow

AGN feedback can strongly influence ISM by removing, heating, or shocking gas. Several observational studies reported evidence of outflows in different gas phases (see Fig. 1.14):

-Hot ionized gas ($T_{\rm gas} \sim 10^{5-8}\,$K, $n_{\rm gas} \sim 10^{6-8}\,{\rm cm}^{-3}$), detected through X-ray absorption lines [Tombesi et al., 2011, Xiang et al., 2025];

-Warm ionized gas ($T_{\rm gas} \sim 10^{3-5}\,$K, $n_{\rm gas} \sim 10^{2-5}\,{\rm cm}^{-3}$), mainly traced through emission lines in the rest-frame UV [Weiner et al., 2009, Pessa et al., 2024, Fernández-Figueroa et al., 2025, Kehoe et al., 2025], optical [Liu et al., 2013, Harrison et al., 2014, Kakkad et al., 2020, Tozzi et al., 2024], and near-infrared [Rupke and Veilleux, 2013b, Ramos Almeida et al., 2019, Speranza et al., 2022];

-Neutral atomic gas ($T_{\rm gas} \sim 10^{2-3}\,$K, $n_{\rm gas} \sim 10^{1-2}\,{\rm cm}^{-3}$), revealed by H I absorption Morganti et al. [2016], Na I D absorption [Concas et al., 2019, Roberts-Borsani et al., 2020, Machuca et al., 2025], and [C II] fine-structure emission [Maiolino et al., 2012,

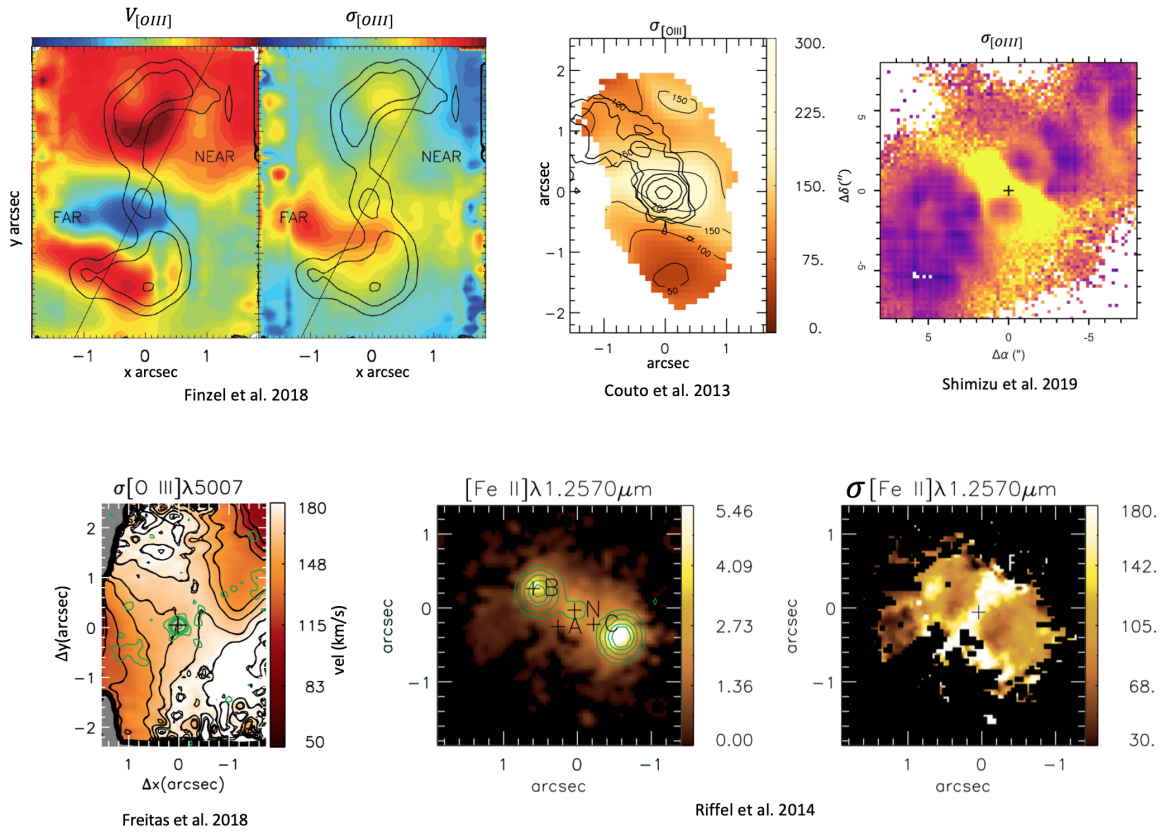

Figure 1.16: Some examples of previous observations of σ enhancement of ionized gas perpendicular to the radio jets f.

Bischetti et al., 2019];
-Molecular gas ($T_{\rm gas} \sim 10^{1-3}$ K, $n_{\rm gas} > 10^3\,{\rm cm}^{-3}$), traced by near-infrared H_2 lines (hot molecular gas) [Rupke and Veilleux, 2013b, Speranza et al., 2022], mid-infrared rotational lines (warm molecular gas) [Riffel et al., 2020], far-infrared OH transitions [Sturm et al., 2011, Veilleux et al., 2013b, Spoon et al., 2013, González-Alfonso et al., 2017], and CO emission lines in the (sub)millimetre regime [Feruglio et al., 2010, Cicone et al., 2014, Fiore et al., 2017, Fluetsch et al., 2019, Lutz et al., 2020, Bischetti et al., 2021].

These diagnostics trace outflows on scales from sub-parsec, for example outflow from the BLR region to several kiloparsecs outflows such as the ionized and molecular phases.

Multi-phase studies indicate that cold molecular gas often dominates the mass budget, followed by neutral atomic and warm ionized phases [Fluetsch et al., 2019, Veilleux et al., 2020, Lutz et al., 2020, Revalski et al., 2022]. In the local Universe, molecular outflows are slower ($v \lesssim 300{-}500\,{\rm km\,s^{-1}}$) and more compact ($r \lesssim 1{-}2\,{\rm kpc}$) compared with ionized outflows ($500{-}1000\,{\rm km\,s^{-1}}$, $r \sim 1{-}10\,{\rm kpc}$). At higher redshift ($z \sim 1{-}3$), studies focus primarily on ionized phases since the strong optical lines are shifted to the infrared. IFU observations of quasars with different radio luminosities reveal fast galaxy-scale ionized outflows [Brusa et al., 2015a, Perna et al., 2015, Bischetti et al., 2017, Harrison et al., 2018b]. Neutral atomic and molecular outflows have also been detected at high z, with some luminous quasars hosting massive, high-velocity winds [Maiolino et al., 2012, Brusa et al., 2018, Bischetti et al., 2019], though [C II]

surveys suggest these are not ubiquitous Decarli et al. [2018]. There is a general consensus that while molecular gas contains most of the mass, the ionized phase carries more kinetic energy. It is still uncertain whether different phases represent successive stages of the same phenomenon Zubovas and King [2014] or independent processes. Deep, spatially resolved, multi-phase observations across diverse AGN luminosities and environments are needed.

In the local Universe, scaling relations suggest that higher AGN luminosities drive more massive, faster outflows Cicone et al. [2014], Fiore et al. [2017]. Recent work with less biased AGN and ULIRG samples Lamperti et al. [2022], Ramos Almeida et al. [2022] suggests the relation is weaker, implying that outflow efficiency depends on host galaxy conditions and not only on AGN luminosity alone.

Disentangling outflows from emission line profiles is challenging since there can be other features such as rotation, inflows, tidal debris, that mimic broad features Concas et al. [2022]. The common way to disentangle outflowing components is from Gaussian parametric fits typically using a narrow component ($\lesssim 400\,\mathrm{km\,s^{-1}}$) for virial motions and one or more broader, shifted components for outflows. Another way to compute outflow propeties is from non-parametric approaches which instead measure velocities at fixed flux percentiles, directly tracing high-velocity gas Harrison et al. [2014].

The parametric method is more efficient when clear broad wings are detected. In case of molecular gas, usually traced by CO, where outflows tend to be slower than ionized counterparts Fiore et al. [2017], Lutz et al. [2020], Revalski et al. [2022], is harder to distinguish outflows from rotation. Otherwise, kinematic modelling with moment maps and PV diagrams compared to disk rotation models is required García-Burillo et al. [2014], Lutz et al. [2020].

Chapter 2

Observational Instruments and Analysis Tools

In this work, we made use of a range of state-of-the-art observational facilities to carry out different projects. In addition, this thesis also employs advanced method of analysis such as Machine Learning and Deep Learning. The core of this thesis is based on data from space observatories, in particular the James Webb Space Telescope (JWST) and the Euclid mission, launched in late 2021 and 2023, respectively. However, we also exploited ground-based instruments such as the 8-meter class telescopes the Very Large Telescope (VLT) and the Gran Telescopio Canarias (GTC). These four telescopes are shown in Figure 2.1. In the following section, we provide a brief overview of the capabilities of these instruments and describe how they were employed in the context of this thesis. We will conclude the section with a brief introduction on Machine Learning and the application in astrophysics.

2.1 IFU Spectroscopy

An Integral Field Spectrograph (IFS) is an advanced technique that provides both spatial and spectral information of an astronomical object. Unlike traditional spectrographs that collect spectra along a single slit, an IFS consist of data cubes, with two spatial dimensions (i.e. [x, y] or [RA, DEC]), and a third wavelength dimension (i.e. λ) containing spectral information. This is achieved by dividing the image into spatial elements, or spaxels, through three different techniques:

- **Lenslet arrays**: is a regular grid of small telescope mirror images, which split the image into light points, which are dispersed by the spectrograph.
- **Optical fibers**: Reformat light collected from different parts of the sky and direct the light in the spectrograph.
- **Image slicers**: the image is split into thin horizontal slices. For example, in NIRSpec the slicer divides the 3" $\times$ 3" field of view into 30 slices of 0.1" $\times$ 3". Each slice produces 30 contiguous spectra on the detector, for a total of 900 spectra, each corresponding to a spatial element of 0.1" $\times$ 0.1".

Integral field spectrographs are also called 3D spectrographs, and the data obtained are arranged in a so-called "data cube" (see Fig. 2.2). In other words, for each pixel (also

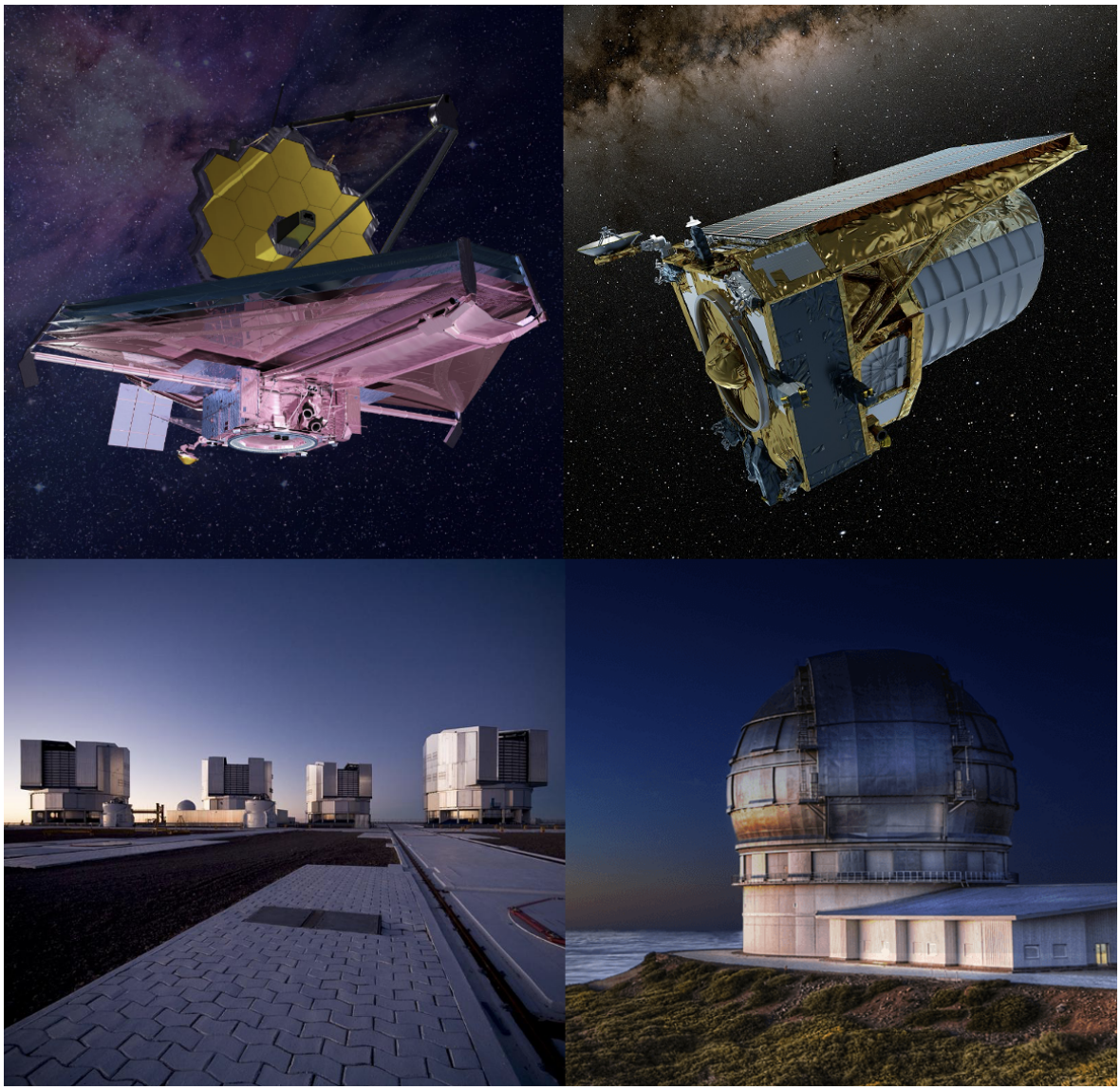

Figure 2.1: Observational facilities used in this thesis. The upper panels show the space-based telescopes: JWST (left) and Euclid (right). The lower panels display the ground-based observatories: the VLT at Paranal (left), used with the MUSE instrument, and the Gran Telescopio Canarias (right), used with MEGARA.

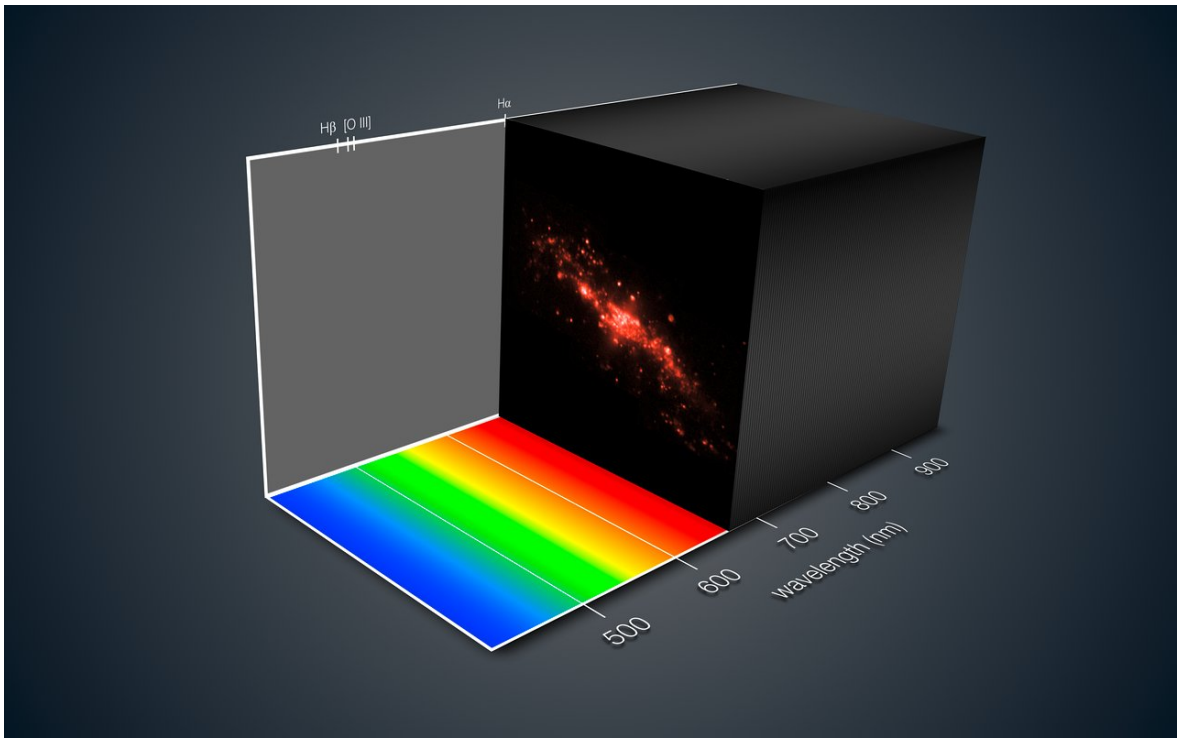

Figure 2.2: Example of structure of a datacube: the data provide monocromatic image of the full field of view at each wavelength, and a 1D spectrum at each spaxel across the field of view. The image is based on data on the polar ring galaxy NGC 4650A that were obtained in early 2014. Credit: ESO/MUSE consortium/R. Bacon/L. Calçada.

called a spaxel in the data cube), we have an independent spectrum produced by the integrated emission within that spaxel. JWST/NIRSpec and VLT/MUSE, therefore, combines imaging and spectroscopy into a single instrument, providing fields of view with high spatial resolution, high resolving power, and a large spectral range. Such an approach enables detailed studies of the physical and kinematic properties of extended astronomical objects, making IFSs particularly powerful tools for investigating galaxies, star-forming regions, and resolved stellar populations.

2.1.1 VLT/MUSE

The Very Large Telescope (VLT) of the European Southern Observatory (ESO) serves as a cornerstone of European ground-based astronomy and stands among the most advanced optical telescopes in the world. It comprises four Unit Telescopes (UTs) with primary mirrors 8.2 meters in diameter. The Multi Unit Spectroscopic Explorer (MUSE) is a second generation instrument installed on the Nasmyth focus of UT4 at the VLT .
MUSE is designed as integral field spectrograph (or integral field unit) to give spectral information at every location of the sky within a two-dimensional area and not only in one dimension like the classical slit spectrograph.
MUSE can operate in two different configurations, the Wide Field Mode (hereafter WFM) and the Narrow Field Mode (hereafter NFM).
MUSE in the WFM has a field of view of 1x1 arcmin^2, sampled at 0.2x0.2 arcsec^2 with a spectral range of 0.465-0.93 μm that let us to study the profile of the most important

emission lines produced in the ionized gas up to z<1. ($H\alpha$, $H\beta$, the oxygen doublets $[OIII]\lambda\lambda 4959, 5007$ and $[OI]\lambda\lambda 6300, 6364$, $[NII]\lambda\lambda 6548, 84$ and $[SII]\lambda\lambda 6717, 6731$). In the other operating mode (NFM), thank to the adaptive optic system (AO), MUSE provide information with very high spatial resolution (∼10 times better than WFM) but a field of view eight times smaller (7.5x7.5 arcsec^2), sampled at 25 milli-arcsec.

2.1.2 JWST/NIRSpec

Launched in 2021, JWST is positioned at the Sun–Earth L2 point and observes the Universe in the infrared with a large, segmented 6.5-meter primary mirror. JWST covers the wavelength range 0.6–27.9 μm with four scientific instruments: the Mid-Infrared Instrument (MIRI), the Near-Infrared Camera (NIRCam), the Near-Infrared Imager and Slitless Spectrograph/Fine Guidance Sensor (NIRISS/FGS), and the Near-Infrared Spectrograph (NIRSpec). Compared to previous space observatories such as Hubble and Spitzer, JWST combines a large aperture, diffraction-limited image quality, and unprecedented infrared sensitivity.

In this work we focus on NIRSpec, which provides near-infrared spectroscopy over 0.6–5.3 μm within a 3.4 × 3.6 arcmin field of view. NIRSpec offers three different entrance apertures: a micro-shutter assembly (MSA) for multi-object spectroscopy, an IFU for spatially resolved spectroscopy, and fixed slits (FSs) for single-target observations. Depending on the disperser used (prism or gratings), NIRSpec achieves resolving powers between $R \sim 100$ and $R \sim 2700$.

In this thesis we used the IFU mode, which provides $3'' \times 3''$ field of view, sliced into 30 slitlets of $0.1''$ width. Each slice is dispersed to create a three-dimensional data cube, where each spatial element corresponds to a spectrum with $0.1''$ spatial sampling. This allows detailed mapping of the spatial and spectral structure of extended sources. A limitation of the IFU mode comes from the physical gap between the two NIRSpec detectors in the focal plane array that causes missing wavelength intervals and is not the same for all slices.

2.1.3 GTC/MEGARA

MEGARA is an optical IFS mounted on the 10.4-meter *Gran Telescopio Canarias* (GTC). Its IFU mode provides high-resolution, spatially resolved spectroscopy over a field of view of 12.5" × 11.3", sampled by 567 fibers with a core diameter of 0.62. MEGARA covers the optical wavelength range from 3650 Å to 9750 Åwith a spectral resolutions from $R \sim 6000$ to $R \sim 20,000$ depending on the grating.

2.2 Euclid

Euclid is a medium-class mission of the European Space Agency (ESA) within the framework of the Cosmic Vision 2015–2025 programme. Its main objective is to deliver high-resolution optical imaging, complemented by near-infrared imaging and spectroscopy, over approximately 14,000 deg^2 of the extragalactic sky. The spacecraft hosts two primary science instruments: the Visible Imaging Instrument (VIS) and the Near Infrared Spectrometer and Photometer (NISP). Both instruments are designed

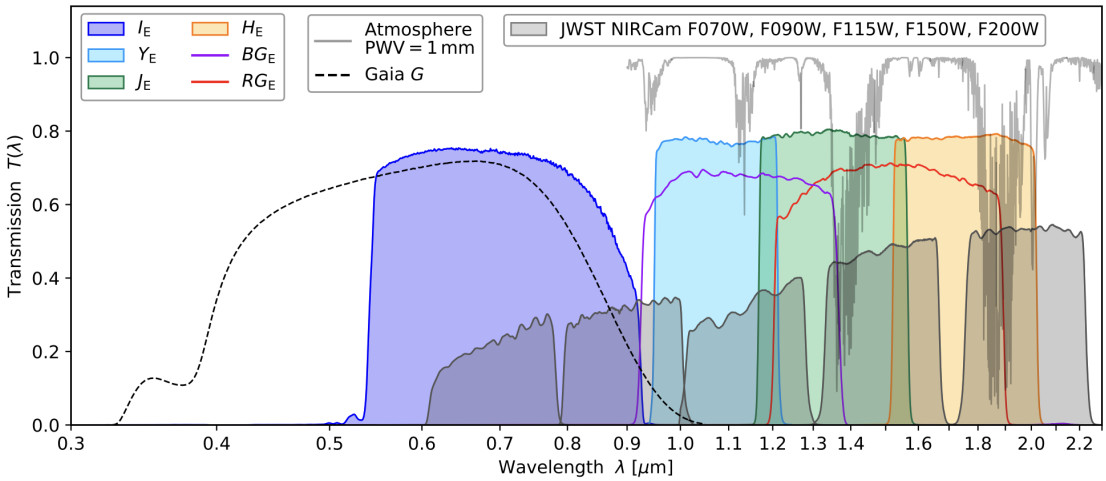

Figure 2.3: Spectral response of Euclid's imaging (VIS: I_E; NISP: Y_E, J_E, H_E) and spectroscopic channels (NISP: BGE, RGE) at the beginning of the mission. The expected transmission loss at the end of the mission due to space weathering and non-volatile contamination is at most 0.05. For reference we show the Gaia G passband from their third data release (Gaia Collaboration et al. [2023]), the atmospheric transmission for a precipitable water vapour level of 1.0 mm (Rothman [2021]), and some of the JWST passbands of their Near Infrared Camera (NIRCam; Rieke et al. [2005]).

to provide high-quality data across a wide field of view (FoV), with high accuracy and precision.

VIS is a large-format imager with a FoV of 0.54 deg^2, sampled at 0.1″ per pixel, and operating in a single broad red passband. Its wide bandpass and high throughput (Fig.2.3) yield a limiting sensitivity of $m_{\rm AB} = 26.7$ for a 5σ point source. NISP, on the other hand, provides both multiband photometry and slitless grism spectroscopy in the wavelength range 920–2020 nm. The photometric channel (NISP-P) offers three passbands: Y_E (949.6–1212.3 nm), J_E (1167.6–1567.0 nm), and H_E (1521.5–2021.4 nm). The designed 5σ point-source depth of NISP-P for the wide survey is 24.0 AB mag, which is exceeded by approximately 0.4 mag. The plate scale of 0.298″ per pixel significantly undersamples the NISP point spread function (PSF), which has a typical FWHM of 1.10, 1.17, and 1.19 pixels in the Y_E, J_E, and H_E bands, respectively, when fitted with a Moffat profile.

2.3 Introduction to Machine Learning

The amount and complexity of data produced by modern galaxy surveys has been steadily increasing in recent years, and forthcoming facilities are expected to deliver imaging and spectroscopy for hundreds of millions of galaxies. Extracting coherent scientific knowledge from such large and multi-modal datasets remains a major challenge for the community. In this context, data-driven approaches, and in particular machine learning, have rapidly emerged as powerful tools to address long-standing problems in astrophysics.

Machine learning (ML) is a subset of artificial intelligence in which algorithms learn directly from data, without explicit instructions by humans. This enables ML algorithms to make predictions and classifications and capture patterns that may be

difficult or impossible to capture with classical approaches. This is particularly important in astrophysics, where the complexity and the huge amount of datasets often prevent the use of purely analytical models.

Machine learning techniques are commonly divided into two main categories, supervised and unsupervised learning. In supervised learning, algorithms are trained on labeled datasets, where both the input data and the corresponding desired outputs are provided. Through this training, the algorithm learns to map input features onto target variables, thereby enabling predictions or classifications for previously unseen data. Widely used supervised learning methods include linear and logistic regression, decision trees, random forests, and neural networks (see, e.g., Connolly et al. [1995], Collister and Lahav [2004], Re Fiorentin et al. [2007], Mahabal et al. [2008], Daniel et al. [2011], Laurino et al. [2011], Bloom et al. [2012], Richards et al. [2012], Krone-Martins and Moitinho [2014], Masci et al. [2014], Naul et al. [2018], D'Isanto and Polsterer [2018], Krone-Martins et al. [2018], Delli Veneri et al. [2019], Ishida et al. [2019], Mahabal et al. [2019], Norris et al. [2019], Reis et al. [2019]).

By contrast, unsupervised learning does not rely on labeled data, but instead identifies patterns and complex relationships directly from the dataset. These methods are typically grouped into three main classes: clustering, dimensionality reduction, and anomaly detection, all of which are highly relevant for astronomical applications.

2.3.1 The use of ML in astronomy

One of the first tasks that scientists tackled was the morphological classification of galaxies. This is a type of supervised learning, which means that in order to train this model, it is necessary to have labels for the galaxies on which the network is then trained. For this reason, there are many citizen science projects in which galaxies are classified by scientists or volunteers in order to train increasingly accurate models. The morphological classification of galaxies was first done by Hubble, but now ML models have become the state-of-the-art for this task. The use of ML is necessary because the amount of galaxy image data has increased dramatically thanks to survey telescopes such as SDSS, DESI, Euclid, etc.

In addition to classification tasks, machine learning is widely used for the detection of gravitational lenses. These lenses produce a distortion of light from objects that are on the same line of sight as another massive object, which may be a galaxy or a galaxy cluster, deflecting the light and producing multiple images of the same object. Strong lensing is very useful for understanding the distribution of matter in the universe and is evidence of dark matter distribution in galaxies, as it is possible to derive the mass of the galaxy and thus understand how much of it is in the form of light and how much is dark matter. As with classification, a widely used method is that of convolutional networks. The basic difference between this problem, i.e., the task of detecting very rare objects such as lenses or double AGNs (discussed at length in Chapter 5), and a classification task is that the problem is severely unbalanced. In fact, the number of lenses or double AGNs is much lower than that of regular galaxies. This leads to two major challenges, both of which are addressed in this thesis. First, it is not feasible to construct a large and representative training dataset based solely on observed objects, due to the intrinsic rarity of the targets of interest. Second, this task requires a very high level of performance, in terms both of accuracy and purity.

Here, accuracy refers to the fraction of objects that are correctly classified over-

all, while purity quantifies the fraction of sources classified as true positives that are genuinely real systems. High purity is especially critical in this context, since even a small level of contamination can result in a large number of false positives, significantly biasing the final sample.

The problem with false positives is in general more difficult to solve. The usual solution consists in visually inspecting the candidates and to remove the false positives, re-train the network finetuning it with the label from visual inspection.

Another important task for ML technique is the estimation of photometric redshifts needed when spectroscopy is not available. Other examples of CNN use include distinguishing between Lyaman α emitters (LAEs) and contaminants (Gurung-López et al. [2020]), the identification of merging galaxies (Ackermann et al. [2018]), and many other uses.

2.3.2 Fundamentals of Deep Learning Algorithms

In this thesis, we used algorithms that are part of a subset of machine learning called deep learning, which uses specific structures called neural networks.

One of the simplest algorithms in deep learning is the Artificial Neural Network (ANN) which can be layered (hence deep) to process information through weighted connections. This allows the network to learn and make predictions or classifications from input data. Neural networks are, in general, supervised machine learning models, which learn from batches of training examples and are considered model-based learning systems.

The perceptron, introduced by Rosenblatt [1958], is one of the earliest and simplest ANN models. It is based on a threshold logic unit (TLU; Fig.2.4), which computes a weighted sum of the inputs and applies a step activation function to produce the output. Activation functions play a crucial role in introducing non-linearity to the model, allowing it to learn complex patterns and relationships in the data. Without non-linear activation functions, a neural network would be equivalent to a linear model, regardless of its depth. Commonly used activation functions include the sigmoid function, which maps inputs to the range (0,1) and is historically used in binary classification tasks, the hyperbolic tangent (tanh), which outputs values between -1 and 1 and is zero-centered, often leading to faster convergence; and the Rectified Linear Unit (ReLU), which outputs zero for negative inputs and the identity for positive inputs, and has become the default choice for deep networks due to its computational efficiency and acceleration in the convergence. All these three functions are shown in Fig.2.5).

A typical perceptron consists of a single layer of TLUs, fully connected to the input layer, with an additional bias term included to improve flexibility. Despite its simplicity, a perceptron can act as a multi-output classifier by combining several TLUs in parallel. Perceptron training is based on iteratively adjusting the weights and the bias in order to reduce the discrepancy between the predicted output and the true label.

A *Multilayer Perceptron* (MLP) is composed of one input layer, one or more layers of TLUs called hidden layers, and one final layer of TLUs called the output layer. This output layer can be a single numerical value, a series of numerical values, or discrete categories, depending on the task and the type of neural network.

The input of a neural network can represent anything, from one-dimensional features to two-dimensional features such as images. When dealing with images and

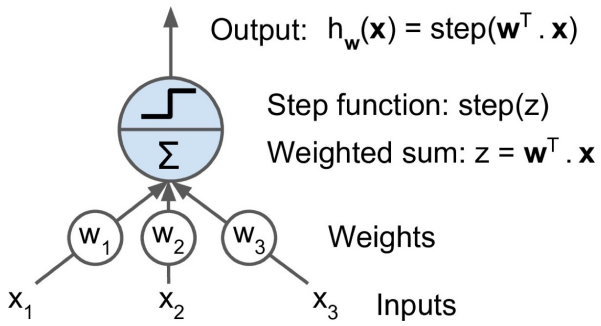

Figure 2.4: Threshold logic unit: an artificial neuron which computes a weighted sum of its inputs then applies a step function.

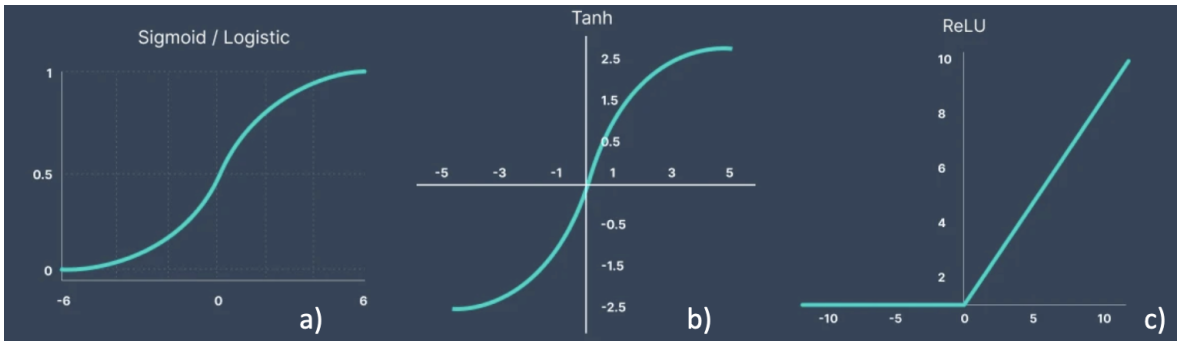

Figure 2.5: Examples of activation functions in neural networks: (a) Sigmoid (Logistic) function, mapping inputs to the range [0,1]; (b) Hyperbolic tangent (Tanh) function, outputting values between -1 and 1; (c) Rectified Linear Unit (ReLU) function, which outputs zero for negative inputs and the identity for positive inputs. These functions introduce non-linearity in neural networks, enabling them to learn complex patterns in data.

classification tasks, MLPs face some limits, such as the disregard for spatial properties and the large number of parameters required to deal with every pixel.

One of the most powerful and popular algorithms for visual tasks are Convolutional Neural Networks (CNNs).

Unlike fully connected networks, neurons in the first convolutional layer are not linked to every pixel of the input image, but only to those within a limited receptive field. Neurons in the following convolutional layers are in turn connected only to local regions of the previous layer. This design, inspired by the structure of the visual cortex, enables the network to first detect simple, small-scale patterns in the earliest layers and then progressively combine them into increasingly complex features at deeper levels. Another important characteristic of CNNs is the sharing of weights across the input space, meaning that the same set of filter parameters is applied across different regions of the input. This considerably reduces the number of parameters compared to fully connected networks. Moreover, CNNs often include pooling layers, which downsample feature maps and increase robustness by making the network less sensitive to small variations in the input, such as local noise in an image. These properties reflect the way real-world images are organized and are key reasons why convolutional neural networks are so effective at image recognition tasks.

Now we need to understand how the network can be trained efficiently to perform the required tasks. This challenge was addressed by the backpropagation algorithm. The main goal of backpropagation is to minimize a cost, or loss function, that measures the difference between the predicted output and the true target. To do this, the algorithm calculates how much each weight in the network contributes to the error, using the chain rule to propagate the error backward from the output layer to the input layer. In this way, backpropagation provides the gradients needed to adjust the weights systematically through optimization methods, allowing the network to improve its performance and learn features of the data.

Chapter 3

The Jet Feedback in Seyfert 2 galaxies

As discussed in the first chapter, jets can impact the interstellar medium, creating cavities, shocks, and turbulence. There is growing evidence that not only radio-loud jets have a significant impact, but also so-called radio-quiet jets can launch outflows, transporting large amounts of material from the sub-pc scale to the kpc scale and finally can produce enhancement of velocity dispersion perpendicularly to the direction of propagation of the jet itself. The main goal of this chapter is to examine the impact of moderately luminous jets on the host galaxy and to explore the interplay between the AGN and its surroundings. First, we investigate the properties of ionized galactic outflows and the physical conditions of the ionized gas in four type 2 AGN at z $\sim$ 0.15 in detail using spatially resolved optical integral field spectroscopic (IFS) observations from the Multi Unit Spectroscopic Explorer (MUSE) at the Very Large Telescope (VLT). We then compare our MUSE observations with radio-emission maps from the Very Large Array (VLA) and e-MERLIN to investigate the effects of moderate-power radio jets ($\sim 10^{44}$erg s^{-1}) on the host galaxy, extending the work of Venturi et al. [2021] on low-power radio (i.e., $\lesssim 10^{44}$ erg s^{-1}) AGN jets to higher jet luminosities.

3.1 Sample selection and data reduction

We analyzed MUSE data of four type 2 AGN (J1000+1242, J1010+1413, J1010+0612, J1100+0846, see Table 3.1). These AGN were selected from Jarvis et al. [2019] for their high bolometric luminosity ($>10^{45}$ erg/s; placing these sources in the quasar regime), the presence of extended ionized outflows in [OIII]5007 and of a radio jet, with the aim to study the properties of the outflows and the relation between the ionized gas and radio jets. The AGN in our sample are classified as 'radio quiet' according to the criterion established by Xu et al. [1999] based on the correlation between radio luminosity at 5 GHz and the [OIII]5007 luminosity. Despite this classification, they exhibit moderate radio luminosity ($\sim 10^{24}$ W Hz^{-1} at 1.4 GHz) and host jets in most cases. To study the morphology of radio emission and its detailed structures, we used the low resolution ($\sim$1 arcsec HPBW) 6GHz VLA and high resolution (0.2 arcsec HPBW) 1.5GHz e-MERLIN interferometric radio observations presented in Jarvis et al. [2019]. In two out of four galaxies (J1000+1242 and J1010+1413) the radio emission, associated with jets [Jarvis et al., 2019]), is extended on 10-20 kpc scales and this allowed us to study in detail the relation between the radio jet and the ionized gas. For J1100+0864 just an ambiguous extended feature ($\sim$ 0.8 kpc north of the nucleus)

is detected with e-MERLIN, while for J1010+0612 the radio emission is not resolved ($\lesssim$ 0.3 kpc). Consistently with Jarvis et al. [2019] we computed the noise using 8σ clipping repeated 10 times across a region 50 times the size of the beam (1" for VLA and 0.25" for e-MERLIN.) For J1000+1242, J1010+1413, and J1100+0846 we also exploit *Hubble Space Telescope* (*HST*) WFC3 and ACS images obtained with the F621M, F689M, and FR551N filters [1]. For the redshifts of our targets, these filters trace the continuum emission of the galaxies. The *HST* images are retrieved from the Hubble Legacy Archive. The radio maps and *HST* images are shown in Fig.3.1.

Table 3.1: Basic properties of the MUSE observations for the four AGN in our sample. (1) Right Ascension. (2) Declination. (3) Estimated redshift from Harrison et al. [2014]. (4) Luminosity distance in Mpc from NASA/IPAC Extragalactic Database (`https://ned.ipac.caltech.edu/`). (5) Starting date of the observations. (6) Mean DIMM seeing measured during the observations at 500 nm and at zenith. (7) Number of exposures. (8) Exposure time per exposure. (9) Total exposure time on target.

Name	RA$^{(1)}$ [hh:mm:ss]	Dec$^{(2)}$ [dd:mm:ss]	$z^{(3)}$	$D_L^{(4)}$ [Mpc]	Date$^{(5)}$ [DD-MM-YYYY]	DIMM$^{(6)}$ [arcsec]	N$^{(7)}$	$t_{\rm exp}^{(8)}$ [s]	$t_{\rm tot}^{(9)}$ [s]
J1000+1242	10:00:13.14	+12:42:26.2	0.1480	732	18-02-2020	0.73	11	700	7700
J1010+1413	10:10:22.95	+14:13:00.9	0.1992	1010	29-01-2020	0.62	8	700	5600
J1010+0612	10:10:43.36	+06:12:01.4	0.0984	468	02-04-2020	0.78	8	700	5600
J1100+0846	11:00:12.38	+08:46:16.3	0.1005	483	03-03-2020	1.03	6	450	2700

Data reduction MUSE data of the four galaxies presented in this work belong to ESO program 0104.B-0476 (PI G. Venturi). All the observations were acquired in seeing-limited wide-field mode (WFM), which covers a field of view (FOV) of $1' \times 1'$ with a sampling of 0.2 arcsec/spaxel. The data consist of 2 Observing Blocks (OBs) for J1010+1413 and J1010+0612, for a total of 8 exposures of 700s each, one OB for J1100+0846 for a total of 6 exposures of 450s each, and 5 OBs for J1000+1242, for a total of 16 exposure of 700s each; five of these exposures were discarded during the data reduction due to the significantly worse seeing (>1"), and we thus combined only 11 exposures to produce the data cube employed in this work for J1000+1242. We estimated the atmospheric optical seeing at the zenith at 500 nm (DIMM) by averaging the mean of DIMM seeing at the start and at the end of the observation over all the exposures. The main technical details of the observations are reported in Table 3.1. Subsequent exposures were dithered and rotated by 90 degrees in order to remove the artifacts produced by the 24 channels associated with each IFU, as well as to optimise cosmic ray removal and background subtraction. The sky emission was subtracted using a sky spectrum extracted from regions free of target emission in the science frame.
The data reduction and exposure combination were carried out with the ESO MUSE pipeline version v1.6, using ESO Reflex, which provides a graphical and automated way to execute the reduction recipes with ESORex (for details, see Weilbacher et al. 2020).

[1]The filters F621M, F689M, and FR551N have a spectral coverage of ∼800, 800 and 200 Å around the central wavelengths 6218, 6876 and 5510 Å, respectively [Rodrigo et al., 2012].

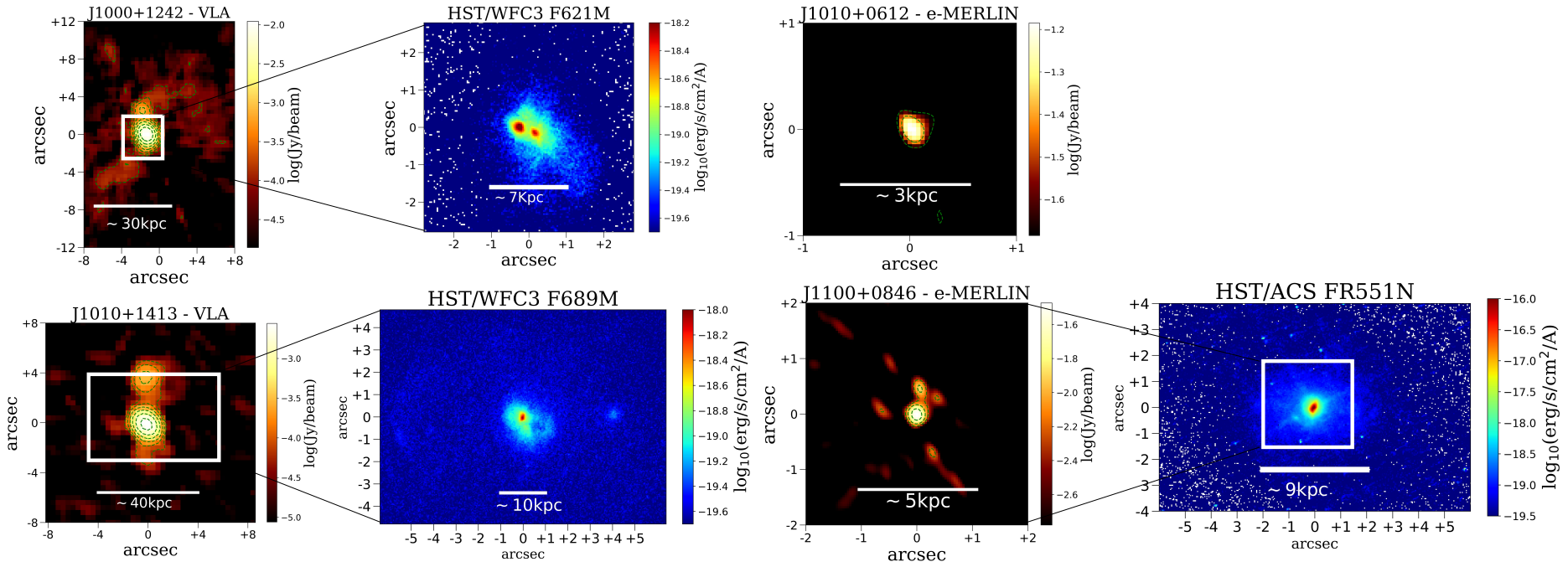

Figure 3.1: Left panels: Low-resolution (∼1 arcsec HPBW) 6 GHz VLA radio images from Jarvis et al. [2019] for J1000+1242 (top) and J1010+1413 (bottom). Right panels: 1.5GHz e-MERLIN data (∼0.2 arcsec HPBW) for J1010+0612 (top) and J1100+0846 (bottom). All panels show a zoomed-in inset with the optical images from *HST*/WFC3. The J1010+0612 radio data are not resolved, and no *HST* data are available for this AGN. The green contours represent [2,4,8,16,32,64,128]σ for the VLA images and [8,16,32,64,128]σ for e-MERLIN.

3.2 Spectroscopic analysis

In this section, we briefly describe the key steps of the analysis of the MUSE optical IFS data cubes to study the emission lines arising from the ISM. The details of the spectral analysis performed in this study can be found in previous works [e.g. Marasco et al., 2020, Tozzi et al., 2021, Cresci et al., 2023a]. Before fitting the emission lines, some pre-processing steps were required. First, it was necessary to remove the contribution of the spatially-unresolved AGN and the stellar continuum, so we performed a Voronoi tessellation [Cappellari and Copin, 2003] to obtain spatial bins with a signal-to-noise ratio (hereafter, S/N) >5 in each wavelength channel (1.25 Å-wide). To remove the continuum, we considered a model which includes the continuum emission from the stars and AGN, and the line emission modeled with a combination of Gaussian functions. Being our objects type 2-AGN, we did not include in the model the unresolved emission of the BLR from the core of the AGN. We used the MILES stellar population synthesis templates to model the stellar continuum [Sánchez-Blázquez et al., 2006, Falcón-Barroso et al., 2011]. We also adopted a third-order multiplicative polynomial and an additive polynomial of degree between 5 and 7 depending on each target to reproduce the low contribution of AGN continuum and the spectral shape, which could be distorted by the reddening. We fitted the model to the observed spectra employing the PPXF code (Penalized PiXel-Fitting; Cappellari and Emsellem 2004). This method fits observed galaxy spectra with a combination of stellar templates, allowing the extraction of the line-of-sight velocity distribution.

After constructing the total model, we finally subtracted the continuum from the cube spaxel by spaxel, rescaling the modeled continuum emission obtained in each Voronoi bin to the median of the observed continuum in each spaxel. In this way, we obtained a cube containing only the contribution of the ionized gas emission lines. We smoothed each slice of the cube with a Gaussian having a dispersion $\sigma_{\rm smooth} = 1$ spaxel, corresponding to 0.2 arcsec. This allowed us to better investigate the ionized gas by enhancing the S/N, while minimizing the degradation of spatial resolution. Then we modelled the emission lines in each spaxel, including Hα, Hβ, the oxygen doublets [OIII]$\lambda 4959, 5007$ and [OI]$\lambda 6300, 6364$, [NII]$\lambda 6548, 6584$ and [SII]$\lambda 6717, 6731$. We parametrized each line with up to three Gaussian components. To reduce degeneracies of the parameters, we kept the velocity and the velocity dispersion of each Gaussian component fixed among all lines, while the flux parameters were left free to vary, with the exception of [OIII] and [NII] doublets, whose flux ratio was kept fixed to the values imposed by atomic physics (0.343 and 0.338, respectively). We performed three different fitting by using 1, 2, and 3 Gaussian components per emission line, respectively. A Kolmogorov-Smirnov (K-S) test on the residuals of the fit was carried out to define the minimum number of components required to provide an acceptable fit in each spaxel [Marasco et al., 2020]. As a final step, we attempted to decouple the kinematics of the ISM, disentangling the different contributions to the emission line profile (for example the rotation or debris merging from the outflows and the gas with high turbulence) in order to assign a physical meaning to each component and study each of them separately. There is not a unique criterion for labeling a single component due to the different nature of the components, however, we classified them as 'narrow' or 'broad' depending on the velocity dispersion of each Gaussian component. Note that 'broad'

[1]We retrieve the ratios from https://www.nist.gov/pml/atomic-spectra-database (Kramida et al. 2023)

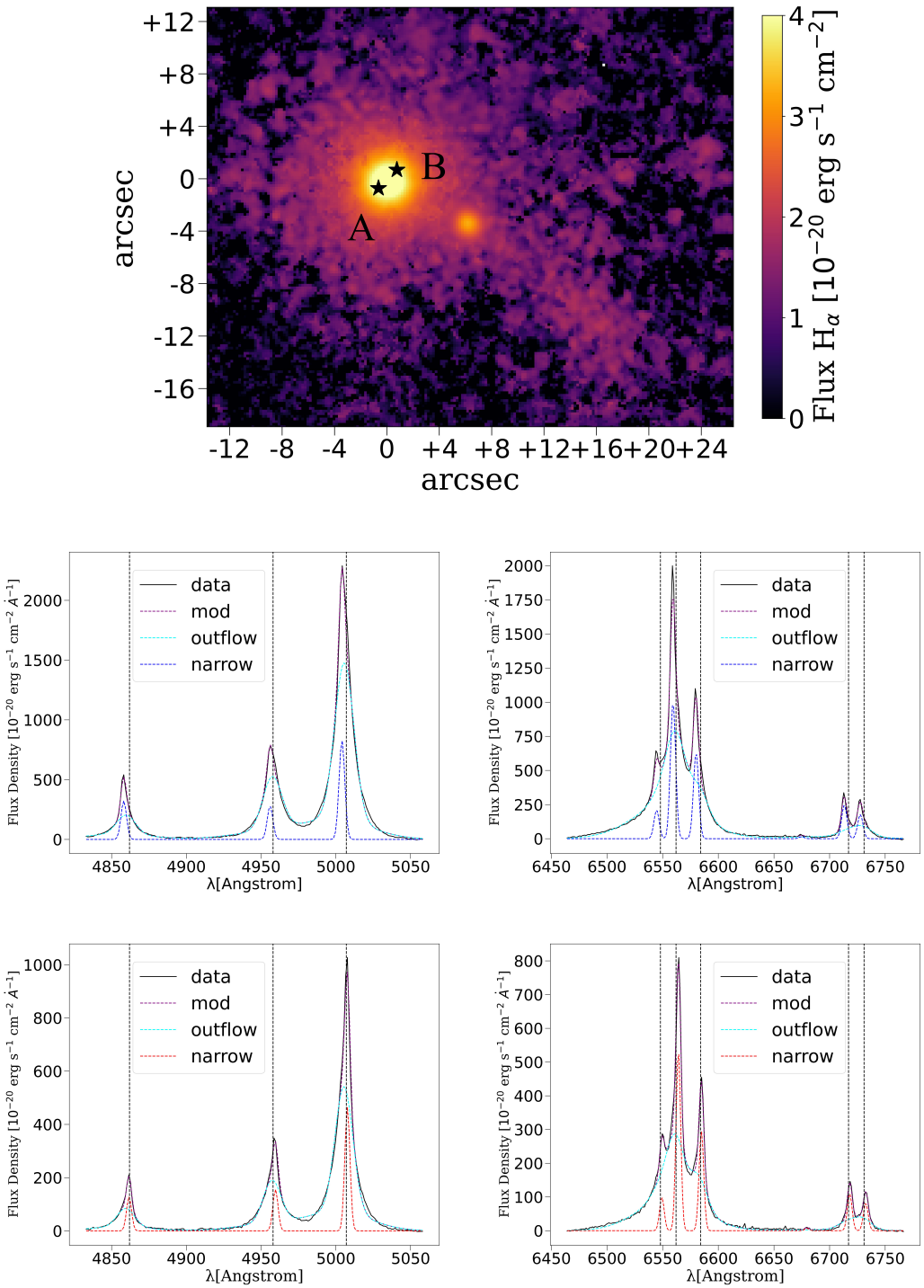

Figure 3.2: Upper panel: Flux density map of J1010+0612 from MUSE. Bottom panels: Spectra extracted from the regions A and B marked with the black stars in the upper panel. The first column shows the spectral range including Hβ and [OIII] doublet while the second column displays that including Hα, [NII] and [SII] doublets. Black lines represent the data subtracted of continuum emission as described in Section 2, purple lines the total model, cyan lines the broad components and red (up) and blue (bottom) lines the narrow components obtained through the decoupling of the line profiles as described in Section 3.2.

should not be confused with the broad emission lines typical of Type 1 AGN, which are emitted from the BLR. In the sources where a rotating disk is clearly observed (J1010+0612 and J1100+0846), we set the threshold value for the velocity dispersion above which we classify the components as 'broad', and below which we classify them as 'narrow', to be 50 km/s larger than the maximum value found for the stellar velocity dispersion (150-200 km/s) to take into account that the ionized gas in the disk could be more turbulent than the stellar kinematics. We stress that, when fitting three Gaussian components to the emission lines, this approach could result in defining either one component as narrow and two as broad or two as narrow and one as broad. Fig.3.2 shows a clear example of the spectral decoupling of the emission line profiles between narrow and broad components in J1010+0612. The red-dashed and blue-dashed lines represent the narrow emission from the disk in the receding and approaching regions of the rotation disk, respectively. The cyan dashed line represents the blue-shifted broad component that we identify as an approaching outflow. In J1010+1413 and J1000+1242, since the stellar kinematics does not show clear rotational features and the ISM kinematics appears more complex, we set the thresholds to different values to decouple the line profile, 350 and 250 km/s, respectively.

3.3 Results

In this section we present the flux, kinematic and emission-line ratio maps of the ionized gas for the four targets in our sample. We mainly focus on the brightest emission line [OIII]λ5007. We present both [OIII] and Hα maps when they show very different characteristics as in J1100+0846 and J1010+0612. We also present for each target the flux of the broad component of Hα that we use to determine the properties of outflowing gas. Moreover we provide also the moment 0, moment 1 and moment 2 maps which are defined as :

$$M_0 = \int I(v)\, dv$$

,

$$M_1 = \frac{\int v\, I(v)\, dv}{\int I(v)\, dv}$$

,

$$M_2 = \sqrt{\frac{\int (v - M_1)^2\, I(v)\, dv}{\int I(v)\, dv}}\,.$$

, respectively, where $I(v)$ is the flux density of the modelled line profile (made up of either one, two or three Gaussians). They represent the flux, the velocity and the velocity dispersion of the total line profile. The flux maps are not corrected for the extinction.

3.3.1 J1000+1242

J1000+1242 is an obscured quasar at z $\sim$ 0.148 ($1'' \sim 3.5$ kpc). The ionized gas morphology shows unambiguous evidence for a merger event, as indicated by the presence of elongated tidal tails (Fig.3.3). In addition, data from *HST*/WC3 F621M (Fig.3.1) reveal two distinct nuclear emission sources separated by approximately 1.5 kpc [Jarvis et al., 2019]. These sources could either represent the double AGN resulting from the

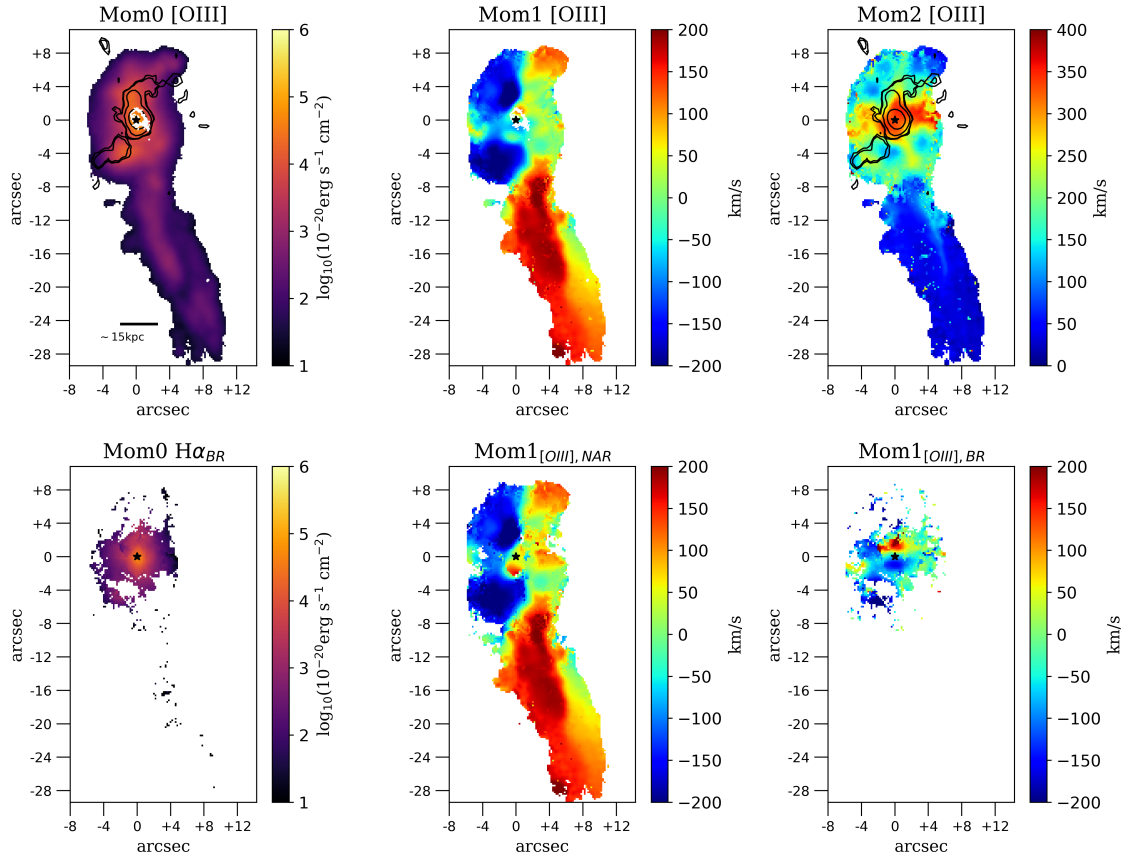

Figure 3.3: Kinematics of the [OIII] line emission in J1000+1242. The upper panels show flux (moment 0), velocity (moment 1) and velocity dispersion (moment 2) of the whole line profile. The lower panels show the flux of the broad component of Hα, the velocity of [OIII] narrow component (middle) and the velocity of [OIII] broad component (right) obtained by the decoupling of the line profile. The black stars indicate the center of the AGN. The black contours of VLA 6 GHz low-resolution ($\sim$ 1" beam) vary from 0.07 to 2 mJy/beam. The white contours represent the HST continuum. An S/N cut of 3 has been applied to the maps for each line.

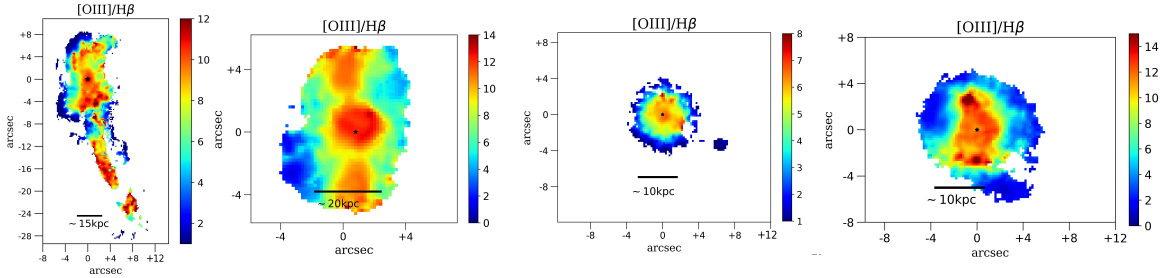

Figure 3.4: Flux map of [OIII]/Hβ ratio. From left to right: J1000+1242, J1010+1413, J1010+0612, J1100+0846. A S/N cut of 3 on the flux of each line has been applied to the maps.

merger or the two opposite sides of the NLR obscured by a dusty circumnuclear ring. However, they are not spatially resolved in our MUSE data. An [OIII] bright region tracing the ionized gas is located in correspondence to the radio structures, as found

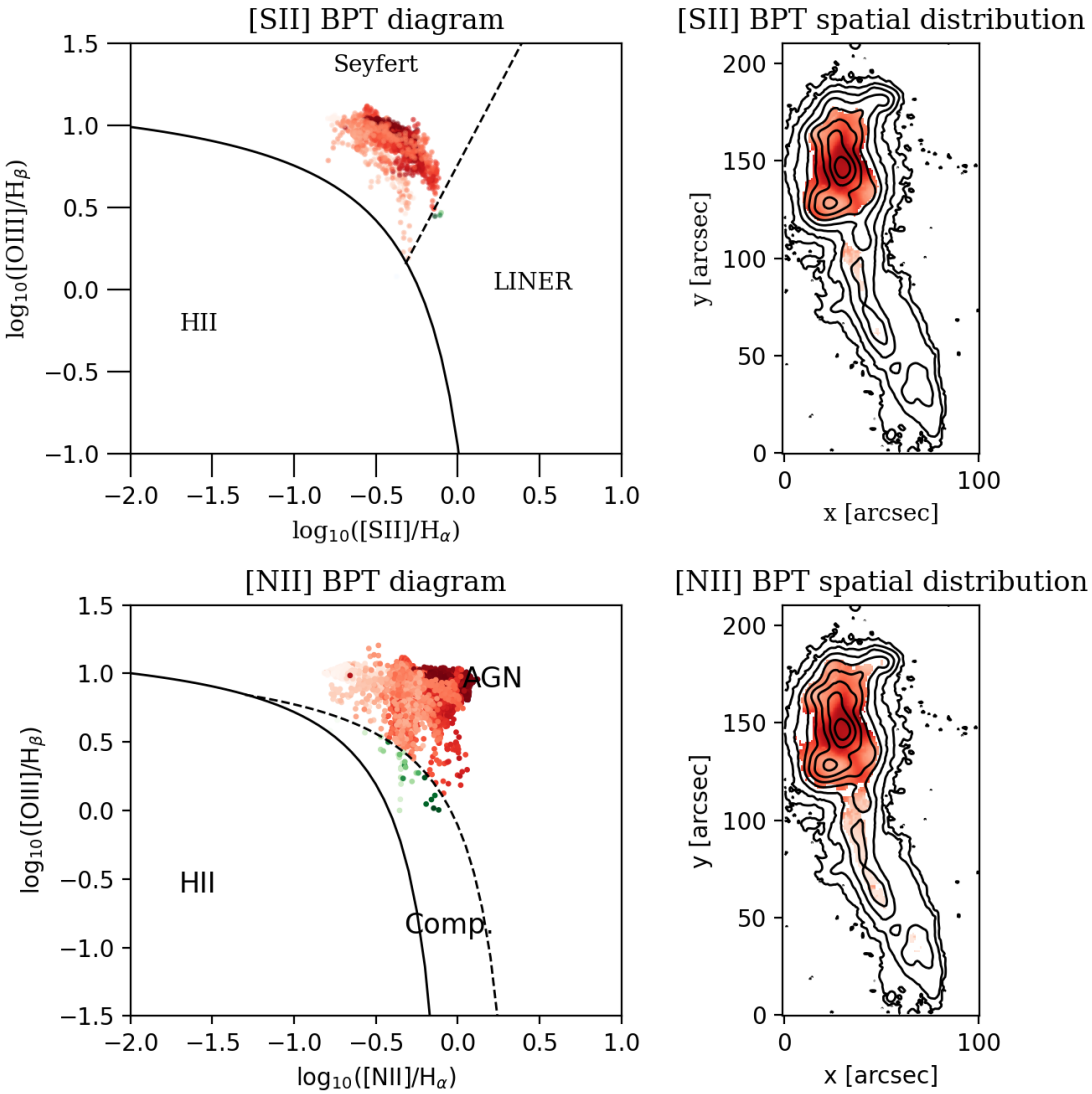

Figure 3.5: Resolved S-BPT ([OIII]/Hβ vs [SII]λ6716,6731/Hα) (Up) and N-BPT ([OIII]/Hβ vs [NII]λ6584/Hα) diagrams (Bottom) of J1000+1242 for each spaxel with S/N>3 in each line. The solid curves define the theoretical upper bound for HII regions [Kewley et al., 2001]. The dashed line in S-BPT represents the Kewley et al. [2006] demarcation between Seyfert galaxies and shocks or LINERs. The dashed curve in N-BPT represents the empirical classification by Kauffmann et al. [2003] to divide pure star-forming from Seyfert–H II composite objects. The black contours represent the Hα intensity map. The data points on the BPT diagram are coloured differently to distinguish different regions. The intensity of the color is proportional to the velocity dispersion of [OIII].

in Jarvis et al. [2019], suggesting a possible connection between the ionized gas and the radio-emitting regions (as in e.g. Riffel et al. 2014, Rodríguez-Ardila et al. 2017, May and Steiner 2017, May et al. 2018, 2020, Cresci et al. 2023a, Venturi et al. 2021). The flux map also reveals the presence of a tidal tail extending for about 20 arcsec in the southern region. It is predominantly observed in the [OIII] line and it is possibly due to the superposition of two distinct tails. These tails also display distinct kinematic properties. Specifically, the easternmost tail exhibits a velocity of 200 km/s,

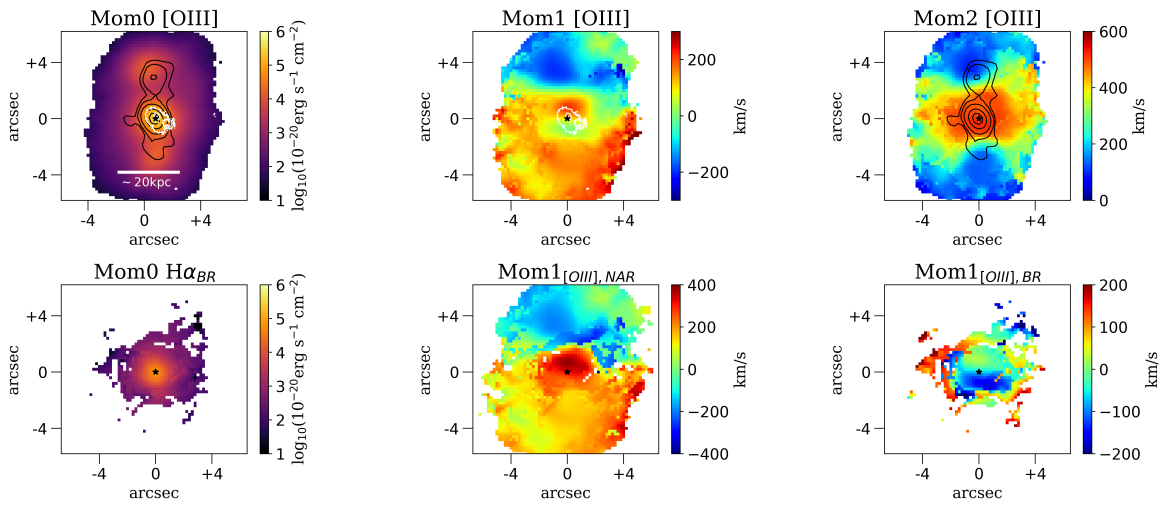

Figure 3.6: Same as Fig.3.3 for J1010+1413.

in contrast, the westernmost fainter tail shows a velocity ranging from approximately 100-150 km/s in its southern end, gradually decreasing towards 0 km/s as it extends northward (Fig. 3.3). The velocity field of the ionized gas also reveals two distinct blue-shifted regions with velocities of ≈ -200 km/s located NE and SE to the nucleus, and a red-shifted region located NW of it. This velocity field might be due to the twisting of the elongated tidal tails.

The velocity dispersion map reveals an increase in the [OIII] velocity dispersion in the region near the nucleus, characterized by an elongated shape oriented W-E and perpendicular to the radio jet (see radio contours in Fig. 3.3), similar to what observed by Venturi et al. [2021] and references therein (see Sect. 3.4).

We computed the velocity of each spectrally decoupled component (narrow and broad; see Sect. 3.2), which are displayed in the bottom panels of Fig. 3.3. The [OIII] broad component shows a velocity gradient of ∼350 km/s extending for 8-10 kpc in the north-south direction, oriented like the radio jet and consistent with slight [OIII] line asimmetry seen in Jarvis et al. [2019]. We interpret the presence of the gradient of [OIII] broad component, with a direction consistent with the radio jet, as an outflow launched by the nuclear radio emission potentially demonstrating a direct connection between a radio jet and the outflows. We also present a map of the [OIII]-to-Hβ flux ratio (Fig. 3.4), sensitive to the ionization state of the emitting gas. The map reveals an extended structure, larger than 20 kpc, with high [OIII]/Hβ (larger than 10), oriented in the same direction as the radio jets, indicating the presence of an AGN ionization cone. We observe that the value of [OIII]/Hβ remains high at large distances from the nuclear sources. We do not exclude that shocks due to the jet, co-spatial with the ionization cone, may also be contributing to the ionization of the gas. To verify this, we use the [OIII]/Hβ vs [SII]/Hα and [OIII]/Hβ vs [NII]/Hα BPT diagrams (e.g Baldwin et al. 1981a, Veilleux and Osterbrock 1987, Kewley et al. 2006, Lamareille 2010, Law et al. 2021, see Fig. 3.5). The map to the right, color-coded according to the location of each spaxel in the diagram to the left, indicates that the main ionization source are the AGN photons. The intensity of the color is proportional to the velocity dispersion of the [OIII] line. We find that the ionization cone exhibits higher values of [OIII]/Hβ and lower values of [SII]/Hα. Conversely, the tidal tails to the south, farther from the nucleus of the AGN, exhibit lower levels of ionization. In the [NII] BPT diagram, the

region with higher velocity dispersion populates the BPT diagram at higher [NII]/Hα ratio, in accordance with a shock scenario [Mingozzi et al., 2019].

3.3.2 J1010+1413

J1010+1413 ($z \sim 0.1992$) is one of the most luminous quasars at $z \sim 0.1$–0.2 in [OIII] ($L_{[\mathrm{OIII}]} \sim 1.69 \times 10^{43}$ erg/s). The *HST*/WFC3 F621M observation revealed a promising dual AGN candidate with the presence of two distinct [OIII]-emitting point sources with a projected separation of 430 pc [Goulding et al., 2019], which cannot be probed with our MUSE observations (having a resolution of FWHM $\sim$ 2 kpc) as in the case of J1000+1242. The morphology and the kinematics of J1010+1413 are really complex as shown also from the continuum image from *HST*/WFC3 F689M in Fig.3.1, probably due to a recent merger [Goulding et al., 2019, Jarvis et al., 2021]. [OIII] shows strong emission around the nucleus, and two lower-luminous [OIII] (as well as in Hα which we do not show) hotspots co-spatial with the radio lobes (see Figs. 3.6 and 3.1). The source is also surrounded by a diffuse halo visible in the continuum (Fig. 3.1).

The velocity map of [OIII] reveals two distinct gradients at different scales and with opposite signs. The first is visible at $\sim$2" scales around the nucleus in NS direction, spanning a velocity range of 200 km/s and $\sim$ 0 km/s. The second one, at higher scales (5"), it is in correspondence of the northern and southern radio lobes which are characterized by a blue-shifted ($\sim$-200 km/s) and a red-shifted ($\sim$200 km/s) velocity, respectively. The [OIII] velocity dispersion map shows that the preferential direction of high velocity dispersion ($\sim$ 500 km/s) aligns perpendicular to the two distinct gradients. This region extends for 20 kpc in the direction perpendicular to the radio jet, as in J1000+1242. In correspondence of the two lobes, the velocity dispersion is lower, as previously observed in other works [Shimizu et al., 2019, Venturi et al., 2021]. The lower velocity dispersion suggests that the lobes could either trace collimated gas pushed by the radio jet or rotational gas of the disk ionized by the AGN. The decoupling of the narrow and broad components was not straightforward in the central region (within 2-3", i.e. 7 kpc from the nucleus) since all components that contribute to the line profile show high velocity dispersion, with values over 300 km/s. However, we chose as a reasonable threshold the value of 350 km/s which allowed us to separate the line profile in a blue-shifted, broader component (up to 500 km/s), that we identified as the outflow, and a red-shifted, narrower component ($<$350 km/s). Since the meaning of this narrower component in this central region is unclear and since it has a sigma dispersion at least up to 300 km/s, we also computed the energetics of the outflow by considering that all the emission is dominated by the outflow, and we included in the outflowing component also the regions in correspondence of the two radio lobes.

The maps of gas excitation show a bipolar region with higher [OIII]/Hβ and lower [SII]/Hα compared to the regions outside of the bicone (see Fig. 3.4 and Fig. 3.7). The regions north-west and south-east of the center is at lower ionization level with higher value of [SII]/Hα and lower value of [OIII]/Hβ. Moreover, regions with lower velocity dispersion populate the BPT diagram at lower [NII]/Hα ratio, as found also in J1000+1242.

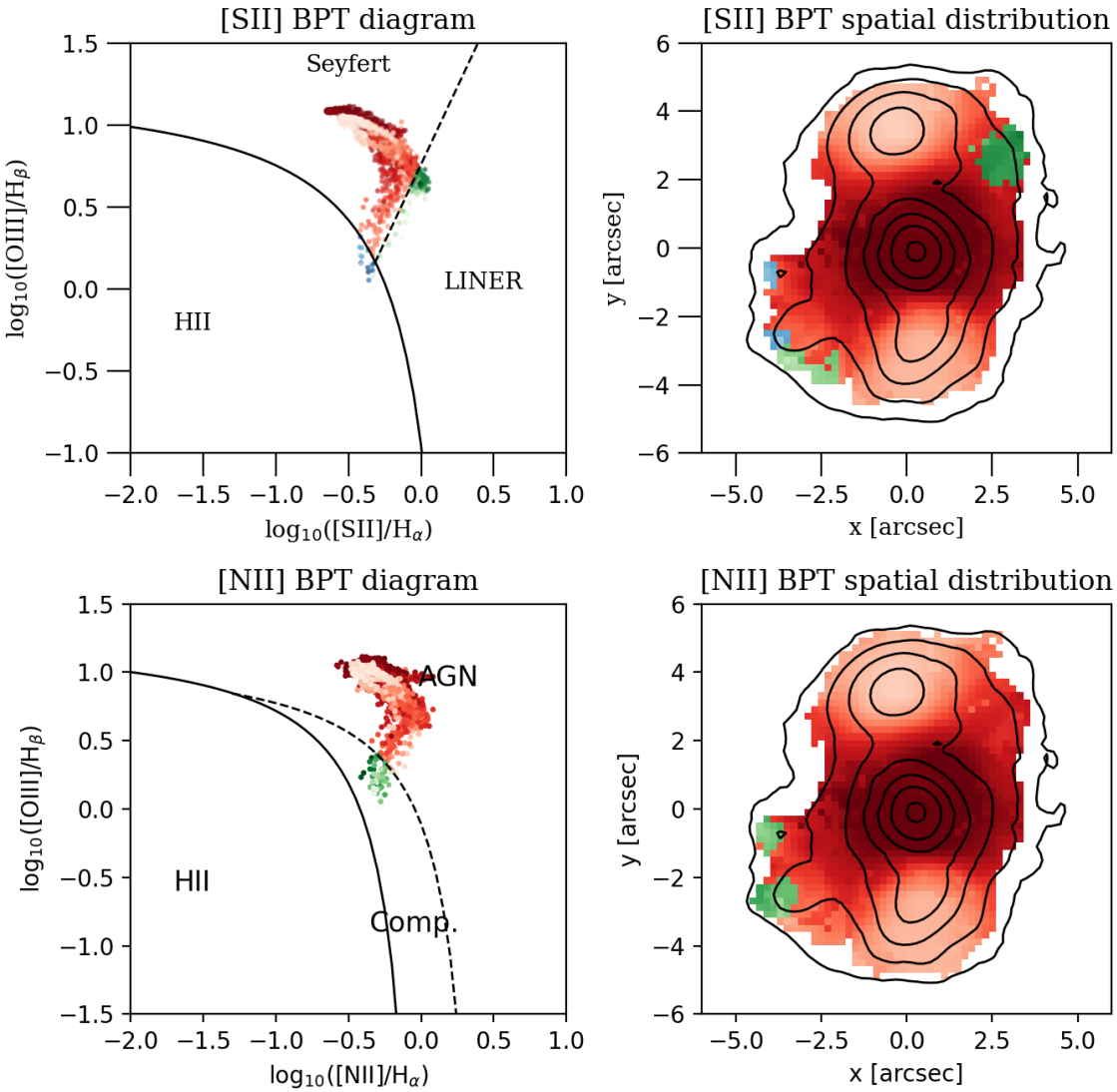

Figure 3.7: Same as Fig. 3.5 for J1010+1413.

3.3.3 J1010+0612

J1010+0612 is the nearest quasar of our sample with z $\sim$ 0.098(1″ $\sim$ 2.3 kpc). The [OIII] line emission is detected in a region limited to the central 7-8 kpc from the nucleus, beyond which the [OIII] flux becomes very faint. The Hα flux is more extended and shows the presence of a companion galaxy located approximately 16 kpc away (Fig. 3.8, left panels in first two rows). The kinematic map of Hα (Fig. 3.8, central panel) reveals a blue-shifted emission to the SE (-50 km/s) of the nucleus and a velocity close to $\sim$ 50 km/s to the NW of the nucleus. This rotational pattern closely resembles that observed in the stellar velocity map (See Fig.3.9), albeit with lower absolute values. This discrepancy is due to the fact that the line profile, as shown in Fig. 3.2, is not just composed by the disc emission, but also includes a significant contribution from a 'blue wing' which contributes in blueshifting the global velocity in the region where the stellar component is receding. Unlike J1000+1242 and J1010+1413, it is not possible to resolve clearly a precise region with higher velocity dispersion, but overall the motion of the gas is highly disturbed in all the central region (up to 10kpc) of

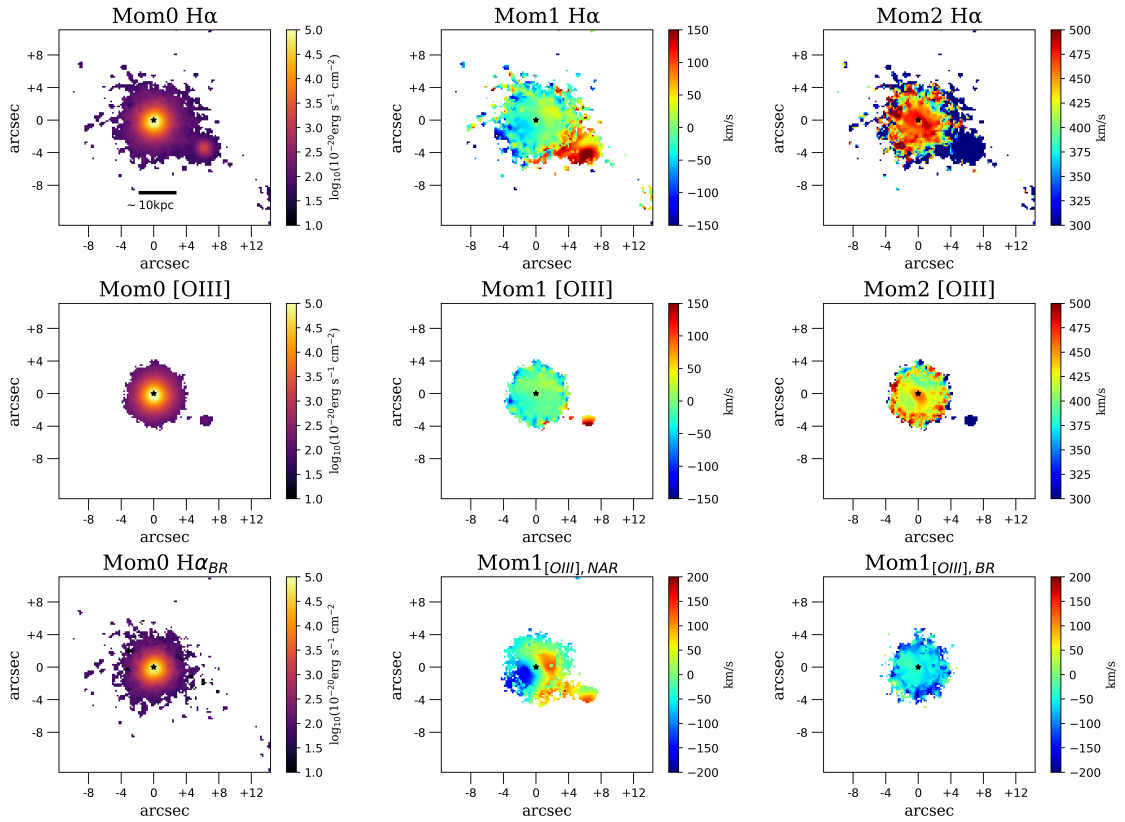

Figure 3.8: Moment 0, 1 and 2 of Ha (top) and same as Fig. 3.3 for J1010+0612.

J1010+0612, showing a velocity dispersion of up to 500 km/s. On the contrary, the velocity dispersion of the companion galaxy decreases, suggesting that the merging is still at an early stage. The two maps displayed in the bottom-center and in the bottom-right panels of Fig. 3.8 show the velocity maps of the narrow and the broad components, respectively. The velocity map of the narrow emission ($V_{[\mathrm{OIII}],\mathrm{NAR}}$) shows a similar rotation as that detected in the stellar kinematics (Fig.3.9), providing clear evidence that the narrow emission traces the ionized hydrogen from the disc. The same rotation pattern is detected also in CO(2-1) [Ramos Almeida et al., 2022]. The velocity map of the broad emission exhibits instead a blue-shifted emission ($V_{[\mathrm{OIII}],\mathrm{BR}}$ ∼100 km/s) that we identify as the outflow. The resolved S-BPT and N-BPT show that the central region is completely ionized by the AGN with [OIII]/Hβ up to 8. The companion galaxy is ionized primarily by HII as shown from S-BPT, and it falls into the Composite region in the N-BPT.

3.3.4 J1100+0846

J1100+0846 is a type 2 AGN hosted in a barred spiral galaxy. The high-resolution *HST*/WFC3 image (Fig. 3.1) reveals a nuclear, elongated emission (∼ 0.4", i.e. ∼ 0.8 kpc) in a direction consistent with the radio structure identified by e-MERLIN. At odds with the other galaxies, the [OIII] and Hα emissions show a different morphology (Fig. 3.11, top-left and mid-left panels). The Hα traces the disc and spiral arms of the galaxy while [OIII] emission shows a broad, circularly symmetric emission around the nucleus, just partially resolved. Clear differences in the two emissions are also observed

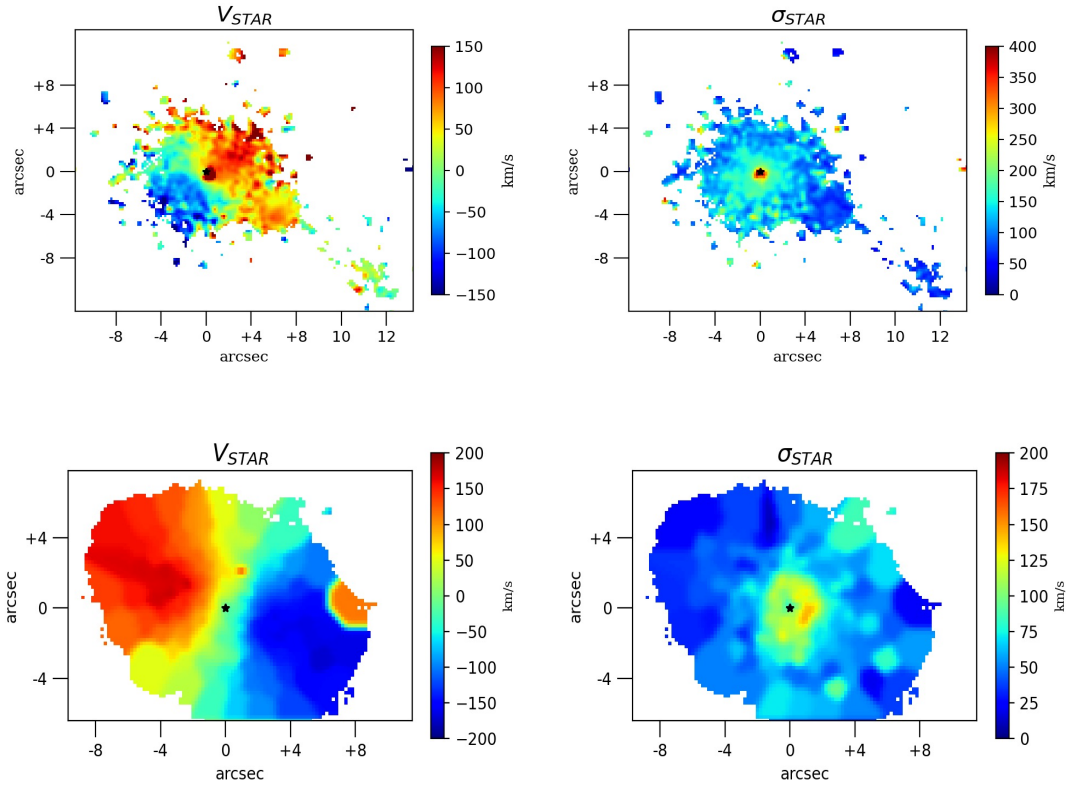

Figure 3.9: Stellar velocity and velocity dispersion computed with ppxf for J1010+0612 (top panels) and J1100+0846 (bottom panels).

in the velocity maps (Fig. 3.11, top-center and mid-center panels). The integrated Hα velocity map traces mainly the rotation of the disc, while the [OIII] velocity is low and close to the systemic velocity of the galaxy. The velocity dispersion maps reveal that in correspondence with the spiral arms the Hα velocity dispersion is low ($\sim$120 km/s), while in the central region the gas shows high turbulence with velocity dispersions of up to 500 km/s in both [OIII] and Hα (Fig. 3.11, top-right and mid-right panels). However, it is not clear if the high-velocity dispersion region is perpendicular to the direction of the jet (determined by the nucleus and the bright hotspot located N/NW of the nucleus, see Fig. 3.1), as it is in J1000+1242 and in J1010+1413. We find that the velocity map of the narrow emission of Hα is considerably smoother compared to the Hα integrated velocity and it matches almost perfectly the rotating stellar velocity V_{STAR} (see Fig.3.9). Also in this case, the rotation pattern is consistent with ALMA observations of CO(2-1) [Ramos Almeida et al., 2022]. $V_{H\alpha,BR}$ resembles the first moment of [OIII]. This suggests that this high-velocity dispersion emission dominates the [OIII] line profile. We identify this emission as an outflow with a direction roughly in the plane of sky, given its low velocities in the line of sight (Fig. 3.11, mid-center panel).

The S-BPT diagram reveals a constant value of [SII]/Hα in each spaxel and the [OIII]/Hβ ratio spans a wide range of values, showing the highest values in the N-S direction, as shown also in Fig.3.4. The ionization is dominated by AGN photons in most of the regions of the target. The same region populates the Composite part of

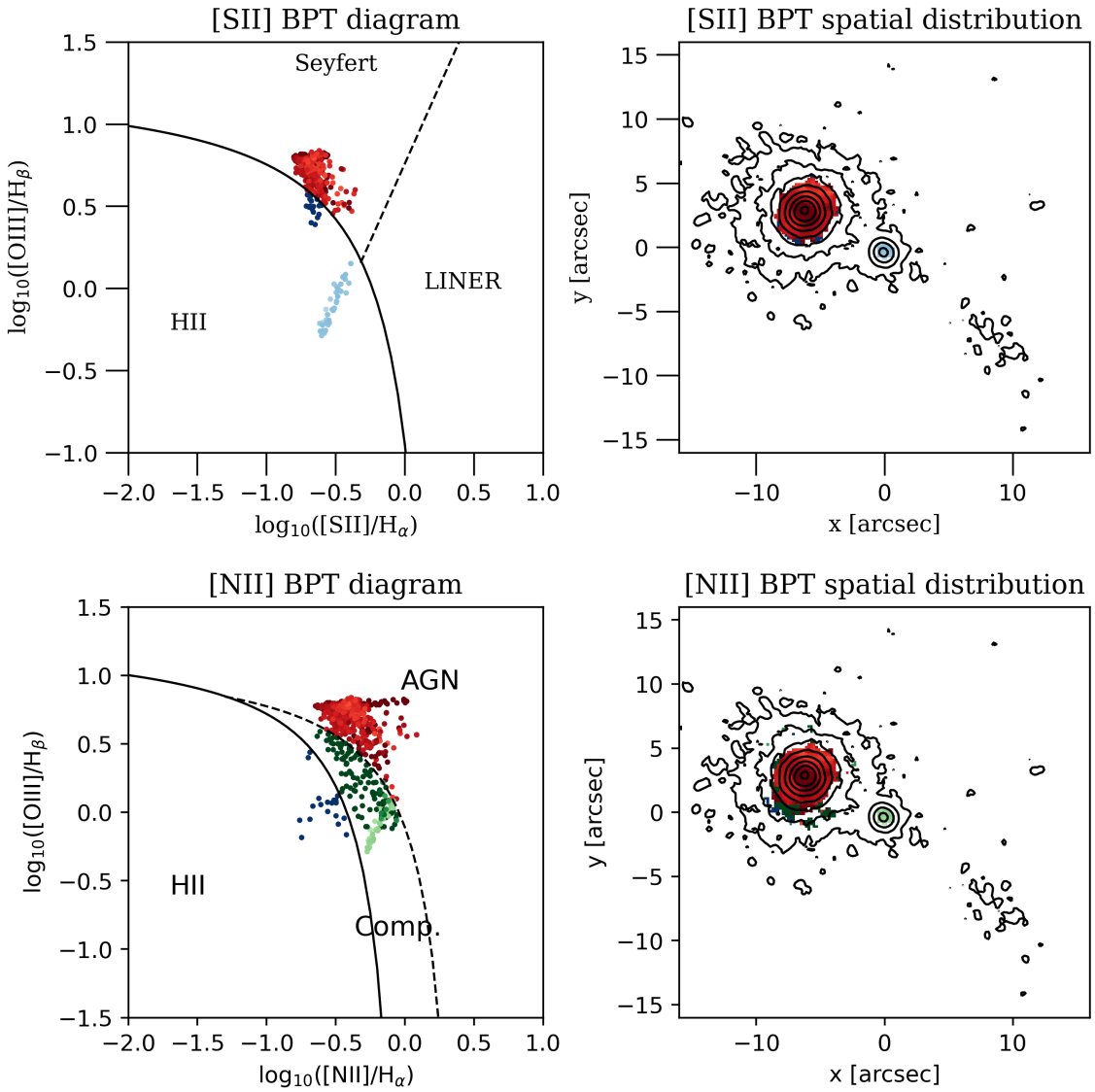

Figure 3.10: Same as Fig. 3.5 for J1010+0612

the N-BPT diagram.

3.3.5 Extinction maps

To derive extinctions, we measured the Hβ/Hα line ratios from each spaxel and scaled it to calculate $E(B-V)$ as follows [Domínguez et al., 2013]:

$$E(B-V) = \frac{2.5}{k(\lambda_{\mathrm{H}\beta}) - k(\lambda_{\mathrm{H}\beta})} \log_{10}\left(\frac{(\mathrm{H}\alpha/\mathrm{H}\beta)_{\mathrm{obs}}}{(\mathrm{H}\alpha/\mathrm{H}\beta)_{\mathrm{in}}}\right) \tag{3.1}$$

where $k_{H\beta} \approx 3.7$ and $k_{H\alpha} \approx 2.5$ are the values of the extinction curve by Cardelli et al. [1989] at Hβ and Hα wavelengths, respectively. We assumed $(\mathrm{H}\alpha/\mathrm{H}\beta)_{\mathrm{in}} = 3.1$, typical of AGN [Veilleux et al., 1995]. A_V is then calculated as $R_V \times E(B-V)$, where R_V (3.1) is the selective extinction and it depends on the physical properties of the dust grains. We show extinction maps in Fig. 3.13. obtained without separating the kinematic components. The highest value of A_V in J1000+1242 is found in the nuclear region

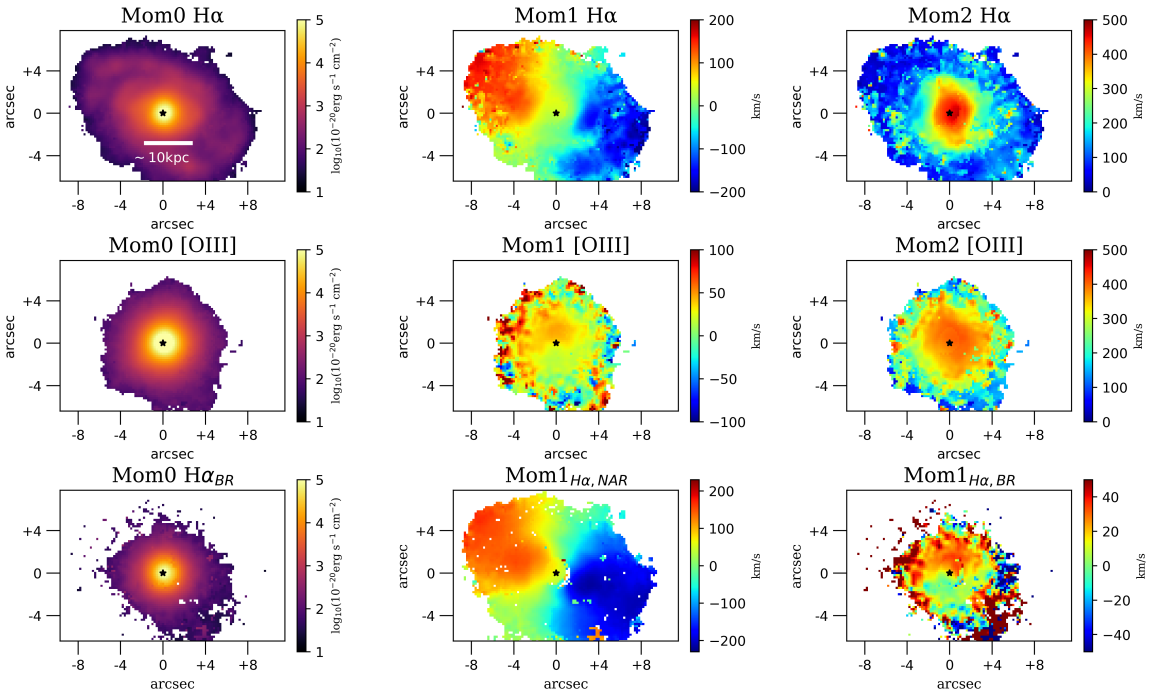

Figure 3.11: Same as Fig. 3.8 for J1100+0846.

(∼2.5 mag). In J1010+1413 and J1010+0612 we find almost constant values (∼1.5 mag) except for a peak of the extinction in the south-east region of J1010+1413 that we previously identified as a region with lower ionization. In J1010+0846 we obtain a peculiar map of the extinction in which the higher values are found within 2" and 4" from the nucleus in the easter region in correspondence with the higher molecular content of CO(2-1) found in Ramos Almeida et al. [2022]. The mean extinction for all targets varies between 1 and 1.8 mag. We used these to correct for extinction the emission line fluxes in our targets spaxel by spaxel.

3.3.6 Properties of ionized outflows

The kinematic structures of the outflows in our objects are varied and complex. To characterize the physical properties of the outflows we adopted the simplified model by Genzel et al. [2011], valid for case B recombination of fully ionized gas with $T \sim 10^4$ K.

The Hα line luminosity can be expressed as

$$L_{\mathrm{H}\alpha} = \int_V f\ n_e\ n_p\ j_{\mathrm{H}\alpha}(n_e, T_e)\ dV \tag{3.2}$$

where f is the filling factor assumed to be 1, n_e the electron density, $n_p = 1.2^{-1} \times n_e$ the proton density assuming 10% number densities of He, and $j_{\mathrm{H}\alpha}$ the emissivity of Hα at $T = 10^4$ K.

The mass of outflowing gas is given by:

$$M_{\mathrm{out}}/M_\odot = 3.2 \times 10^5 \left(\frac{L_{\mathrm{H}\alpha}}{10^{40}\ \mathrm{erg\ s^{-1}}}\right)\left(\frac{n_e}{100\ \mathrm{cm^{-3}}}\right)^{-1} \tag{3.3}$$

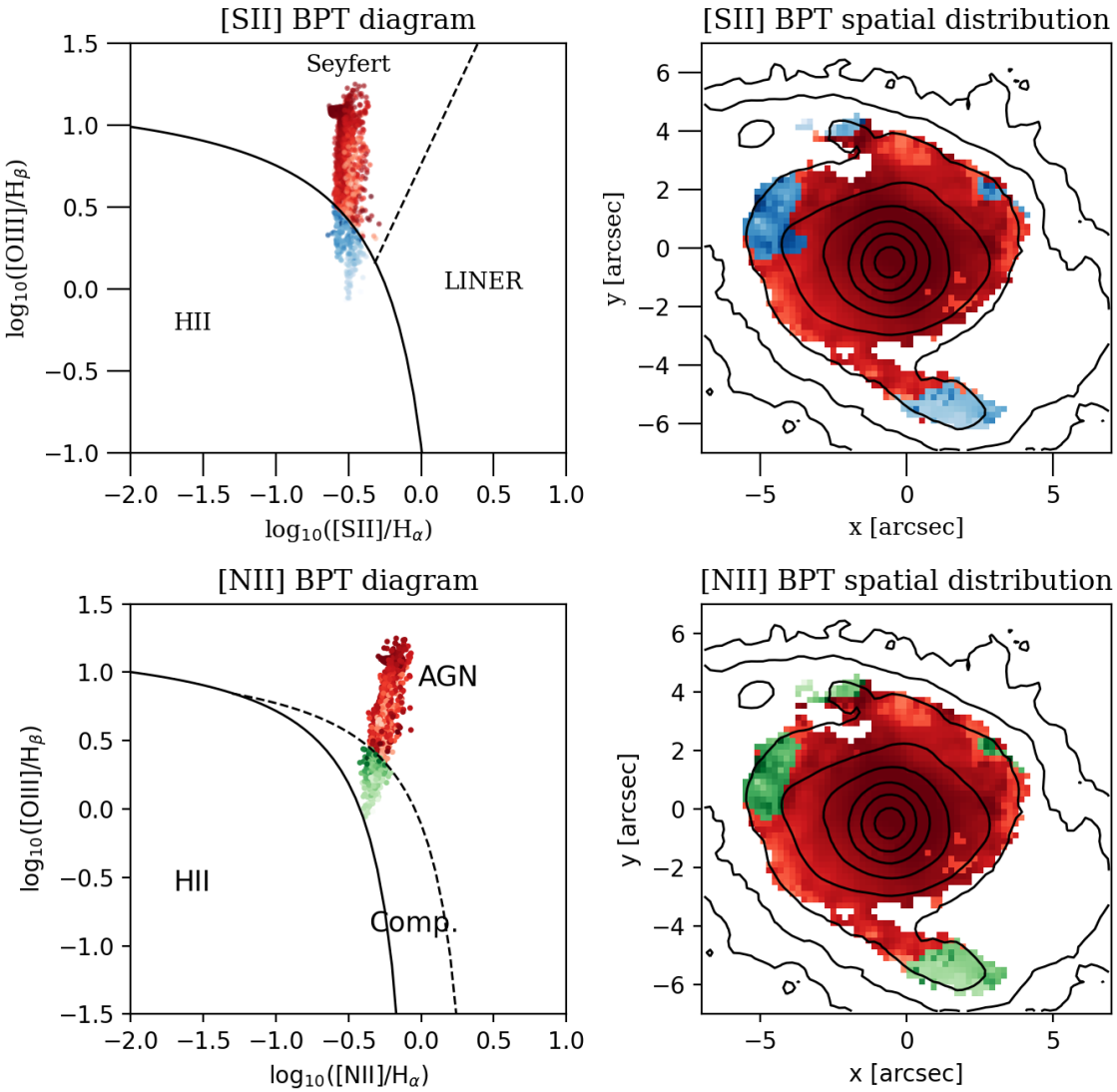

Figure 3.12: Same as Fig. 3.5 for J1100+0846.

where we assumed no dependence between $j_{\mathrm{H}\alpha}$ and n_e.

We determined the mass of the ionized outflows for each spaxel by considering in the Eq. 3.3 only the contribution of the "broad" component of Hα. Then we summed up all the contributions from all the spaxels to obtain the total mass of the outflow. The total outflow masses M_{out} derived for our sample range between 1×10^7 $\mathrm{M}_\odot$ and 1×10^8 $\mathrm{M}_\odot$. Assuming a simplified model of conical outflow with opening angle Ω, a radially constant mass loss rate and outflow velocity v_{out}, out to a radius R, we can compute the mass outflow rate as:

$$\dot{M}_{\mathrm{out}} = C\frac{M_{\mathrm{out}} v_{\mathrm{out}}}{R}. \tag{3.4}$$

where C depends on the adopted outflow history; in our case we adopted a constant mass outflow rate that leads to C = 1 [Lutz et al., 2020]. As an estimate of the radius of the outflow, we assumed the maximum extension of the blueshifted gas in the broad [OIII] component, defined as the distance at which the line flux reaches 10% of its total flux. Note that in all of our targets, this radius extends more than three times the seeing

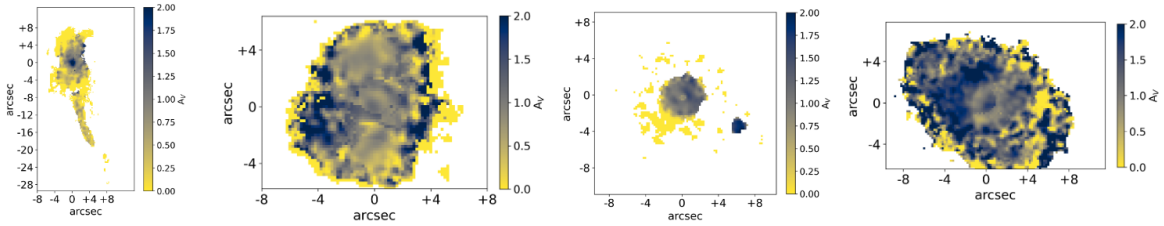

Figure 3.13: Extinction maps from the Balmer decrement Hα/Hβ (in units of magnitude). From left to right: J1000+1242, J1010+1413, J1010+0612, J1100+0846. A S/N cut of 3 on the flux of each line has been applied to the maps.

of the observations. To estimate the electron density of the outflow we employed the optical [SII]λ6717/[SII]λ6731 ratio using the Osterbrock and Ferland [2006] theoretical relation assuming a typical electron temperature of 10^4 K. We computed the density spaxel by spaxel using the broad component of [SII] resulting from the decoupling of the line profiles. To enhance the S/N, we integrated the flux of the [SII] doublet over the spaxels where a physical density could be extracted, and calculated an average density for the outflow. Note that in the assumed scenario the average volume density of the outflowing gas is proportional to R^{-2} but in our case we consider a mean value for the density. We used the PYNEB[Luridiana et al., 2015] software package to convert the doublet ratio in an electron density. The values of outflow densities are reported in Table 3.2. To be consistent with other results in literature [Fiore et al., 2017, Fluetsch et al., 2019], we assumed that the bulk wind velocity is a combination of the velocity and the width of the outflow Gaussian component(s). In particular we adopt the definition of the velocity in Rupke and Veilleux [2013a] as

$$v_{\rm out} = v_{\rm broad} + 2\sigma_{\rm broad} \tag{3.5}$$

where $v_{\rm broad}$ is the central velocity of the broad component compared to the systemic velocity and $\sigma_{\rm broad}$ is the velocity dispersion of the broad component. The concept is that when we observe the line profile of the gas moving away, this will appear as the combination of different velocities inclined at different angles with respect to to our line of sight. Consequently, only the highest observed velocities represent the actual velocity of the outflowing material. We computed it in each spaxel where the outflow is located and we then calculated the average of the outflow velocities. We then assigned the standard deviation of the values in that region as the uncertainty on $\rm v_{out}$.

We also computed the kinetic energy and the kinetic power of the outflow, as $E_{\rm out} = \frac{1}{2} M_{\rm out} v_{\rm out}^2$ and $\dot{E}_{\rm out} = \frac{1}{2} \dot{M}_{\rm out} v_{\rm out}^2$, respectively. Their values are reported in Table 3.2 (see also Speranza et al. 2024 for a comparison of outflow properties in J1010+0612 and J1100+0846). We also estimated the kinetic coupling efficiency, defined as $\epsilon = \dot{E}_{\rm out}/L_{\rm bol,AGN}$, finding values $\sim 10^{-3} - 10^{-4}$. These values are in accordance with values found in literature from observational works [Costa et al., 2018, Harrison et al., 2018a], but are lower compared to coupling efficiencies employed by fiducial AGN feedback models from Di Matteo et al. [2005]. There is, a priori, no reason why the ratio kinetic coupling efficiency, as inferred from observed outflows, should match the feedback efficiencies assumed in state-of-the-art cosmological simulations. In our case, the relatively low values of $\dot{E}_{\rm kin}/L_{\rm AGN}$ may indicate that the overall impact of the outflow on the galaxy may be limited.

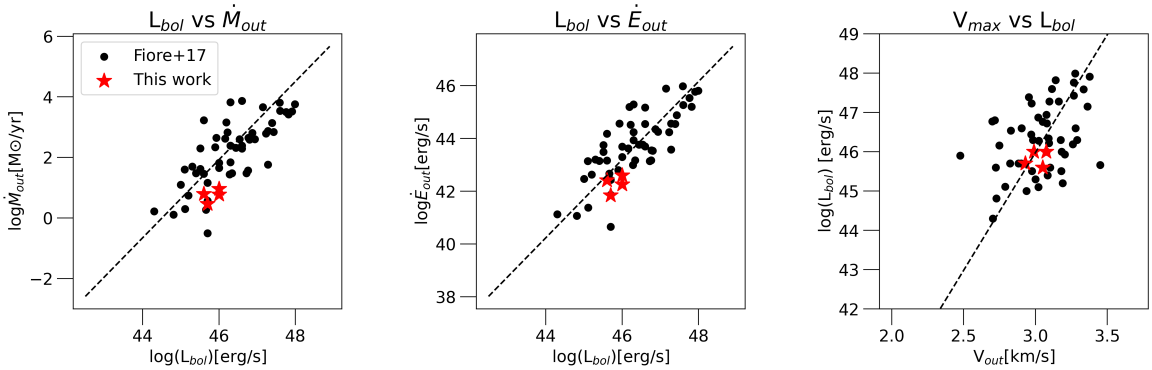

Figure 3.14: Left: Mass outflow rate as a function of the AGN bolometric luminosity. The black dots mark the ionized outflow measurements from Fiore et al. [2017] and red stars are our estimate for the four galaxies of our sample. The black dashed line is the best-fit correlation from Fiore et al. [2017] for their ionized outflow sample. Middle: Kinetic power as a function of the AGN bolometric luminosity. Right: AGN bolometric luminosity as a function of the maximum outflow velocity.

3.4 Discussion

3.4.1 Comparison with ionized outflows in AGN in literature

We compared our results with other works in literature. Fiore et al. [2017] studied the dependence of the properties of outflows on AGN bolometric luminosity in a sample covering $L_{\rm bol,AGN}$ between $\sim 2 \times 10^{44}$ erg s^{-1} and $\sim 10^{48}$ erg s^{-1}. For the targets presented in this work, we adopted the AGN bolometric luminosities calculated by Harrison et al. [2014] through mid- to far-infrared SED fitting to archival photometric data.

Left and middle panels of Fig. 3.14 show the mass outflow rates and the kinetic powers as a function of $L_{\rm bol,AGN}$. The black dots represent the sample of Fiore et al. [2017], who found a good correlation with $L_{\rm AGN}$ with log-linear slopes of 1.29 $\pm$ 0.38 and 1.50 $\pm$ 0.34 for the two above quantities, respectively (dashed black lines). Although Fiore et al. [2017] used a smaller value for the electron density (200 cm^{-3}) for all galaxies in their sample compared to the densities inferred in this work from [SII] (Table 3.2) and they assumed a decreasing mass outflow rate with time (C = 3), we found values for the mass outflow rates and the kinetic power (red stars in Fig. 3.14) which are in accordance with those found for type 2 AGN with similar bolometric luminosity [Fiore et al., 2017]. In Fig. 3.14 we checked the relation between AGN bolometric luminosity and the wind velocity, $v_{\rm out}$, defined as in Eq. 3.5, finding also in this case a good agreement between the results for the AGN in our sample and those in 3.14.

3.4.2 Enhancement of velocity dispersion perpendicular to the radio jet

By comparing the VLA radio maps at low resolution with the maps obtained from our analysis, we note a strongly enhanced gas velocity dispersion in the direction perpendicular to the jet in J1010+1413 and J1010+1242 (Fig. 3.15). The phenomenon is not clear in J1100+0846 and it is not observed in J1010+0612. In those cases an enhance-

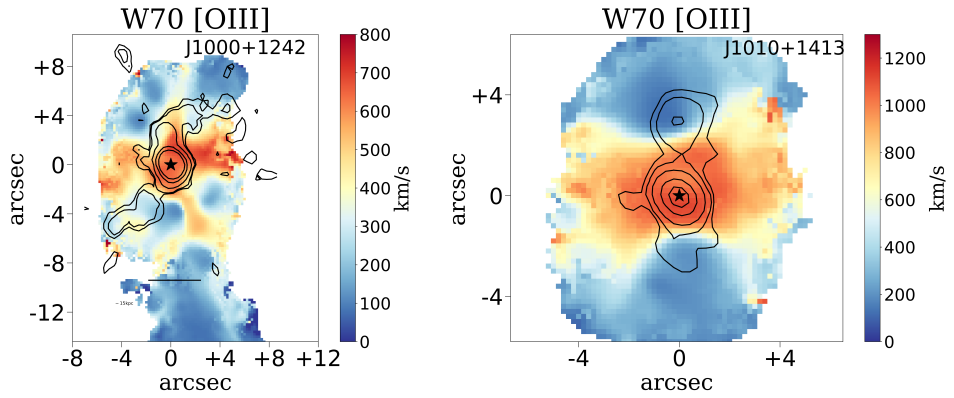

Figure 3.15: Enhancement of [OIII] W70 perpendicularly to the radio jet. Black contours represent the VLA low-resolution (∼1 arcsec beam) radio emission at 6 GHz. J1100+0864 and J1010+0612 are not shown in this plot since the phenomenon studied is not evident due to the poorly resolved radio emission.

ment of velocity dispersion is detected in the central regions (Figs. 3.8 and 3.11), but the radio jet is poorly or not resolved in the data, and thus it is not straightforward to define a jet direction to be compared with the high velocity dispersion region.

We explore the possible origin for this phenomenon in the rest of this Section.

Equatorial outflows

A possible explanation for the enhancement of the emission line width in the direction perpendicular to the radio jets could be an equatorial outflow [e.g Couto et al., 2014, Riffel et al., 2015, Freitas et al., 2018, Shimizu et al., 2019, Ruschel-Dutra et al., 2021], predicted by some models to originate from the BH accretion disc. However, we observed a significantly blue-shifted and red-shifted emission on each side of the nucleus, respectively, that we identified as high-velocity outflows, solely in the direction of the radio jet and the ionization cone. No net blue-shift or red-shift of the broad component is detected instead in the elongated, high-velocity dispersion region. Although no velocity shift is expected from a perfectly radial outflow with no extinction, ionized outflows in QSOs commonly exhibits blueshifted wings, particularly in dusty objects, due to the obscuration of the receding part of the outflow located behind the host [Bae and Woo, 2014, Carniani et al., 2015, Balmaverde et al., 2016, Woo et al., 2016, 2017, Fiore et al., 2017]. Moreover, the fact that no clear velocity gradients (blue-shifted on one side, red-shifted on the other) in these high velocity dispersion regions have been observed in other works in literature [e.g. Venturi et al., 2021, Ruschel-Dutra et al., 2021], suggests that the enhancement of the velocity dispersion in the direction perpendicular to the jet and ionization cone is unlikely to be due to an equatorial outflow.

An alternative explanation is that the velocity dispersion enhancement could be the result of beam smearing which could lead to the blending of spectral line profiles at different velocities along the line of sight, resulting in an increase of the velocity dispersion at the systemic velocity of the galaxy [Durré and Mould, 2019, Shin et al., 2019]. We exclude the possibility of beam smearing because the scale on which we observe this line-width enhancement is larger than the spatial resolution of the observation.

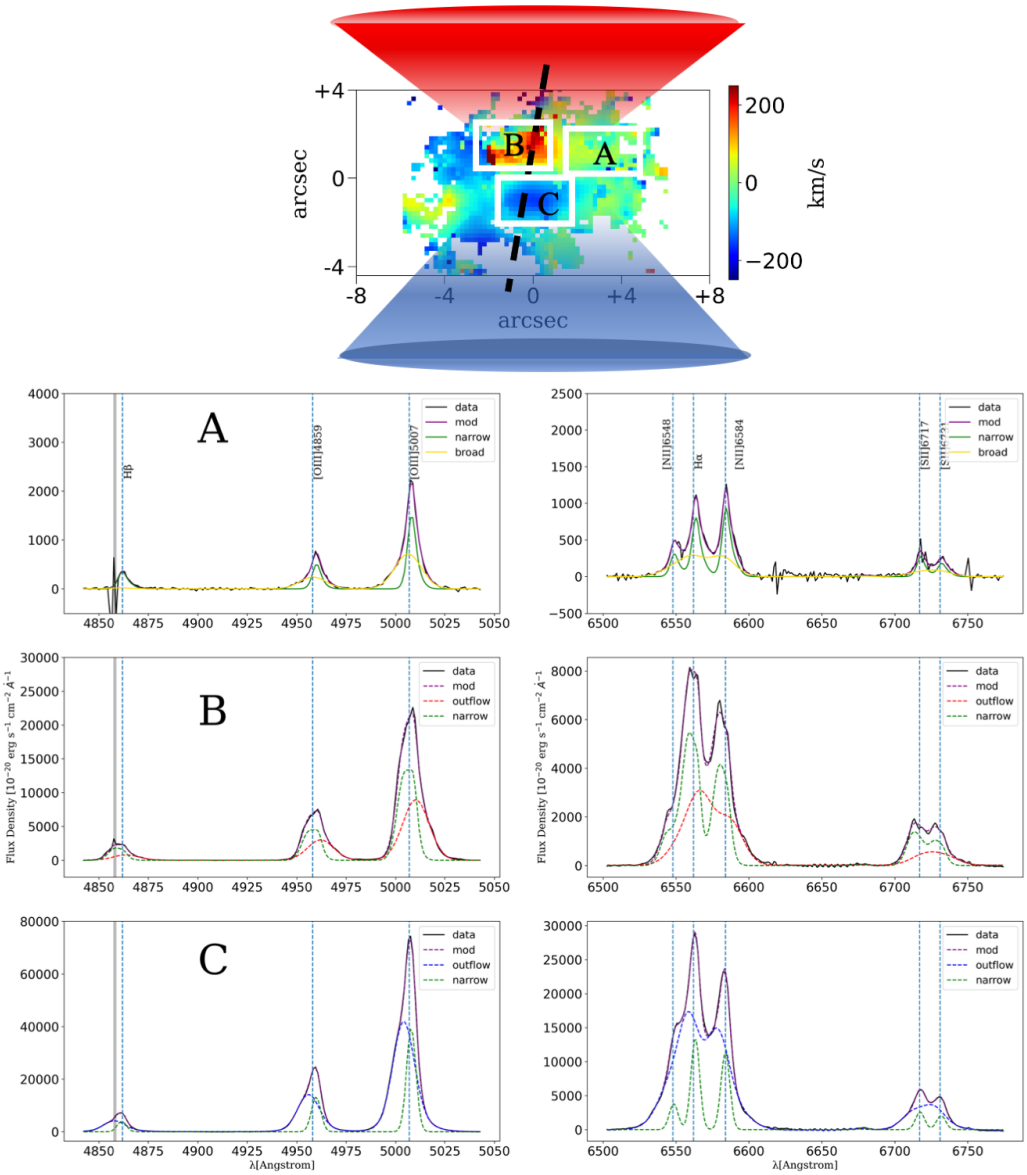

Figure 3.16: Upper panel: velocity of the broad component $V_{[OIII],BR}$ in J1000+1242, also reported in Fig. 3.3, zoomed in the central region. The axis of the outflowing bicone (traced by the red- and blue-shifted motions in regions B and C, respectively) is parallel to that of the radio jet and ionization cones, while turbulent gas is located perpendicularly (region A). Black dashed lines indicates the ionization cone where the outflow is detected. The black dashed line indicates the direction of the radio jet. Bottom panels: Integrated spectra extracted from white rectangles in the correspondent subregions (A,B,C) in the upper panel. Left panels: Hβ, [OIII] doublet; right panels: Hα and [NII] and [SII] doublets. Data are shown in black, the total best fitting model in purple, the narrow component in green, the broad component in region A tracing turbulent gas in yellow, the red-shifted outflow in red and the blue-shifted one in blue. The grey shaded area indicates the region excluded from the fit due to a bad sky subtraction.

Turbulence injected by the jet in the ISM

We conclude that the most plausible explanation for the observed phenomenon is the interaction between the radio jet and the ISM of the host galaxy, through the injection of turbulent energy in the direction perpendicular to the jet, consistent with Venturi et al. [2021]. As discussed in that work, the increased velocity dispersion in an extended region perpendicular to the jet and ionisation cone axis (along which high-velocity outflows are present) is only observed in galaxies hosting a radio jet, even if with low radio power ($<10^{44}$ erg/s).

Fig. 3.16 summarizes this scenario. The map on top represents the velocity of the [OIII] broad component (in J1000+1242) that we decoupled from the narrow component as discussed in Sect. 3.2. We identify two regions with different properties, the first parallel to the radio jet and to the ionization cones (labelled as B and C), the second perpendicular to the radio jet (labelled as A). The former presents an [OIII] velocity gradient of $\sim$ 400 km/s, tracing an outflow, while the latter exhibits an [OIII] velocity close to the systemic velocity of the galaxy. Three representative spectra of the regions are shown in the figure. In the spectrum extracted from the southern outflowing cone (C), we observe a blue-shifted wing (blue line) representing the approaching outflow, in the one extracted from the northern outflowing cone (B), the broad component is red-shifted. The spectrum extracted from the region perpendicular to the jet (A) presents instead a fairly symmetric profile with high velocity dispersion due, according to interpretation discussed above, to the turbulence injected by the jet in the ISM.

Venturi et al. [2021] reported that this phenomenon occurs exclusively in AGN hosting a small scale ($\sim$1 kpc) low-power ($\lesssim 10^{44}$ erg s^{-1}) radio jets with small inclinations ($\lesssim$45°) with respect to the galaxy disc (Querejeta et al., 2016). To our knowledge, no line-width enhancement perpendicular to the jet has been detected in galaxies whose radio jets are directed perpendicular to the galaxy disc, or at most an increased line width has been found on very small scales ($\sim$20 - 40 pc) around the jet base. At variance with Venturi et al. [2021], the angular resolution of our observations does not allow for the determination of the jet inclination with respect the galaxy disc. Although the inclination of the jet cannot be quantified, the cospatiality of radio hotspots with the most intense emission in ionized gas suggests that there is a strong interaction between the jet and the ISM. These aspects strongly suggest that the origin for the enhanced line width perpendicular to the radio jets could be the interaction between the jet and the ISM in the galaxy disc. Supporting this scenario, the most recent hydrodynamic simulations of jet-ISM interaction show that when the inclination angle of the radio jet to the galactic disc is large, the radio jet can easily escape without significant interaction with the disc and without widely broadening the line profile; instead, when the jet is co-planar or at small inclinations angles to the disc, the jet remains trapped in it and strongly and extensively perturbs the ISM [Mukherjee et al., 2016, 2018a,b, Meenakshi et al., 2022]. In the two targets which clearly exhibit the turbulent motions perpendicular to the jet (J1100+0864 and J1010+0612), the morphology of the host galaxy is unclear due to the disturbances induced by the mergers. As a result, it is not straightforward to establish a correlation between this phenomenon and the inclination of the jet with respect to the galaxy disc in our sample.

Comparing the the Seyfert galaxies presented by Venturi et al. [2021] and those analyzed in this work, we note that in the latter the enhanced line velocity widths perpendicular to radio jets are detected over a much larger scale, $\sim$ 10 kpc. This may be

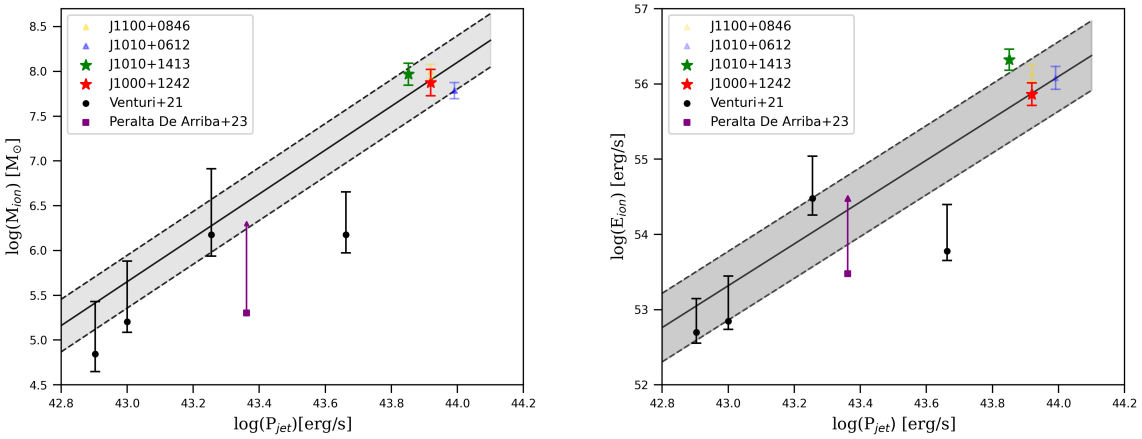

Figure 3.17: Left: Mass of the gas having enhanced velocity dispersion ([OIII] W70 $>$ 300 km/s) as a function of jet kinetic power. The black dots mark the ionized mass measurements from Venturi et al. [2021] for local Seyfert galaxies, while the coloured symbols are our estimates for the ionized mass of the turbulent gas in our sample. The stars are used for those targets in which the enhanced velocity dispersion perpendicular to the jet is well observed, while the less transparent triangles are used for those target in which this phenomenon is not clear as in case of J1100+0864 or not observed as J1010+0612. The quantities have been calculated consistently with Venturi et al. [2021]. The purple squares mark the measurements from Peralta de Arriba et al. [2023] that represent a lower limit of our estimations. Right: Kinetic energy of the high velocity dispersion gas as a function of jet kinetic power. The correlation holding over more than one order of magnitude in jet power and ∼3 dex in mass and kinetic energy suggests a connection between the radio jet and the high velocity dispersion gas.

probably due to the fact that the power of the radio jets in the galaxies of our sample is almost an order of magnitude higher than in the case of the Seyferts in their work and for this reason they are able to induce this phenomenon on a larger scale.

Table 3.2: Properties of the high-velocity ionized outflow. (1) AGN bolometric luminosity from Harrison et al. [2014]. (2) Total mass in outflow. (3) Outflow electron density estimated from [SII] doublet ratio. (4) Outflow radius. (5) Maximum outflow velocity, $v_{\rm out}$, estimated as in Fiore et al. [2017]. (6) Mass outflow rate. (7) Outflow kinetic power. (8) Total energy in outflow. (9) Coupling efficiency, $\dot{E}_{\rm out}/L_{\rm AGN}$. The second line for J1010+1413 reports the outflow properties obtained when considering that all the line emission comes from outflowing gas (see Sect. 3.3).

Name	log $L_{\rm AGN}^{(1)}$ [erg s^{-1}]	$M_{\rm out}^{(2)}$ [10^7 M$_\odot$]	$n_{\rm e,out}^{(3)}$ [cm^{-3}]	$R_{\rm out}^{(4)}$ [kpc]	$v_{\rm out}^{(5)}$ [km s^{-1}]	$\dot{M}_{\rm out}^{(6)}$ [M$_\odot$ yr^{-1}]	$\dot{E}_{\rm out}^{(7)}$ [10^{42} erg s^{-1}]	$E_{\rm out}^{(8)}$ [10^{56} erg]	$\epsilon^{(9)}$
J1000+1242	45.7	1.9	1230 ± 450	6	850 ± 115	2.9	0.7 ± 0.7	1.5 ± 0.5	4×10^{-4}
J1010+1413	46.0	5.2	360 ± 100	7	1190 ± 100	9.1	4 ± 2	7.4 ± 2.4	1.2×10^{-3}
		10		17		6.7	2.2	12.2	6.7×10^{-4}
J1010+0612	45.6	3.7	360 ± 100	7	1123 ± 155	6.2	2.6 ± 2.5	4.9 ± 1.5	2×10^{-3}
J1100+0846	46.0	5.3	336 ± 100	9	977 ± 120	6.0	1.8 ± 2.8	5.2 ± 2.5	5.5×10^{-4}

In order to test if the described scenario is feasible from the energetic point of view, that is, if the jets are sufficiently powerful to drive the observed gas perturbations, we estimated the mass of ionized gas $M_{\rm ion}$ which undergoes this phenomenon and

compared it with the jet power. In order to have a direct comparison with the results obtained by Venturi et al. [2021] at lower jet powers ($<10^{44}$ erg/s), we computed the kinetic power of the jets through the following relation from Bîrzan et al. [2008]:

$$\log P_{\rm jet} = (0.35 \pm 0.7)\ \log P_{1400} + (1.85 \pm 0.10) \tag{3.6}$$

where $P_{\rm jet}$ is the jet kinetic power (in units of 10^{42} erg s^{-1}) and P_{1400} is its radio luminosity at 1400 MHz (in units of 10^{24} W Hz^{-1}), taken from Jarvis et al. [2019]. In order to investigate possible systematic effect in the estimation of $P_{\rm jet}$, we use the relation in Heckman and Best [2014]:

$$P_{\rm jet} = 4 \times 10^{35}\,(f_W)^{3/2}\,(10 \times P_{1400})^{0.86}\ \ {\rm W} \tag{3.7}$$

where f_W is a factor that keeps into account all the uncertainties and has a value $\sim$20 [Blundell and Rawlings, 2000]. We find values of $P_{\rm jet}$ consistent with those found with Eq.3.6 except for J1010-1413, which is slightly out of the errors. The values are reported in Table 3.3.

To compute the mass, we first spatially integrated the Hα flux from the MUSE maps from regions with [OIII] W70 $>$ 300 km/s (and S/N $>$ 3) and calculated its luminosity. Then, we estimated the mass of ionized gas through Eq. 3.3, considering all the emission of Hα (not only the broad components) and computing the electron density from the ratio of the total emissions of the [SII] doublet lines, [SII]λ6717/[SII]λ6731. By doing so, we included in the turbulent gas all the gas which contributes to the total line emission, possibly including also spaxels containing emission from both outflows and disc. Despite the fact that a clear spatial comparison of the enhanced velocity dispersions with the radio jets is not possible for J1010+0612 and J1100+0846, we computed the turbulent gas mass also for these objects and we reported in the plots with fainter markers.

Fig. 3.17 reports the mass of turbulent gas versus the power of the jets. By plotting our sample together with the nearby Seyfert galaxies from Venturi et al. [2021], Peralta de Arriba et al. [2023], we see a correlation between the power of the jet and the turbulent gas mass. This suggests that more powerful jets are able to affect larger quantities of ISM and reinforces the scenario in which jets are responsible for the enhancement of emission line width in the perpendicular direction. The best-fit relation is:

$$\log(M_{\rm ion}) = 2.4 \log(P_{\rm jet}) - (98.5 \pm 0.25) \tag{3.8}$$

where $M_{\rm ion}$ is the mass of ionized gas in solar masses and $P_{\rm jet}$ is the kinetic power of the jet in erg/s.
To be consistent with Venturi et al. [2021] and Peralta de Arriba et al. [2023], we estimated the kinetic energy of the gas in the same region as $E_{\rm ion} = M_{\rm ion}\sigma^2_{\rm ion}/2$ where $\sigma_{\rm ion}$ is the velocity dispersion of Hα. We employed the velocity dispersion to calculate the ionized gas energy because it is an indicator of the turbulence produced by the radio jets. The right panel in Fig. 3.17 shows that there is a correlation between the kinetic energy of the high-velocity dispersion gas and the kinetic power of the radio jets. This indicates that jets can inject energy into the ionized gas and be responsible for the enhancement of line emission. The best-fit relation is:

$$\log(E_{\rm ion}) = (2.62 \pm 0.01) \log(P_{\rm jet}) - (59.7 \pm 0.4). \tag{3.9}$$

The correlations found further support the scenario in which the jet is responsible for injecting turbulence in the ISM over a wide range of radio jet powers. In principle, this could be a significant mechanism of feedback, since the high turbulence injected by the jet in the ISM could prevent the cooling of the gas and additional star formation [Mandal et al., 2021]. The results are shown in Table 3.3.

Table 3.3: Properties of the radio jets and the ionized gas involved in the velocity dispersion enhancement perpendicular to the jets. (1) Radio luminosity from Jarvis et al. [2019]. (2) Kinetic power of the jet estimated from its radio luminosity with Eq. 3.6 from Bîrzan et al. [2008]. (3) Kinetic power of the jet estimated from its radio luminosity with Eq. 3.7 from Heckman and Best [2014]. (4) Electron density from [SII] doublet ratio. (5) Mass of ionized gas computed with Eq. 3.3. (6) Kinetic energy of ionized gas, $E_{\rm ion} = M_{\rm ion}\sigma^2_{\rm ion}/2$. (7) Jet travelling time. (8) Total kinetic energy of jet, $E_{\rm jet} = P_{\rm jet}t_{\rm jet}$.

Name	$\log L^{(1)}_{1.4\ \rm GHz}$ [W Hz^{-1}]	$P^{(2)}_{\rm jet}$ [10^{43} erg s^{-1}]	$P^{(3)}_{\rm jet}$ [10^{43} erg s^{-1}]	$n^{(4)}_e$ [cm^{-3}]	$M^{(5)}_{\rm ion}$ [10^7 M$_\odot$]	$E^{(6)}_{\rm ion}$ [10^{56} erg]	$t^{(7)}_{\rm jet}$ [Myr]	$E^{(8)}_{\rm jet}$ [10^{56} erg]
J1000+1242	24.2	$8.3^{+2.5}_{-2.0}$	7.3	510	7.5 ± 2.4	0.7 ± 0.3	7.5	195
J1010+1413	24.0	$7.1^{+1.8}_{-1.5}$	4.9	390	9.3 ± 2.5	2.1 ± 0.8	3.6	80
J1010+0612	24.4	$9.8^{+3.0}_{-2.5}$	10.9	280	6.1 ± 1.4	1.2 ± 0.5	0.04	1.2
J1100+0846	24.2	$8.3^{+2.5}_{-2.0}$	7.3	260	10.0 ± 2.0	1.4 ± 0.4	0.1	2.3

To infer whether the jet is sufficiently powerful to be a viable mechanism of negative feedback, we compare the total kinetic energy produced by the jet $E_{\rm jet}$ in its travelling time $t_{\rm jet}$ with the energy computed for the high-velocity dispersion ionized gas $E_{\rm ion}$. If we assume that the computed value of $P_{\rm jet}$ represents an average value over its travelling time, we can compute $E_{\rm jet}$ as $P_{\rm jet}t_{\rm jet}$ [Venturi et al., 2021]. To estimate the jet travelling time we use the Eq. (A1) from Mukherjee et al. [2018b] with the same parameters employed for IC5063, and we consider the jet radius as the largest linear size computed in Jarvis et al. [2021] (divided by 2). The travelling times and the kinetic energies of the jet are listed in Table 3.3. Dividing the total energy $E_{\rm ion}$ by the kinetic power of the radio jet $E_{\rm jet}$ we find values on the order of 10^{-3}–10^{-2} for J1000+1242 and J1010+1413. This indicates that the jet, with a low efficiency of energy transfer, is potentially capable to inject the required energy into the ISM and be responsible for the observed phenomenon also in radio quiet and luminous AGN. In J1010+0612 and J1100+0846, where the enhanced velocity dispersion is still high in the central region but is not observed in the direction perpendicular to the jet, the energies of the disturbed gas and the radio jets are comparable. For this reason, also for these targets, we cannot exclude that the jet contributes to injecting turbulence into the ISM.

3.5 Conclusions

In this chapter, we investigated the relation between the radio emission and the ISM of four luminous type 2 AGN (J1000+1242, J1010+1413, J1010+0612, and J1100+0846) using VLT/MUSE optical data combined with VLA and e-MERLIN radio observations. The analysis of [O III] and Hα emission-line profiles revealed ionized outflows with velocities up to ∼1000 km,s^{-1} and extensions up to 15–20 kpc. In the two sources with extended radio emission, the outflows are aligned with the radio jets and AGN

ionization cones. A key result is the detection of a strong (W70 $\sim$ 1000 km,s^{-1}) and spatially extended (up to 20 kpc) enhancement in velocity width perpendicular to the jets and ionization cones, consistent with turbulence induced by jet–ISM interactions in at least two targets of the sample. For the other two galaxies, the radio data are extended on smaller scales than we can probe with our MUSE data. The radio data therefore prevent a reliable assessment of the radio jet direction and interaction with the ISM. Other recent works (e.g., Venturi et al. 2021, Girdhar et al. 2022) observed the same phenomenon in other AGN hosting jets with a low kinetic power ($P_{\rm jet} < 10^{44}$erg s^{-1}). This was interpreted as due to the interaction between the jet and the ISM in the host galaxy disk.

Combining the results of our work and those of Venturi et al. [2021], we found a correlation between the kinetic power of the radio emission and the mass and energy of the ionized gas involved in the phenomenon, in accordance with the possible scenario of an interaction between the radio jet and the ISM. We found that the jets are powerful enough to inject the kinetic energy observed in the line width enhancement region into the ISM. This mechanism might represent an important channel of AGN feedback that needs to be taken into account. Moreover, the targets in which we detected this phenomenon have a higher bolometric luminosity and higher radio power emission than most objects in which this phenomenon was observed (but still lower than the powerful jets in radio-loud sources). This suggests that jets with low power might play a significant role in AGN feedback even in radiatively powerful sources (also see Girdhar et al. 2022). Through spatially resolved S-N BPT diagrams, we found that the main contribution to the ionization arises from the AGN photons, with an enhancement of [NII]/Hα in the region with a high velocity dispersion perpendicular to the ionization cones. This may be ascribed to shocks due to the interaction between the jet and the ISM [Mingozzi et al., 2024].
However, to shed light on the effect of the radio jets on the host galaxy and further investigate the incidence and properties of the observed enhanced line widths perpendicular to the radio jets, a larger sample with high-quality integral field spectroscopic data is needed in the optical and IR bands to assess to which extent the phenomenon affects the molecular phase in addition to the ionized phase.

Chapter 4

The nuclear environment of ULIRGs

ULIRGs represent a key evolutionary phase in the merger-driven transformation of galaxies, characterized by intense star formation, heavy dust obscuration, and often powerful AGN activity.

As we showed in Chapter 1, ULIRGs are commonly interpreted as a key stage in the evolutionary pathway linking starburst galaxies to quasars [Sanders et al., 1988, Hopkins et al., 2008]. In this picture, major mergers between gas-rich systems drive large-scale inflows of gas, giving rise to intense star formation and rapid growth of the central SMBH, ultimately triggering AGN activity. As the interaction advances, energetic outflows powered by both stellar processes and the AGN emerge, altering the surrounding interstellar medium and potentially regulating ongoing star formation and black hole accretion through feedback [Di Matteo et al., 2005, Silk, 2013].

Galactic outflows are expected to be more important at high redshift ($z \sim 1-2$) during the peak of the cosmic SF and SMBHs accretion [Madau and Dickinson, 2014], and hence where the feedback mechanisms may be maximized [Brusa et al., 2015b, Talia et al., 2017, Perrotta et al., 2019, Kakkad et al., 2020, Cresci et al., 2023b]. Remarkably, recent observations have revealed some similarities between local ULIRGs and distant starbursts at redshift $z \sim 2$ [Arribas et al., 2012, Hung et al., 2014, Bellocchi et al., 2022, McKinney et al., 2023] and they highlight the importance of understanding the outflow phenomena occurring in local ULIRGs. In fact, the proximity of these sources allows for more detailed observations that are characterized by angular resolution and signal-to-noise ratios higher than those focusing on more distant galaxies.

Several studies have demonstrated the presence of multiphase (ionized, neutral, and molecular) gas outflows in ULIRGs [Sturm et al., 2011, Bellocchi et al., 2013, Veilleux et al., 2013a, Arribas et al., 2014, Feruglio et al., 2015, Cazzoli et al., 2016, Fluetsch et al., 2021, Perna et al., 2021, Lai et al., 2022, Bohn et al., 2024], however, it is still unclear what the effects of these outflows are on the host galaxies.

Investigating nuclear regions of ULIRGs with spatially resolved spectroscopy is therefore crucial to disentangle the interplay between star formation, AGN feedback, and the surrounding interstellar medium, understanding which phenomena occur during this active phase and which the effect on the galaxy are. In particular, as presented in Chapter 2, JWST/NIRSpec provides an unprecedented opportunity to probe these obscured environments, as its near-infrared capabilities allow us to penetrate the dense dust that limits optical observations.

In this chapter, we present a detailed analysis of two archetypal ULIRGs, Arp 220 and Mrk 231, with separate sections dedicated to each object. The primary goal of

this chapter is to investigate their nuclear regions in order to characterize the physical processes governing galaxy evolution, with particular emphasis on galactic multiphase outflows and merger activity.

4.1 Arp220

Arp 220, the nearest and most representative example of an ULIRG. Previous works have revealed that ULIRGs commonly host multiphase outflows, including ionized, neutral, and molecular gas components, spanning a wide range of physical conditions [Sturm et al., 2011, Bellocchi et al., 2013, Veilleux et al., 2013a, Arribas et al., 2014, Feruglio et al., 2015, Cazzoli et al., 2016, Fluetsch et al., 2021, Perna et al., 2021, Lai et al., 2022, Bohn et al., 2024]. In particular, multiwavelength observations of Arp 220 have already provided clear signatures of such complex, multiphase winds and their interplay with the host galaxy [Arribas et al., 2001, McDowell et al., 2003, Colina et al., 2004, Perna et al., 2020, Wheeler et al., 2020, Lamperti et al., 2022, Ueda et al., 2022].

Arp 220 is located at a distance of $\sim$ 78 Mpc, and has an IR luminosity of log $(L_{IR}/L_{\odot}) = 12.2$ [Pereira-Santaella et al., 2021], and a stellar mass of log $(M_*/\ M_{\odot}) \sim$ 10.8 [U et al., 2012]. It is a late-stage merger containing two compact ($<$ 150 pc), highly obscured nuclei (east and west) separated by $\sim$ 370 pc (1") that dominate the IR luminosity (e.g., Scoville et al. 2007, see Fig. 4.1). The two nuclei are sites of intense SF, with SFR $\sim 200 - 250$ $M_{\odot}$ yr^{-1}[Nardini et al., 2010, Varenius et al., 2016] and extremely high SFR surface densities $\Sigma_{SFR} \sim 10^3 - 10^4$ $M_{\odot}$ $yr^{-1}kpc^2$, from radio and far-IR (FIR) observations [Barcos-Muñoz et al., 2015, Pereira-Santaella et al., 2021]. There is still no convincing direct evidence for the presence of AGN activity in either of the two nuclei [Iwasawa et al., 2001],[Perna et al., 2024].

This section presents a kinematic examination of the nuclear region of Arp 220 observed with the Integral Field Spectrograph (IFS) unit of the NIRSpec instrument on board the JWST [Jakobsen et al., 2022, Böker et al., 2022] collected as part of the JWST/NIRSpec IFS Guaranteed Time Observations (GTO) survey: Resolved structure and kinematics of the nuclear regions of nearby galaxies (program lead: Torsten Böker). Our goal is to investigate the spatially resolved gaseous and stellar kinematics in the innermost 1 kpc of Arp 220, and better understand the feedback processes affecting this ULIRG system.

4.1.1 Observation and data reduction

Arp 220 was observed using the JWST/NIRSpec instrument in IFS mode [Böker et al., 2022], as part of the JWST observing program 1267 (PI: D. Dicken), on March 6, 2023. These NIRSpec observations were combined in a single proposal with independent MIRI GTO observations of the same target.

The dataset comprises two distinct pointings, each employing the first four positions of the medium cycling dithering pattern with 15 groups per integration and one integration per exposure, using the NRSIRS2RAPID readout pattern. The first set is centered at the midpoint between the coordinates of the western (W) and eastern (E) nuclei, while the second set is offset by approximately 1" toward the northwest to encompass the Hα and [N II] emission shell [Lockhart et al., 2015, Perna et al., 2020]. Each set has a total integration time of 933 seconds and utilises three high-resolution

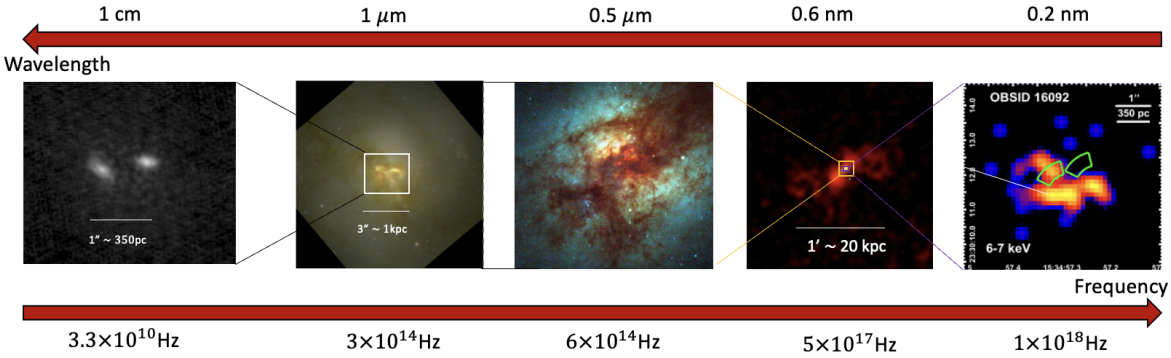

Figure 4.1: Arp 220 multi-band observations from radio to X-ray. The radio band is from VLA at 33 GHz, 1μm is from NIRCam downloaded form MAST portal, the optical image is from Wilson et al. [2006], soft X-ray at 0.2-1.0 keV is from McDowell et al. [2003], while X-ray at 6-7 keV is from Paggi et al. [2017].

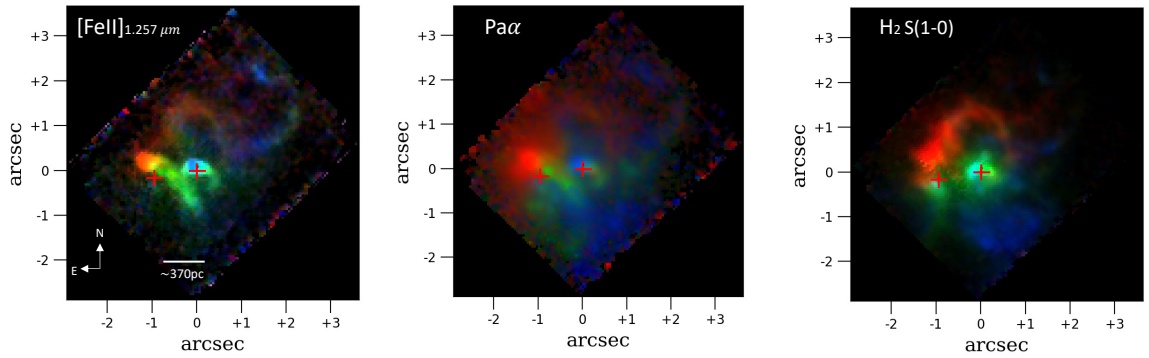

Figure 4.2: Three-color emission line images of Arp 220. The emission line maps are obtained integrating the continuum-subtracted data-cube around [Fe II] 1.257 μm (left), Paα (center), and H_2 1–0 S(1) 2.122 μm (right) in the velocity ranges -400 km s$^{-1}<$ v < -200 km s^{-1}(blue), -200 km s$^{-1}<$ v < 200 km s^{-1}(green) and 200 km s$^{-1}<$ v $<$ 400 km s^{-1}(red), with respect to the median value between z_E^* and z_W^*, $z_m = 0.0181$. The red crosses mark the position of the two nuclei.

(R $\sim$ 2700) configurations: G140H/F100LP, G235H/F170LP, and G395H/F290LP, covering wavelength ranges of 0.97 – 1.82 μm, 1.66 – 3.05 μm, and 2.87 – 5.14 μm, respectively. However, we focus solely on the first two configurations, as our objective is to study the kinematics of the emitting gas, with its strongest transitions occurring at wavelengths below 2.4 μm.

The data reduction of Arp 220 observations is described in detail in Perna et al. [2024]. Here we summarize the relevant information. We used the JWST pipeline v1.8.2 with CRDS context 1063. A patch was included to correct some important bugs that affect this specific version of the pipeline; $1/f$ noise and outliers were corrected following the approaches described in Perna et al. [2023] and D'Eugenio et al. [2023], respectively. The combination of the exposure for the eight dither positions was done with a drizzle weighting method that allowed us to sub-sample the detector pixels [Law et al., 2023], resulting in cube spaxels with a size of 0.05" (corresponding to $\sim$ 20 pc/spaxel) and covering a field of view (FoV) of 5"$\times$ 4". The absolute astrometric registration was performed using ALMA high-resolution maps of millimeter continuum emission, as described in Perna et al. [2024]. The final data cubes showed strong

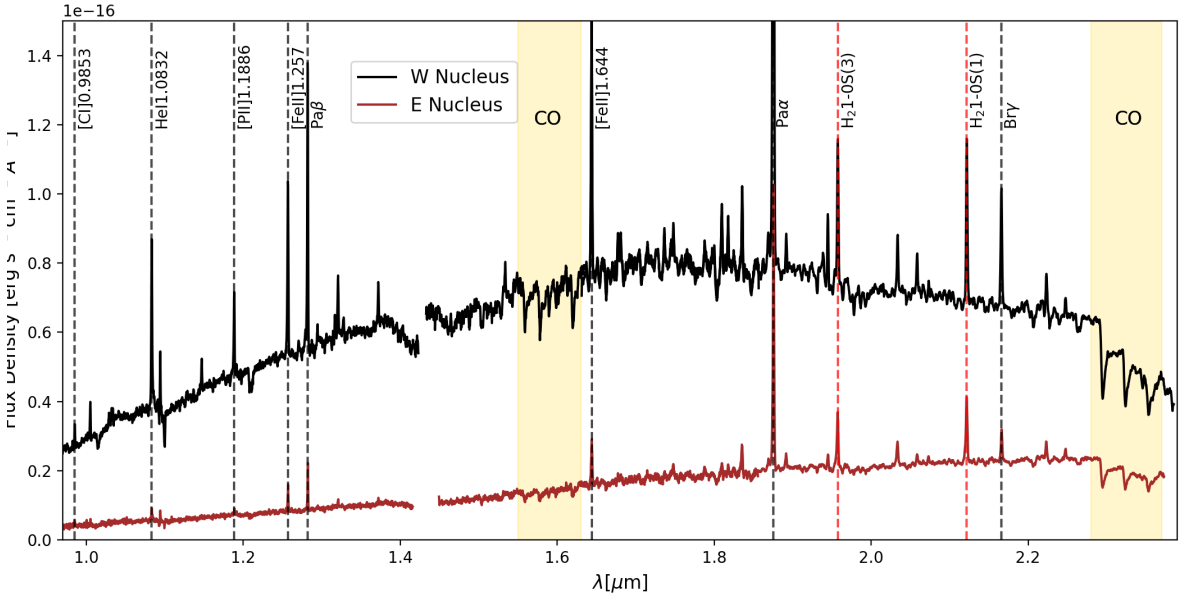

Figure 4.3: Arp 220 W and E nuclear spectra. The spectra were extracted from a circular aperture of radius 3 spaxels (corresponding to 0.15") and are reported in units of flux density as a function of rest-frame wavelength. Red dashed vertical lines identify H_2 lines; black dashed lines identify ionized gas transitions. Gold-filled areas mark the position of the main CO stellar absorption lines.

"wiggles", sinusoidal modulations caused by the undersampling of the point spread function (PSF). We corrected these artifacts by applying the methodology described in Perna et al. [2023].

Figure 4.2 shows the three synthetic narrow-band images generated from the reduced data cube of Arp 220 obtained for the brightest emission lines in the wavelength range covered by NIRSpec. The positions of the W and E nuclei are marked for visual purposes. This figure illustrates the quality of NIRSpec data and provides a preview of the intricate gas kinematics within the innermost regions of Arp 220.

We show in Fig. 4.3 the integrated spectra of the E and W nuclei up to 2.4 μm, extracted from a circular aperture of radius 3 spaxels (corresponding to 0.15") centered at the positions defined in Perna et al. [2024], reported in Table 4.2. The spectra are shown in the rest-frame, according to the systemic redshift of each nucleus: z=0.01840 for the E and z=0.01774 for the W [Perna et al., 2024, see also Sect. 4.1.2]. The spectra show many hydrogen recombination lines, including Paschen (Pa) and Brackett (Br) transitions, but also many forbidden iron lines ([FeII]), and roto-vibrational transitions of molecular hydrogen (H_2). This allowed us to study the physical and kinematic properties of the gas in different phases. The CO absorption bandheads in the spectral ranges 1.5–1.7 μm and 2.2–2.4 μm are prominent, and can be used to measure the stellar kinematics.

4.1.2 Spectral fitting analysis: Stellar and gas components

In this section we describe the spectroscopic analysis carried out to study the kinematics and morphology of the nuclear region of Arp 220.

The analysis is divided into three steps: the first is the modeling and the subtraction of the stellar continuum, the second is a preliminary fit of the emission lines to build a model that can be used to study the integrated properties of each emission line. The third step is the disentangling of the different kinematic components associated with the most prominent emission lines.

Modeling of the stellar continuum

To fit the stellar continuum, we used the penalized pixel-fitting routine (pPXF) [Cappellari and Emsellem, 2004, Cappellari, 2017] to convolve stellar spectra templates with a Gaussian velocity distribution. We did not attempt to extract the Gauss–Hermite terms h3 and h4, since the quality of our data is not sufficient to obtain this information from the fit (see also e.g., Cappellari et al. 2009, Engel et al. 2011b, Crespo Gómez et al. 2021). We binned spaxels together using the Voronoi binning scheme of Cappellari and Copin [2003], to achieve a minimum S/N. We established a target minimum S/N = 30 per wavelength channel for each bin (following e.g., Belfiore et al. 2019). We used the MARCS stellar population synthesis templates [Gustafsson et al., 2008] to model the stellar continuum; these templates cover the wavelength range 0.96 – 20 μm with a constant spectral resolution $\Delta\lambda/\lambda = 20000$. We also adopted a third-order multiplicative and additive polynomials to better reproduce the spectral continuum shape. To improve the quality of the fit, we included in the total model the most prominent emission lines (see Table 4.1) parameterized with two Gaussian components.

We conducted separate fits for the cubes G140H and G235H, with the latter restricted to wavelengths below 2.4 μm, to avoid spaxels affected by the NIRSpec detector gap. Wavelengths falling within the gap in G140H were appropriately masked during the fit procedure. Fig. 4.4 shows the fit with pPXF of the spectra extracted from the W and E nuclei, highlighting the most important features in absorption (black dashed lines) to constrain stellar kinematics. We note that the pPXF best fits does not perfectly reproduce the observed spectra. However, this does not affect our goal: we do not require a realistic model of the stellar populations in Arp 220, we only need an accurate stellar continuum model and a measurement of the stellar kinematics.

After constructing the total model, we subtracted the model of the continuum from the cube spaxel by spaxel, rescaling the modeled continuum emission obtained in each Voronoi bin to the median flux of the observed continuum in each spaxel. In this way, we obtained a cube containing only the contribution of the emission lines.

Multi-Gaussian emission line fit

After the subtraction of the continuum, we smoothed each wavelength map of the cube (i.e., image generated with a spectral pixel wide synthetic filter) with a Gaussian having a dispersion of 1 spaxel (i.e., 0.05"), to enhance the S/N. We then performed separate spectral fits for the atomic and molecular gas line groups listed in Table 4.1 since each gas phase may be dominated by different kinematic components, as illustrated in Fig. 4.2 (see also e.g., May and Steiner 2017, Perna et al. 2024). All lines within each group were simultaneously fitted using one, two, or three Gaussian components. We tied the velocity v and the velocity dispersion σ of each Gaussian component among all lines of the group, while the fluxes are left free to vary. Then, we chose the number of Gaussian components for each spaxel by performing a Kolmogorov-Smirnov (KS) test on the distribution of the residuals with N and $N + 1$ components to define the

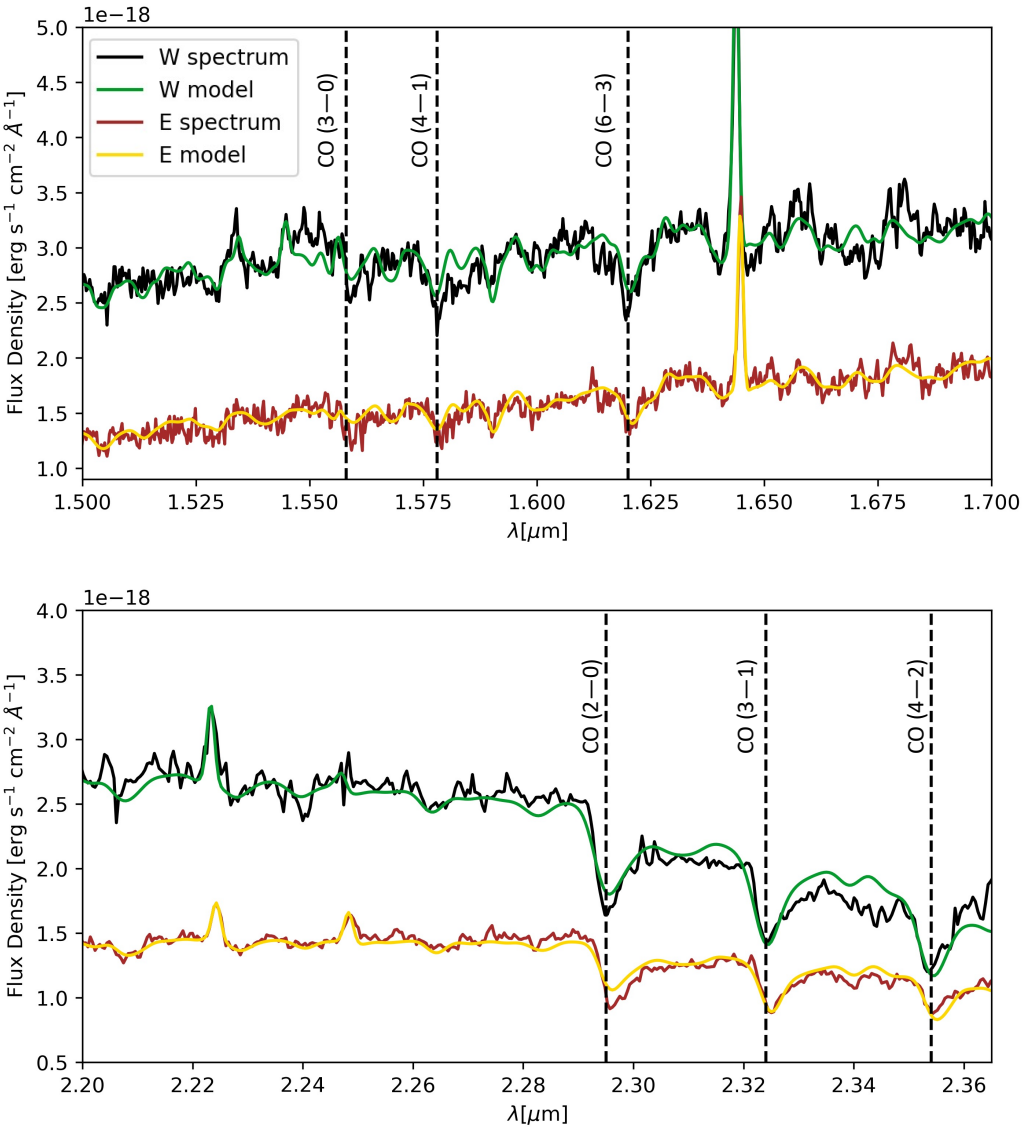

Figure 4.4: Arp 220 W and E nuclear spectra with pPXF best-fit models. The CO absorption features are in the 1.5–1.7 μm band (upper panel) and 2.2–2.36 μm (bottom panel). Black and green curves respectively refer to the data and the model of the W nucleus spectrum. Brown and gold curves respectively refer to the data and the model of the E nucleus spectrum. Black dashed vertical lines indicate the position of the main CO absorption lines.

minimum number of components required to provide an acceptable fit in each spaxel [Marasco et al., 2020]. Consequently, the number of Gaussian components is not based on a physical model but it is constrained on just a statistical analysis; a detailed, physical decomposition is presented in Sect. 4.1.3.

Figure 4.5 shows the three moment maps calculated on the whole modeled line profile (consisting of either one, two, or three Gaussians) of the brightest emission lines: H_2 $1-0$ $S(1)$ 2.122 μm, Paα, and [Fe II] 1.257. For each transition, we masked spaxels with S/N<3. These maps allowed us to identify the different kinematic and

Table 4.1: Fit emission lines. Vacuum wavelengths are taken from Perna et al. [2024].

Atomic Gas	λ_{vac} (μm)	Hot Molecular Gas	λ_{vac} (μm)
[CI]	0.9824	$H_2 1-0\ S(7)$	1.7481
	0.9853	$H_2 1-0\ S(6)$	1.7880
Paγ	1.0941	$H_2 1-0\ S(5)$	1.8359
Paβ	1.2821	$H_2 1-0\ S(4)$	1.8920
Paα	1.8756	$H_2 1-0\ S(3)$	1.9577
Brγ	2.1661	$H_2 1-0\ S(2)$	2.0339
HeI	1.0832	$H_2 1-0\ S(1)$	2.1220
	1.8690	$H_2 1-0\ S(7)$	2.2235
	1.8702		
[PII]	1.1471		
	1.1886		
[FeII]	1.2570		
	1.3725		
	1.3209		
	1.2787		
	1.6440		
[OI]	1.3168		

morphological components of the system, traced by ionized and molecular gas, and described in Sect. 4.1.3.

Systemic velocity

Following Perna et al. [2024], we determined the redshift of the two nuclei from the centroid of the atomic hydrogen lines in the nuclear spectra. The systemic velocities correspond to $z_E^{gas} = 0.01840 \pm 0.00001$ and $z_W^{gas} = 0.01774 \pm 0.00001$. We also computed the redshift from the stellar continuum model, finding $z_E^* = 0.0183 \pm 0.0002$ and $z_W^* = 0.0179 \pm 0.0003$, slightly different from the redshift found for the gas, but still consistent within the errors (see Table 4.2).

Table 4.2: Coordinates and systemic redshift of the two nuclei of Arp 220 from Perna et al. [2024].

	W nucleus	E nucleus
RA (J2000)	15:34:57.224	15:34:57.294
DEC (J2000)	+23:30:11.515	+23:30:11.353
redshift (gas)	0.01774 ± 0.00001	0.01840 ± 0.00001
redshift (stars)	0.0179 ± 0.0003	0.0183 ± 0.0002

In this work, the large-scale (> 100 pc) stellar and gas kinematics maps are derived by using as a reference the redshift reported in Perna et al. [2020], which corresponds to the median value between z_E^* and z_W^*, $z_m = 0.0181$ (e.g., Fig. 4.5). This redshift allows us to obtain a symmetric stellar velocity gradient, associated with the kiloparsec-scale disk also identified with optical and cold molecular line tracers [Perna et al., 2020] and references therein). In contrast, the small-scale motions of the ionized and hot

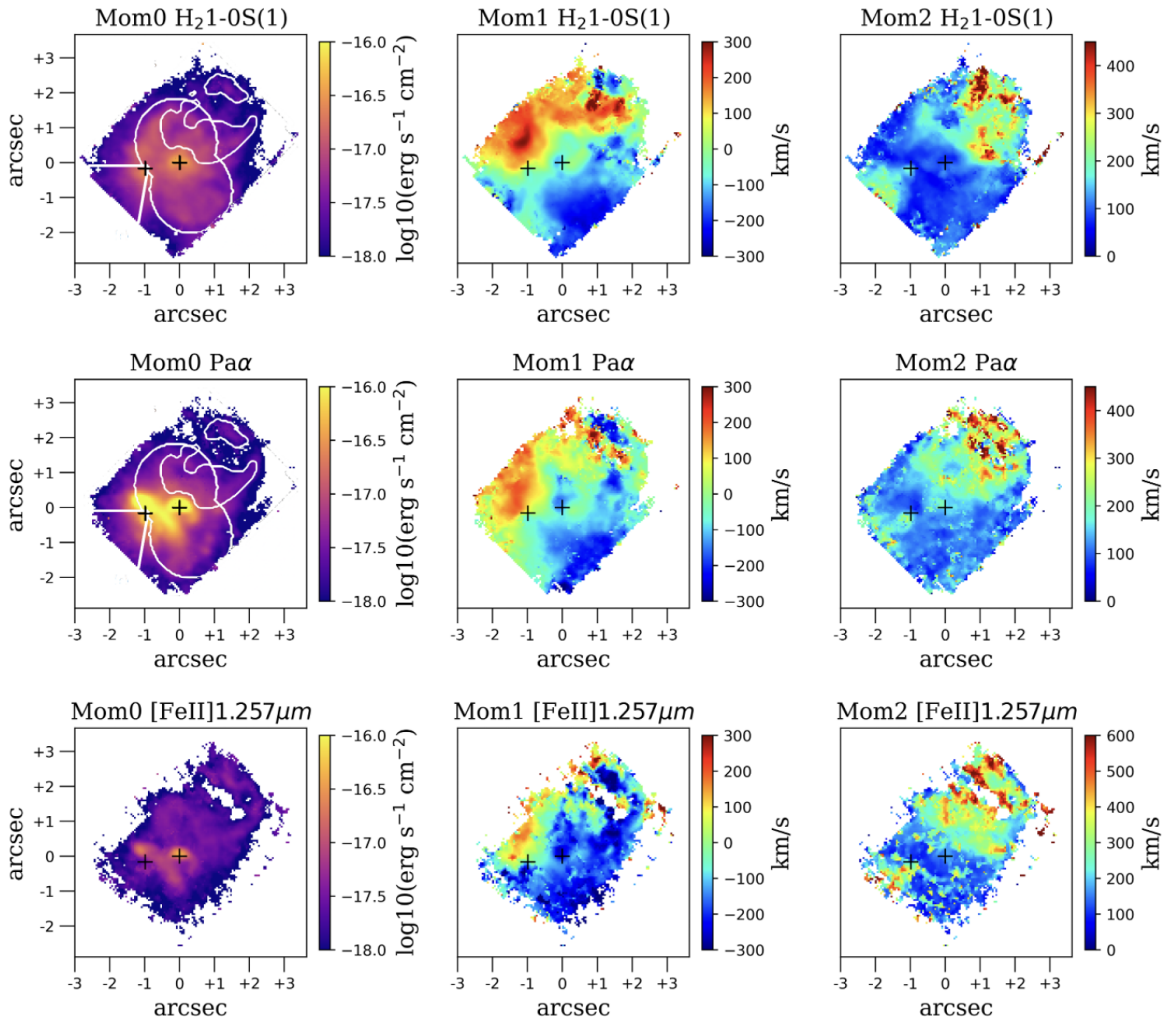

Figure 4.5: Moment maps of hot molecular gas (H_2 1-0S(1), top) and ionized gas (center: Paα, bottom: [Fe II] 1.257μm). The moment-1 was computed with respect to $z_m = 0.0181$. An S/N cut of three on the flux of each emission line was applied to the maps. The black "+" symbols mark the position of the E and W nuclei. White contours represent the edges of the masks described in Sec. 4.1.3.

molecular gas around the E or W nucleus are measured relative to the zero velocity inferred from z_E^{gas} and z_W^{gas}, respectively.

4.1.3 Spectral fitting analysis: Separating rotations and outflows components

The morphology and kinematics of the nuclear region of Arp 220 are quite complex. Figs. 4.2 and 4.5 reveal a superposition of circum-nuclear and large-scale disks as well as multiple outflows that have already been observed in optical and submillimeter tracers [Scoville et al., 2017, Perna et al., 2020, Lamperti et al., 2022, Ueda et al., 2022]. Emission lines often display multipeak and asymmetric spectral profiles, requiring the use of multiple Gaussian components for modeling. Conventional methods usually employed to separate a disk from an outflow structure across the entire galaxy (e.g., based on velocity or velocity dispersion criteria; Tozzi et al. 2021, Venturi et al.

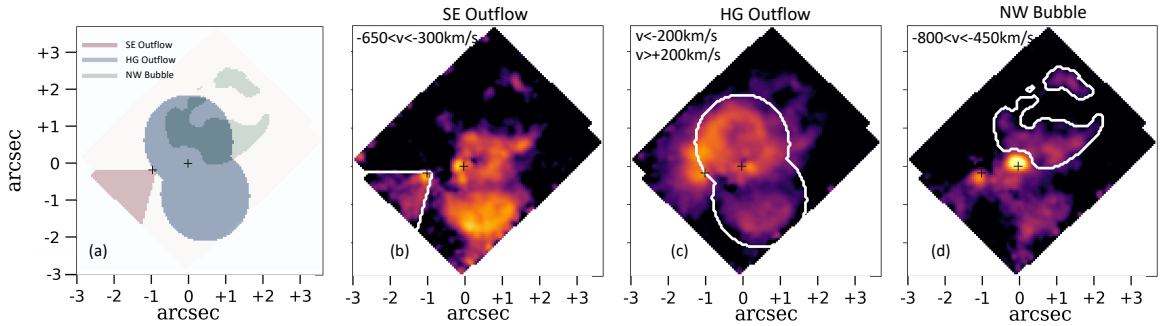

Figure 4.6: Arp 220 outflow regions. (a): Composite view of the isolated outflow regions: southeast outflow (red), hour-glass outflow (blue), northwest outflow (green). (b): Channel map between -650 and -300 km s^{-1}in the H_2 transition with respect to the systemic redshift of the E nucleus. The white curve indicates the edges of the SEO mask. (c): Sum of channel maps < -200 and > 200 km s^{-1}in the H_2 transition with respect to the systemic redshift of the W nucleus. The white curve indicates the edges of the HG region. (d): Sum of H_2 and Paα channel maps between -800 and -450 km s^{-1}with respect to the systemic redshift of the E nucleus. The white curve indicates the edges of the NWB region.

2021), may not be straightforward for Arp 220. Hence, in this work we opted for an alternative approach, focusing on individual regions where the separation of distinct kinematic components is facilitated by dedicated criteria and by the high spatial resolution of NIRSpec data. In particular, we first selected and modeled the most easily distinguishable outflow components, subtracted them, and then gradually move on to the more complex ones.

Our method consists of three steps. The first is the identification of a region with specific morphology and/or kinematics, and hence the construction of a spatial mask to isolate it. We then fitted all spaxels within the selected region with N Gaussians, where N represents the number of the kinematically distinct components we wanted to characterize. As the fit of a complex line profile is subject to degeneracy, the value N is quite critical and depends on the detectability of the morphological and kinematic features we aim to describe. We considered in our model the most intense transitions of the atomic (Paα) and molecular gas (H_2 $1-0$ $S(1)$ 2.122 μm, hereafter H_2 unless otherwise specified) in the G235H cube. We also included in the fit the HeI 1.869 μm and He 1.870 μm lines since they can contaminate the profile of Paα (see, e.g., Fig. B.3 in Perna et al. 2024). We fitted together the transitions of atomic and molecular gas assuming for each line the same v and σ and varying the fluxes. As we show in the next sections, this is a reasonable assumption for this system. In the second step, we defined a criterion to isolate an outflow among the components identified in the mask. Then, we constructed a model cube containing only the isolated component, used for further analysis presented in the following sections.

This three-step process is iterative, implying that each time we aimed to characterize a specific feature, we initially created a mask and then fitted a new model on the residual cube built by subtracting all previously detected and isolated components. The criteria used to define all masks and outflow components are introduced in the next sections

Fig. 4.6a illustrates the masks for all the identified outflow regions. They encompass a conical outflow launched by the E nucleus (i.e., the southeast outflow, SEO

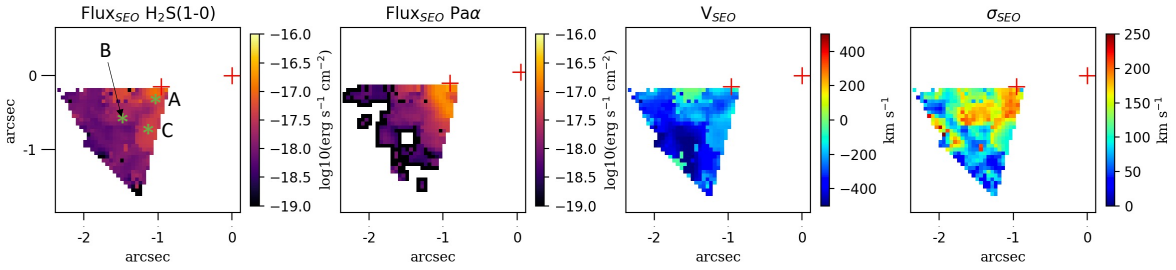

Figure 4.7: SE conical outflow flux and velocity maps. From left to right: flux of H_2 and Paα lines, velocity, and velocity of the Gaussian component attributed to the SE outflow. The velocities are relative to the systemic velocity of the E nucleus. Red crosses indicate the positions of the two nuclei. Green asterisks in the first panel indicate the spaxels presented in Fig. 4.8.

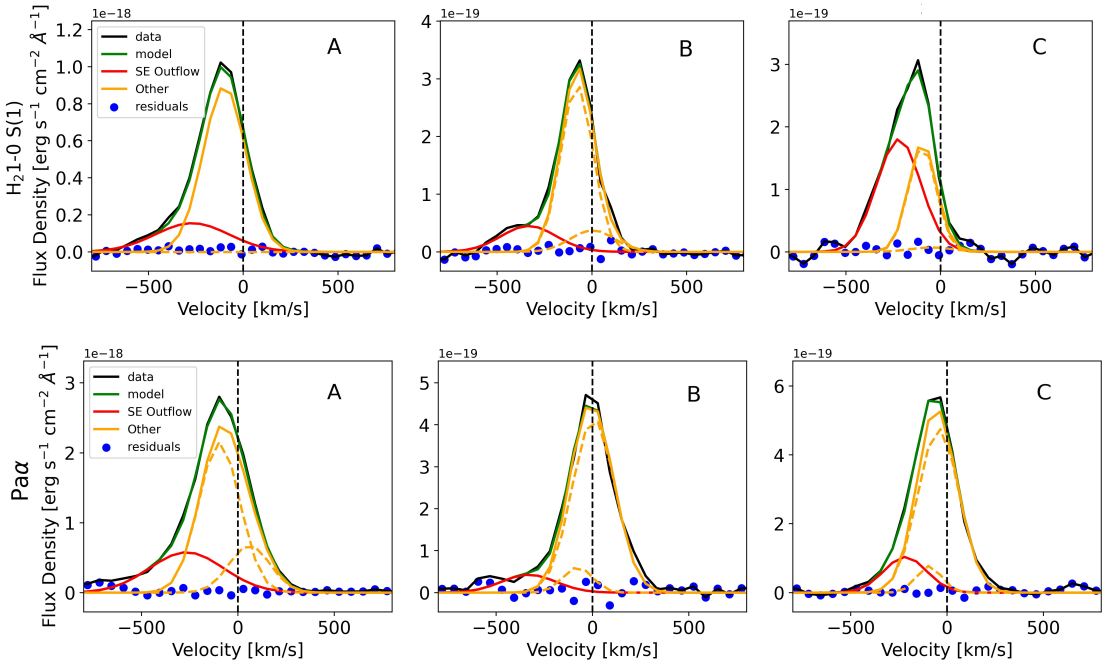

Figure 4.8: Spectra extracted from the SE outflow cone. The solid black curves represent the line profiles of H_2 (top) and Paα (bottom) extracted from the spaxel close to the E nucleus (A), in the central part of the cone (B), and at the edge of the collimated outflow (C), as labeled in Fig. 4.7. The multi-Gaussian fits are depicted by dashed orange curves for the disk components and solid red curves for the outflow component. The total model for the disk is shown as a solid orange curve, and the combined model for both disk and outflow is displayed in green. The blue dots indicate the residuals. The velocities are computed with respect to the systemic velocity of the E nucleus.

hereinafter), an hourglass-shaped outflow originating from the W nucleus (HGO), and a northwestern bubble (NWB). There is another feature of particular interest that affects just a few spaxels and is therefore not reported in the figure: a compact outflow observed in the W nucleus mainly in the ionized phase (WNO). In the next subsections, we provide detailed analyses of each identified region.

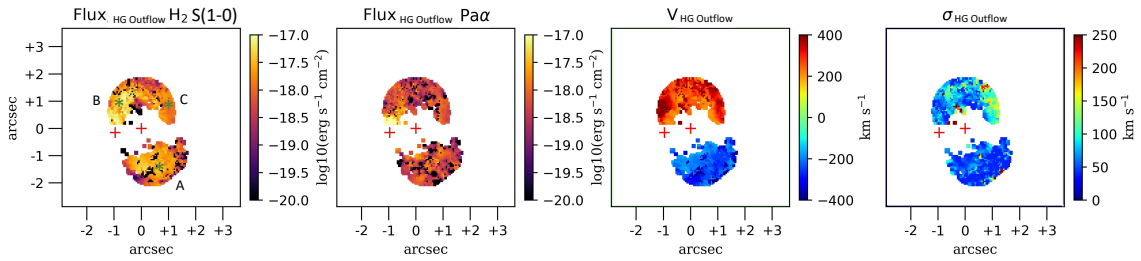

Figure 4.9: HG outflow flux and velocity maps. From left to right: flux of H_2 and Paα lines, velocity, and velocity dispersion of the Gaussian component attributed to the HG outflow. The velocities are relative to the systemic velocity of the W nucleus. Red crosses indicate the positions of the two nuclei. Green asterisks in the first panel indicate the spaxels presented in Fig. 4.10.

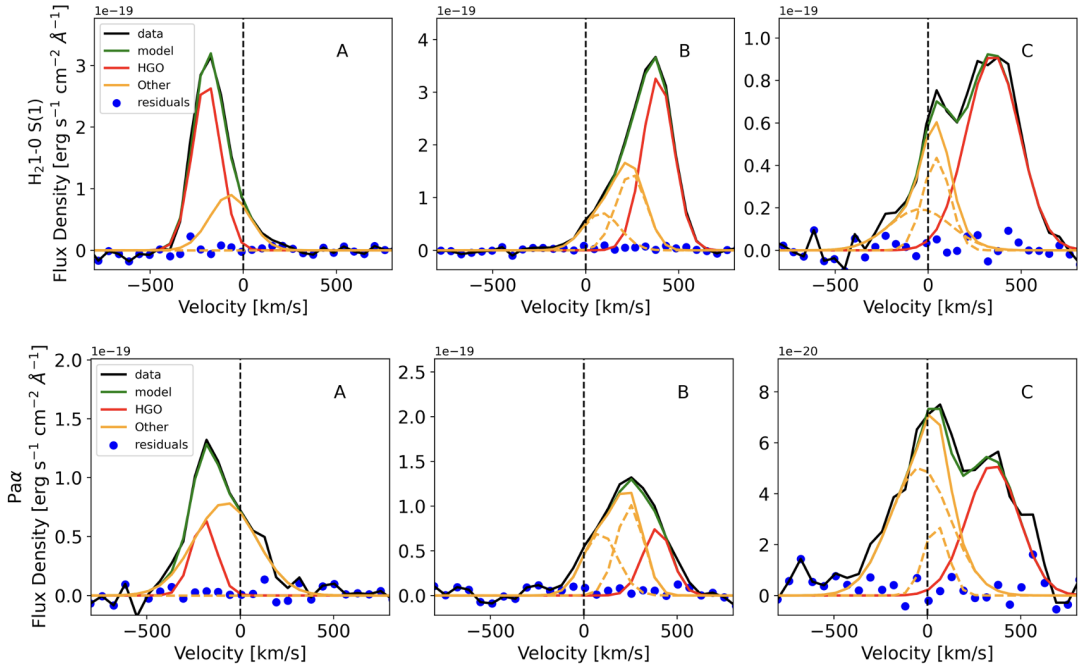

Figure 4.10: Spectra extracted from the HG outflow region. The solid black curves represent the line profiles of H_2 (top) and Paα (bottom) extracted from the spaxels marked in Fig. 4.9. The red curve refers to the HG outflow. Orange dashed curves identify the additional components used for the fit. The combined model is displayed in green, while residuals are blue dots. The velocities are computed with respect to the systemic velocity of the W nucleus.

Southeast conical outflow from E nucleus

Figure 4.6b shows H_2 emission in the velocity range $[-650, -300]$ km s^{-1}with respect to the systemic velocity of the E nucleus. In this figure, a high-velocity conical region situated southeast of the E nucleus is clearly visible (demarcated by white lines). This region has also elevated velocity dispersion (> 150 km s^{-1}), as shown in the moment-2 maps of both ionized and hot molecular gas in Fig. 4.5, hence indicating the presence of an outflowing component.

We selected the region with enhanced flux in the $[-650, -300]$ km s^{-1}map (red area in Fig. 4.6a) and, within this region, fitted both the ionized gas and the molecular gas with three Gaussian components to model: 1) the high-velocity gas, 2) the rotating disk at a large scale that covers the entire FoV, and 3) the emission from the small circum-nuclear disk around the E nucleus. Among these three Gaussian components, we assigned the most blueshifted to the outflow. The flux, the velocity and the velocity dispersion of the SEO in H_2 and Paα are reported in Fig. 4.7. Since we associated only one Gaussian component to the outflow, the velocity and the velocity dispersion is the same for both ionized and hot molecular gas. The velocity varies between -100 km s^{-1}, observed close to the nucleus and at the edges of the cone, and -400 km s^{-1}at larger distances (~ 400 pc). High velocity dispersions (up to 200 km s^{-1}) are observed in the center of the conical outflow and close to the nucleus, while at the edges of the cone σ is about two times lower.

Figure 4.8 shows the spectra of the hot molecular (top) and ionized gas (bottom) extracted from three spaxels within the conical outflow; specifically near the E nucleus, at the center, and at the edge of the cone. In all spaxels, we observe a prominent wing extending toward negative velocities; this wing is reproduced by a Gaussian component with $v < -250$ km s^{-1}, which we associated with the SEO (red curves in the figure). We also note that the SEO emission is more prominent and contributes more to the total line profile in the hot molecular phase than in the ionized one, especially in the off-nuclear regions. Figure 4.8 also shows that our multi-Gaussian approach is capable of simultaneously reproducing the profiles of ionized and hot molecular gas, hence supporting the validity of our assumption about the presence of a mixed, multiphase ISM in each kinematic component.

As explained in this section, our approach consists of an iterative process: the best-fit model component attributed to the SEO is subtracted spaxel by spaxel from the original data cube before performing new fits to characterize the remaining kinematic structures observed in the NIRSpec data. This method helps in reducing the fit degeneracy.

Hourglass outflow from the W nucleus

As shown in Fig. 4.2, both the ionized and molecular gas exhibit a shell-shaped morphology at high redshifted ($v > 200$ km s^{-1}) velocities in the region north of the W nucleus. Additionally, the hot molecular gas shows a blueshifted shell-like structure in the region southwest of the same nucleus. The blue- and redshifted gas forms an 'hourglass' (HG)-like shape, compatible with an outflow launched from the W nucleus. This structure is even clearer in Fig. 4.6c, showing the sum of H_2 spectral channel maps at $v < -200$ km s^{-1}and $v > 200$ km s^{-1}(with respect to the systemic velocity of the W nucleus), used to define our mask (white contours in the figure).

Within the HG region, we fitted simultaneously the hot molecular and the ionized gas using three Gaussian components, taking into account the large- and small-scale gas rotations as well as the outflow. To assign a Gaussian component to the HG outflow (HGO), we discarded the components with absolute velocities < 180 km s^{-1}. Among the remaining ones, we attributed to the outflow the component with highest absolute velocity. The threshold (180 km s^{-1}) represents a compromise: with a smaller velocity threshold, we would have included in the outflow also part of the rotational disk at larger scales; with a higher value, we would have missed part of the contribution of the outflow.

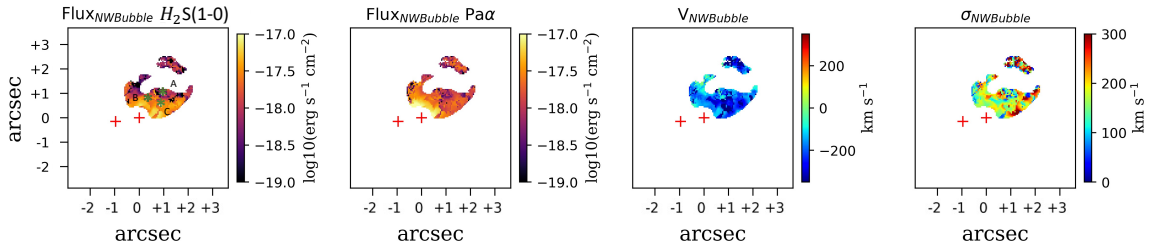

Figure 4.11: NW bubble flux and velocity maps. From left to right: flux of H_2 and Paα lines, velocity, and velocity dispersion of the Gaussian component attributed to the outflow. The velocity is referred to the E nucleus. Red crosses indicate the positions of the two nuclei. Green asterisks in the first panel indicate the spaxels presented in Fig. 4.12.

Figure 4.9 shows the flux, velocity and velocity dispersion of the gas component attributed to the outflow. The flux is dominated by the hot molecular gas over the ionized one. The velocity field is rather symmetrical with respect to the W nucleus and varies between -300 and 400 km s^{-1}. The highest observed velocity is located to the east in the redshifted shell, corresponding to an increase in molecular gas emission line flux. It is unclear whether this high-velocity gas is still part of the HGO, or whether it may represent a redshifted counterpart of the conical SE outflow associated with the E nucleus (Sect. 4.1.3).

Figure 4.10 shows the spectra extracted from three spaxels within the HG region (A, B, C in Fig. 4.9), to illustrate our fitting procedure and the separation of the kinematic components. The red curve refers to the component attributed to the outflow, while the orange curves refer to the other components used for the fit. We note that the line profiles in this region are very broad and multiple components are needed to model them. Nevertheless, despite differences in the line profiles of the hot molecular and ionized gas at specific positions, the multi-Gaussian fits successfully reproduce these profiles, confirming the reliability of our fit decomposition.

Northwest bubble

We identified a large scale bubble in the north west of the NIRSpec FoV, mostly visible in the [Fe II]transitions (Fig. 4.2). Figure 4.6d displays the sum of spectral channel maps at $v < -450$ km s^{-1}(with respect to the systemic velocity of E nucleus) of Paα and H_2. We created the mask for the NW bubble (NWB) by selecting those spaxels with enhanced flux in these velocity channels, excluding the region around the W nucleus (white curve in the figure). This nuclear region was already included in Sect.4.1.3, but since its outflow kinematics are slightly different from those of the HG outflow, this region is discussed in Sect. 4.1.3.

The emission that contributes to the line profiles in this mask comes from the bubble and the large-scale rotating disk. Consequently, we fitted the emission lines with two Gaussian components. No specific boundaries on velocity and velocity dispersion were used during the fit. We assigned the most blueshifted component to the outflow. This Gaussian component also exhibits a higher velocity dispersion with respect to the one associated with the disk.

Figure 4.11 shows the flux, velocity and velocity dispersion of the gas component attributed to the outflow. In this region, the fluxes of Paα and H_2 are very similar,

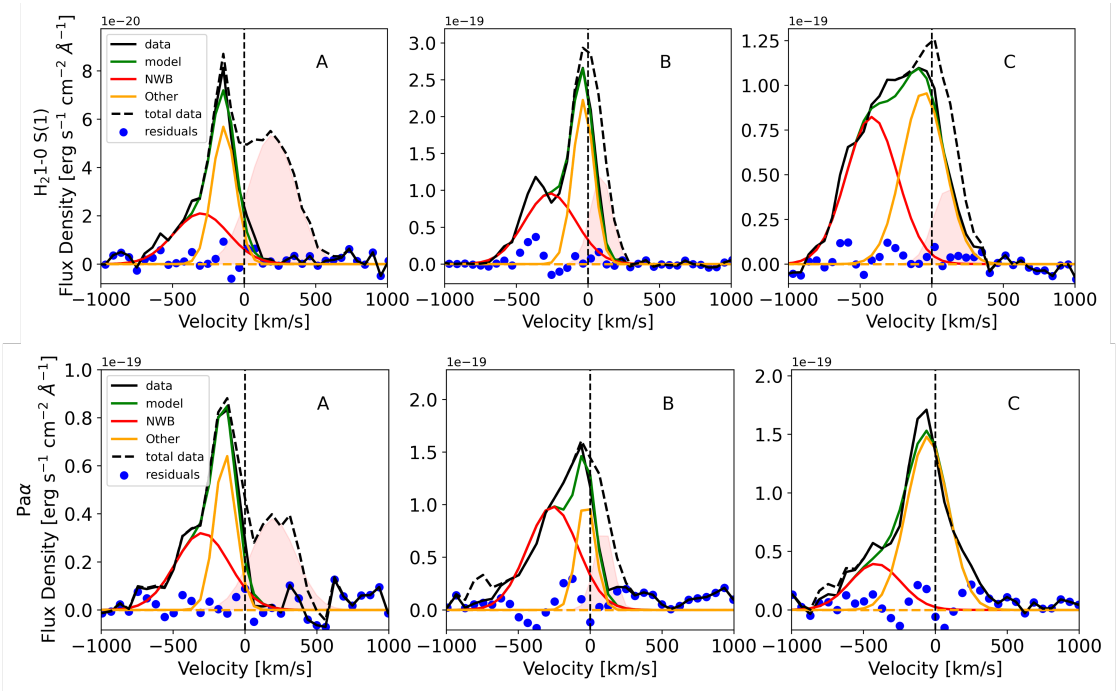

Figure 4.12: Spectra extracted from the NW bubble region. Line profiles of H_2 (top) and Paα (bottom) are shown at the position of the three spaxels labeled in Fig. 4.11. The black dashed curves represent the spectra from the original cube, highlighting the contribution attributed to the HGO (red-shaded area) that we have already isolated and subtracted; the black solid lines represent the spectra fitted to identify the NW bubble. The red Gaussian profiles identify the isolated NW bubble, while orange profiles identify the rotating disk component. The combined model is displayed in green. The velocities are computed with respect to the systemic velocity of the E nucleus.

except in the area closest to the W nucleus, where the ionized phase dominates. The velocity ranges between -100 and about -450 km s^{-1}, with velocities dispersion $>$ 150 km s^{-1}.

Figure 4.12 shows the fit of Paα and H_2 in three spaxels extracted from the bubble. The black dashed curve represents the spectra from the original cube, highlighting the component (red-shaded area) attributed to the HGO that we have already isolated and subtracted. The red curves represent the NWB component, while the orange curves correspond to the other components used in the fit. In all panels, the nature of the Gaussian components is clear: the outflow component is blueshifted and broader than the disk component.

Compact outflow from the W nucleus

There is another kinematic feature in the W nuclear region that has not been isolated yet. It is a nuclear outflow (WNO) that is visible in the ionized gas phase (see also Perna et al. 2024). However, it affects just a few spaxels and cannot be isolated in the moment maps (Fig. 4.5) nor in the velocity channel maps (e.g., Fig. 4.2). Therefore, once all the features described before (i.e., the SEO, the HGO, and the NWB) have been subtracted, we fitted the residual cube with two components to model the WNO and the perturbed rotating gas (i.e., large-scale rotation over the entire FoV, or small-scale

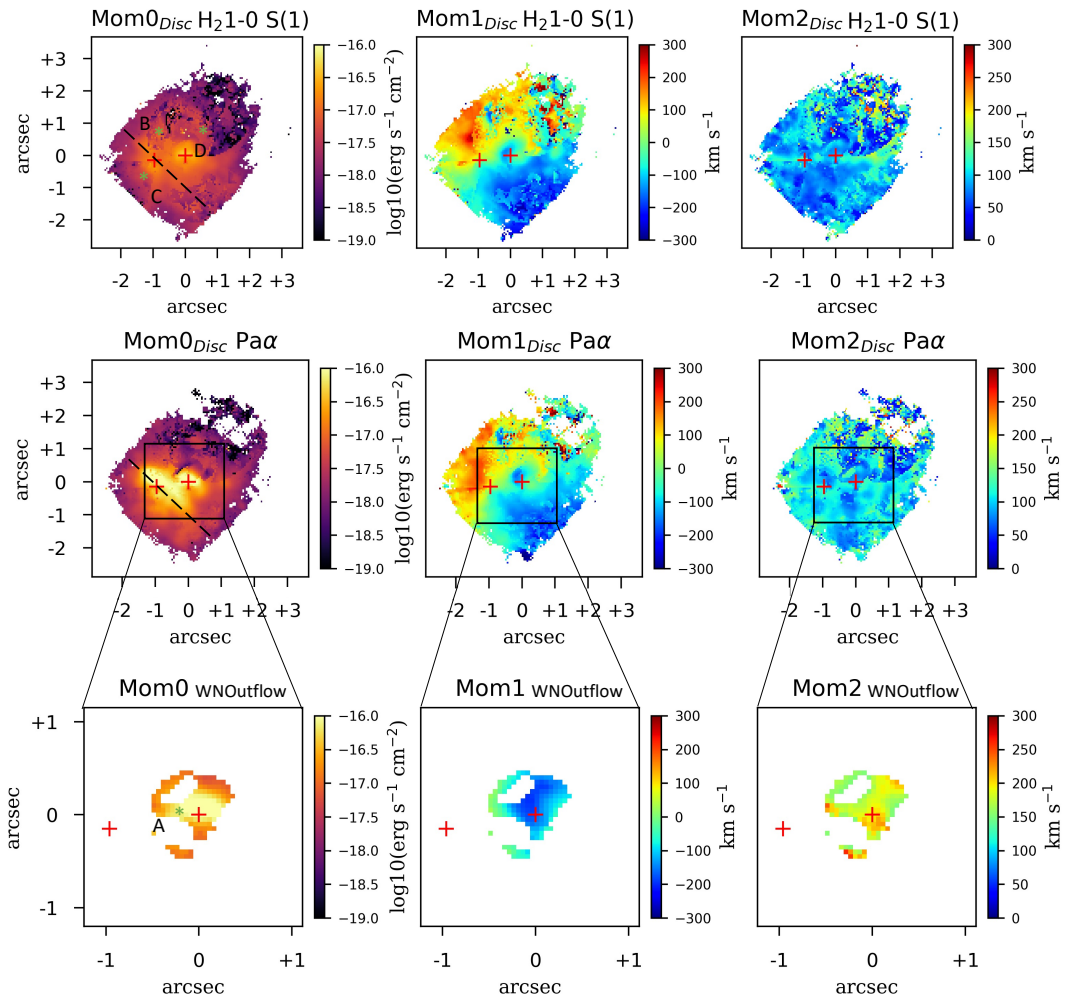

Figure 4.13: Moment maps of the large-scale rotating disk and the W nuclear outflow. Top and middle panels: moment-0 (left), moment-1 (center), and moment-2 (right) maps of $H_2$1-0S(1) (top) and Paα (middle) of the Gaussian components attributed to the perturbed disk. The black-dashed line in the velocity maps show the large-scale disc mean kinematic major-axis (PA = 45°). Bottom panels: Paα moments maps of the Gaussian components attributed to the W nuclear outflow. Velocities are referred to z_m in the first two rows. Velocity in the zoom-in inset is referred to the systemic velocity of the W nucleus.

rotating nuclear discs).

We attributed to the WNO the components with $\sigma > 150$ km s^{-1}within a radius of 0.4" (150 pc) around the nucleus. In the more external regions, we associated both the components to the perturbed rotating gas. Figure 4.13 shows the three moments of the components attributed to the perturbed disk in H_2 and Paα (top and central panels) and of the WNO (bottom panels). The WNO kinematics are characterized by blueshifted velocities up to -200 km s^{-1}and a velocity dispersion of $\sim 150-200$ km s^{-1}.

Figure 4.14 shows the spectrum extracted from a random spaxel (marked in the bottom panel of Fig. 4.13) to illustrate the fit decomposition for the ionized and hot molecular gas phases. The differences in the line profile of the two gas phases are evident: the broad, blueshifted wing that is observed in Paα is not observed in the molecular gas.

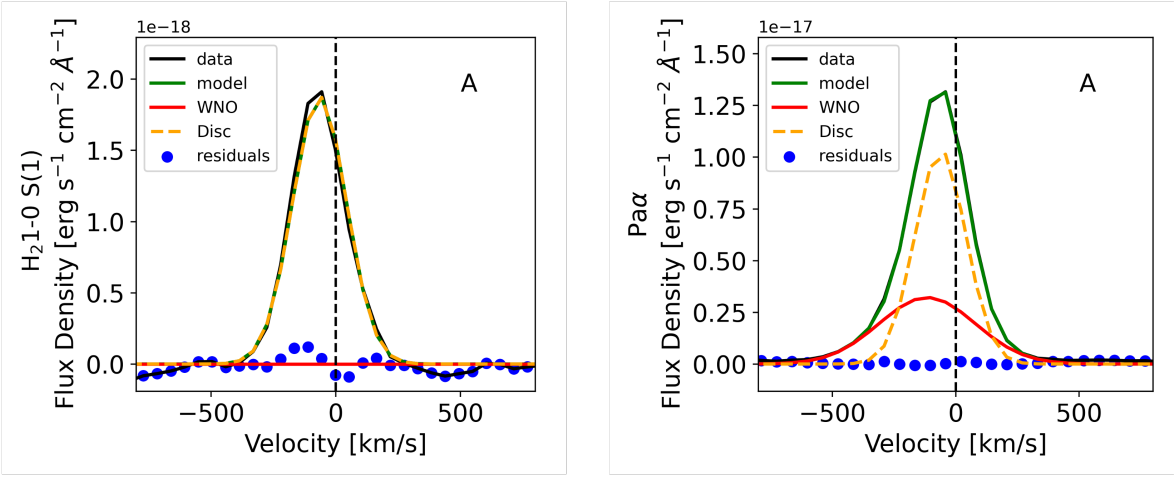

Figure 4.14: Spectrum extracted from the WNO. Line profiles of H_2 (left) and Paα (right) extracted from a spaxel labeled in the bottom panel of Fig. 4.13). The two component fits are represented by the dashed orange (disc component) and red (outflow component) curves; the combined model is displayed in green. The velocities are computed with respect to the systemic velocity of the W nucleus.

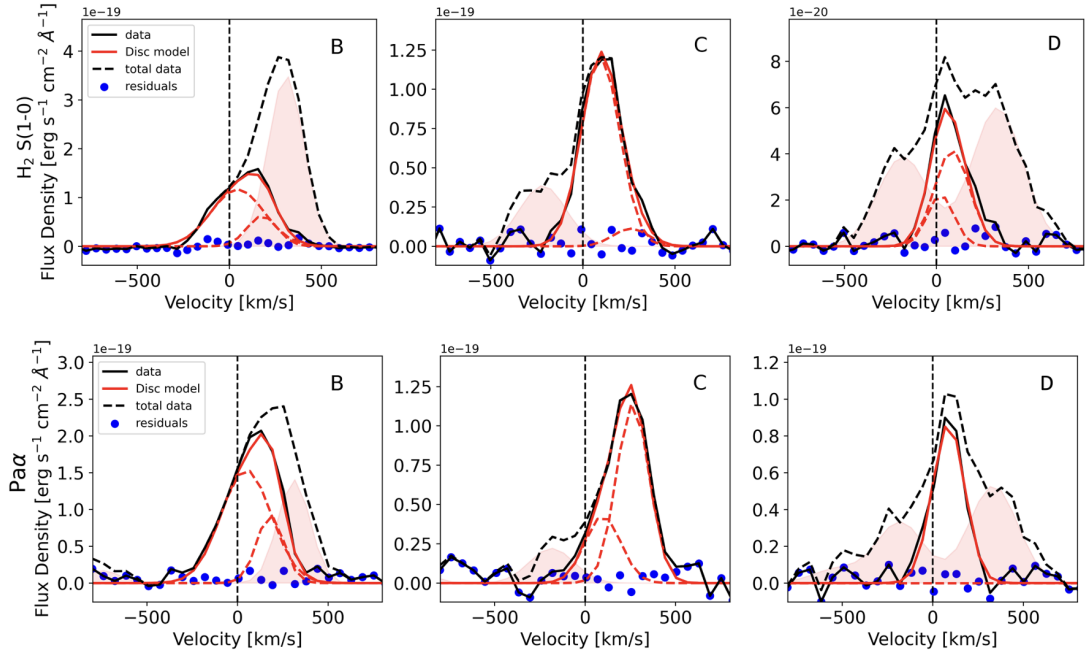

Figure 4.15: Spectra extracted from the kiloparsec-scale disk. Line profiles of H_2 (top) and Paα (bottom) at the position of the three spaxels labeled in Fig. 4.13. The black dashed curves represent the spectra from the original cube, highlighting the contribution attributed to the HGO and SEO (red-shaded area) that we have already isolated and subtracted; the black solid lines represent the spectra fitted to identify the large-scale disk. The red dashed curves show the components associated with the disk model. The total disk model is shown with a solid red curve. Velocities are computed with respect to z_m.

Perturbed rotating disk

The moment maps of hot molecular and ionized gas shown in Fig. 4.5 already suggested a large-scale rotation pattern, although strongly affected by several outflow features. These additional kinematic components were isolated and subtracted. After the subtraction of the components associated with the WNO, we assigned to the perturbed rotating gas all the components having $\sigma < 200$ km s^{-1}. In fact, the components with higher velocity dispersion might represent residuals of outflowing gas that we did not model in the previous steps. Figure 4.13 (top and central panels) shows the moment maps of the isolated perturbed rotating gas, with contributions from both circum-nuclear discs in the vicinity of the E and W nuclei and the large-scale disk. The Moment-1 velocities are defined with respect to $z_m = 0.0181$, which is more appropriate for the kiloparsec-scale disk (see Sect. 4.1.2).

We observe a symmetric velocity gradient with respect to the E nucleus, with velocities from -250 km s^{-1}(northeast) to $+250$ km s^{-1}(southwest). The Moment-1 map in the northwest part of the FoV is instead disturbed due to the non-perfect subtraction of HGO and NWB contributions. Moreover, significant deviations from a large-scale rotational patter are also observed in the vicinity of the W nucleus: this is due to the presence of a small-scale disk surrounding the W nucleus (see also e.g., Scoville et al. 2017). We calculated the position angle (PA)[1] of the major kinematic axis of the large-scale disk by fitting the Moment-1 map of Paα and for H_2 with the FIT KINEMATIC PA code [Cappellari et al., 2007, Krajnović et al., 2011], obtaining 51$\pm$7° and 39$\pm$7°, respectively. In Sect. 4.1.4, we use the average of these two values to construct the position-velocity (PV) diagram.

The velocity dispersion of the perturbed rotating disk reaches values up to 150 km s^{-1}, significantly lower than in the velocity dispersion map obtained before the subtraction of the outflowing features (Fig. 4.5). Moreover, the kinematics of Paα are more perturbed compared to that of the hot molecular gas, as also seen in Armus et al. [2023].

Figure 4.15 shows three single-spaxel spectra extracted from the HG region (B), the SEO cone (C), and an overlapping region of the HG and NW bubble (D) (See Fig. 4.13). After the subtraction of the outflow components, the line profiles are now rather symmetrical; the second component used in the fit procedure (red dashed curves) either is much fainter than the first component, or shows similar velocity shifts and line widths. Therefore, the attribution of both components to the disk is well justified.

4.1.4 Stellar kinematics

Figure 4.16 presents the stellar kinematics maps obtained with pPXF. In particular, they are created from the analysis of the G235H cube, which is less affected by dust attenuation than the G140H cube and shows more prominent CO stellar absorption features in the wavelength range 2.2–2.4 μm (Fig. 4.3).

As shown in the inset panel of Fig. 4.16, the stellar velocity field of Arp 220 presents two nuclear discs rotating in opposite directions separated by 1", with a velocity offset of ~ 120 km s^{-1}(see also Wheeler et al. 2020, Sakamoto et al. 1999). The stellar velocity dispersion is higher in the nuclear positions, and then decreases throughout a region

[1]The position angle is measured on the receding half of the galaxy, taken anticlockwise from the north direction on the sky (east of north).

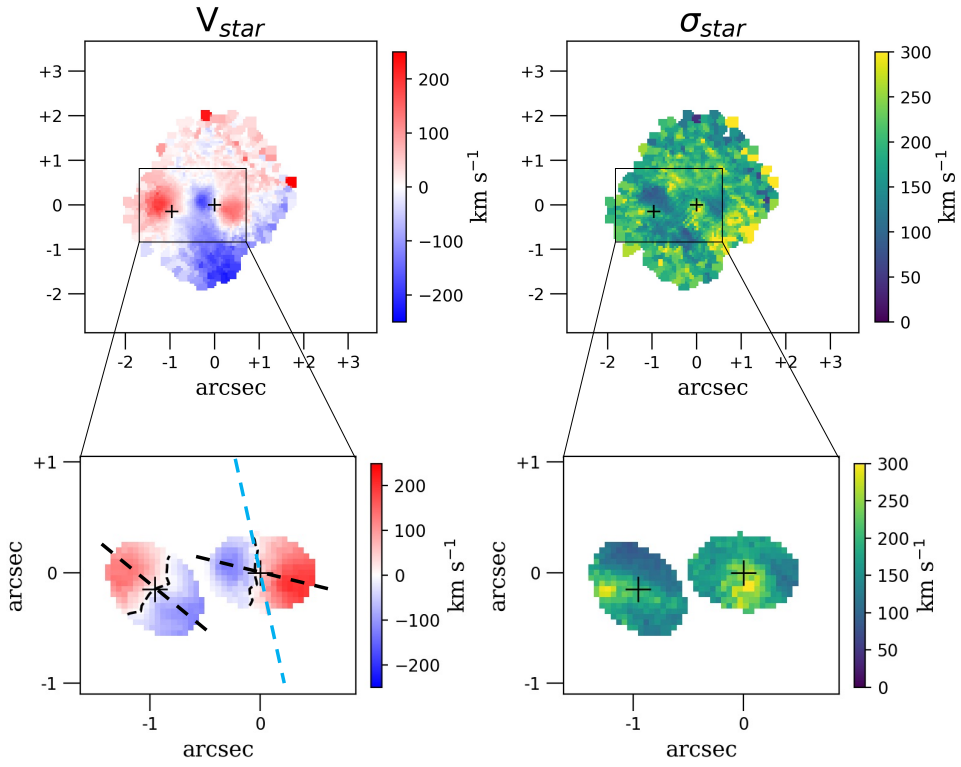

Figure 4.16: Stellar kinematics maps. Top panels: Stellar velocity (left, in the frame z_m) and velocity dispersion (right). Bottom panels: Stellar velocity (left) and velocity dispersion (right) around the two nuclei shifted with respect to the rest-frame velocity of each nucleus. Black dashed lines refer to the major axis of the two nuclei (W: PA = 257°, E: PA = 45°). Light blue dashed line refers to the axis of HG outflow (PA = 13°).

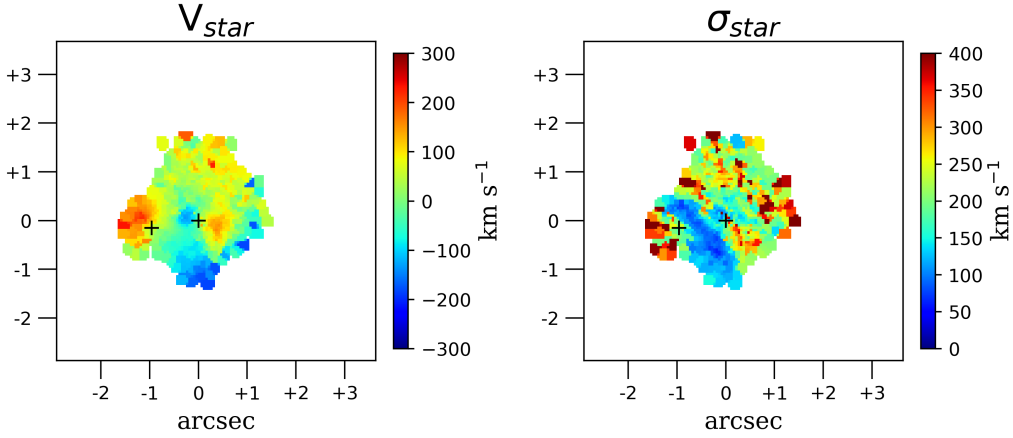

Figure 4.17: Stellar kinematics derived from the analysis of the first cube (grating G140H/F100LP).

crossing the two nuclei, in correspondence with the bright elongated region observed in

the Paα Moment-0 map (Fig. 4.13). Moreover, in the E nucleus, the velocity dispersion increases toward the east, while in the W nucleus it increases in the south direction. In the outermost regions north of the two nuclei, the velocity dispersion reaches about 200 km s^{-1}, consistent with the values found in Perna et al. [2020]. As a safety check, we derived the kinematic stellar maps also from the G140H gratings and we found that are consistent with those derived from G235H as we see in Fig. 4.17.

In the next two sub-sections we compare the stellar and gas kinematics making use of PV diagrams.

Stellar and gas kinematics around the W nucleus

In this section we compare the gas and stellar kinematics around the W nucleus. We constructed a PV diagram of both the ionized gas and the hot molecular gas (Fig. 4.18), centered on the W nucleus with a PA $\sim 257\pm6^{\circ}$ directed along the major axis of rotation of the circumnuclear stellar disk calculated with the FIT KINEMATIC PA code (dashed black line in Fig. 4.16). We set the zero velocity at the redshift of the W nucleus (z^*_W). The ionized gas (upper panel) reaches blueshifted velocities higher than those of the hot molecular gas (bottom panel). The stellar component (black star symbols in the plots) follows the kinematics of ionized gas, while it appears to rotate faster than the hot molecular gas.

In the PV diagram along the circumnuclear disk's minor axis (PA $\sim 347\pm6^{\circ}$), the ionized outflow (WNO), discussed in Sect. 4.1.3, is evident. It extends about 0.3" from the W nucleus and exhibits velocities reaching up to 600 km s^{-1}both in the blue- and redshifted sides. However, this feature is not detected in the hot molecular gas, probably due to the dissociation of the H_2 molecules or, more in general, to different physical conditions (e.g., in terms of magnetic field and electron density in the outflowing gas; see, e.g., Kristensen et al. 2023).

We also constructed a PV diagram along the axis of the HG outflow (PA = 13°, left panel of Fig. 4.18), which is not exactly perpendicular to the axis of rotation of the circumnuclear disk. Ionized gas dominates the emission within 0.5" radius of the W nucleus, and decreases considerably at larger distances; instead, the H_2 emission is more diffuse. The high blue- and redshifted velocities spans a range of -200 km s$^{-1}<$ $v < 300$ km s^{-1}at a distance of about 1.5" (600 pc), delimiting the HG outflow. To summarize, around the W nucleus we found 1) a relatively good match between stellar and gas kinematics, 2) a strong nuclear ionized outflow (blue and redshifted) in addition to the HG outflow.

Stellar and gas kinematics around the E nucleus

Figure 4.19 shows the PV diagram along the major axis of the stellar rotational disk centered at the position of E nucleus (PA = 45°). Since it was not possible to decouple the contribution of the small-scale disk surrounding the E nucleus from the large-scale disk, the major axis of the small-scale disk was assumed to be aligned with the one of the large-scale disk computed in the previous subsection. We set the zero velocity at the redshift of the E nucleus (z^*_E).

The stellar component follows the rotation of the gas around the nucleus. In the ionized gas (Fig. 4.19, top), a peak in the flux is observed at redshifted velocities ~ 250 km s^{-1}, representing a bright clump at the north of the E nucleus (NE cluster in Perna et al. 2024), not observed in the hot molecular phase.

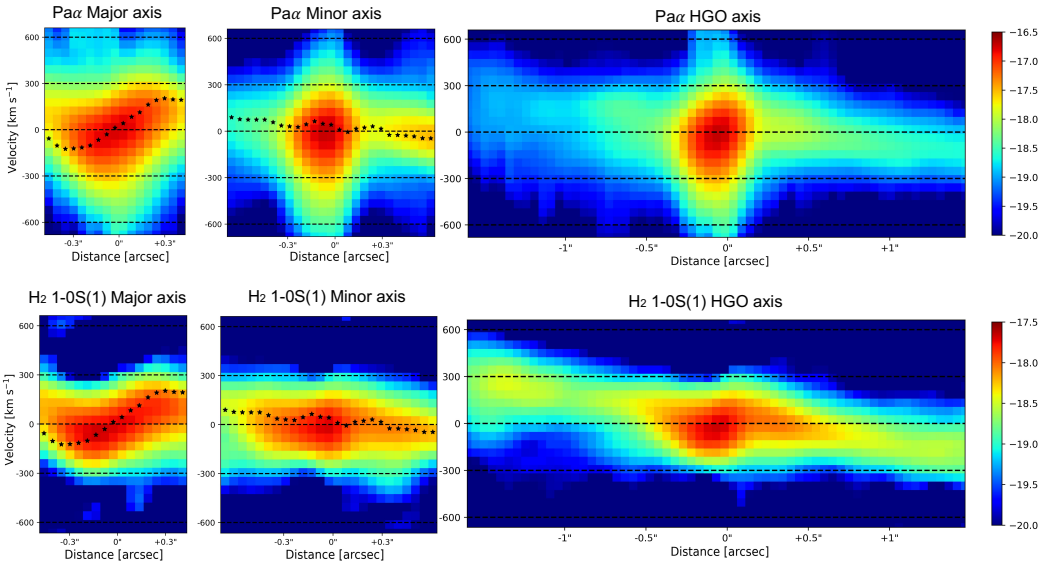

Figure 4.18: Position-velocity diagram for ionized gas (top) and hot molecular gas (bottom) of W nucleus with positions varying along the disk major axis (PA = 257°, left, with positive distances toward west), the disk minor axis (PA = 347°, center, with positive distances toward north); and HG outflow axis (PA = 13°, right, with positive distances toward southwest). Black stars represent the stellar velocity. The zero-velocity refers to z^*_W.

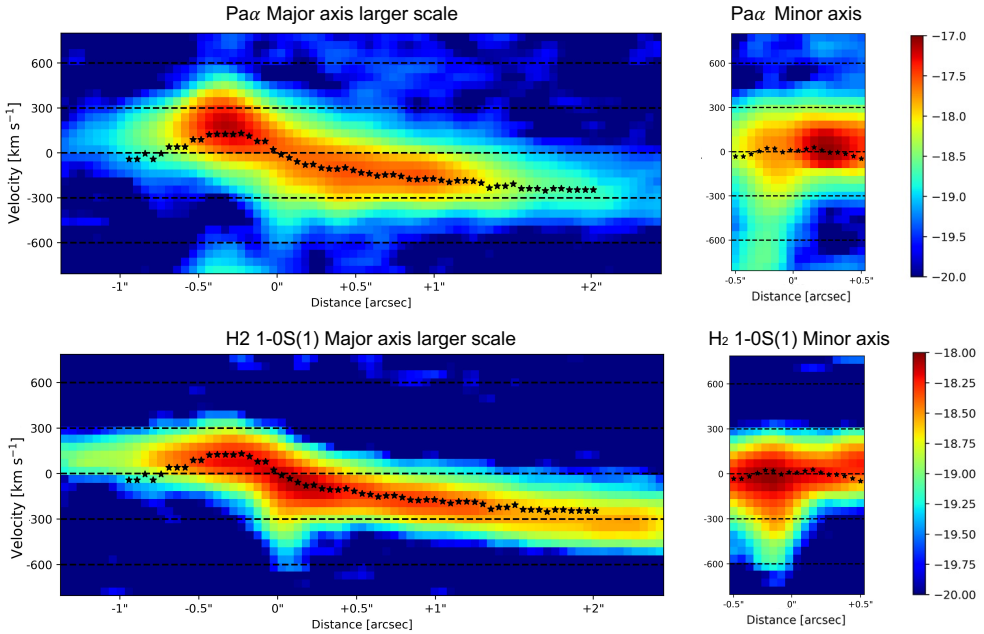

Figure 4.19: Position-velocity diagrams of large-scale rotational disk centered on the E nucleus. In the left panels, the positions vary along the mean kinematic major axis (PA = 45°), with positive distances toward south-west. In the right panels, the positions vary along the minor axis (PA = 135°), with positive distances toward north-west. The upper panels show the PV diagrams of Paα, while the lower panels show PV diagrams of H_2 1-0 S(1). Black stars identify the stellar kinematics. The zero-velocity refers to z^*_E.

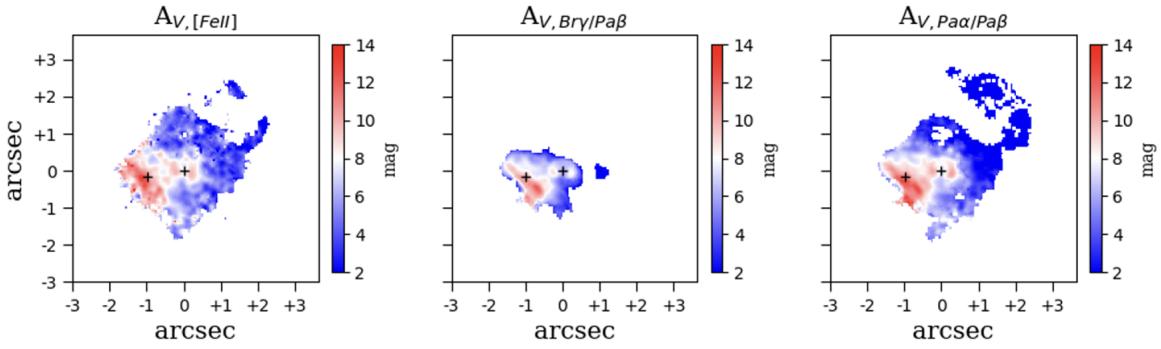

Figure 4.20: Dust attenuation maps from the[Fe II] 1.257 μm to [Fe II] 1.640 μm ratio (left), Brγ/Paβ (middle) and Paα/Paβ (right).

A blueshifted nuclear outflow is observed in both the hot molecular gas (bottom) and the ionized gas (top), reaching velocities of about -600 km s^{-1}. This emission forms the vertex of the SE conical outflow we isolated in Sect. 4.1.3.

4.1.5 ISM properties

Attenuation

We used the emission-line ratios [Fe II] 1.644/1.257, Brγ/Paβ and Paα/Paβ as attenuation diagnostics. We measured the line ratios from each spaxel, and scaled them to calculate $E(B-V)$ as follows [Domínguez et al., 2013]:

$$E(B-V) = \frac{2.5}{k(\lambda_{L1}) - k(\lambda_{L2})} \log_{10}\left(\frac{(L1/L2)_{obs}}{(L1/L2)_{in}}\right) \quad (4.1)$$

where L1 and L2 are the lines used for the diagnostic, and k(λ_{L2}) and k(λ_{L1}) are the values of the reddening curve evaluated at L1 and L2 wavelengths. The intrinsic ratios are taken respectively from Bautista and Pradhan [1998], Hummer and Storey [1987] and from CLOUDY [Ferland et al., 2017] assuming a temperature of 10^4 K and a density $n_e = 100$ cm^{-3}. We adopted the Calzetti et al. [2000] attenuation law valid between 0.12 to 2.2 μm with R$_v$ = 4.05 estimated from optical-IR observations of four starburst galaxies.

Figure 4.20 shows the dust attenuation maps estimated from the different emission line ratios with a cut in S/N (>3) for each line, as $A_V = 4.05 \times E(B-V)$. The attenuation A_V varies between 2 and 14 mag, reaching higher values in the E nucleus (consistent with Perna et al. 2024) and lower values in the outer part of the FoV. The three attenuation maps computed with different line ratios are consistent. The attenuation computed from Eq. 4.1 integrating the fluxes in the central region (where the S/N of the faintest line Br$\gamma > 3$) varies less than 20% between the three attenuation diagnostics. These values are also consistent with the stellar attenuation computed by Engel et al. [2011a] through the K band, A$_v = 6 - 12$, while our values are a factor 2-3 higher than their estimates through Paα/Brγ.

Star formation

We derived the SFR from the Paα extinction corrected luminosity by summing the contribution of the perturbed rotating discs as defined in Sect. 4.1.3, excluding all the

outflow components. We used the Paα flux corrected for the dust attenuation spaxel per spaxel derived from the Paα/Paβ, resulting in an increase of the Paα flux of a factor $\sim$2.2, and we followed Reddy et al. [2023]:

$$\mathrm{SFR(Pa}\alpha) \left[M_{\odot} yr^{-1}\right] = \mathrm{C(Pa}\alpha) \times \mathrm{L(Pa}\alpha) \left[ergs^{-1}\right] \tag{4.2}$$

where C(Paα) = 3.90$\times 10^{-41}$ assuming an upper mass cutoff of the IMF of 100 $M_{\odot}$ and a solar metallicity. We derived a total SFR of $\sim$ 8 $M_{\odot}$ yr^{-1}. The value of SFR found with the recombination line is significantly lower than ones computed in a similar area with FIR and radio data ($\sim$ 200 $M_{\odot}$ yr^{-1}, from Varenius et al. 2016 and Pereira-Santaella et al. 2021), possibly indicating that a large fraction of the SF is totally blocked by dust at NIR wavelengths [Giménez-Arteaga et al., 2022, Perna et al., 2024].

The largest contribution to the emission of recombination lines comes from the elongated region located between the two nuclei with relatively faint H_2 emission. In Fig. 4.25a we show the ratio of the total Paα flux to the total H_2 flux, which peaks up to 30 north of the E nucleus and drops to values less than one in the outermost regions. We also observed blobs in which the ratio reaches values of approximately two (in log: 0.3-0.4 from Fig.4.25a); one of the largest is located about 1" west of the W nucleus. These blobs lie along a preferential NS direction, probably along a filament or dust lane where SF is more intense.

Figure 4.25b shows the SFR surface density map, Σ_{SFR}. The Σ_{SFR} is highest in the elongated region between the two nuclei (10–40 $M_{\odot}$ yr^{-1} kpc^{-2}), while the other regions have value $<$ 1 $M_{\odot}$ yr^{-1} kpc^{-2}. The Σ_{SFR} calculated over the entire FoV ($\sim$ 1.5 kpc $\times$ 1.5 kpc) has a value of $\sim$3 $M_{\odot}$ yr^{-1} kpc^{-2}. Similar values are reported in a sample of ULIRGs studied with VLT/SINFONI [Piqueras López et al., 2012], ranging between 0.4 and 2 $M_{\odot}$ yr^{-1} kpc^{-2}. Based on FIR measurements, the SFR surface densities of the nuclear region of Arp 220 reaches values higher than 10^3 $M_{\odot}$ yr^{-1} kpc^{-2}. As discussed in Perna et al. [2024], this discrepancy may be explained taking into account different factors: the high obscuration caused by the dust, the different scale times of SF that the two bands (FIR and NIR) trace and to the possible presence of AGN that is completely obscured in the NIR. Typical star formation surface density values computed in radio band in ULIRGs are $50 - 1000$ $M_{\odot}$ yr^{-1} kpc^{-2} in the nuclear region ($<$ 1 kpc^2), and $5 - 500$ $M_{\odot}$ yr^{-1} kpc^{-2} on scales of few kiloparsec [Lucatelli et al., 2024].

Outflows properties and energetics

In this section, we estimate the outflow energetics of the molecular and of the ionized gas. To estimate the mass of the outflowing gas in the hot molecular phase, we followed Scoville et al. [1982] and Mazzalay et al. [2013]:

$$M_{\mathrm{out,\ H_2}} = 5.1 \times 10^{13} \left(\frac{D_{\mathrm{L}}}{\mathrm{Mpc}}\right)^2 \left(\frac{F_{1-0\ \mathrm{S(1)}}}{\mathrm{erg\ s^{-1}cm^{-2}}}\right) 10^{0.4\mathrm{A}_{2.2\mu\mathrm{m}}} M_{\odot} \tag{4.3}$$

where $M_{\mathrm{out,\ H_2}}$ is the hot molecular mass traced by H_2, D_L is the luminosity distance, and $A_{2.2\mu\mathrm{m}}$ is the attenuation at 2.2 μm. This equation assumes thermalized gas conditions and T = 2000 K, with a population fraction in the (ν, J) = (1, 3) level of $f(1,3) = 0.0122$. We applied Eq. 4.3 for each spaxel and then we summed over the region of the spatially resolved outflows (namely, the SEO, the HGO, the NWB, and the WNO) to compute the total masses. We computed $A_{2.2\mu m}$ as shown in Sect. 4.1.5

through Paα/Paβ, since it involves the lines with higher S/N among the line ratios considered. However, when computing the properties of the outflow in the spaxels where we could not infer the attenuation due to low S/N <3 in Paα and Paβ, we assumed A_V corresponding to the mean value in the defined region.

To compute the ionized outflow mass, we adopted the simplified model by Genzel et al. [2011], valid for case B recombination of fully ionized gas with $T \sim 10^4$ K that we adopted in Chapter 3. The mass of outflowing gas is given by the Eq. 3.3, where $L_{H\alpha}$ is derived from $L_{Pa\alpha}$ corrected for attenuation assuming a theoretical ratio Paα/Hα = 0.11, and n_e is the electron density.

The determination of the ionized gas mass is significantly influenced by n_e, which can span a few orders of magnitude, from 10^2 to 10^4cm^{-3} [Villar Martín et al., 2014, Perna et al., 2017, Förster Schreiber et al., 2019, Isobe et al., 2023]. We derived the electron density through the line ratio [Fe II]1.677 μm/[Fe II]1.644 μm. We fitted the integrated spectrum around the lines of interest considering in the model also the Br11 line, since it is blended with [Fe II]1.677 μm. Since the latter line is very faint at spaxel level, we integrated the spectra over the individual outflow regions SEO (Fig. 4.7), HGO (Fig. 4.9), NWB (Fig. 4.11), and WNO (Fig. 4.13, bottom panels), to infer average electron densities for each outflow. Moreover, due to the low S/N of [Fe II]1.677, we considered the total profile of [Fe II]1.677 μm and 1.644 μm, without distinguishing the contribution of non-outflowing components. We obtained electron densities in the range log (n_e/cm^{-3}) $\approx 3-4$ from the relation in Koo et al. [2016].

We found that the region with the highest electron density is the WNO ($n_e = 5000^{+2500}_{-2000}$ cm^{-3}). For the HGO, we found $n_e = 3800^{+2200}_{-1300}$ cm^{-3}. We also integrated the spectrum and computed the electron density in both the red- and blueshifted region of the HG outflow, separately. We found $n_e = 1600^{+800}_{-500}$ cm^{-3} for the redshifted and a 3σ upper limit of 5×10^4 cm^{-3} in the blueshifted part. In the SEO and in the NWB the emission of [Fe II] 1.677 μm is not detected, resulting in upper limits on the electron density: $< 1.7 \times 10^4$ cm^{-3}, and < 1800 cm^{-3}, respectively. All the inferred values are reported in Table 4.3.

The n_e estimates through the [Fe II]transitions are higher (a factor $\sim$ 10-100) than those found from the [S II]doublet in the optical band with MUSE (170 cm^{-3}, Perna et al. 2020). This may indicate a gas stratification in the nuclear regions of Arp 220, with [Fe II]emission, having higher critical density ($N_c \sim 10^4$ cm^{-3}), tracing the densest part of the ISM, and [S II]($N_c \sim 10^3$ cm^{-3}) tracing the more diffuse gas. It is worth noting that using a constant density of $n_e \sim 10^2$ cm^{-3}, as the one derived by Perna et al. [2020] using [S II], could lead to an overestimation of the gas masses and the energetics, because this line emission likely traces partially ionized gas with lower densities [Davis et al., 2011, Revalski et al., 2022]. On the other side, our estimation of the n_e from [Fe II]doublet comes only from the nuclear (WNO) and the most compressed regions (HGO), where the faint [Fe II] 1.677 μm line is detected. Thus, this electron density may not be representative of the density in the full FoV. Therefore, we chose to estimate the outflow properties with electron density estimations from both [Fe II]and [S II]that may represent reasonable lower and upper boundaries.

For each isolated outflow in Sect. 4.1.3, we determined the mass outflow rate, $\dot{M}_{out}$, at a given radius R_{out} by using the assumptions of a constant outflow speed v_{out} and spherical (or multiconical) geometry. Following Lutz et al. [2020], we have

$$\dot{M}_{\rm out} = 1.03 \times 10^{-9} \left(\frac{v_{\rm out}}{\rm km\ s^{-1}}\right) \left(\frac{M_{out}}{M_\odot}\right) \left(\frac{R_{out}}{kpc}\right)^{-1} \times C M_\odot\ yr^{-1} \tag{4.4}$$

where C is a factor that depends on the outflow history. We adopted a constant mass outflow rate (C=1). We calculated the radius from the flux maps of each outflow. In particular, we measured R_{out} as the maximum extension from the corresponding nucleus. Specifically, for the HGO and WNO, we calculated the distances from the W nucleus, while for the SEO and NWB we calculated them from the E nucleus. We associated the NWB to the E nucleus, in order to have a more conservative estimation of the mass outflow rate. This choice is also motivated by the fact that the outflows launched by the W nucleus are oriented along the NS direction (Sect. 4.1.3), while the one of the E nucleus is along the SE direction. Moreover, the 100 pc scale molecular outflow launched by the E nucleus and traced by CO [Wheeler et al., 2020] is similarly oriented along the SE-NW direction.

We used the definition of the outflow velocity in Rupke and Veilleux [2013a] as

$$v_{\rm out} = |v_{\rm broad}| + 2\sigma_{\rm broad}, \tag{4.5}$$

where $v_{\rm broad}$ and $\sigma_{\rm broad}$ are the velocities relative to the systemic velocity of the nucleus from which the outflow originates, and the velocity dispersion of the outflowing component, respectively. We computed the outflow velocities as the flux-weighted average of the outflow velocity of each spaxel. We assigned the standard deviation of the values in that region as the uncertainty on $\rm v_{out}$. The properties of the ionized and molecular gas outflows for the analyzed regions are reported in Table 4.3.

The outflow masses and the mass outflow rates of the hot molecular gas vary from 700 $\rm M_\odot$ in the SEO to 2000 $\rm M_\odot$ in the HGO, and from 6×10^{-4} $\rm M_\odot\ yr^{-1}$ for the NWB to 1×10^{-2} $\rm M_\odot\ yr^{-1}$ for the HGO, respectively. For the ionized gas, the outflow mass varies from a minimum of 5×10^3 $\rm M_\odot$ for the SE outflow to a maximum of 9×10^4 $\rm M_\odot$ fort the WNO, calculated with the density from the [Fe II]doublet. The highest mass outflow rate of ionized gas is measured in the WNO with a value of 8 $\rm M_\odot\ yr^{-1}$, estimated using the density from the [S II], while the lowest is measured in the NWB with a value of 0.4 $\rm M_\odot\ yr^{-1}$.

We also computed the kinetic energy and the kinetic power of the outflow as $E_{\rm out} = \frac{1}{2} M_{\rm out} v_{\rm out}^2$ and $\dot{E}_{\rm out} = \frac{1}{2} \dot{M}_{\rm out} v_{\rm out}^2$, respectively. We found that the contribution to the energetics of the ionized outflow is about 1-3 orders of magnitude higher than that of the hot molecular gas, depending on the density used in the computation. The kinetic energy of the ionized gas outflows ranges between 1.7×10^{54} erg for the SEO to 4.6×10^{54} erg for the WNO, estimated with [S II].

Three-dimensional outflow modeling

To measure the geometrical parameters of SEO, HGO and the NWB outflows we used the modeling framework called Modeling Outflows and Kinematics of AGN in 3D ($\rm MOKA^{3D}$) presented in Marconcini et al. [2023]. By assuming a geometry and a simple constant radial velocity field, the model is able to retrieve the outflow inclination with respect to the line of sight (LOS), and the intrinsic outflow velocity. Full details and the implementations of the model are discussed in Marconcini et al. [2023]. Here we just show the results of the model for the hot molecular gas, by using a conical geometry for the SEO and two expanding bubbles for HGO and NWB, assuming a constant radial

velocity (See Figs. 4.21,4.21,4.23). We also assumed an intrinsic dispersion velocity of 30 km $s^{-1}$to account for the turbulent nature of the bubbles. Since we found that the ionized gas has a similar kinematics, the results of the model for the ionized phase would be the same. We did not attempt to model the WNO since it is very compact and we could not establish a clear geometry to be assumed.

In Fig. 4.24 we show the 3D model of the outflows detected in the nuclear region of Arp 220. The geometry parameters derived from MOKA^{3D} are as follows.

- The aperture of the SEO is 80° with an inclination respect to the LOS of 70° and PA of 230° measured clockwise from north. This is consistent with a conical outflow launched perpendicular from the E circumnuclear disk having an almost edge-on orientation, according to Wheeler et al. [2020]. The velocity retrieved for the SEO by MOKA^{3D}is ∼700 km s^{-1}, consistent within $< 1\sigma$ with the velocities computed as defined as in Eq. 4.5), but slightly higher.

- The HGO has an inclination of –60° with respect to the LOS and a velocity of ∼400 km $s^{-1}$for the blueshifted side, and 120° and ∼600 km $s^{-1}$for the redshifted side. The discrepancies between the velocity in the redshifted and blueshifted side could be explained by the possible ISM porosity and hence different propagation of the bubbles. The inclination of the W circumnuclear disk is ∼120° with respect to the LOS [Wheeler et al., 2020], which mean that the axis of the bubble is not exactly perpendicular to the disk, but has an offset of about 30°.

- For the NWB we found an inclination of 68° with respect to the LOS and a velocity of ∼750 km s^{-1}, also in this case slightly higher than our flux-weighted velocity measurement.

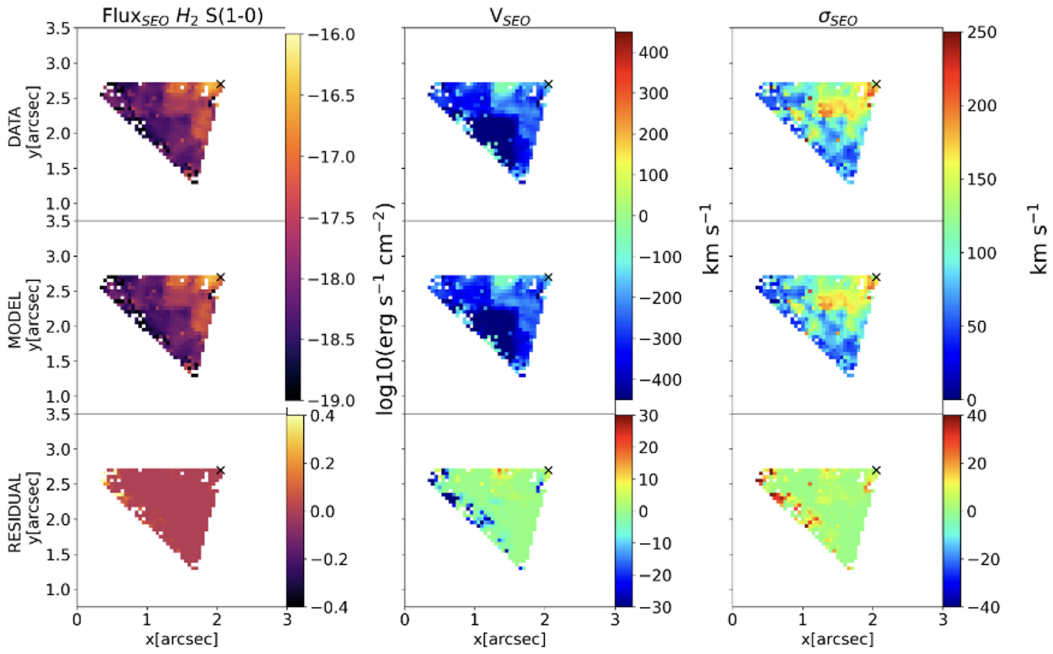

Figure 4.21: Comparison between the flux and velocity of H_2 (top panels) and MOKA^{3D}weighted model (middle panels) for the SE conical outflow. The bottom panels present the residuals obtained subtracting the model from the data.

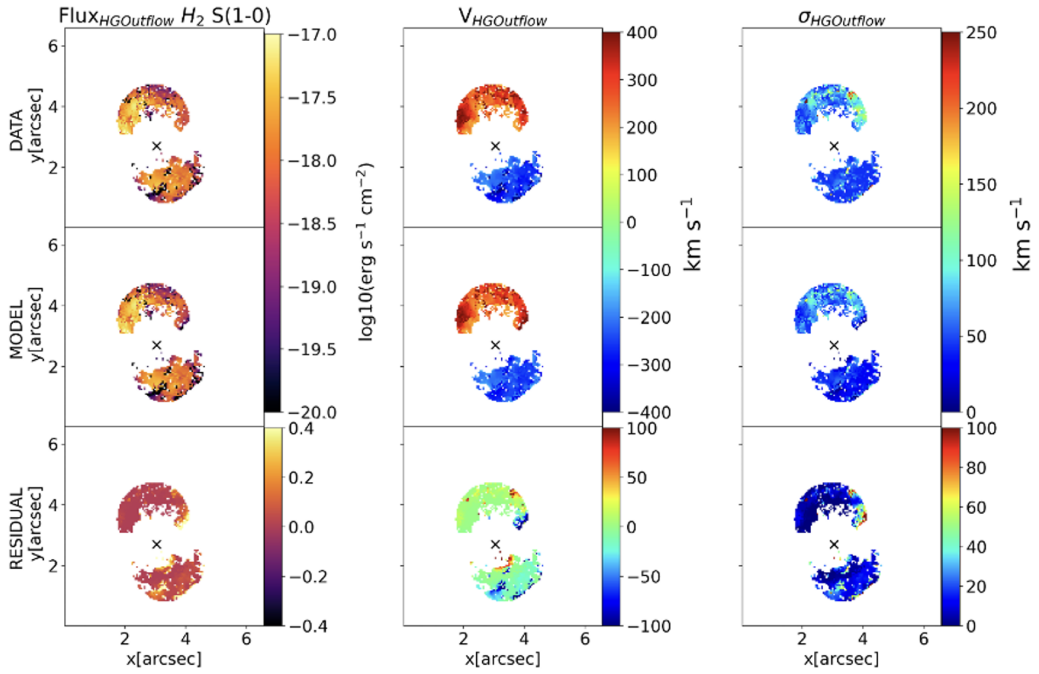

Figure 4.22: Same as 4.21 for the HG outflow.

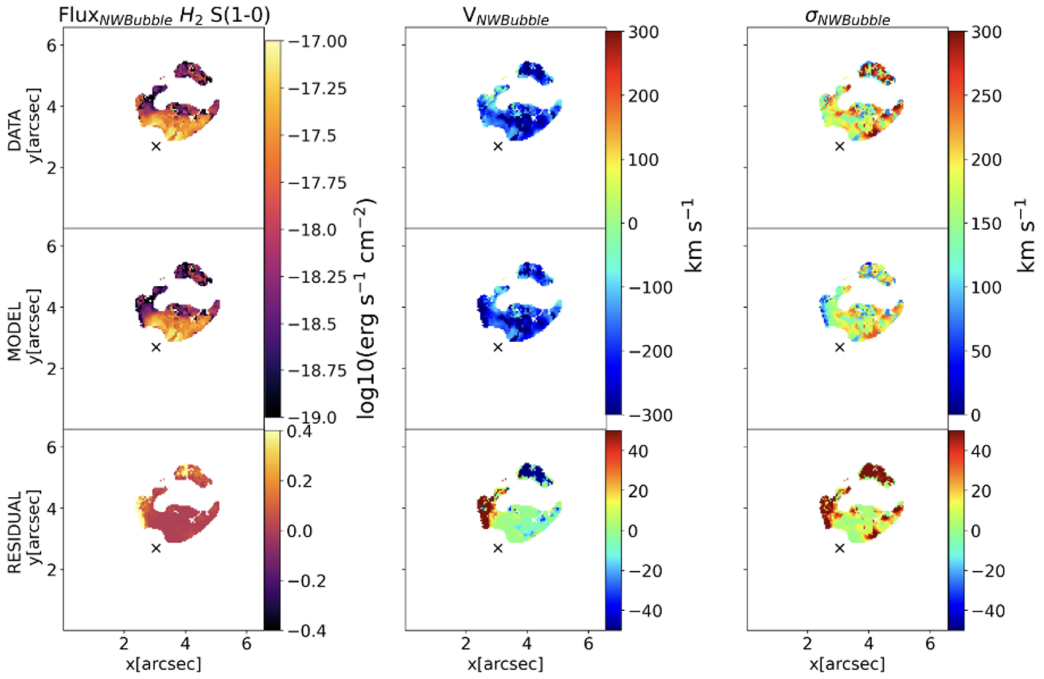

Figure 4.23: Same as 4.21 for the NW bubble.

In all outflows, the velocities defined by Eq. 4.5 seem to underestimate the velocities found by the MOKA^{3D} even though they are consistent within 1-2σ. This is due to the fact that the model takes into account the intrinsic velocity of the outflow corrected for all projection effects. In conclusion, the kinematic outflow properties inferred with MOKA^{3D}and the method outlined in Sect.4.1.5 are consistent within the uncertainties.

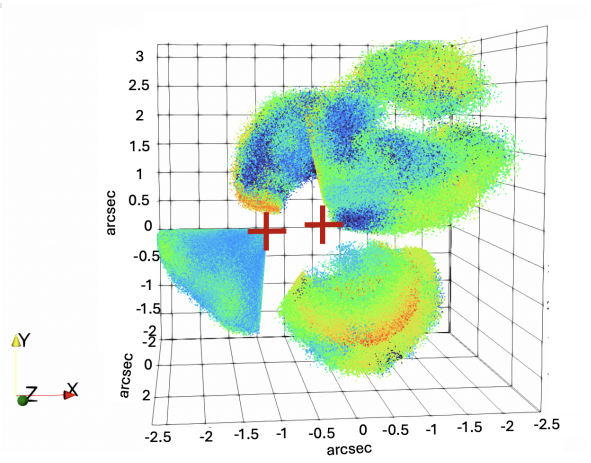

Figure 4.24: Three-dimensional representation of the hot molecular outflow structures detected in Arp 220 modeled with MOKA3D. The XY represents the plane of the sky, while the Z axis is the LOS. The color intensity represents the intrinsic cloud emission, bluer colors represent lower emission clouds, while redder colors represent high-emission clouds. (See Marconcini et al. [2023] for the details of the model.)

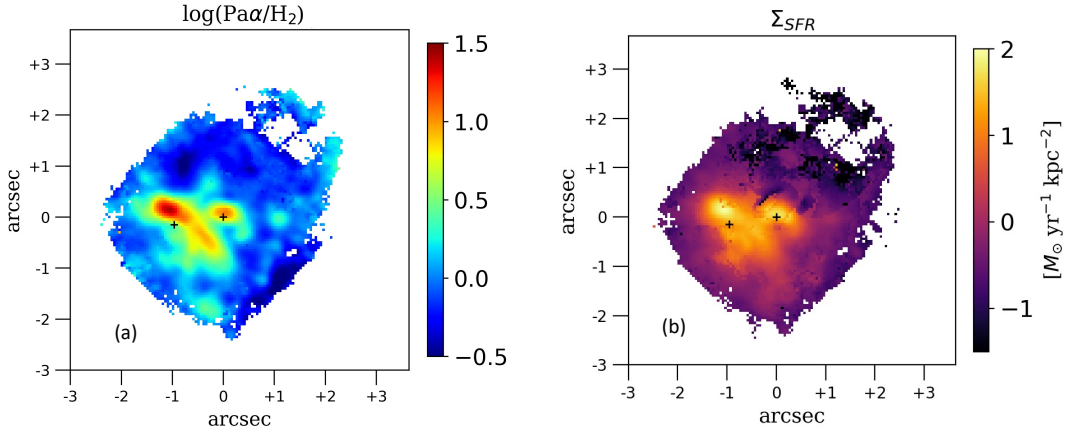

Figure 4.25: Maps of ionized over hot molecular gas ratio and SF surface density. (a) Spatially resolved flux ratio $\log(\mathrm{Pa}\alpha/\mathrm{H_2})$ computed from the total profile of the two lines. (b): Surface density map of the SFR inferred from Paα after subtraction of the outflowing components.

4.1.6 Discussion

The ubiquity of multiphase outflows in ULIRGs was established through spatially resolved observations in the visible band, thanks to integral field instruments like VIMOS and MUSE [Arribas et al., 2014, Westmoquette et al., 2012, Venturi et al., 2021, Musiimenta et al., 2024], in the near IR band with Gemini/NIFS, Keck/OSIRIS, and VLT/SINFONI [Engel et al., 2011b, Riffel et al., 2015, Storchi-Bergmann et al., 2010, Pereira-Santaella et al., 2016, Emonts et al., 2017, U et al., 2019, Schönell et al., 2019], and in the radio band with ALMA [Pereira-Santaella et al., 2016].

Simulations show that outflows likely contain cold, dense clouds that are accelerated by a stream of warm and hot gas [Wagner et al., 2012, Zubovas and King, 2014]. However, the direct comparison of outflows identified with different tracers (and

facilities), required to test such predictions, has been so far limited to very few targets. A key challenge in studying the direct impact of outflows on the ISM is the need for both high sensitivity and spatial resolution. Ground-based near-IR integral field facilities like SINFONI, OSIRIS and NIFS mainly traced the hot molecular (e.g., H_2) and ionized (Brγ) gas with high spatial and spectral resolution. However, due to limitations in sensitivity and the presence of airglow emission lines, it has not always possible to fully characterize these outflows and compute directly their properties [Riffel et al., 2014, Emonts et al., 2017, U et al., 2019, Bianchin et al., 2022]. This is critical in order to characterize the connection between the warm molecular and the ionized gas outflow with the cold molecular gas. In fact, thanks to the advent of millimeter/submillimeter telescopes such as ALMA, high-spatial-resolution images of cold molecular gas in nearby galaxies have enabled us to reveal the structure and the morphology of starburst-driven and AGN-driven molecular outflows in high details [Salak et al., 2020, Lamperti et al., 2022, Holden et al., 2024].

The multiphase outflows

Cold molecular outflows have been detected in the nuclear region of Arp 220 with different emission line tracers, such as HCO^+, H_2O, H_2O^+, OH, and OH^+ [Sakamoto et al., 2009, González-Alfonso et al., 2012, Veilleux et al., 2013a, Tunnard et al., 2015, Martín et al., 2016, Zschaechner et al., 2016]. However, most of them are unresolved and therefore their morphology could not be constrained. Spatially resolved outflows studies have been conducted by Barcos-Muñoz et al. [2018a] and Wheeler et al. [2020] with ALMA, and Perna et al. [2020] with MUSE. Thanks to the possibility of resolving multiphase outflows with NIRSpec, we can compare the outflow properties of hot molecular and ionized phases derived in this work, with those obtained from previous observations for cold molecular gas and ionized gas at larger scale. This will help us understand the connection between multiphase and multiscale outflows. After discussing the structures of these outflows, we examine the mechanisms responsible for launching them.

W nucleus-driven outflows

Barcos-Muñoz et al. [2018b] reported a cold molecular outflow launched by the W nucleus, traced by HCN(1-0), extending for 120 pc, with a deprojected velocity of 850 km s^{-1} and a lower limit of the H_2 mass for the redshifted and blueshifted component of $\gtrsim 8\times10^6 M_\odot$ and $\gtrsim 2\times10^6 M_\odot$, respectively. These lower limits consider the possible presence of additional outflowing material at lower velocities, not accounted due to its overlap with the disk emission. Wheeler et al. [2020] found an upper limit for the total H_2 molecular mass of $\lesssim 2\times10^7 M_\odot$ for the redshifted outflow, and $2\times10^6 M_\odot$ for the blueshifted, traced by CO(3–2) gas. The upper limit here accounts the possible contamination of $H^{13}CN$ (4–3) emission, very close to the CO(3–2) transition.

We detected an HG-shape outflow originating from the W nucleus extending for 600 pc, with a hot H_2 outflowing gas mass of 2000 $M_\odot$. The redshifted region accounts for $\sim$ 1200 $M_\odot$, while the blueshifted for $\sim$800 $M_\odot$. This outflow is in the same direction as the cold molecular outflow detected in Wheeler et al. [2020], with receding gas northward and approaching gas southward. Therefore, we can reasonably assume that cold and hot molecular outflows are connected and associated with the same outflow event. Under this assumption, the total mass of the hot and cold molecular gas result

in an estimated hot-to-cold molecular gas ratio of $\approx 10^{-4}$, obtained considering both receding and approaching gas. This order-of-magnitude estimate is consistent with the values $1 - 7 \times 10^{-5}$ found in nearby ULIRGs [Pereira-Santaella et al., 2016, Emonts et al., 2017, Pereira-Santaella et al., 2018, Lamperti et al., 2022].

After comparing the total outflowing mass of ionized and total molecular gas in the W nucleus and hence accounting for both HGO and WNO, we report a mass outflow ratio between the two phases of 0.16 assuming [S II]-based electron densities ($\sim 6 \times 10^{-3}$ with the density estimated with [Fe II]). This is not unusual since the molecular phase usually dominates the mass outflow rate budget, exceeding the ionized gas phase by one to three orders of magnitude [Rupke and Veilleux, 2013a, García-Burillo et al., 2015, Carniani et al., 2015, Fiore et al., 2017, Cresci et al., 2023b].

Perna et al. [2020] identified an extended structure associated with high-velocity ionized gas (see their Fig. 19, velocity channel 125 km s^{-1}< |v| < 375km s^{-1}) from northeast to southwest, that appears to be aligned with the hourglass-shaped outflow launched from the W nucleus. This suggests that the HGO could even be connected to the outflow detected at larger scales. Alternatively, they could trace different ejection events along the same direction.

E nucleus-driven outflows

Wheeler et al. [2020] reported a collimated and extended molecular outflow in the E nucleus traced by CO transitions (J= 3 → 2). The outflow found in the present work (SEO), launched from the E nucleus, is consistent with the direction of the outflow observed in the cold molecular gas, blueshifted toward the south direction. Wheeler et al. [2020] reported a mass for the blueshifted outflow of 2.7×10^6 M$_\odot$, which, under the assumption that the CO outflow is associated with the SE outflow detected in our data, would lead to a hot-to-cold molecular gas ratio of $\sim 3 \times 10^{-4}$. This is compatible with the value we inferred in Sect. 4.1.6 for the outflow launched by the W nucleus.

We attributed the NW bubble to the E nucleus, since this structure could represent the counterpart of the blushifted outflow detected in the SE direction. However, unlike the HGO, in this case there is no clear blushifted and redshifted part of the outflow. This may be due to different gas ejection events, or to the fact that the redshifted part of the outflow is more obscured. Another possibility is that we included part of the redshifted outflow launched from the E nucleus in the HGO, since the two outflows may overlap, as we can see in Fig. 4.6c. From Fig. 4.24 we see that MOKA^{3D}assigns a higher flux weight to the clouds of the HGO near the W nucleus. This suggests the possibility of contamination from the redshifted counterpart of the SEO.

We find that the mass of the ionized gas in the NW bubble, assuming $n_e = 170$ cm^{-3}, is $\sim 6 \times 10^5$ M$_\odot$, with a total energy of $\sim 2 \times 10^{54}$ erg. Lockhart et al. [2015] estimated the properties of the NW bubble using Hα+[NII] narrow band imaging obtained with HST/WC3 with a resolution of 0.0396"/pixel, corresponding to 15 pc. They used assumptions different from ours on the density, on velocity of the bubble and also on the geometry. In fact, they adopted $n_e = 10$ cm^{-3}, about one order of magnitude lower than that used in this work, a velocity of 250 km s^{-1}, around a factor 2 lower and a shell-like geometry. Despite these different assumptions, their derived outflow mass (3.2×10^6 M$_\odot$) and energy (2.0×10^{54} erg) are in agreement, within a factor of two, with our results.

We also compared the outflows detected with NIRSpec with the larger scale outflows observed with MUSE in Perna et al. [2020]. In that case, the most extreme velocities

for the ionized outflow are observed along PA = 138° [2]; these extreme motions are aligned with X-ray emission and with the minor axis of the stellar disk. The SEO and the NWB are found along the same PA, but at < 1 kpc scales, which might suggest that they are related to the kiloparsec-scale atomic outflow presented in Perna et al. [2020]. The ionized, large-scale bubble observed in MUSE ($\sim$ 10kpc) and the NW bubble could be, also in this case, the results of different outflow episodes. These multiple bubbles at different distances are very similar to those predicted by the TNG50 cosmological simulation as a result of AGN feedback [Nelson et al., 2019] and to those observed in NGC 1275 [Fabian et al., 2003, Sanders and Fabian, 2007] and in the Teacup [Venturi et al., 2023].

The launching mechanism

The presence of AGN in the Arp 220 nuclei has been investigated in many previous works [Teng et al., 2015, Paggi et al., 2017, Yoast-Hull and Murray, 2019, Perna et al., 2024], but conclusive evidence confirming their existence remains elusive. Furthermore, understanding whether outflows are powered by AGN or starburst presents an even greater challenge; in this section we relate the energetics of the Arp 220 multiphase outflows to the properties of AGN (if present) and SF, and we discuss possible scenarios.

To evaluate the effect of the outflows on the SF activity, we can compare their energetics with the SFR. However, the SFR varies depending on the band in which it is calculated, spanning values from 150 $M_\odot$ yr^{-1} in the radio band [Varenius et al., 2016] to 0.5 $M_\odot$ yr^{-1} through Paα [Perna et al., 2024] in the W nucleus, and from 80 to 0.17 $M_\odot$ yr^{-1} in the E nucleus. Since the SFR measurements obtained from optical and near-IR features may be significantly affected by dust attenuation, leading to underestimation, we focus on the case where the SFR is calculated using the radio band.

Summing all the contributions of the outflows in the ionized and molecular phases in each nucleus, we derive a mass loading factor η of ~ 0.13 and 0.15 and a $\dot{E}_{out}$ of 1.1×10^{42} erg s^{-1} and 9×10^{41} erg s^{-1} for the W and E nuclei, respectively. We note that these values are only marginally affected by the densities used, since the main contribution comes from the cold molecular gas. These values are similar to those measured in other local ULIRGs (Arribas et al., 2014, Chisholm et al., 2017, Lamperti et al., 2022) and high-z star-forming galaxies [Genzel et al., 2014, Heckman et al., 2015, Newman et al., 2012, Perna et al., 2017, 2018]. Moreover, they are in agreement with models where feedback from supernovae is the main outflow driver [Finlator and Davé, 2008, Heckman et al., 2015].

Following Veilleux et al. [2005], we can derive the expected energy outflow rate by assuming proportionality with SFR (measured from radio band) and assuming solar metallicity. We derive $\dot{E}_{SFR} = 1 \times 10^{44}$ erg s^{-1} for the W nucleus and 6×10^{43} erg s^{-1}for the E nucleus. Comparing these values expected for stellar activities with those obtained in previous paragraph, we find $\dot{E}_{out}/\dot{E}_{SFR}$ of the order of a few percent, in agreement with a starburst-driven outflow expectations.

Paggi et al. [2017] estimated AGN luminosities in the $2 - 10$ keV X-ray band of 0.5×10^{42} erg s^{-1} and 1.6×10^{42} erg s^{-1} for the W and E nuclei that lead to AGN bolometric luminosities of 2.5×10^{43} erg s^{-1} and 8.3×10^{43} erg s^{-1}, respectively. We also estimated the AGN luminosity from the total IR luminosity, assuming an AGN

[2]Measured anti-clockwise from the north.

contribution of 6% to L_{bol} [Perna et al., 2021] and using the relative contribution of each nucleus measured in the ALMA continuum maps by Pereira-Santaella et al. [2021]: $L_{bol} = 2.5 \times 10^{44}$ erg s^{-1} (W) and 1.1×10^{44} erg s^{-1} (E). It is worth noting that the AGN bolometric luminosity of the W nucleus inferred from FIR measurements is approximately 1 dex higher than the X-ray-based estimate, highlighting the challenges in constraining AGN activity in Arp 220. The outflow energetics computed in this section result in kinetic coupling efficiency values $\dot{E}_{out}/L_{AGN} = 0.005 - 0.05$ for the W nucleus, and $\dot{E}_{out}/L_{AGN} = 0.009 - 0.01$ for the W nucleus. These values are consistent with both theoretical predictions of kinetic coupling efficiencies in energy-conserving ($\sim$ 0.005–0.05, e.g., Hopkins and Quataert 2010, Zubovas and King 2012, Costa et al. 2014, King and Pounds 2015b) and radiation pressure-driven outflows ($\sim$0.001–0.01, e.g., Costa et al. 2018, Ishibashi et al. 2018).

These results show that there are no arguments at present to prefer SF- to AGN-driven outflows, since both of the scenario are possible. We note, however, that the typical dynamical timescales $t_{dyn} = R_{out}/v_{out}$ associated with the outflows in Arp 220 are approximately 1 Myr (see Table 4.3). In contrast, the SFR $\approx$ 100 M$_\odot$ yr^{-1} used to compare outflow energetics with expectations for starburst-driven outflows reflects the SF history over a much longer period (up to 100 Myr; Kennicutt and Evans 2012). Following on these arguments, we consider two scenarios. In the former, we assume that the SFR in the past few million years is $<<$ 100 M$_\odot$ yr^{-1}. This would be consistent with the SFR measured in the host from UV, optical and near-IR observations [Chandar et al., 2023, Perna et al., 2020, Perna et al., 2024, Giménez-Arteaga et al., 2022], as well as with the emission from supernovae and supernovae remnants at wavelengths from 2 to 18 cm which can be responsible for up to 20% of the total radio emission at GHz frequencies (but see the detailed discussion in Varenius et al. 2019). In this framework, the mass loading factors and outflow energetics would imply the presence of AGN winds, as SF would not provide enough energy to explain the outflow properties ($\eta > 40$, $\dot{E}_{out}/\dot{E}_{SFR} > 3$). In the second scenario, we assume the presence of extremely high attenuation at the position of the two nuclei, of $A_V > 100$: such attenuation is required to match the SFR(PAH 3.3 μm) $\sim$ 1 M$_\odot$ yr^{-1}with measurements from FIR and GHz frequencies. With this assumption, both starburst- and AGN-driven winds can be responsible for the observed outflows, according to the outflow energetics computed in this work.

In conclusion, further investigations are required to constrain the current SFR and the AGN activity in the nuclear regions of Arp 220. This information is essential for understanding the mechanisms driving the multiphase and multiscale outflows observed in this galaxy.

4.1.7 Conclusion

In conclusion, we analyzed the nuclear region of the merging ULIRG Arp 220 using JWST/NIRSpec integral field spectroscopy, unveiling its multiphase outflow structure on sub-kiloparsec scales. By mapping the ionized (Paα) and hot molecular (H_2 2.12 µm) gas, we identified high-velocity outflows emerging from both nuclei. Through detailed kinematic modeling with MOKA^{3D}, we constrained their geometry and orientation. The W nucleus drives an hourglass-shaped multiphase outflow inclined by $\sim$60° and extending up to 600 pc, along with a compact ionized component reaching 550 km s^{-1}. The E nucleus launches a conical outflow directed southwestward, reaching 600

km s^{-1}, and a larger blueshifted bubble extending to ∼1 kpc with velocities up to 1100 km s^{-1}, aligned with the kiloparsec-scale structure previously observed in MUSE data. Combining JWST and ALMA data, we derived a hot-to-cold molecular gas ratio of $\sim 10^{-4}$ and found that the cold molecular phase dominates the outflow mass budget ($\dot{M} \sim 20$ $M_\odot$ yr^{-1}), followed by the ionized and hot molecular components. The inferred energetics and mass-loading factors (~ 0.1) are compatible with both intense star formation and moderate AGN activity, suggesting that both could be responsible for powering the outflows. These observations establish a physical connection between compact ($\lesssim$ 100 pc) outflows and extended (>1 kpc) ionized structures, revealing that each nucleus contributes independently to the global feedback process. Moreover, the complex, multidirectional morphology seen in this merging system contrasts with the collimated outflows typically seen in isolated systems, suggesting that the chaotic dynamics of the merger can disturb the ISM on large scales, potentially leading to a more widespread and uniform suppression of star formation across the galaxy.

4.2 Mrk231

Mrk 231 stands out as the nearest ULIRG hosting a luminous quasar. With a bolometric infrared luminosity of $\log[L_{\rm IR}/L_\odot] = 12.37$ and a star formation rate of $\sim$ 170 $M_\odot$ yr^{-1} [e.g., Rupke and Veilleux, 2011], Mrk 231 exhibits both an active nucleus and a young, dusty starburst. Its redshift, $z = 0.0422$, corresponds to a distance of 178 Mpc (1 arcsec = 0.863 kpc). The galaxy is undergoing a dynamic, multi-phase, and multi-scale outflow process, capable of transforming the host from a gas-rich merger remnant into a quiescent, spheroidal "red and dead" system [e.g., Rupke and Veilleux, 2011, Feruglio et al., 2015, Fischer et al., 2010, Cicone et al., 2014].

Mrk 231 is classified as a FeLoBAL quasar, showing broad absorption lines from low-ionization species such as Fe II. Recent work by Leighly et al. [2025] has highlighted similarities between FeLoBALs and the newly identified "Little Red Dots" (LRDs), which display heavily reddened optical continua, strong UV emission, X-ray weakness, and, in some cases, broad Balmer absorption. Like LRDs, Mrk 231 exhibits a peculiar spectral energy distribution (SED) with enhanced FUV emission and a reddened optical band, making it a potential local analog of distant obscured quasars, albeit with higher metallicity.

Although Mrk 231 is formally considered radio-quiet ($\log P_{1.4\ \rm GHz} = 24.15$ W Hz^{-1}), it exhibits features typical of radio-loud sources, such as blazar-like flares with flux densities of several mJy at ∼20 GHz [e.g., Reynolds et al., 2013]. Jets can play a key role in triggering outflows, and indeed, Mrk 231 exhibits multi-phase outflows detected across ionized, neutral, and molecular gas [e.g., Feruglio et al., 2015, Aalto et al., 2015, Morganti et al., 2016].

Mrk 231 also displays a weak and heavily absorbed X-ray spectrum with a 2–10 keV luminosity of 4×10^{42} erg s^{-1} [Feruglio et al., 2015]. The nucleus is likely Compton-thick ($N_{\rm H} \gtrsim 10^{24}$ cm^{-2}), exhibiting a flat, reflection-dominated continuum and a faint Fe Kα emission line. The far-ultraviolet (FUV) spectrum, presented by Veilleux et al. [2013a, 2016], reveals a remarkable absence of absorption lines, in stark contrast to the numerous absorption features seen in the near-ultraviolet (NUV) spectrum.

Mrk 231 exhibits very weak or absent high-ionization emission lines across multiple wavelength regimes. In the optical, lines such as He II λ4686 and [O III] λ5007 are extremely faint or undetected [e.g., Rupke et al., 2002]. Similarly, the near-

infrared spectrum shows little to no high-ionization emission, such as [Si VI] 1.96 μm [Leighly et al., 2014], and the mid-infrared spectrum lacks strong [O IV] 25.89 μm, [Ne V] 14.32, 24.32 μm, and [Ne VI] 7.65 μm lines [Armus et al., 2007].

Moreover, recent polarimetric studies (e.g., Biedermann et al. [2025]) support the hypothesis that Mrk 231 may host a binary SMBH system, originally proposed by Yan et al. [2015] and argued further by Veilleux et al. [2016], Leighly et al. [2016].

In this section, we will analyze the kinematics of Mrk231 using both NIRSpec and MEGARA data. In the first case, we will study Mrk231 with a resolution of 0.1", corresponding to approximately 90 pc at redshift 0.0422 in a region of 2"x2", i.e., in the inner kpc from the nucleus in the IR band. In the case of MEGARA, we will study the optical band with a resolution of 0.4" but with a wide FOV (12.5" $\times$ 11.3").

We combine optical and infrared spectroscopic data to characterize the full set of hydrogen recombination lines associated with the BLR. We also identify and characterize the outflowing regions, particulary in [OII] line and taking into account their multiphase nature as showed by previous studies in the literature.

Furthermore, by exploiting ancillary multi-band observations, we investigate the peculiar SED of Mrk 231 providing additional support for the binary black hole scenario previously proposed for this source.

4.2.1 Observations

Mrk 231 was observed using the JWST/NIRSpec instrument in IFS mode [Böker et al., 2022], as part of the JWST observing program 1268 (PI: R. Maiolino), on April 1, 2023. These NIRSpec observations were combined in a single proposal with independent MIRI GTO observations of the same target. The target was observed with NIRSpec in all three bands (F100LP/G140H, F170LP/G235H, and F290LP/G395H). Two exposures of 1750.664 s each were obtained in each band: one centered on the nucleus and one centered on the shell, located approximately 4" from the galaxy center (see Fig.4.26). The observations were taken with the NRSIRS2RAPID readout pattern [Rauscher et al., 2017] with 15 groups per integration and one integration per exposure, using a 4-point dither pattern.

We downloaded the fully calibrated data from the MAST archive, reduced with pipeline version 1.15.1 and CRDS context 1293. We note that the F170LP/G235H and F290LP/G395H cubes are saturated at the position of the AGN (within a radius of 3 pixels). Inspection of the count-rate maps confirmed that the nuclear pixels are flagged as SATURATED. To verify whether any usable groups were available, we reran Stage 1 of the reduction using pipeline v1.17.1 and CRDS context 1322, setting steps.ramp_fit.suppress_one_group = False, following the guidance provided in the Tips and Tricks for Working with the JWST Pipeline[3]. Despite this, the nuclear spaxels remain saturated in each dither position, confirming that no unsaturated groups are present from which to estimate a reliable slope for these datasets.

.

The MEGARA data were observed on May 26, 2019, as part of the GTC1-19AGMEG program (PI: Cristina Catalán Torrecilla) and provided already reduced in private communication by the PI.

The *HST*/COS observations of Mrk 231 were obtained with the G140L grating on 2014 December 13 over six orbits (PI: S. Vielleux). The combined COS spectra cover

[3] https://jwst-docs.stsci.edu/jwst-science-calibration-pipeline/

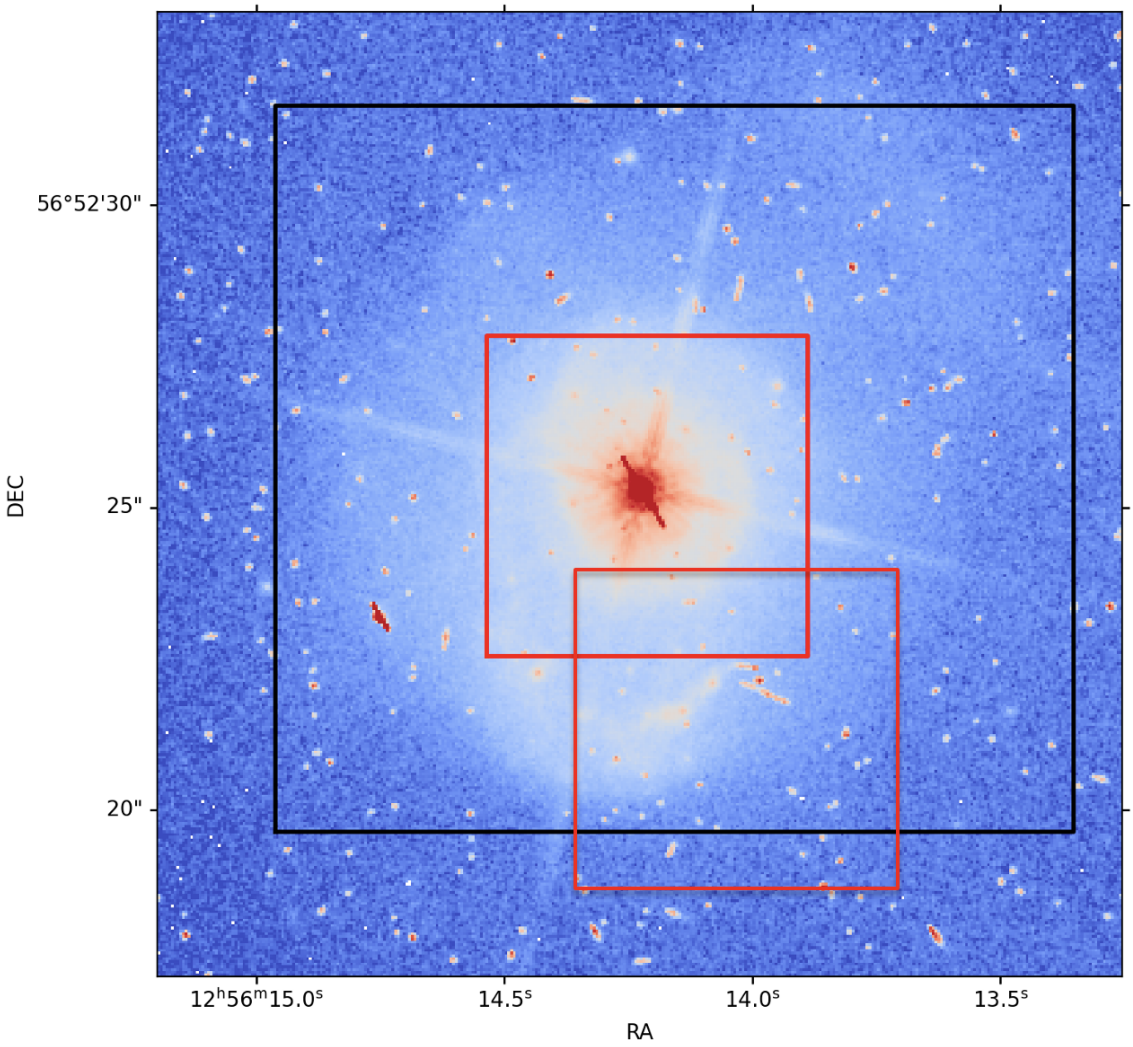

Figure 4.26: HST/F814W image overlaid with the NIRSpec field of view (red contours; $5.2'' \times 5.2''$) and the MEGARA field of view (black; $\sim 12.5'' \times 11.3''$). The two NIRSpec pointings are centered on the nucleus and the shell.

$\sim$ 1100–1900 Å ($\sim$ 1050–1825 Å in the rest frame) at a spectral resolving power of $R = \lambda/\Delta\lambda \sim$ 2000–5000. The STIS spectrum covers the NUV range from 1800 – 3180 Å(1750 – 3050 Åin the rest frame) at a spectral resolving power of R $\sim$ 500. Both the observations were downloaded from MAST portal and are already reduced.

4.2.2 Spectral features of Mrk 231

In this section, we describe the spectroscopic analysis performed to investigate the kinematics and morphology of the nuclear region of Mrk 231. Figure 4.27 shows the integrated spectra of the nuclear region, extracted from a circular aperture with a radius of five spaxels (corresponding to 0.5") after removing the saturated central spaxels

The spectra display numerous hydrogen recombination lines both from the broad line region and from the narrow line region, including Paschen (Pa) and Brackett (Br) transitions, as well as several forbidden [Fe II] lines and ro-vibrational transitions of molecular hydrogen (H_2). The near-infrared spectrum of Mrk 231 has been previously

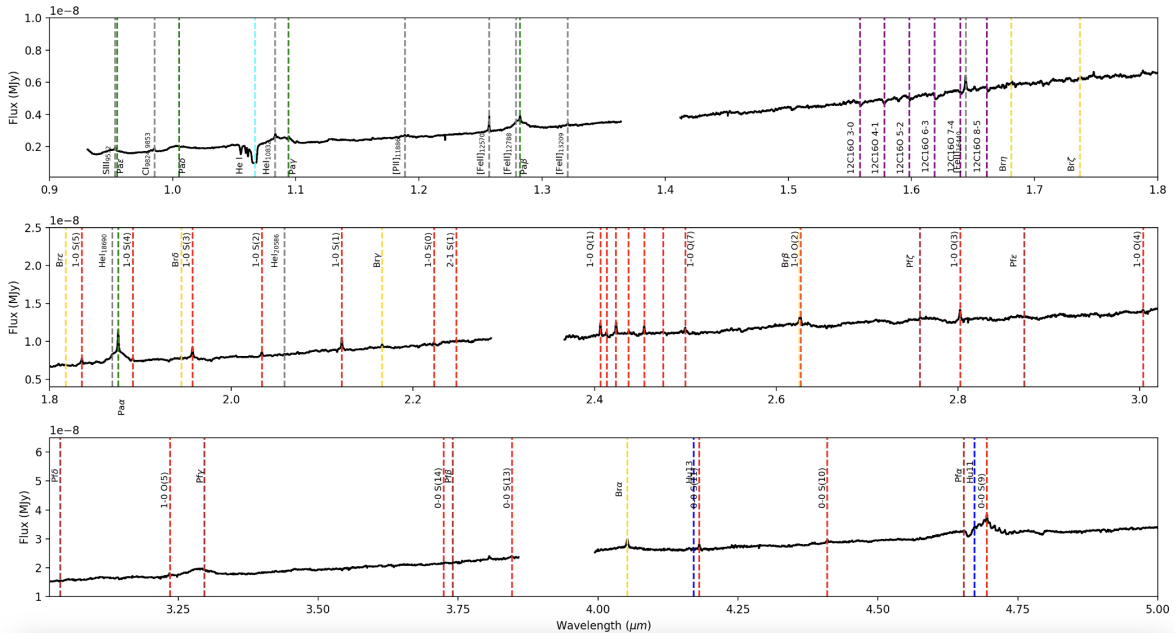

Figure 4.27: Mrk231 nuclear spectra. The spectra are extracted from circular aperture of radius 5 spaxels (corresponding to 0.5"), and reported in units of flux density as a function of rest-frame wavelength. Red dashed vertical lines identify H_2 lines; grey dashed lines identify ionized gas transitions; green, yellow, brown and blue lines identify the Paschen, Brackett, Pfund and Humphreys series, respectively. Purple dashed lines identify the position of the main CO stellar absorption lines.

studied by Leighly et al. [2014] with SpeX [Rayner et al., 2003] on the NASA Infrared Telescope Facility (IRTF) with a resolution of 330 km/s, who reported the broad absorption line (BAL) features of the He I λ10830 transition in absorption.

4.2.3 Fitting spectra in NIRSpec and MEGARA

We carried out similar fitting strategies for NIRSpec and MEGARA data. We first extracted the nuclear spectrum by integrating the data cube within a circular aperture of five pixels radius, centered on the peak of the continuum flux distribution. For NIRSpec data, we first subtracted the wiggle features using the `WICKED` code [e.g., Dumont et al., 2025, Perna et al., 2025]. The stellar continuum was modeled using the XLS spectral template library of Verro et al. [2022], convolved with the appropriate instrumental resolution and combined with a multiplicative Legendre polynomial of degree N to account for broad spectral shape variations and residual calibration uncertainties.

The fit was performed in the entire wavelength range of 9330-18000 Åfor the first band of NIRSpec, excluding the region in the gap and the BAL system in HeI*. We only performed the total fit of NIRSPec data for the first band, the only one that is not saturated. For the other NIRSpec bands, only the local continuum around the line of interest was subtracted. For MEGARA we considered the range 3650-6000 Å, excluding also in this case the region affected by the BAL.

The fit included the broad emission components of the recombination lines in each spectral coverage: Hδ, Hϵ, Hγ and Hβ Balmer lines, along with the narrow emission features of [OII] doublet, Hβ, and Hγ in MEGARA. While we fit Paδ, Paγ, Paδ, Brη in the first band of NIRSpec. A maximum velocity dispersion of 1500 km s^{-1} was imposed

for the narrow-line components, in order to distinguish them clearly from the broader emission associated with the BLR.

For both bands, we considered the emission of FeII. For the optical band, the broad Fe II emission was modeled using the semi-empirical templates of Kovacevic et al. [2010], which consist of 65 individual Fe II transitions in the wavelength range 4000–5500 Å. These lines are grouped into five distinct sets, four based on theoretical predictions and one derived from the observed spectrum of I Zw 1. In our fitting procedure, the relative intensities within each group were allowed to vary freely, while all lines shared the same velocity shift and velocity dispersion. We also add a line of the FeII at 5538Å. In the NIR, we did not use the empirical templates, instead we added the emission from the most relevant Fe II transitions, including Fe II λ9997Å, λ10501Å, λ10863Å, and λ11126 and He ii (λ10124Å) blended with Paschenδ.

The first phase of the integrated fit is necessary to build a broad line region model composed of FeII and broad recombination lines. Once we built the model for the BLR, we included it in the full fit spaxel by spaxel using `pPXF`. At this stage, the BLR template is kept fixed in shape, and only its normalization is allowed to vary. We fitted the template of the BLR inside a radius region of 10pxl corresponding to around 4". We first tried to fit the datacube without using any additive or multiplicative polynomials in pPXF, but this didn't allow us to properly reproduce the spectra in all spaxels. As a result, we couldn't reliably constrain the stellar continuum. After testing, we found that including three additive and one multiplicative Legendre polynomial produce a reliable fit.

We then subtracted the contribution from the stellar continuum and the unresolved BLR, including both the Fe II emission and the broad emission lines. The resulting datacube contains only the emission lines and was smoothed using a 1-pixel Gaussian kernel to enhance the signal-to-noise ratio. However, to study the recombination line transitions from the BLR, we also created a cube by subtracting only the stellar continuum.

4.2.4 BLR

To study the BLR in better detail, we used the cube with the stellar continuum subtracted and we integrated the signal over the five central spaxels. This approach was chosen because in the `pPXF` fit, the BLR was modeled using a single kinematic component, forcing all recombination lines to share the same first and second moments. However, this assumption is not appropriate for a stratified BLR, where different recombination lines may originate at different radii and therefore exhibit distinct kinematic properties. Furthermore, the χ^2 computed by `pPXF` is evaluated over the entire spectrum, as the fitting procedure simultaneously accounts for all spectral components (continuum, NLR, BLR). This approach is appropriate when the goal is to model BLR recombination lines for subtraction purposes, in order to study the spatially resolved gas. However, it is not optimal when the goal is to model the BLR with a physical model, since each transition should ideally be treated independently to properly model their specific line profile. The least contaminated line is Paschen β, which displays a nearly perfect Lorentzian profile. The same is true for Paschen α; however, this line falls within a saturated spectral channel but a reliable fit is shown in Fig 4.29 . Accordingly, we modeled each BLR recombination line and Helium with a Lorentzian profile, while the Fe II, CrII, OI and other blended lines emission was fitted using Gaussian pro-

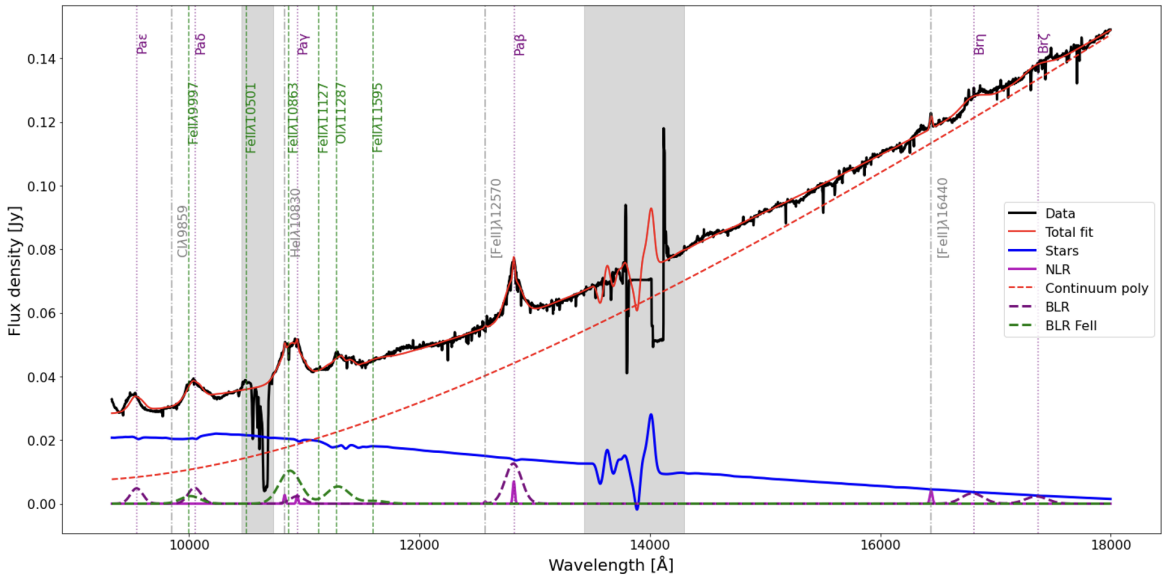

Figure 4.28: Mrk231 nuclear spectra. The spectra are extracted from circular aperture of radius 5 spaxels (corresponding to 0.5"), and reported in units of Jansky as a function of rest-frame wavelength. The black line shows the observed flux, while the red line indicates the total best-fit model. The blue line represents the stellar contribution, and the dashed red line the polynomial continuum. Dashed purple lines indicate the recombination BLR emission (Paschen and Brackett series), whereas dashed green lines mark the permitted FeII transitions from the BLR. Grey shaded regions are the masked region during the fit.

files. Table 4.4 presents the measured fluxes of the emission lines fitted in the spectrum and displayed in Fig. 4.29. A detailed analysis of BLR models is beyond the scope of this chapter. However, the fluxes of the recombination lines deviate significantly from the simple case B recombination scenario. Using a basic `CLOUDY` BLR grid models, we find that the observed BLR properties are consistent with a model characterized by a density of 10^9 cm^{-3}, an ionization parameter of $U \sim 10^{-3}$, and an extinction of $A_V \sim 3$ mag.

4.2.5 NLR

Once the continuum was subtracted, we performed independent, pixel-by-pixel spectral fits for each emission line using the `SpecUtils` package from the `Astropy` library [Astropy Collaboration et al., 2013]. For the recombination lines, we adopted two kinematic components: a Lorentzian profile to model the broad-line region and a Gaussian profile to fit the narrow emission. Given the high luminosity of the central source, the wings of the PSF extend over most of the NIRSpec field of view, potentially requiring the inclusion of both components even at large distances from the nucleus. In these regions, the Bayesian Information Criterion (BIC) was used to determine the appropriate number of components to be fitted in each spaxel, allowing the BLR component to be discarded at larger radii when not required.

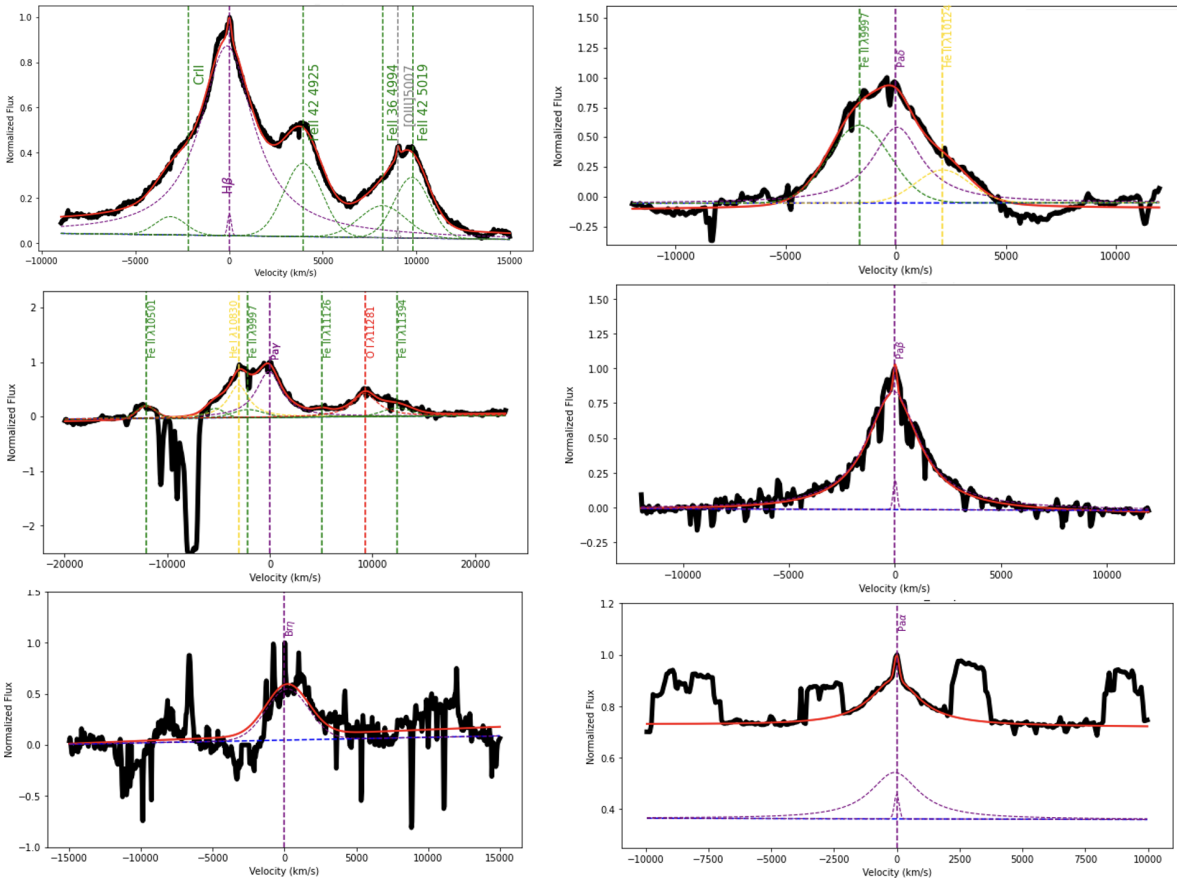

Figure 4.29: BLR recombination lines in Mrk 231. Hβ (upper left), Paschen δ (upper right), Paschen γ (middle left), Paschen β (middle right), Br η (bottom left), and Paschen α (bottom right). The black curves show the observed spectra, while the red curves represent the total model. The purple components correspond to the hydrogen recombination lines, the gold components to He I emission, the green dashed curves to permitted Fe II transitions, and the red dashed curve to O I emission. Vertical lines indicate the rest-frame wavelengths of the transitions. Fluxes and velocity measurements are reported in Table 4.4.

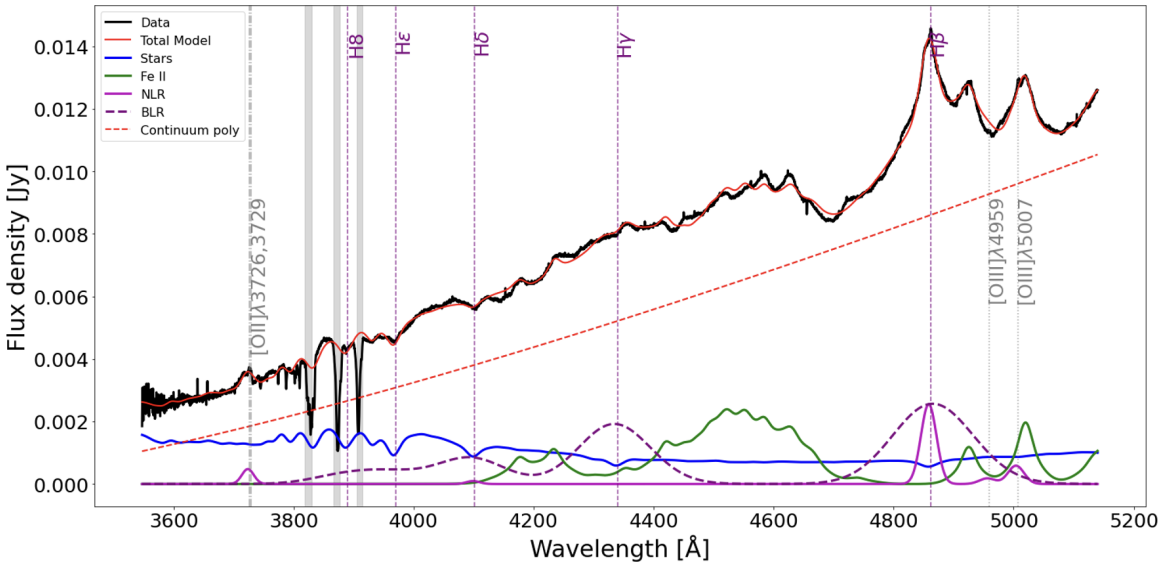

Figure 4.30: MEGARA spectra of Mrk 231 extracted with apertures of 5 pixels. The observed data are shown in black, the best-fit total model in red, the stellar continuum in blue, the Fe II emission from the BLR in green, the BLR component in dashed purple, and the narrow emission lines in purple. Purple vertical dashed lines represent the recombination lines while grey vertical line represent the [OII] doublet.

The inner 5 kpc of Mrk 231

In the nuclear region, at the AGN position, the line profiles of Hβ are dominated by a single, very broad component and no distinct narrow emission is detected. In contrast, about 1" (860 pc) east of the nucleus and outside from the central region, the separation between the broad and narrow emission line components is clear due to a more pronounced narrow line peak.

The *JWST*/NIRSpec data, which provide higher spatial resolution, reveal that the enhancement of the flux of the narrow component identified in the MEGARA spectra originates from a compact, bright clump located east of the nucleus, identified also in MIRI (Alonso Herrero et al. [2024]). As shown in Fig.4.31 the narrow component of the recombination lines (Hβ in MEGARA and Paα in NIRSpec) follows a rotation pattern with a maximum velocity of approximately 70 km/s.

In addition to the bright clump located east of the nucleus, a second, fainter, and more elongated clump is detected to the north. This clump exhibits a blueshifted velocity of approximately -50 to -100 km s^{-1} and deviates from the rotational pattern of the disk, suggesting that it may trace a tidal structure spiraling around the nucleus that may be identified as the T2 and T3 identified with the acquisition image of LBT in Misquitta et al. [2024].

On larger scales, 4" (3.5kpc), the MEGARA velocity maps show that the shell exhibits velocities close to the systemic value of the galaxy with velocity dispersion of about 70km/s.

High-velocity clumps

The MEGARA data revealed two additional bright [O III] clumps located at projected distances of 2.6 kpc and 5 kpc from the nucleus, with radial velocities of -420 km s^{-1}

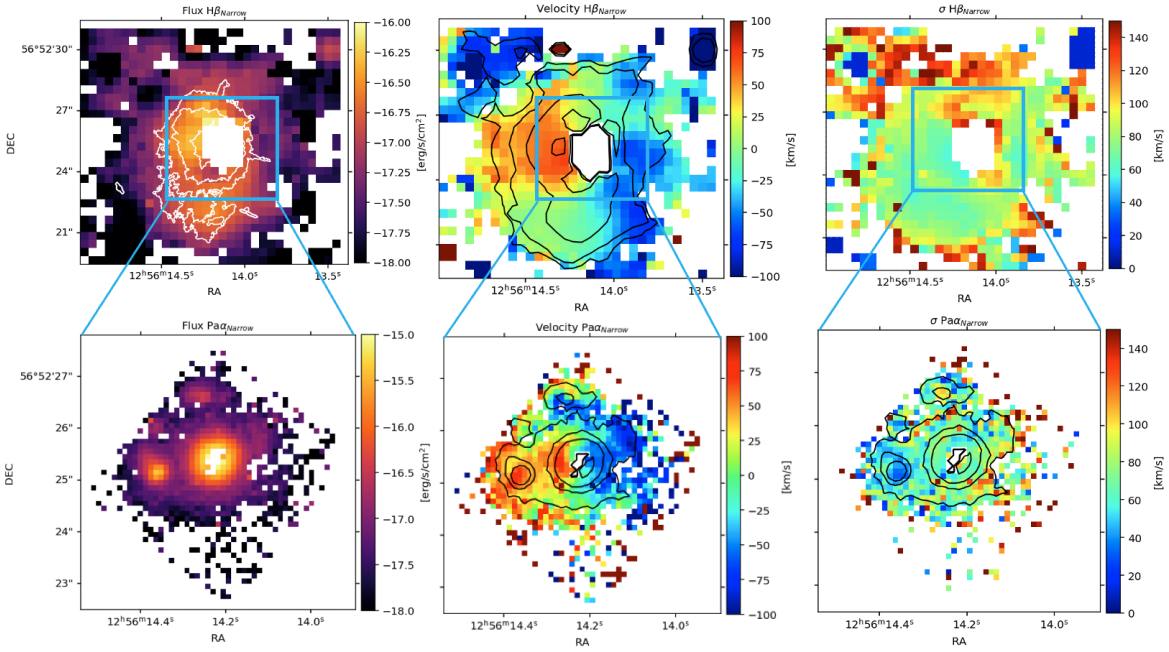

Figure 4.31: Kinematics of narrow component of Hβ from MEGARA and Paα from NIRSpec. White contours represent arbitrary HST flux thresholds while black contours represent the flux of the considered line shown in the left panel.

(clump A) and $-900\,\mathrm{km\,s^{-1}}$ (clump B), respectively. As these clumps are kinematically decoupled from the surrounding components, their contributions could be isolated. Although the NIRSpec cube centered on the shell apparently did not show any prominent structures apart from detector artifacts, we were able to identify these two faint clumps in the Paα and Paβ emission. This detection enabled us to investigate the physical properties of these high-velocity clumps, in particular their ionization and the extinction. To do this, it was necessary to account for the different spatial resolutions of the two instruments. Therefore, we extracted the spectra from circular apertures centered on each clump, with radii corresponding to 2.5 FWHM of the respective PSF. Figure 4.32 shows the *HST* image of Mrk 231 with the FOVs of the two NIRSpec observations, centered on the nucleus and on the shell. The cyan and blue contours mark the positions of clumps A and B, respectively. Both clumps A and B are located near the star formation shell, respectively to the northwest and southwest of the shell. Figure 4.32 also shows the extracted spectra of [OIII], Paβ, and Paα from the two clumps. In addition to the high-velocity component of the clump, a systemic velocity component with higher velocity dispersion is also observed, especially in [OIII]. To minimize aperture-related uncertainties, we estimated the extinction from the Paschen recombination lines, adopting an intrinsic Paα/Paβ ratio of 2.07 and using the extinction law implemented in the `qsogen` package from Temple et al. [2021]. Despite the relatively large flux uncertainties caused by the low signal-to-noise ratio of the lines, clump A shows an extinction of $A_V \sim 2$ mag, while clump B exhibits an extinction consistent with zero. We also extracted a spectrum from a 6-spaxel aperture located between clumps A and B, inside the shell observed in MEGARA and HST. Increasing the aperture helps to mitigate instrumental effects related to PSF sampling and allows us to isolate the emission line to estimate the extinction within the shell. As for the clumps, we used the Paα/Paβ ratio to measure the extinction. We found $A_V \simeq 4$ mag,

higher than the one found in the two clumps.

The nature of the two high-velocity clumps is intriguing. We note that the clump farther from the nucleus shows a higher velocity and a higher [OIII]/Hβ and a lower extinction. This trend may suggest three different scenario: a geometric effect, in which both clumps are outflowing clouds photoionized by the central AGN: the faster clump could lie closer to the edge of the ionization cone, while the slower one is located nearer the cone axis, where the extinction is higher. Another scenario may be an accelerating outflow, as predicted by theoretical models [e.g. King, 2005, Zubovas and King, 2012, Marconcini et al., 2025], where the wind progressively removes dust and clears the ISM, thus encountering less resistance at larger distances. A third interpretation is that these clumps correspond to gas within tidal tails. While the relatively low velocity dispersion measure in the clumps might favor this latter scenario, the very high LOS velocity of the outer clump ($v \approx -920$ km,s^{-1}) instead supports an origin related to the AGN-driven outflow.

Outflow

The clearest evidence for an ionised outflow in our dataset is provided by the [O II]$\lambda\lambda 3726, 3729$ doublet in the MEGARA observations. The line exhibits a pronounced blue wing reaching velocities of ~ -1600 km s^{-1}. This outflowing component extends to the south of the nucleus over a projected distance of approximately 1.5 kpc (1.7"). From Fig. 4.33, it can be seen that the blue wing of [O II], integrated between -1500 km s^{-1} and -900 km s^{-1}, overlaps with an enhancement of the blue continuum integrated between 3740–3840 Å. This indicates that the blue continuum emission and the outflow are co-spatial, suggesting that the outflow may trigger new star formation, enhancing the blue emission. An alternative scenario, involves the presence of a binary black hole. This spatial overlap between the blue continuum and the outflow traced by [O II] may also be attributed to the scattering of AGN UV radiation by a dusty outflow. We also show two spectra extracted from two pixels about 1" away from the nucleus, one to the south in the outflowing region (blue curve in Fig.4.33) and one to the north where the blue wing disappears (yellow curve).

Density

Thanks to the high spectral resolution of MEGARA, we were able to compute the density from the [O II] λ3729 to [O II] λ3726 ratio. The allowed [O II] doublet ratio is typically constrained to values below 1.5; however, in many spaxels, the fit reached the physical limits of this range. The map of the [O II] ratio is shown in Fig. 4.34. We found that in the shell region, the derived electron density is below 200 cm^{-3}, while the central region shows an increase in density. Another interesting feature is the density enhancement associated with blue-shifted (-500 km s^{-1}), highly ionized emission traced by the [OIII]. We interpret this as a possible outflow compressing the surrounding gas.

4.2.6 Stellar kinematics

The resulting stellar velocity (v$_*$) and velocity dispersion (σ_*) maps are shown in Fig. 4.35. As observed in the molecular gas [Feruglio et al., 2015], the stellar component displays a rotating disk extending out to $\sim$ 1" ($\sim$ 900 pc), reaching rotational

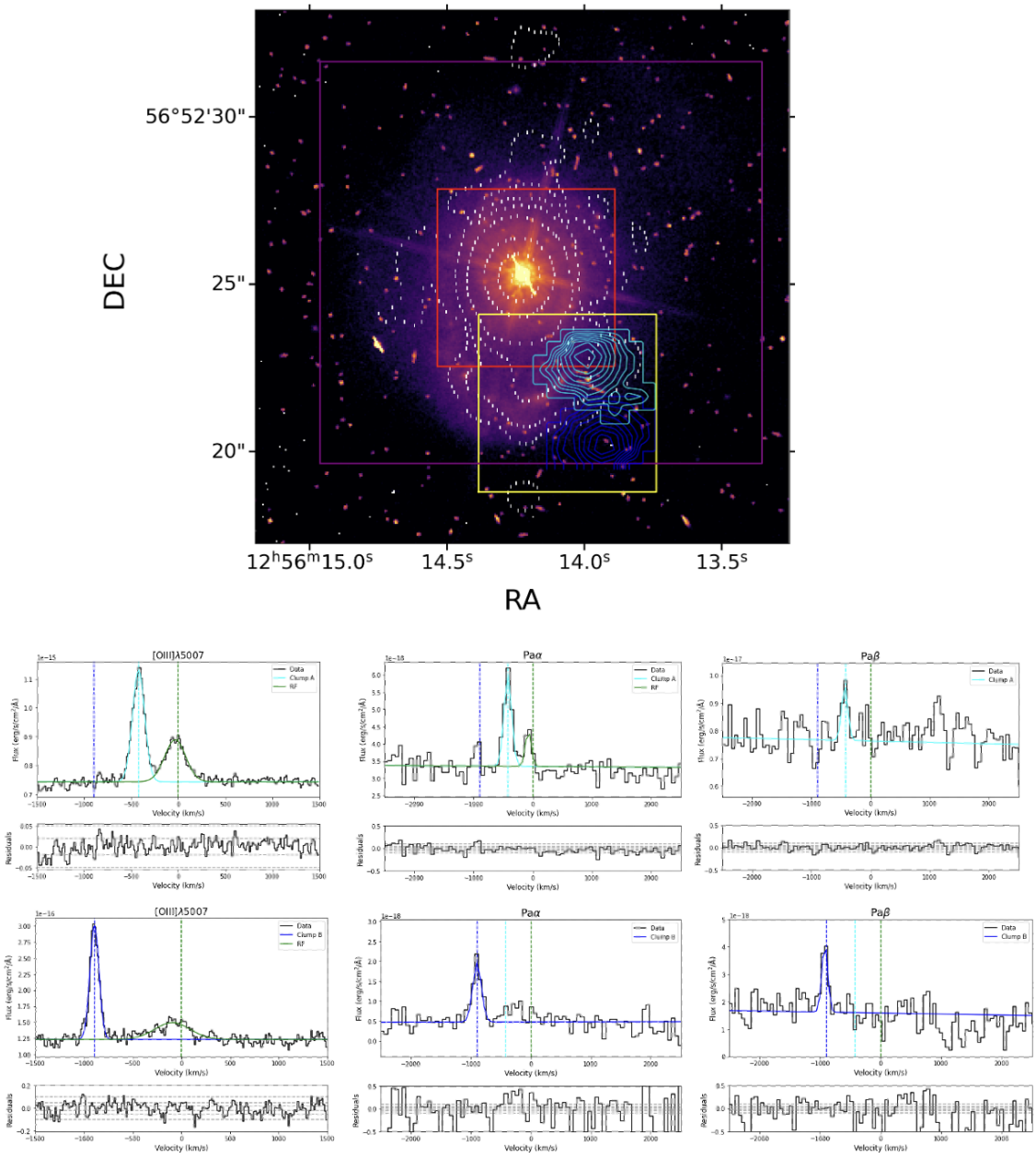

Figure 4.32: HST image of Mrk231. White contours represents the radio band in Silpa et al. [2021], red and yellow squares represent the Nirspec FOV while purple square represent MEGARA FOV. Cyan and blue contours represent the high velocity clumps, clump A and B, respectively. Bottom panel: [OIII], Paschen α, Paschen β of clump A (top) and clump B (bottom). The rest frame corresponds to a redshift of z = 0.0422.

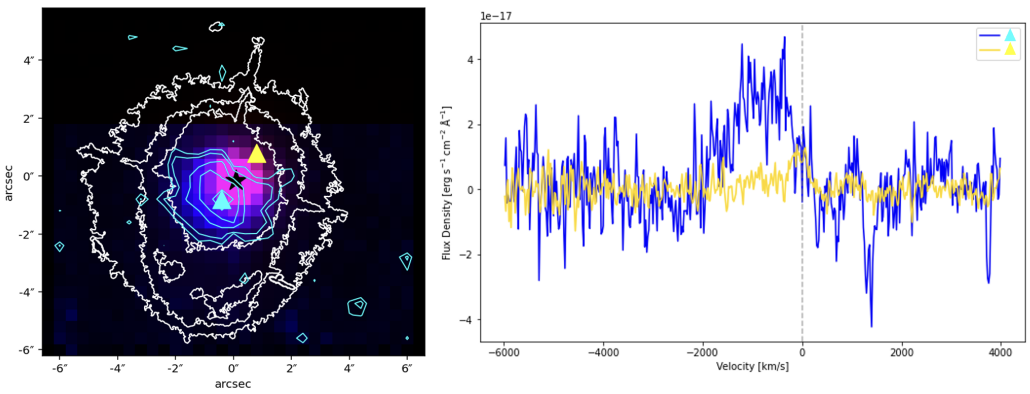

Figure 4.33: Two-color image of the continuum integrated between 3740–3840 Å (blue) and 5095–5105 Å (red). White contours show the HST continuum, while cyan contours trace the [O II] outflow integrated between −1500 and −900 km s^{-1}. The black star marks the Hβ nucleus, and the cyan and yellow triangles indicate the pixels from which the spectra on the right panel were extracted. The blue wing of the [O II] line is stronger to the south in correspondence with the blue continuum, gradually decreasing toward the north.

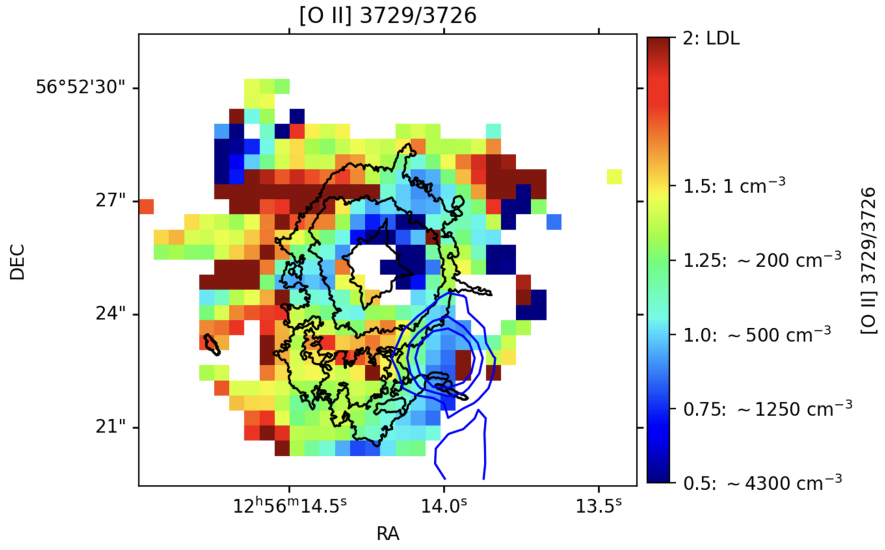

Figure 4.34: [O II] doublet ratio. Black contours shows the HST images, while blue contours represent the [OIII] blueshifted emission from the clump A.

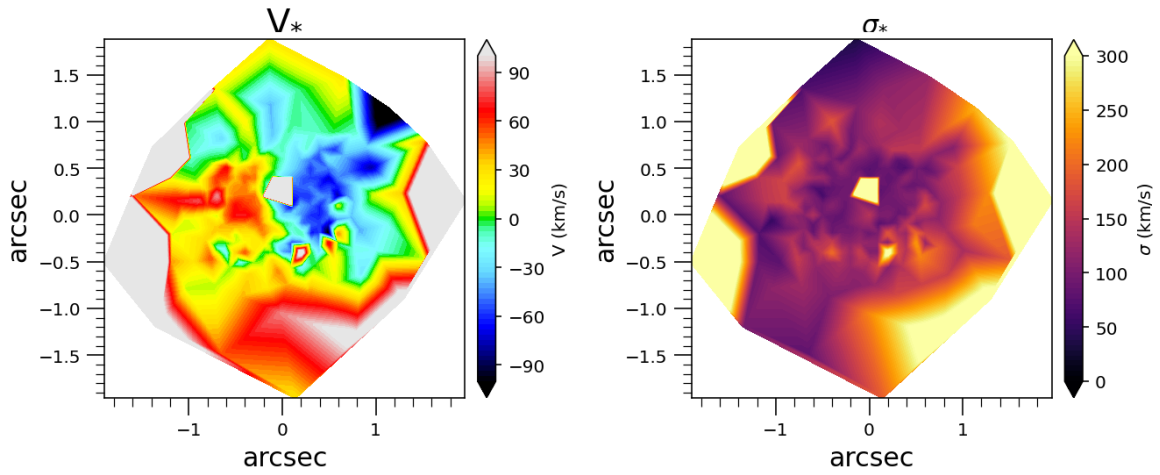

Figure 4.35: Stellar kinematics calculated from the CO absorption lines between 1.5 and 1.8 μm

velocities up to ~ 60 km s^{-1}. The central ~ 0.2" could not be measured due to masked saturated spaxels. Overall, the stellar kinematics closely follow those of the narrow molecular gas component tracing the nuclear disk.

4.2.7 Outflows properties and energetics

Following Carniani et al. [2015], we derive the mass of the ionised outflow using the luminosity of the [O II]$\lambda\lambda$3726, 3729 doublet. The ionised-gas mass is

$$M_{[\mathrm{O\,II}]} = 3.4 \times 10^3 \, m_p \, C \, \frac{L_{[\mathrm{O\,II}]}}{(10^{[\mathrm{O/H}]-[\mathrm{O/H}]_\odot}) \, j_{[\mathrm{O\,II}]} \, \langle n_e \rangle}, \tag{4.6}$$

where $L_{[\mathrm{O\,II}]}$ is the luminosity of the [O II] $\lambda\lambda$3727, 3729 doublet, m_p is the proton mass, C is the condensation factor, and we adopt a total emissivity of the [OII] doublet

$$j_{[\mathrm{O\,II}]} = 2.89 \times 10^{-21} \ \mathrm{erg\,s^{-1}\,cm^3}.$$

and we have assumed n(O1+) = 1/2 n(O).

$$M_{[\mathrm{OII}]} \simeq 1.88 \times 10^8 \ C \ \left(\frac{L_{[\mathrm{OII}]}}{10^{44} \ \mathrm{erg\ s^{-1}}}\right) \left(\frac{500}{\langle n_e \rangle}\right) 10^{-[O/H]+[O/H]_\odot} \ M_\odot.$$

The luminosity is computed from the outflowing component of the doublet as $L_{[\mathrm{OII}]} = 4\pi D_L^2 F^{\mathrm{out}}_{[\mathrm{OII}]}$. The mass outflow rate is estimated with the thin-shell approximation:

$$\dot{M}_{\mathrm{out}} = \frac{M^{\mathrm{out}}_{[\mathrm{OII}]} \ v_{\mathrm{out}}}{R_{\mathrm{out}}}.$$

To derive the outflow velocity, we first computed the flux-weighted mean velocity and velocity dispersion of the broad component in the spaxels where the outflow is detected,

$$v_{\mathrm{broad,mean}} = \frac{\sum_i v_{\mathrm{broad},i} \, F_i}{\sum_i F_i}, \qquad \sigma_{\mathrm{broad,mean}} = \frac{\sum_i \sigma_{\mathrm{broad},i} \, F_i}{\sum_i F_i},$$

where F_i is the line flux in each spaxel. We defined the outflow velocity as

$$v_{\rm out} = |v_{\rm broad,mean}| + 2\,\sigma_{\rm broad,mean},$$

.

We obtained a characteristic outflow velocity of $v_{\rm out} \simeq 2070$ km s^{-1}. Using the total luminosity of the broad [O II] doublet and adopting an electron density of $n_{\rm e} = 1000$ cm^{-3}, the corresponding mass of ionized gas involved in the outflow is $M_{\rm ion} \sim 10^5\,M_\odot$. Assuming an outflow radius of $R \simeq 1.4$ kpc, corresponding to the maximum distance at which outflowing emission is detected, we derive a mass outflow rate of $\dot{M}_{\rm out} \approx 0.15\ M_\odot\,{\rm yr}^{-1}$.

This value is significantly lower than the SFR measured in the nuclear region (23–40 M$_\odot$ yr^{-1}; Alonso Herrero et al. [2024], ~ 170 M$_\odot$ yr^{-1};Rupke and Veilleux [2011]). This suggests that the ionized-phase outflow is not strong enough to substantially suppress ongoing star formation.

The multiphase nature of outflows

Several studies have highlighted the multi-phase nature of the outflow in Mrk 231. Comparing the different gas phases provides a comprehensive view of the outflowing process [e.g., Feruglio et al., 2015, Morganti et al., 2016, Rupke and Veilleux, 2013b]. In particular, the molecular outflow, traced by CO and HCN emission [Feruglio et al., 2015, Aalto et al., 2015], dominates the mass outflow rate and is concentrated within the inner few hundred parsecs, close to the nucleus. Similarly, the OH outflow traces scales of ~ 100 pc and contributes moderate mass outflow rates of 70–100 M$_\odot$ yr^{-1}, with some estimates reaching up to ~ 1000 M$_\odot$ yr^{-1} [González-Alfonso et al., 2014].

The neutral phase is traced by Na ID absorption [Rupke and Veilleux, 2013b] and represents the most extended component, spanning several kiloparsecs while still carrying a mass outflow rate of ~ 420 M$_\odot$ yr^{-1}. Neutral atomic gas is also detected via H I 21 cm [Morganti et al., 2016]; in this case, although it traces the same neutral phase as Na ID, it is more compact, extending only up to ~ 200 pc.

The ionized outflow, traced by [O II] emission in this work, is more extended than the molecular and neutral H I 21 cm phase, reaching up to ~ 1.4 kpc, and exhibits higher velocities ($v \sim 2000$ km s^{-1}). Interestingly, the ultra-fast outflows detected in Fe Kα that reach extreme velocities ($\sim 20,000$ km s^{-1}), have a mass outflow rate of 0.3-2$M_\odot$ yr^{-1} comparable to those found for the ionized gas traced by [OII] [Feruglio et al., 2015].

These results confirm that Mrk 231 hosts a stratified, multi-phase outflow, where different gas phases dominate at distinct spatial scales. Moreover, the phase that contributes more to the feedback, as shown in Arp220, is the molecular phase.

4.2.8 The binary BH model

As described in Veilleux et al. [2016], Mrk 231 exhibits a peculiar SED, characterized by a weak UV continuum and an excess of FUV emission. Traditional models invoking standard reddening or obscuration have struggled to reproduce this steep UV drop and overall SED shape (see Fig.4.36). To address this discrepancy, Yan et al. [2015] proposed an alternative explanation involving a milli-parsec scale binary black hole system with minimal reddening effects. In their model, the lower-mass black hole (4.5×

$10^6\,M_\odot$) accretes matter through a thin disk, primarily accounting for the faint UV emission. The more massive component ($1.5 \times 10^8\,M_\odot$), on the other hand, accretes at a low rate and radiates inefficiently via an advection-dominated accretion flow (ADAF). Encompassing both black holes is a circumbinary disk that dominates the optical and IR output of the system. The observed steep decline in the UV spectrum is then naturally explained as the emission deficit arising from the innermost regions of this circumbinary structure. However, as noted by Veilleux et al. [2016] and Leighly et al. [2016], this scenario may have some observational problems. One of this is the stability of the Lyα profile over a period of $\sim$3 yrs ($\sim$3 x torb). Another problem arising from this model is that there are no evident BAL features in the FUV despite a number of broad low-ionization absorption line systems, such as Na I D, Ca II, Mg II, Mg I, and Fe II, have been identified in the optical-to-UV spectrum.

SED

To address these problems, we propose here an alternative binary black hole model. Following a similar approach to that of Yan et al. [2015], we model the SED from the FUV to the NIR using two QSO components. In our framework, an obscured QSO dominates the near-ultraviolet (NUV) to optical and IR emission, while an unobscured QSO component accounts for the FUV. For each component, we adopt the QSO template from Temple et al. [2021], which parametrizes the luminosity at 3500 Å, extinction, and host-galaxy contribution. By combining these two templates, we obtained the best-fitting (Fig.4.36, top panel) parameters reported in Table 4.5. Consistent with the results of Yan et al. [2015] and Biedermann et al. [2025], our analysis demonstrates that the peculiar SED of Mrk 231 can be naturally explained within a binary black hole scenario.

UV lines

When observed with HST/COS, the brightest FUV lines, such as Lyα and CIV, show a double-peaked profile: one component centered at ~ -1400 km, s^{-1} and a second at ~ -4500 km, s^{-1}, the latter being consistent to originate from the BAL as reported by Veilleux et al. [2013b]. It is well known that Lyα is often self-absorbed, especially in BAL systems. It is also known that the CIV line follows the so-called Baldwin effect, showing an anti correlation between its blueshift and equivalent width. In the case of Mrk231, Lyα and CIV show very similar kinematic behavior, which is quite unusual for both the CIV, as it reaches very high velocity, and even more so for Lyα, in which the rest frame and red-shifted component is totally absorbed. Moreover, both Lyα and CIV reach very high velocities (up to -1500 km,s^{-1}) and large velocity dispersions (FWHM $\sim$1300 km,s^{-1}). While typical Lyα nebulae exhibit line widths of about 500–600 km/s, recent studies have reported broader Lyα emission (FWHM $\sim$1000 km,s^{-1}) in the vicinity of BAL quasars [Ginolfi et al., 2018]. However, the velocities observed in Mrk 231 are significantly higher than those usually measured in such systems. From the previous paragraph, we showed that the FUV spectral region is dominated from the secondary, unobscured BH. Moreover, the FUV emission lines show a systemic blueshift with respect to the primary obscured BH, which instead dominates the optical line emission, where in fact all the emission lines show a systemic velocity. Thus, the most promising test of the model lies in the NUV, where lines may have contributions from both nuclei. The only bright line in this wavelength range

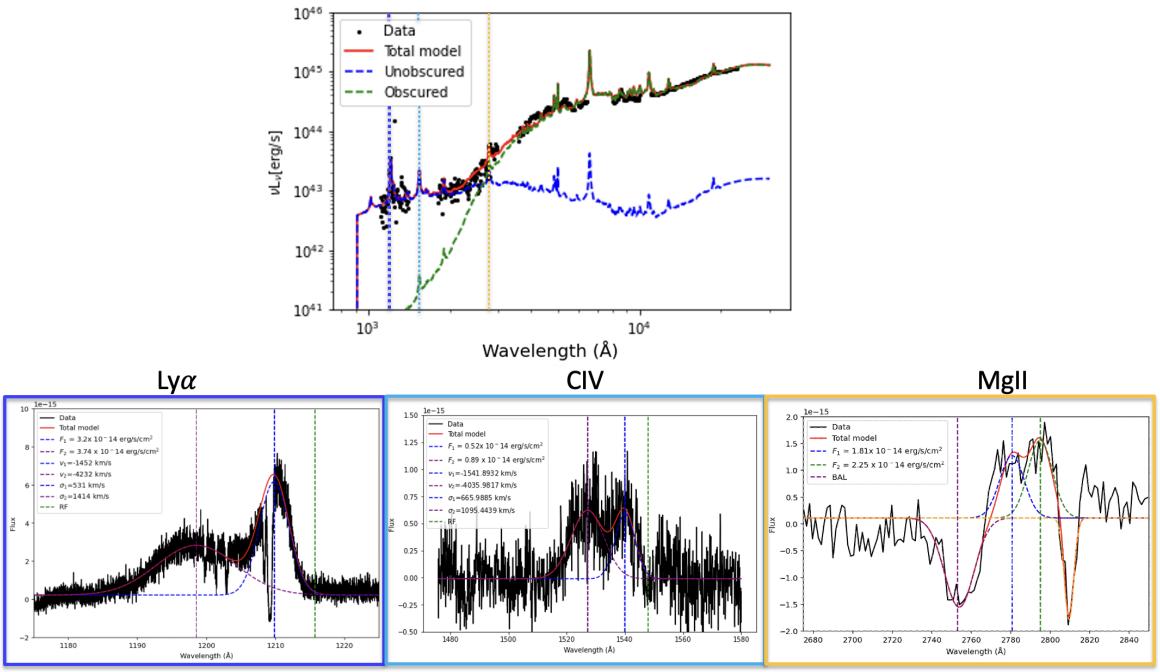

Figure 4.36: Top panel: SED model based on the binary black hole (BBH) scenario. The primary, obscured AGN dominates the optical and infrared emission (green dashed curve), while the secondary, unobscured AGN dominates the UV emission (blue dashed line). Bottom panel: Fits of UV emission lines. The Lyα and C IV lines, located in the spectral region dominated by the secondary AGN, display double-peaked profiles corresponding to the rest-frame velocity of the secondary AGN (~ -1400 km s^{-1}; blue dashed vertical line) and the BAL component (~ -4200 km s^{-1}; purple dashed vertical line). The Mg II line, which arises in a region where both AGN may contribute, shows peaks corresponding to the rest frames of both the secondary and the primary AGN (green dashed vertical line).

is MgII. This spectral region is heavily contaminated by FeII emission and by BAL absorption in MgI and MgII. Moreover, the resolution of STIS is not good enough to verify this scenario. However, after subtraction of a pseudo-continuum and of the absorption features, a broad residual emission remains in the NUV; this excess can be fitted with two kinematic components: one at the systemic velocity of the primary AGN (green curve in Fig.4.36) and one at ~ -1500 km, s^{-1} at velocities consistent with those observed in Lyα and CIV (blue curve). This velocity shift of the line profile in the FUV, NUV and optical regime, consistent with the SED shape, supports our double black hole model.

Radio data

In Ulvestad et al. [1999], high-resolution VLBA observations of Mrk 231 revealed a compact double radio source separated by about 1 pc (see Fig. 4.37, left). These two components are oriented at a position angle significantly misaligned with respect to the larger-scale north–south radio jet at 40 mas scale (30 pc, Fig. 4.37, right)) . Wang et al. [2021] analyzed multi-epoch VLBI data of Mrk 231 and found that this double feature, interpreted as an inner jet, advances at a sub-relativistic speed of about 0.013,c. Over roughly 30 years, the jet's position angle changed from $-113°$ in the inner parsec to

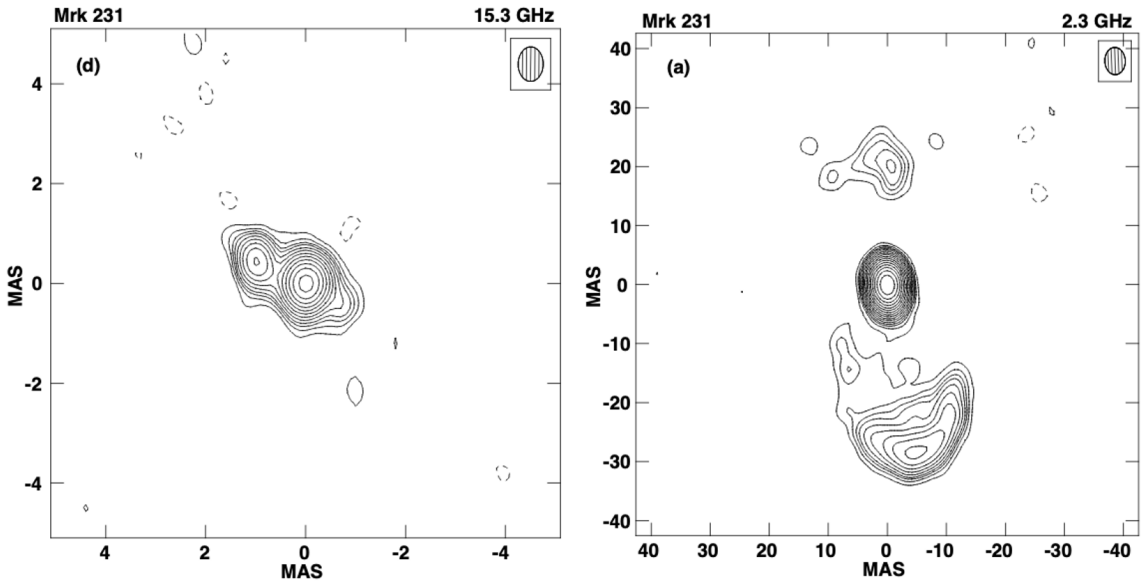

Figure 4.37: VLBA images in 1996 at a frequency of 15.3 GHz (left) and 2.3GHz (right). Image from Ulvestad et al. [1999]

$-118°$ at a projected distance of 1 mas.

Given the observed radio morphology, we considered whether a binary black hole scenario could be consistent with previous consideration. In particular, we explore the possibility that the component observed at -1400 km s^{-1} in Lyα and CIV might correspond to a secondary AGN orbiting the primary at a projected distance of about 1 pc as. In other words, if the double radio sources, previously interpreted as a consequence of jet precession, were instead associated with two distinct AGN, such a configuration could explain both the observed velocity offset in the UV emission lines and the change in position angle measured over the past $\sim$30 years. Assuming a black hole mass of $2.3 \times 10^8, M_\odot$, as calculated by Leighly et al. [2016] from infrared emission lines and from Misquitta et al. [2024], the expected rotational velocity at a distance of $\sim$1 pc from the nucleus is indeed comparable to that observed in the blueshifted component. Moreover, it is possible to trace an orbital configuration for the secondary source that simultaneously reproduces the observed change in PA in the radio morphology (see Fig.4.38) and the observed velocity (assuming the blue-shifted component of Lyα and CIV is coming from the secondary BH). We identified a single model capable of matching both the LOS velocity of $\sim$-1400 km s^{-1} and the observed PA variation. This model requires an orbital inclination of $i = 310°$ (where $i = 0°$ corresponds to a face-on) and position angle of about 150° as shown in the orbit in Fig.4.39. The only limitation to this model is that such a configuration is feasible only if the mass of the primary black hole is $\sim 10^9 M_\odot$. Of course, our model does not take into account possible initial conditions that could alter the orbit of the secondary and potentially reproduce the observed velocities, even for smaller masses of the primary black hole.

Polarization

The polarization properties of Mrk 231 are also quite peculiar [Biedermann et al., 2025]. The degree of polarization increases towards shorter wavelengths, reaching unusually

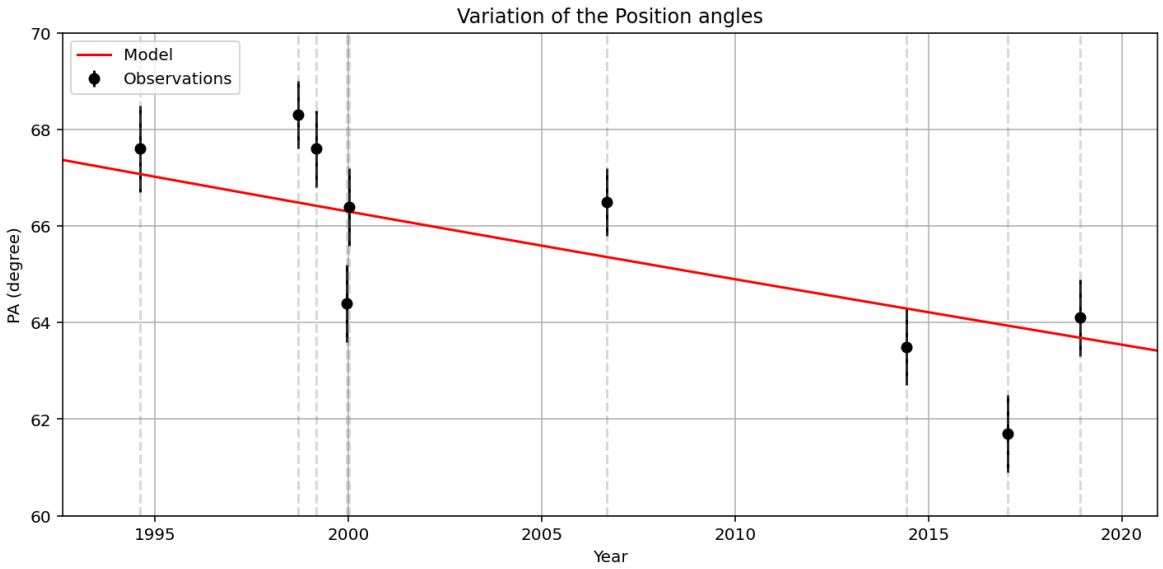

Figure 4.38: Observed position angle (PA) from 1995 to 2018. Black dots represent the PA reported in Wang et al. [2021] while red curve represents the best model of binary black hole that at the same time is able to match the observed PA as a function of time while having an observed velocity of -1400km/s.

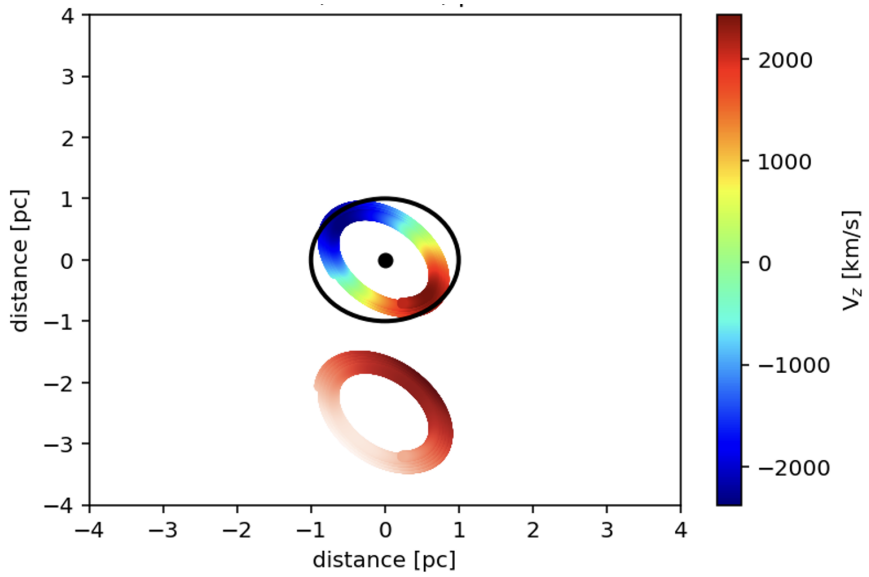

Figure 4.39: Model of the orbit of the secondary BH. The orbit is color-coded with the velocity observed along the LOS. While the other orbit is color coded with the vicinity to the observer. Black circle represents 1pc distance.

high values around 3000Å(∼15%) compared to typical Seyfert 1 galaxies (∼1%), and then drops sharply at wavelengths below 1600 Å. This decreasing trend in the UV can been explained as dilution by emission of obscured and unpolarized stellar light or by a binary SMBH whose far-UV emission would be unobscured and slightly polarized, while the primary component emitting in the optical would be obscured and strongly polarized Biedermann et al. [2025]. This scenario represents exactly what we have described in these paragraphs in fact, the primary AGN starts to dominate at around 3000Å.

Additional observables addressed by the BBH model

The first issue addressed by this model concerns the stability of the Lyα emission. In the previous configuration, the orbital period was of the order of 1.2 years, which would imply appreciable variations in velocity over the course of years, which have not been observed. In the current model, the orbital period would be significantly longer ($\sim 10^4$yr) and therefore no measurable variations in Lyα velocity are expected.

The second observable addressed is the fact that absorption lines are detected only in the near-UV and optical bands, indicating that the BAL region intercepts the LOS of the primary AGN, but not of the far-UV source (secondary AGN). This BBH model naturally explains the observation, in fact, if the secondary source, responsible for the far-UV emission, lies in front of the primary at a projected distance of ∼1 pc, the BAL material can absorb the primary source while leaving the far-UV emission from the secondary unabsorbed.

However, although this model can address some of the problems present in other proposed binary models, there may be some difficulties, such as the high extinction difference even if the two sources are relatively close together. This could actually be addressed if we assume that the hot dust present near the nucleus at 1.6 pc (Lopez-Rodriguez et al. [2016]) is responsible for the UV obscuration of the primary BH. The secondary BH, being in front, is less affected by the dust.

4.2.9 Conclusion

In this section, we used NIRSpec and optical MEGARA IFU observations to constrain the kinematics of both the gas and stars in the inner 5 kpc around the nucleus of Mrk231. The AGN of Mrk231 is surrounded by a starburst disk of about 900 pc that rotates at a maximum velocity of about 60 km/s, a sign that even in the case of Mrk231, as in the case of Arp220, despite the merging features and powerful outflows, the rotating disks is not destroyed. We studied two clumps with high velocity (-400–900 km/s) but low velocity dispersion near the star formation shell observed about 4" from the nucleus. These clumps show an extinction that decreases with distance, while a velocity that increases with distance from the center. The most fascinating scenario that may explain these observations is that the clumps are clouds inside an accelerating outflow that clears out the gas and dust, but also a geometric effect cannot be ruled out. The fairly low FWHMs could favor the scenario that these clumps are located in tidal tails, however, this scenario is disadvantaged by the high systemic velocity of these clouds.

We also studied the nuclear ionized outflow traced by the [O II] doublet, which extends over ∼1.4 kpc and reaches velocities of $\sim$2000 km s^{-1}. As observed in Arp220, also in Mrk231 the contribution of ionized gas to the overall mass outflow rate is

negligible compared to that of molecular gas, which dominates the feedback process and is primarily responsible for clearing gas from the nuclear regions. Nevertheless, similar to Arp220, the ionized component is more spatially extended than the molecular gas, suggesting that it may impact the ISM at larger distances.

Interestingly, the [O II] outflow is cospatial with regions of enhanced blue continuum, potentially indicating ongoing positive feedback. Alternative interpretations are also possible, as the UV continuum could instead arise from scattered AGN light on the outflowing region rather than from local star formation.

We also used ancillary data to propose a new binary model that successfully explains several observational features that previous binary models could not reproduce. In this model, the two black holes are separated by approximately 1 pc, consistent with the morphology seen in the radio images. The unobscured secondary AGN is predicted to orbit the primary at a velocity of about 1400 km/s, consistent with the velocity offsets observed in the Lyα and CIV emission lines, which in our interpretation originate from the secondary black hole that, as indicated by the SED, dominates the FUV emission.

Table 4.3: Properties of the high-velocity molecular and ionized outflows of Arp220.

General properties of the nuclei in Arp220				
	E Nucleus		W Nucleus	
SFR(radio/FIR)$^{(1)}$	60–80		110–150	
SFR(Paα)$^{(2)}$	0.17		0.52	
$L_{AGN}^{IR}$$^{(3)}$ [erg s^{-1}]	1.1×10^{44}		2.5×10^{44}	
$L_{AGN}^{X}$$^{(4)}$ [erg s^{-1}]	8.3×10^{43}		2.5×10^{43}	
Hot-to-cold$^{(5)}$	3×10^{-4}		1×10^{-4}	
General properties of the outflows				
	SEO	HGO	NWB	WNO
$R_{out}^{(6)}$ [kpc]	0.4	0.6	1	0.15
$n_e^{(7)}$ [10^3 cm^{-3}]	< 17	$3.8^{+2.2}_{-1.3}$	< 1.8	$5^{+2.5}_{-2}$
$v_{out}^{(8)}$ [km s^{-1}]	600 ± 150	400 ± 140	600 ± 180	400 ± 70
$t_{dyn}^{(9)}$ [Myr]	0.65	1.5	1.7	0.42
$A_v^{(10)}$ [mag]	8.9	4.5	3	8
Hot Molecular Gas				
$M_{out}^{(11)}$ [10^4 M$_\odot$]	0.07	0.2	0.1	
$\dot{M}_{out}$ [M$_\odot$ yr^{-1}]	0.001	0.001	0.0006	
$E_{out}^{(12)}$ [10^{52} erg]	0.2	0.3	0.36	
$\dot{E}_{out}^{(13)}$ [10^{40} erg s^{-1}]	0.009	0.006	0.007	
Ionized gas, assuming [Fe II]-based n_e				
M_{out} [10^4 M$_\odot$]	0.5	4	6	9
$\dot{M}_{out}$ [M$_\odot$ yr^{-1}]	0.007	0.025	0.03	0.26
E_{out} [10^{52} erg]	1.7	6	18	16
$\dot{E}_{out}$ [10^{40} erg s^{-1}]	0.08	0.12	0.3	1.4
Ionized gas, assuming [S II]-based $n_e = 170$ cm^{-3}				
M_{out} [10^4 M$_\odot$]	50	90	60	270
$\dot{M}_{out}$ [M$_\odot$ yr^{-1}]	0.7	0.6	0.4	8
E_{out} [10^{52} erg]	170	130	190	460
$\dot{E}_{out}$ [10^{40} erg s^{-1}]	8	2.7	4	40
Total (ionized, hot and cold molecular)				
M_{out} [10^4 M$_\odot$]	400	2090	560	270
$\dot{M}_{out}$ [M$_\odot$ yr^{-1}]	5.7	12	3.2	8
E_{out} [10^{52} erg]	1170	3570	1940	460
$\dot{E}_{out}$ [10^{40} erg s^{-1}]	53	71	39	40
$\mu^{(14)}$	0.08	0.09	0.05	0.06
$\dot{E}_{out}/L_{AGN}^{IR}$	5×10^{-3}	3×10^{-3}	4×10^{-3}	2×10^{-3}
$\dot{E}_{out}/L_{AGN}^{X}$	6×10^{-3}	0.03	5×10^{-3}	0.02
$\dot{E}_{out}/\dot{E}_{SFR}^{radio/FIR}$	0.009	0.007	0.006	0.004

Notes: (1)–(2) SFR computed from radio/FIR [Varenius et al., 2016, Pereira-Santaella et al., 2021] and Paα [Perna et al., 2024], respectively. (3) AGN luminosity from IR. (4) AGN luminosity from X-rays [Paggi et al., 2017]. (5) Hot-to-cold ratio. (6) Outflow radius. (7) [Fe II]-based electron density. (8) Outflow velocity (flux-weighted average). (9) Dynamical time. (10) Average attenuation. (11) Outflow mass. (12) Outflow kinetic energy. (13) Outflow kinetic power. (14) Outflow mass loading factor. The AGN luminosity refers to the nucleus from which the outflow originates. SEO and NWB correspond to the E nucleus, HGO and WNO to the W nucleus.

Table 4.4: Emission lines identified in the continuum-subtracted integrated spectrum of Mrk 231.

Emission line	Wavelength (Å)	Profile type	Flux (erg s^{-1} cm^{-2})
Hβ	4861	Lorentzian	3.87×10^{-13}
Hβ	4861	Lorentzian	2.56×10^{-15}
Fe II	4925.29	Gaussian	9.1×10^{-14}
Fe II	4994.74	Gaussian	4.6×10^{-14}
[O III]	5007	Gaussian	7.9×10^{-16}
Fe II	5019.84	Gaussian	6.6×10^{-14}
Cr II	4825.48	Gaussian	5.0×10^{-14}
Paδ	10049	Lorentzian	1.64×10^{-13}
Fe II	9997	Gaussian	1.5×10^{-13}
He II	10124	Lorentzian	5.0×10^{-14}
Paγ	10938	Lorentzian	4.14×10^{-13}
He I	10830	Lorentzian	2.2×10^{-13}
Fe II	10501	Gaussian	5.22×10^{-14}
Fe II	10746	Gaussian	4.3×10^{-14}
Fe II	10863	Gaussian	5.4×10^{-14}
Fe II	11126	Gaussian	1.05×10^{-14}
O I	11287	Gaussian	1.8×10^{-13}
Fe II	11394	Gaussian	8.2×10^{-14}
Paβ	12818	Lorentzian	4.84×10^{-13}
Paβ	12818	Lorentzian	8.5×10^{-15}
Brη	21661	Lorentzian	5.29×10^{-14}
Paα	18756	Lorentzian	4.84×10^{-13}
Paα	18756	Gaussian	1.78×10^{-14}

Table 4.5: Best-fit parameters for the two possible AGN in Mrk231.

Parameter	Unobscured AGN	Obscured AGN
$\log L_{3000}$ (erg s^{-1})	41.43	44.09
A_V (mag)	0.46	3.31
$\mathrm{Fra_{gal}}$	4.55×10^{-3}	6.80×10^{-5}

Chapter 5

PEACE: Probing Entwined AGN Candidates with Euclid

As we extensively saw in Chapter 1, the formation and growth of SMBHs are closely linked to the evolution of their host galaxies. In particular, galaxy mergers are thought to play a central role in driving gas inflows toward the central regions, potentially triggering both star formation and AGN activity [e.g. Hernquist, 1989, Hopkins et al., 2008, Blecha, 2017]. When two galaxies merge, the SMBHs in their nuclei become part of the same post-merger galaxy, and eventually merge together, typically on timescales of the order of Gyr [e.g. Khan et al., 2012]. In the final stages of a merger, both SMBHs may be simultaneously active, forming a dual AGN system (i.e. two accreting SMBHs within a single merged galaxy). These systems provide a unique laboratory for studying SMBH growth, AGN triggering, and the interplay between galaxy evolution processes and nuclear activity.

In this chapter, we explore the application of ML techniques to the identification of dual AGN systems in imaging data, with a particular focus on the first *Euclid* quick release, Q1 [Euclid Quick Release Q1, 2025]. In Sect. 5.1 we describe the input catalogue of AGN, the data used in this work, which consists of the *Euclid* Q1 data, and the ML training set (Sect. 5.1.3) as well as the architecture of the CNN. In Sect. 5.2 we present the results obtained from simulations, compare our method with other standard techniques and discuss the identification of an optimal classification threshold. In Sect. 5.3 we apply our CNN to the Q1 data, we discuss foreground contamination, we extract the photometry exploiting the four *Euclid* bands and present a sample of dual AGN candidates. In Sect. 5.4 we compare our results with both simulation and observational works from the literature.

5.1 Euclid Data

This work is based on imaging data from the *Euclid* mission, which is conducting two major surveys: the *Euclid* Wide Survey (EWS) and the *Euclid* Deep Survey (EDS). The EWS [Euclid Collaboration: Scaramella et al., 2022] is designed to cover approximately one-third of the sky, amounting to $\sim$ 14 000 deg^2, while avoiding the Galactic and ecliptic planes. The Deep Survey, in contrast, focuses on three carefully selected regions – the Euclid Deep Field (EDF) North, South, and Fornax – and achieves significantly greater depth through repeated exposures. In this study, we use data from the *Euclid* Q1 release [Euclid Collaboration: Aussel et al., 2025], which includes

Table 5.1: List of QSO catalogues used to compile the search list.

Catalogue	Properties	Number	Ref
Milliquas v8.0	Spectroscopy from literature	729 519	Flesch [2023]
Quaia G20.5	*Gaia* and *WISE* colours	878 145	Storey-Fisher et al. [2024]
eRosita	X-ray flux	177 971	Merloni et al. [2024]
WISE	*WISE* colours	2 275 316	Assef et al. [2018]
Gaia/unWISE	*Gaia* and WISE colours	1 228 393	Shu et al. [2019]
TOT (excluding duplications)		3 295 296	

~ 63 deg^2 of imaging of the EDFs acquired to the depth of the Wide Survey. We use the `pdMerBksMosaic` data products [Euclid Collaboration: Romelli et al., 2025], which include background-subtracted mosaics and associated point spread function (PSF) catalogues (`catalogue-PSF`). For this analysis, we consider all Q1 fields which span approximately 350 tiles, each with a field of view of 0.57 deg^2 , corresponding to $0.75° \times 0.75°$. These observations reach a $\sim 10\sigma$ magnitude limit of 24.5 in the Visible Instrument (VIS) filter, $I_{\rm E}$ [Euclid Collaboration: Cropper et al., 2025], and a $5\,\sigma$ magnitude limit of 24.5 in each of the filters of the Near Infrared Spectrometer and Photometer (NISP), namely $Y_{\rm E}$, $J_{\rm E}$, and $H_{\rm E}$ [Euclid Collaboration: Jahnke et al., 2025]. The Q1 data give us a first glimpse into the possibilities of efficiently searching for dual AGN at sub-arcsec separations over the full *Euclid* survey of $\sim 14\,000$ deg^2.

5.1.1 Input QSO catalogue

The dual/lensed search strategy consists of looking for close companions near previously classified QSOs. We created the input QSO list by merging several external catalogues of both spectroscopically confirmed QSOs and robust photometric QSO candidates selected in various ways. Our aim is to privilege completeness over purity, while discarding the most unreliable candidates. More accurate assessments of the nature of candidate double systems could be later performed on an individual basis, e.g. with AO-assisted spectroscopy. For each catalogue we only selected the QSOs falling within the EWS footprint, i.e. excluding objects within 23° from the Galactic plane and 10° from the ecliptic plane. We also excluded QSOs close to the largest galaxies in the Local Group, e.g., Large Magellanic Cloud (LMC), Small Magellanic Cloud (SMC), M31, and M33. Table 5.1 reports the catalogues used and the number of objects obtained from each of them. In particular:

- Milliquas v8.0 [Flesch, 2023]: a compilation of all the known QSOs with a reliable redshift. Most of its entries are from the Sloan Digital Sky Survey (SDSS) QSO catalogue DR16Q [Lyke et al., 2020], the DESI EDR QSO catalogue [Chaussidon et al., 2023], the LAMOST survey [Jin et al., 2023], and the 2DF QSO survey [Croom et al., 2004].
- *WISE*: Assef et al. [2018] presented a catalogue of about 4.5 million QSO candidates based on *WISE* colours. To decrease the number of false positives, following Stern et al. [2012], we further select the objects with *WISE* colour $W1 - W2 > 0.8$ and having $W1 < 18.5$ and $W2 < 16.0$ (77% of the original sample).

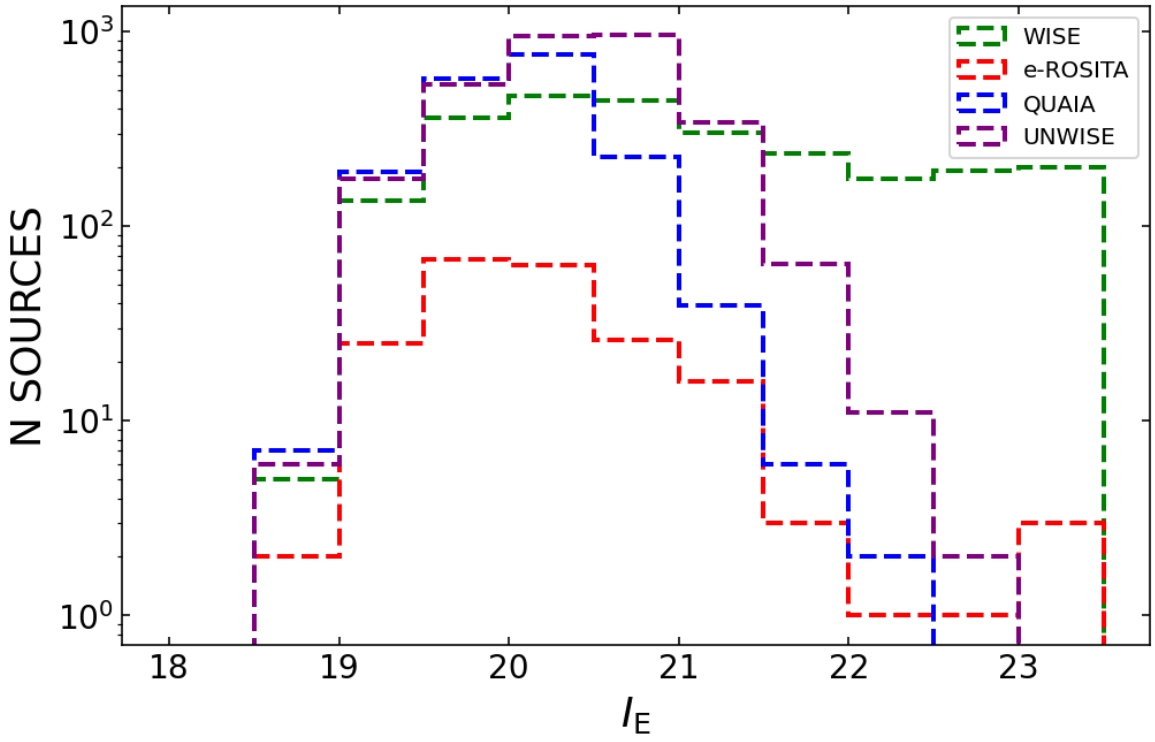

Figure 5.1: Number of Q1 AGN sample in $\Delta = 0.5$ magnitude bins as a function of the selection method: *WISE* (green dashed line), e-ROSITA (red), QUAIA (blue), and UNWISE (purple).

- Quaia: Storey-Fisher et al. [2024] drew an all-sky QSO catalogue combining *Gaia* candidates [Gaia Collaboration et al., 2016] with unWISE infrared data (based on the *WISE* survey).
- eRosita: Merloni et al. [2024] present catalogues of both point-like and extended sources using the data acquired in the first six months of survey operations (eRASS1; completed in June 2020) over half of the sky, whose proprietary data rights lie with the German eROSITA Consortium. From their full catalogue, we selected all the sources that are clearly detected (DET_LIKE_0 $>$ 9) and not extended (parameter EXT $=$ 0).

We crossmatched the different catalogues using a 5" search radius to find duplicate sources. When a duplication is found, the coordinates derived from the *Gaia* and spectroscopic catalogues are preferred over those from eRosita and *WISE*. The final catalogue has about 3.29 million sources (see Table 5.1).

5.1.2 Euclid VIS stamps

Starting from the catalogue described in the previous section, we performed cutouts of the VIS images of $5'' \times 5''$ and 4' $\times$ 4' around each AGN in the catalogue, ending up with 15 000 AGN images in the Q1 data. We used `SExtractor` [Bertin and Arnouts, 1996] for object detection in both types of cutouts, employing specific parameters to optimise performance. In particular, the goal to use `SExtractor` in the small ($5'' \times 5''$) cutouts was to measure object properties and apply selection cuts in magnitude and size for

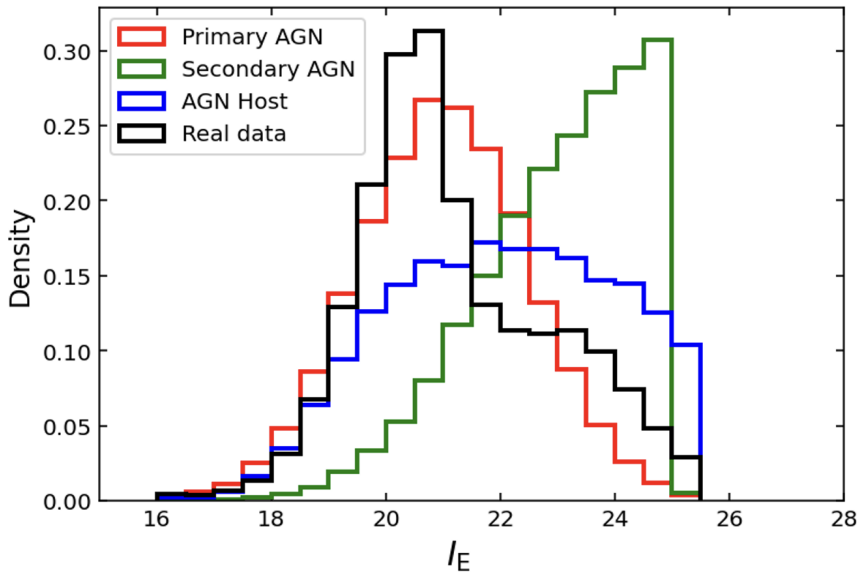

Figure 5.2: Distribution of I_E of the primary AGN (red), secondary AGN (green) and the associated host galaxy (blue) in simulations compared to the distribution of I_E of the considered sample of AGN in Q1 (black) in 0.5 magnitude bins.

our final input sample. The larger 4' × 4' cutouts were processed with `SExtractor` to build a catalogue of host galaxies, which were then used in the simulation described in the following section. The `SExtractor DETECT MINAREA` was set to 2, the DETECT THRESH was set at 1.5 times the background RMS noise, allowing us to detect faint objects. We applied a $4-$pixel Gaussian filter (indicating that the sources are smoothed with a Gaussian kernel with $\sigma = 4$ pixel) and set the parameter that defines the minimum contrast between the two sources to consider them separated to 0.005. These parameter choices were tailored to improve detection sensitivity. MAG ZERO is provided in the header of each tile [Euclid Collaboration: Romelli et al., 2025]. In this way, for each small cutout, we generated a source catalogue and assigned to the AGN candidate from the external catalogue the magnitude I_E of the brightest detected object within the cutout. We flagged those sources which were not centred in a square of $0.3''$ around the coordinates of the external catalogue. We centred the image in the pixel with the highest flux. For each AGN we keep track of the *Gaia* magnitude, the *WISE* colours and, the selection method.

In Fig. 5.1 we report the number of sources in 0.5 magnitude bins of I_E for different selection methods. We see that most of the QSOs in our catalogue are selected through (UN)WISE colour.

5.1.3 Simulations

The simulations described in this section were specifically designed for training and validating a neural network to detect single and dual AGN systems. Our strategy is based on adding synthetic AGN sources, represented by PSFs, into real *Euclid* VIS galaxy images to create realistic examples of both single and dual AGN systems. We generated a dataset comprising 100 000 synthetic images, 50 000 containing a single AGN source and 50 000 containing a dual AGN system in the VIS band. Each AGN was modelled as a point source. When downloading the Q1 tiles, we also downloaded

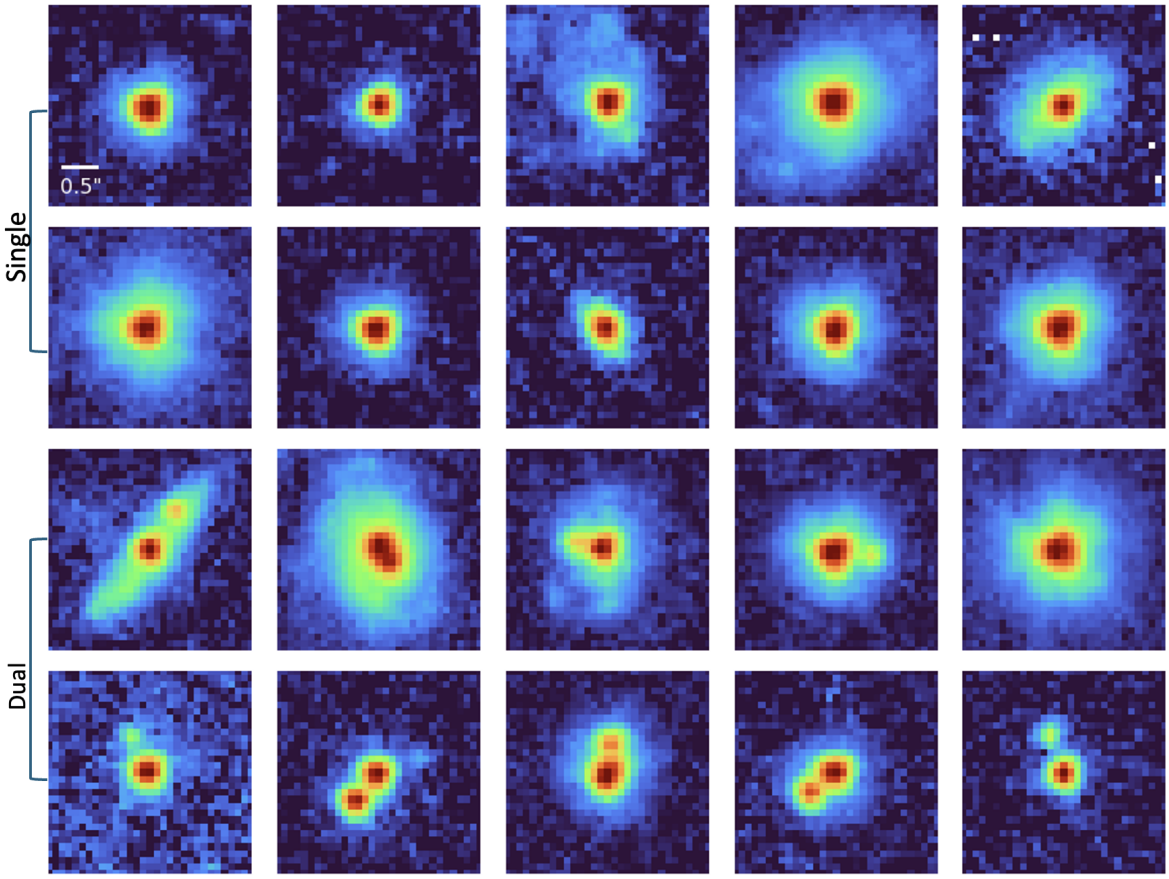

Figure 5.3: Examples of ten simulations of a single AGN (first two rows) and of a dual AGN (second two rows) in I_{E} band. The size of each cutout is $3'' \times 3''$.

the grid of PSFs provided by the official pipeline (catalogue PSF). From each tile, we made cutouts of 200 randomly chosen PSFs throughout the field. The PSFs taken from the catalogue PSF are undersampled (19×19), so we used drizzle [Gonzaga et al., 2012] to oversample them using the 'turbo' kernel to keep the flux constant. We split the 100 000 simulations (50 000 single sources, 50 000 double sources) into 60% assigned to the training set and of the remaining 40%, 20% to the validation set and 80% to the test set.

The magnitude of each primary AGN was drawn from a Gaussian distribution centred at $I_{\mathrm{E}} = 21$ with a standard deviation of $\sigma = 1.2$, chosen to closely match the observed magnitude distribution of the AGN from the external catalogue, as shown in Fig. 5.2. A priori, the relative contributions of the AGN and its host galaxy to the total observed luminosity are unknown. Previous studies have shown that this contribution can vary significantly with luminosity and redshift. For instance, Rakshit et al. [2020], analysing a sample of approximately 500 000 QSOs at $z < 0.8$, found that the host galaxy contribution decreases with increasing total luminosity. At bolometric luminosities around 10^{45} erg s^{-1}, the host galaxy can contribute up to 80% of the total emission. Extending to higher redshifts ($z \sim 1.5$), Schramm and Silverman [2013] demonstrated that, particularly for AGN with lower luminosities, the host galaxy contamination can be even more significant, even exceeding the 90% of the total. Given this uncertainty, we developed simulations covering a broad parameter space to robustly explore the possible contributions of the AGN and its host galaxy. However, the main

purpose of including host galaxies was to enhance the training of the neural network by introducing more realistic and challenging cases while preserving the underlying physics.

We associated to each point source a host galaxy with a flux between 0 and 10 times that of the point source and with CLASS_STAR < 0.5, where CLASS_STAR, taken from `SExtractor`, is defined as the probability to be a point source (1) or an extended object (0). In the case of host galaxies dimmer that $I_{\rm E}$=27.5, we just added random noise to the image as they would be below the detection limit of *Euclid*. To select the random noise, we computed for each tile the median and the median absolute deviation (MAD) and we made random cutouts of the FOV of the tile, accepting the cutout if the mean is less than the median and the $\sigma < 2$ MAD. We designed 50 000 simulations with single objects and we ended up with 2% of simulated AGN painted without the host galaxy. Additionally, we added to each stamp a secondary source with a separation drawn from a uniform distribution between $0.1''$ and $0.8''$ from the primary AGN and whose magnitude was imposed to vary uniformly in magnitude between that of the primary and 25 mag, the limiting AB magnitudes ($10\,\sigma$ for point-like sources) achieved in each footprint.

We explored several sets of simulations, each differing in some aspects to better capture the important features. The main differences between the simulation sets include: the distribution of magnitudes of the primary and secondary objects; the relationship between the AGN and host galaxy magnitudes; the distribution of projected separation between sources; the PSF used to model the AGN; and the level and standard deviation of the noise. These parameters are critical for the neural network because it has to be trained on data as close as possible to the *Euclid* dataset, while learning to recognize features. The main problem of using a neural network to identify dual AGN is inherent to their rareness, which poses a serious challenge to the training of the network. For this purpose, it is necessary to simulate many of such sources, which makes the distribution of simulated objects different from that of the *Euclid* data. This in itself is true for dual AGN, but it is also true for the simulated magnitude distributions of the two sources; in fact, the probability of having more faint primary and secondary objects will be larger than the probability of having bright objects, but this leads to imbalances in the simulations from which the network can learn biased features. However, in this work we focus on the simulation setup described above, which provided the best performance in training and validating our model with the Q1 data. Some examples of simulated single and double AGN are shown in Fig. 5.3.

Comparison between data and simulations

We compare the statistical properties of our simulated AGN with those measured on observational data using the mean signal level, the standard deviation, and the Gini coefficient. The Gini coefficient is defined as

$$G = \frac{\sum_{i=1}^{n} \sum_{j=1}^{n} |x_i - x_j|}{2n^2 \bar{x}}, \tag{5.1}$$

where x_i is the flux in pixel i, n is the total number of pixels, and $\bar{x}$ is the mean flux. It defines the flux distribution in an image; higher values indicate that the flux is concentrated in the center (for instance, when the image is dominated by an unresolved AGN), while lower values correspond to AGN with more diffuse host galaxy. From Fig. 5.4 we see that the simulations reproduce the observed distributions well, with both samples occupying the same region of parameter space.

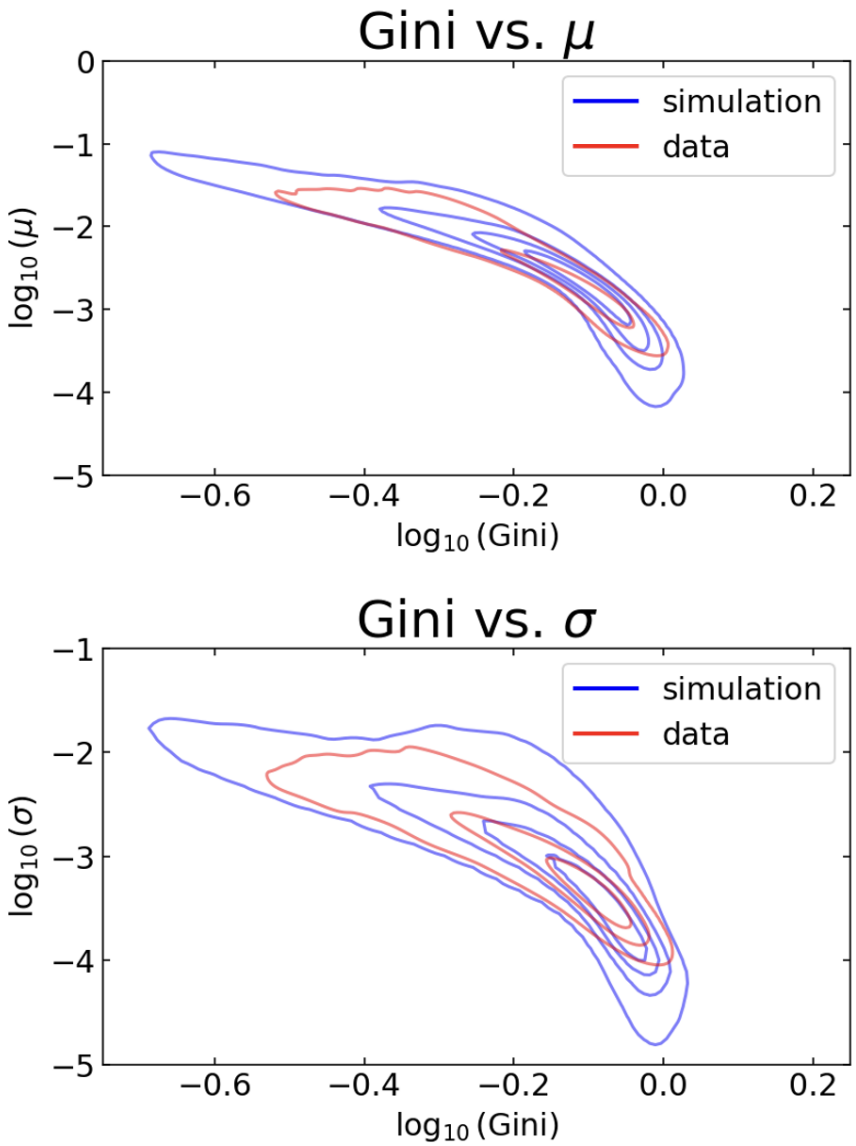

Figure 5.4: Comparison of the statistical properties of the simulations (blue) and the data (red). The upper panel shows the Gini coefficient vs. mean of the signal in logarithm. The lower panel shows the Gini coefficient vs. standard deviation of the signal in logarithm. In both panels, the contours represent kernel density estimates of the respective distributions with 5 levels.

5.1.4 Convolutional neural network classifier

The images were labelled with 2 if they contained dual sources with separations greater than 0.25″, 1 if they contained dual sources with separation less than 0.25″ or 0 if single sources. The 5″ × 5″ stamps are centred in the brightest pixels and cut into a 30 × 30 pixels (3″ × 3″), which is first processed by a 2D convolution layer with a 4 × 4 filter size, then subsampled by a 2 × 2 max pooling layer. Two more identical units follow, with a growing dimensionality of the output space in the convolution, for a total of 2 convolutional layers and 2 max pooling layers. Each of these convolutional layers is followed by a ReLU activation layer. The output of these units is then processed through three single fully-connected layers. For the classification problem we used

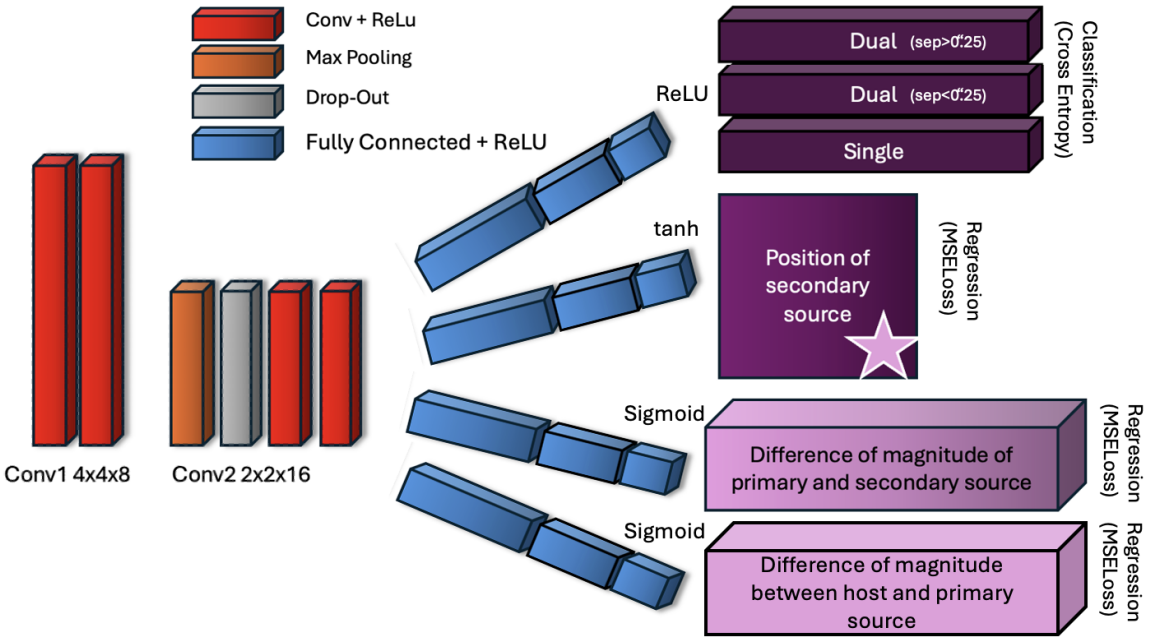

Figure 5.5: Architecture of the convolutional neural network used for classification and feature extraction. The model consists of two convolutional layers (Conv1: $4\times4\times8$, Conv2: $2\times2\times16$) with ReLU activation, followed by max pooling and dropout layers. Fully connected layers ($2304 - 80 - 20$) process the features for output into multiple targets: the position of the secondary source, the difference in magnitude between primary and secondary sources, and the difference in magnitude between the host and primary source. Each output branch uses a different final activation function and loss: ReLU and cross-entropy loss function for the classification task, hyperbolic tangent for the position, and sigmoid for the magnitude differences. The loss functions are the mean squared error when applied to regression task.

the cross-entropy cost function and found the weights using the ADAM [Kingma and Ba, 2014] optimisation method. Note that in PyTorch [Paszke et al., 2019], no explicit softmax activation function is needed in the final layer, as it is handled internally by the cost function. The use of the ADAM optimizer improved the learning rate compared to tests with stochastic gradient descent (SGD). To prevent overfitting and enhance generalisation, we added dropout layers which randomly drop out a fraction (30%) of neurons during the training phase. We implemented our network as a multitask model, enabling it to predict, in addition to the nature of the system, the position of the secondary, the magnitude difference between the secondary and the primary, and the magnitude difference between the host and the primary. Multitask neural networks are powerful tools because they allow a model to learn several related tasks simultaneously, improving the performance while reducing the risk of overfitting, especially when the tasks are correlated. This approach often leads to more robust models and can capture structures in the data more effectively than training separate models for each task [Ruder, 2017, Crawshaw, 2020, Ginolfi et al., 2025].

We built another block in our CNN that predicts the coordinates x and y of the secondary AGN. To increase the effectiveness of the network, we made it so that the position of the secondary can vary between -1 and 1, thus normalising to the maximum distance that the secondary can reach in our simulations. The activation function used

for this task is a tanh function (so that it varies between -1 and 1). We assigned to the single sources the position of the secondary source at the value $x = 0$, $y = 0$. This can also give us an indication for detecting false positives, that is, single objects classified as dual; in fact when the network detects dual but predicts secondaries with coordinates very close to (0,0), we can discard this prediction.

We also added two branches to the neural network to predict the magnitude difference between the primary and secondary sources ($\Delta I_{\mathrm{E},21}$) and, though more difficult, the difference in magnitude between the primary and its host galaxy ($\Delta I_{\mathrm{E,H1}}$). For the single objects, we imposed as the true label of $\Delta I_{\mathrm{E},21}$ the maximum among those simulated in the double objects, so as to normalise all the sample between 0 and 1 and without restricting in a smaller parameter space the double objects. We did the same for the difference between the magnitude of the primary and that of the host galaxy. We used the mean squared error as the loss function for the regression tasks. For the multi-task learning framework, we computed the total loss as the sum of all individual task losses, with the classification loss contributing more strongly to the optimization process due to its relative scale compared to the other tasks. The final architecture of our model is illustrated in Fig. 5.5.

5.2 Simulation results

In this section, we present the results of our neural network applied to the simulated datasets. In particular, we study how the completeness and accuracy vary as a function of both the physical parameters of the systems and the quantities predicted by the network. We also compare the performance of our approach with standard methods, and select the most suitable network architecture for the application to the real data.

5.2.1 ROC curve and comparison with standard method

We evaluated the performance of the CNN by analysing its receiver operating characteristic (ROC; Bradley [1997]) curve. This curve is constructed by varying the threshold probability used to classify galaxies as dual or single, considering the number of True Positives (TPs), True Negatives (TNs), False Positives (FPs), and False Negatives (FNs). The TP rate, also called completeness, which measures the fraction of true mergers correctly identified, and the FP rate, which indicates the fraction of single AGN incorrectly classified as dual, are computed as follows:

$$\mathrm{TPR} = \frac{\mathrm{TP}}{\mathrm{TP} + \mathrm{FN}}, \tag{5.2}$$

$$\mathrm{FPR} = \frac{\mathrm{FP}}{\mathrm{FP} + \mathrm{TN}}. \tag{5.3}$$

Figure 5.6 shows the ROC curves for the test set. We used a one-vs-rest (OvR) approach, defining classes 1 and 2 as the positive class and class 0 (single sources) as the negative class. The probability of the positive class was then computed as the sum of the predicted probabilities for classes 1 and 2. The perfect classifier reaches the top left corner, with the maximum TP rate and a FP rate of 0. Hence, we can use the area under the curve (AUC) as a metric of performance. The AUC curve in our CNN reaches 0.98. We want to compare the performance of our CNN with the

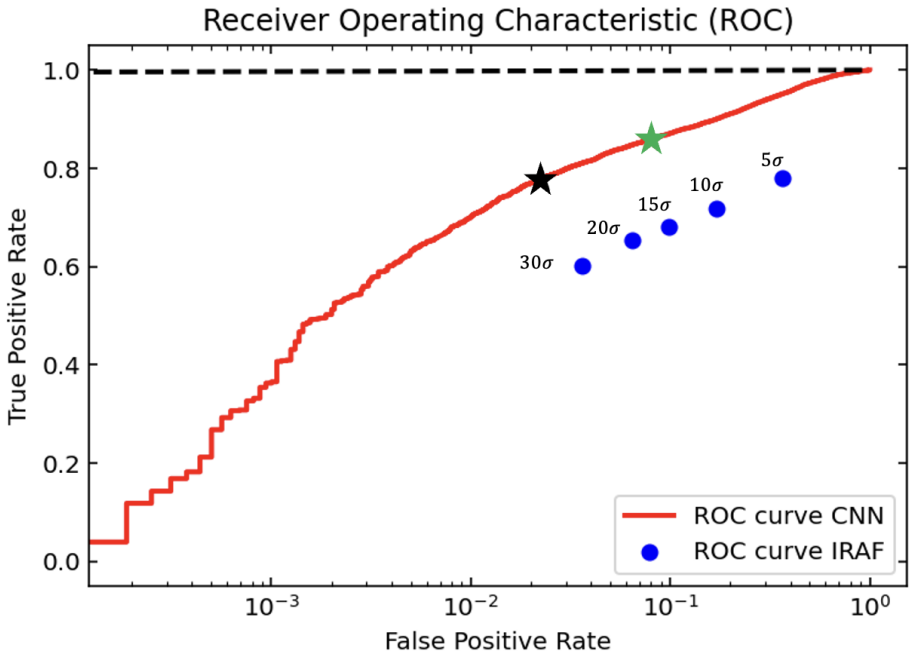

Figure 5.6: ROC curve comparing the performance of the two detection methods in log scale. The red curve represents the ROC of the CNN, while the blue points correspond to the ROC obtained using the `IRAFStarFinder` algorithm with varying detection thresholds (5, 10, 15, 20, 30 σ). The green star marks the threshold closest to an ideal classifier, while the black star indicates the threshold that minimises the difference between the FPs and TPs assuming a real case scenario (see Sect. 5.2.4).

performance of standard methods such as `SExtractor`[1] or the `IRAFStarFinder` module of `photutils` [Bradley et al., 2021]. The deblending method adopted in SExtractor is based on multi-thresholding and works on any kind of object but it is unable to deblend components that are so close that no saddle is present in their profile. A better optimiser for point source detection is `IRAFStarFinder` that searches images for local density maxima that have a peak amplitude greater than a threshold above the local background and have a PSF FWHM similar to the input FWHM. Therefore, we measured the ROC curve of the standard method with `IRAFStarFinder` increasing 5, 10, 15, 20, 30 σ, and with a minimum detection separation from the limit imposed by the algorithm (2×FWHM). Obviously, these values are simply for the purpose of having a direct comparison between the two curves. We first calculated the true positives by applying the algorithm to all simulations with dual objects and then the false negatives by applying the algorithm to the single objects. For the calculation of TP, we considered the correct detection if the algorithm finds at least one source within 0.8″ of the primary source. Detection of sources at larger distances this means that the network has detected other source present in the field (foreground objects). We note that this represents an upper limit to TPs since we consider a correct detection even if the algorithm detects possible contamination within 0.8″ (clumps, structure in the galaxy). For the calculation of FNs, we applied the algorithm to single sources considering an incorrect prediction if it finds more than one source within 0.8″. The ROC curves of the neural network and `IRAFStarFinder` predictions are shown in Fig. 5.6 as red line

[1] `https://sextractor.readthedocs.io/en/latest/Introduction.html`

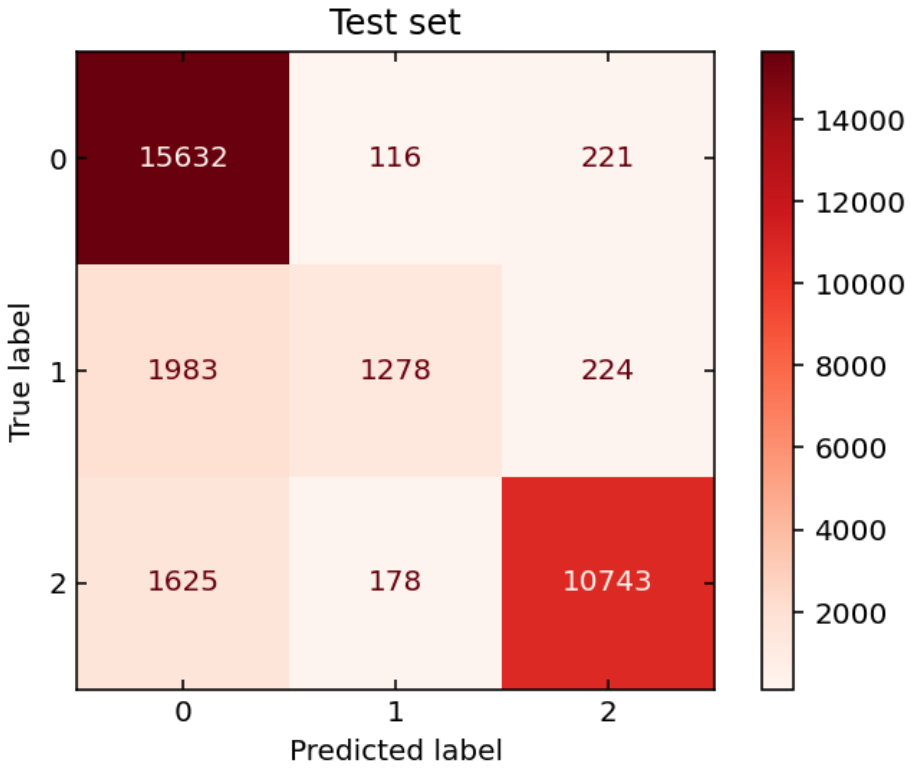

Figure 5.7: Confusion matrix. 0: single AGN, 1: dual AGN with separation less than 0.25″, 2: dual AGN with separation greater than 0.25″.

and with blue dots for increasing sigma, respectively. The ROC curve of the CNN lies above that of `IRAFStarFinder`, indicating that the CNN achieves higher completeness and precision across all detection thresholds. Classical methods do not reach the same level of completeness as the CNN without substantially increasing the number of false positives.

5.2.2 Confusion matrix

Figure 5.7 shows the confusion matrix, where the y-axis represents the true labels and the x-axis represents the predicted labels. The labels are defined as follows: 0 corresponds to a single AGN, 1 to a dual AGN with separation $< 0.25''$, and 2 to a dual AGN with separation larger than $0.25''$. If we consider dual candidates labelled as 1 or 2, we find 337 false positives, corresponding to approximately 2%, and a completeness of about 78%. This leads to a F1 score, defined as the harmonic mean of the precision and completeness (recall) scores, of 0.86. If, instead, we restrict the analysis to candidates labelled as 2 (dual AGN), the precision increases to 98.6%, with a completeness of 68% and a F1 score of 0.80. However, these global metrics are not necessarily meaningful in a real case scenario since the true distributions of source separations and magnitudes are unknown. In particular, in the limiting case where all dual AGN lie at separations $\sim 0.25''$, where some models predict the peak of their number density [Saeedzadeh et al., 2024], the completeness metric would lose significance, since many of them would not be detected. What is more important is to understand how precision and completeness vary across the physical parameter space.

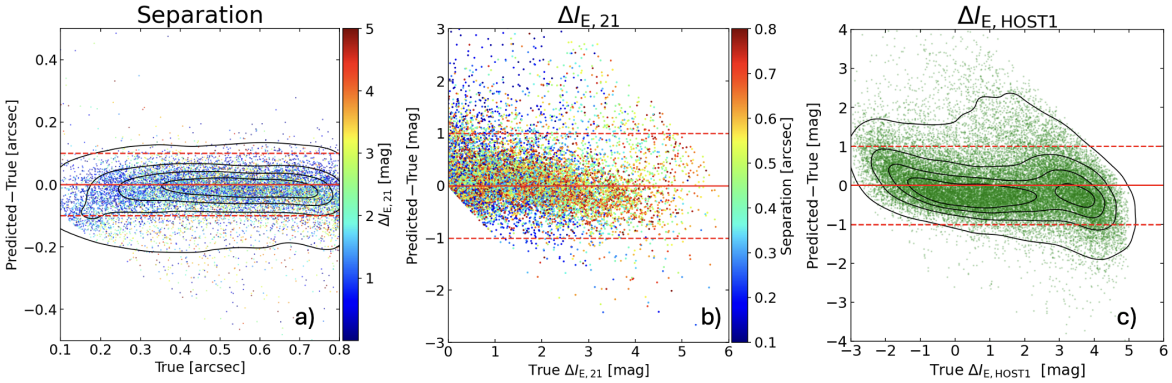

Figure 5.8: Prediction of the CNN of objects classified as dual AGN. Scatter plots comparing true values (x-axis) with the difference of the predicted values and the true values (y-axis) for different parameters derived from the CNN. (a) Predicted separation (in arcsec) between the two sources. The colour bar represents the $\Delta I_{\mathrm{E},21}$ for the data points. (b) Prediction of the ΔI_{E} between the secondary and primary sources ($\Delta I_{\mathrm{E},21}$). The colour bar represents the separation in arcsec of the two sources. (c) Prediction of the magnitude difference (ΔI_{E}) between the host and primary source $\Delta I_{\mathrm{E,H1}}$. Red dashed lines indicate perfect predictions and ± 0.1 in arcsec error margins (± 1 in px) and ± 0.5 in mag.

5.2.3 Predictions of the model

As shown in Fig. 5.5, the network has four different end layers that predict the nature of the AGN, but also the exact location of the secondary source, $\Delta I_{\mathrm{E},21}$, $\Delta I_{\mathrm{E,H1}}$. Figure 5.8 shows the network predictions, where the x- and y-axis are respectively the true value, and the difference between the network prediction and the true value. Panel a) presents the predictions of the separation between the two objects computed as $d = \sqrt{(x_0 - x_{\mathrm{pred}})^2 + (y_0 - y_{\mathrm{pred}})^2}$ where x_0 and y_0 are the central pixel of the primary source, while x_{pred} and y_{pred} are the coordinates of the secondary source predicted by the CNN. The plot only includes sources that are predicted to be dual sources. When the network is not able to detect a secondary component, it also cannot accurately assign a distance, increasing the scatter in the plot. We see that the prediction is correct within $\pm 0.1''$. Panels b) and c) show ΔI_{E} between the secondary and primary source ($\Delta I_{\mathrm{E},21}$) and ΔI_{E} between the host and primary ($\Delta I_{\mathrm{E,H1}}$). The prediction of $\Delta I_{\mathrm{E},21}$ shows the scatter from the true value of $\sim \pm 0.5$ mag that increases when separations are small. This is mainly due to the fact that, at close separations, the network can no longer perform precise photometry.

5.2.4 Threshold to filter

In order to choose the best thresholds for filtering, it is also necessary to consider the number of dual AGN that we expect. According to simulations the number of dual AGN can vary between 0.1 and 10% of all AGN [Steinborn et al., 2016, Rosas-Guevara et al., 2019, Volonteri et al., 2022, Puerto-Sánchez et al., 2025], so being a class of rare objects, it is necessary to choose a metric such that the FPR are minimised compared to TPR. To do this, the output of the neural network can be used to filter out objects that most likely represent contaminants. We try to understand how completeness and precision vary as a function of network output by changing the thresholds of the

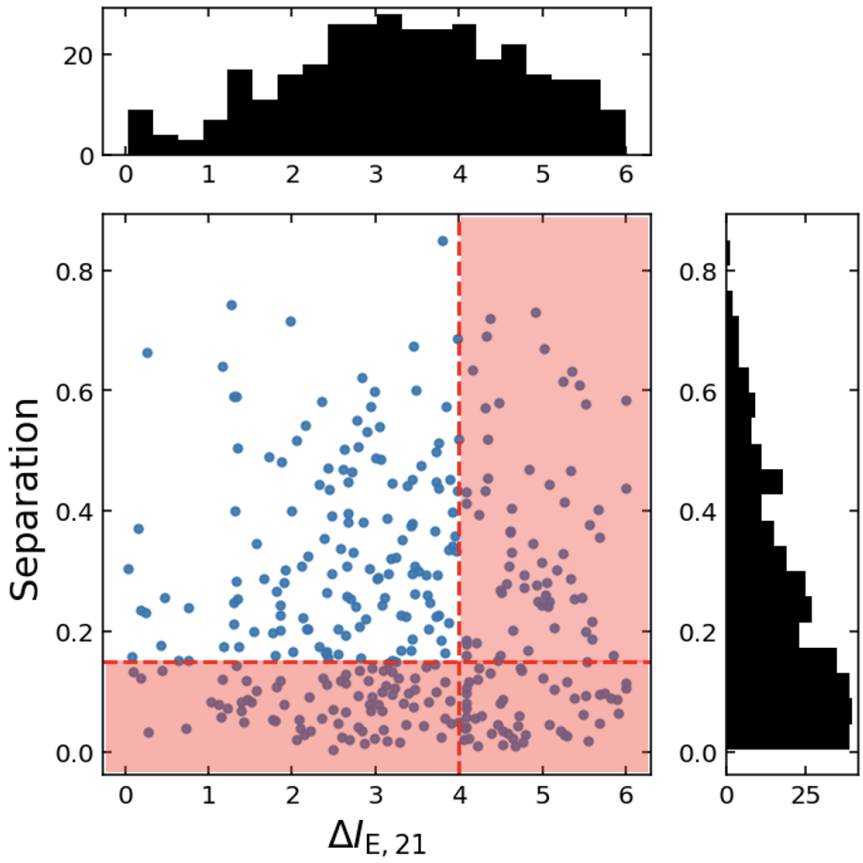

Figure 5.9: CNN prediction of separation and the magnitude difference between the primary and secondary sources ($\Delta I_{\mathrm{E,21}}$) for FP objects. The top and right histograms show the distribution of $\Delta I_{\mathrm{E,21}}$ and of the separation of FPs, respectively. The red shaded regions indicate the excluded objects, defined by a separation smaller than 15″ and $\Delta I_{\mathrm{E,21}}$ higher than 4.

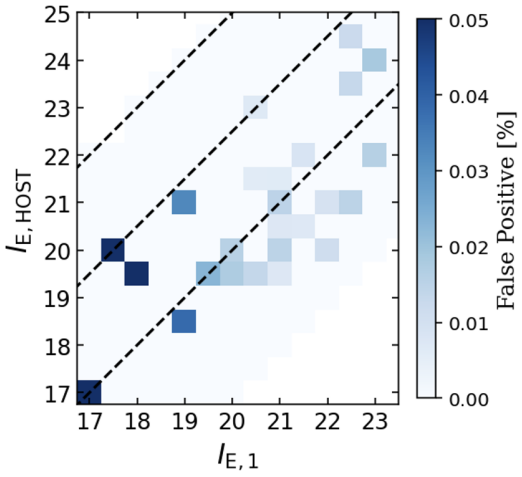

Figure 5.10: FP rate in bins of magnitude of the host galaxy, $I_{\mathrm{E,HOST}}$, and of magnitude of the primary AGN, $I_{\mathrm{E,1}}$.

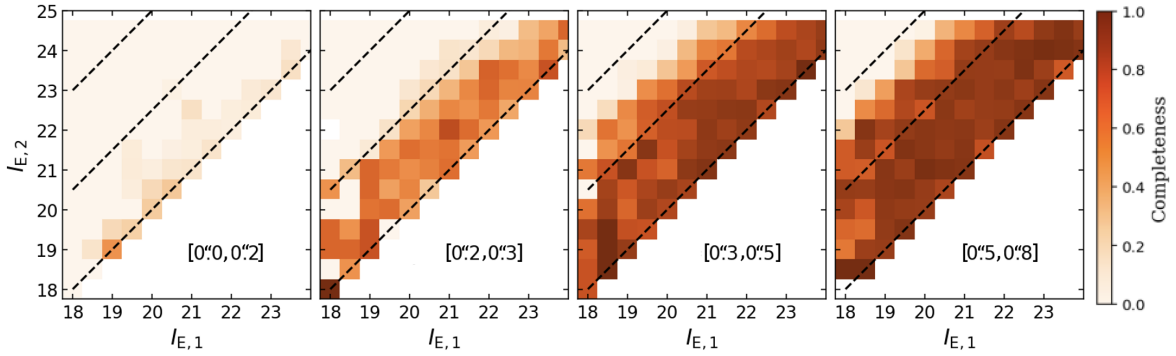

Figure 5.11: Completeness in bins of $I_{\mathrm{E,1}}$ and $I_{\mathrm{E,2}}$ for different separation ranges. The black dashed lines represent flux ratios of 1, 10, and 100 between the primary and secondary sources.

output. In particular, we vary the threshold of each parameter for the prediction of all dual systems in bins of magnitude of the primary, secondary, and separation. This allows us to estimate the expected completeness in real observations for each region of parameter space. We perform the same analysis for systems labelled as single, in bins of magnitude of the primary and of the host, to estimate the number of false positives. For each trained network and for each value of the decision threshold applied to the network output, we calculate the TPR and FPR with Eqs. (5.2) and (5.3).

To determine the optimal classification threshold, we adopted a modified selection metric defined as

$$(\mathrm{TPR}\ f_{\mathrm{dual}} - \mathrm{FPR}\ f_{\mathrm{single}})\ N_{\mathrm{QSO}}, \tag{5.4}$$

where f_{dual} and $f_{\mathrm{single}} = 1 - f_{\mathrm{dual}}$ represent the assumed fractions of dual and single AGN, respectively, and N_{QSO} is the total number of QSOs in the input sample. This metric approximates the expected number of true positives minus false positives, and was evaluated in the separation range of $0.2''$ to $0.6''$, where the number of dual AGN is expected to be higher. Assuming a dual AGN fraction of 1% and $N_{\mathrm{QSO}} = 6000$, the resulting optimal thresholds is 0.9 and typically yield an expected net number of true

detections (TP − FP) between 10 and 20. However, this estimate relies on several assumptions, in particular that the separation and magnitude distributions of dual AGN in the real data mirror those used in our simulations, an approximation that may not reflect reality.

Investigation of false positives

We investigated the behaviour of the CNN in relation to false positives, that are sources labelled as single but predicted to be class 1 or 2 by the network. Figure 5.9 shows the CNN predictions for $\Delta I_{\mathrm{E},21}$ and separation for the 337 false positives identified out of a total of 15 969 sources. Some of these FPs represent foreground contamination that may be present because we used stamps of real galaxies in which there is a non-zero probability that a foreground source is present. Another kind of FPs are galaxies with disturbed morphology, that may be misclassified. To better isolate probable FPs, we applied a posteriori physical threshold, selecting only those with $\Delta I_{\mathrm{E},21} < 4$ and separation $< 0.15''$. This additional cut allows us to eliminate more than half of the FPs though at the cost of also removing some TP. This choice is justified by physical considerations and helps to improve the overall robustness of the classification.

We studied the classification accuracy as a function of only the parameters available for single AGN: the magnitude of the primary source and that of the host galaxy. As shown in Fig. 5.10, the overall precision decreases when the host galaxy is particularly bright although it remains high (i.e., produces a low FP rate) with the chosen threshold.

5.2.5 Detection accuracy

We investigate how the completeness varies as a function of physical parameters, specifically the magnitudes of the primary and secondary components and their separation, using the selected thresholds. We apply the CNN with a classification threshold of 0.9, a minimum separation of 015, and $\Delta I_{\mathrm{E},21} < 4$ as described in Sect. 5.2.4.

Figure 5.11 shows the resulting completeness across this parameter space. At separations between 02 and 03, the CNN achieves an average completeness of approximately 60% in classifying dual sources with a contrast of up to a factor of ten. For larger separations, dual objects with $\Delta I_{\mathrm{E},21} < 4$ are detected with very high completeness. However, at separations greater than 05–06, standard deblending algorithms, such as `IRAFStarFinder`, perform better in terms of detection accuracy, but as described in Sect.5.2.1, they do not reach the performances of the CNN.

5.3 Application to Q1 data

Starting from the initial dataset of approximately 15 000 AGN cutouts, we applied a series of selection criteria to refine the sample. We restricted the I_{E} range of the primary source to 18–23.5 and ISOAREA < 450, where the ISOAREA is defined as the area (in number of pixels) above the detection threshold, in order to remove very extended sources, and removed duplicate entries. Moreover, we excluded any QSO whose coordinates did not correspond to a detected source within $0.3''$. After applying these cuts, we ended up with 5993 cutouts, a sample size that is sufficiently to robustly test our method and to provide a realistic estimate of the number of dual systems to be followed-up with spectroscopic observations.

5.3.1 Application of the CNN

We first preprocessed the images by normalising the pixel values between 0 and 1. Each image was then centred on the pixel with the maximum flux, following the same procedure used during the training of the CNN on the simulated data (see Sect. 5.1.4). Finally, we applied the neural network on the preprocessed images. We found 265 candidates classified as dual systems. Using the threshold defined in Sects. 5.2.4 and Sect. 5.2.4, we identified a sample of 49 objects that meet the selection criteria, representing the $\sim 0.8\%$ of the initial sample. In this selected candidates, given the high precision of the neural network, we aimed to minimise contamination from objects with bright host galaxy structures. The main contaminants are represented by foreground sources, such as stars, and it is therefore necessary to estimate the expected number of such contaminants. The distribution of the separations predicted by the neural network is shown in Fig. 5.13.

5.3.2 Foreground contamination

Quantifying contamination from foreground stars within our candidate pair sample is inherently challenging. In this section, we provide a statistical estimate of the expected number of chance alignments with foreground sources along the line of sight, compared to systems that are more likely to be physically associated with the primary source, such as dual or lensed AGN or clumpy structure in the galaxy.

To estimate the probability of contamination from unrelated sources, we performed a simple statistical test by making random square cutouts across the analysed fields of view. Specifically, we extracted 20 000 random $2'' \times 2''$ cutouts and ran `SExtractor` on each of them. The size of the cutouts was chosen to avoid truncating sources at separation of around $1''$. The estimated number of contaminants depends on both the limiting magnitude and the separation from the center within which sources are classified as contaminants. For example, by restricting to $I_{\rm E} < 25$ and separations $< 0.8''$, `SExtractor` finds 605 contaminants. When extending the limits to $I_{\rm E} < 26$ and separations $< 1"$, the number increases to 1650 out of 20 000, corresponding to approximately 8% contamination. If we consider only those with CLASS STAR $>$ 0.5, which would represent the true contaminants of dual or lensed AGN, `SExtractor` identifies 82 (0.4%: 24 out of ~ 6000) and 175 (0.87%: 52 out of ~ 6000) contaminants in the two respective thresholds.

We also provide estimates of the contaminants using the official catalogue provided by the *Euclid* pipeline (MER catalogue). For each MER tile catalogue, we randomly generated a set of RA and Dec positions uniformly distributed within the boundaries defined by the minimum and maximum RA and Dec of the tile. For each generated coordinate, we associated the closest object in the catalogue. We repeated this procedure 100 000 times. Under the previous thresholds, we find $\sim 7\%$ contamination for $I_{\rm E}$ < 26 and separation $< 1"$, and $\sim 3\%$ for $I_{\rm E} < 25$ and separation $< 0.8''$. When using PROB POINT LIKE (the estimation uses a "star probability cube") in the MER we found only 169 sources out of 100 000 images (0.17%).

It is important to note that all of the contaminant sources identified in our statistical test are detectable by the source extraction algorithm, as this method does not depend on the presence of a primary object. However, the most important question for our analysis is: how many of these contaminants would actually be detected by our CNN? Another noteworthy aspect is that, while it is possible to make sharp cuts in magnitude

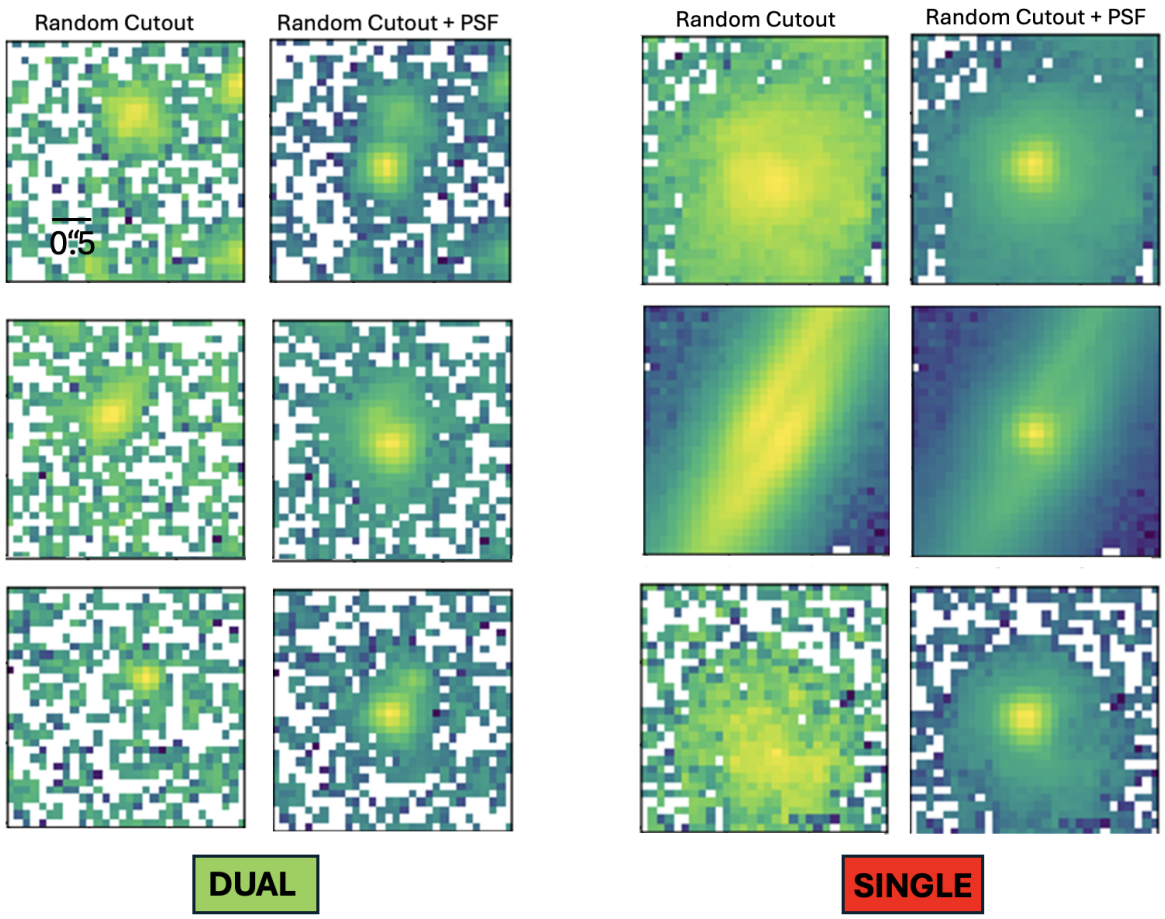

Figure 5.12: Application of the CNN to the foreground contaminants. The left panel shows examples predicted as dual systems; the right panel shows examples predicted as single systems. In both panels, the first column represents random cutouts and the second column the random cutouts + PSF.

and separations for the contaminants when using `SExtractor`, the dual candidates (in this case, foreground contaminants) found by the CNN do not necessarily meet the criteria for magnitude and separation. This is because the CNN was trained with normalised images between 0 and 1 and with secondary sources at separations up to $0.8''$. Thus, it is not possible to include a cut in magnitude of the secondary, and most likely, it is not certain that the network only detects sources up to $0.8''$. Moreover, the network has been trained to detect point-like secondary objects (secondary AGN or lensed QSO), so it is not clear a priori how the network behaves with extended contaminants (e.g., galaxies). To estimate how many contaminants we expect from the neural network, we added to the random cutouts a point source with a $I_{\rm E}$ between 18 and the $I_{\rm E}$ of the contaminant (if present) following the same distribution of our input QSO sample. We compare the number of contaminants estimated by `SExtractor` with the number of contaminants estimated by the CNN. The network finds in total 118 contaminants out of 20 000 images, so around 30 contaminants out of the initial sample of $\sim$6000 QSOs. We note from Fig. 5.12 that, as expected, the network tends to consider as contaminants mostly systems with point source contaminants.

In the real case, the presence of a galaxy host can significantly affect the detectability of a nearby secondary source, especially when the host is brighter than the com-

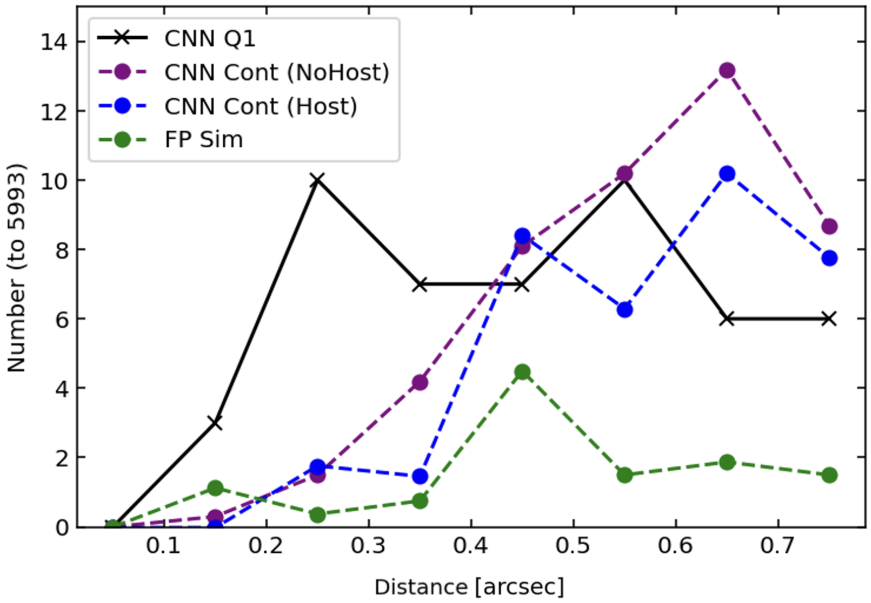

Figure 5.13: Comparison between the number of dual candidates found by CNN and the expected contaminants. The number is normalized by the total number of AGN considered after the cuts (5993). Dual AGN candidates found by CNN in bins of separation (in black), number of expected contaminants classified dual by the CNN once we added a primary source without (purple) and with (blue) host galaxy, andfalse positives expected from simulations (in green).

panion. In particular, faint secondary sources are more easily detected when no host is present. As a result, the number of contaminants estimated from random cutouts tends to exceed the number of pair sources identified around primary QSOs in the Q1. This difference is due to the presence of host galaxy structure in real systems, which lowers the efficiency of detecting nearby companions. We then included a host galaxy in the simulated cutouts, modelled with a Sérsic profile and a magnitude ranging between $I_{\mathrm{E,1}}$=−1 to $I_{\mathrm{E,1}}$=+4 and convolved with the PSF. When applying the CNN to these images, we find that the number of contaminants is reduced compared to the case without a host galaxy (blue line in Fig. 5.13).

Another important aspect involves the number of expected FPs from simulations. While the network has shown high precision overall, we observed that in some cases, single systems in simulations were misclassified as dual systems. To account for these different contaminants, we include the histogram of predicted distances for FPs in the simulations, shown in green in Fig. 5.13. In other words the green line represents the FPs that we expect from simulations. We note that the dual sources identified in the Q1 sample by the network with separations of 0.2″–0.4″ exceed the number expected from foreground objects and false positives caused by clumpy galaxy structure. This excess is likely indicative of a population of dual candidates (see Fig. 5.14). At larger separation ($>0.5''$), the number of contaminants is consistent with the number of detected double sources. While this does not rule out the presence of dual AGN candidates at these higher separations, the probability of finding good candidates with secondary sources brightest than 25 mag is lower. As we address in Sect. 5.3.2, at larger separations it is possible to exploit the four *Euclid* bands to give a probability that the secondary source is an AGN.

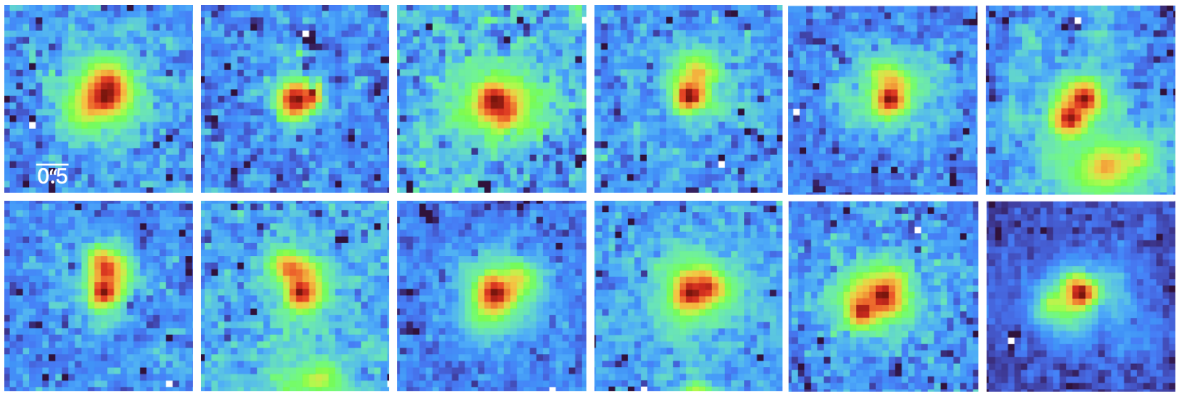

Figure 5.14: Dual AGN candidates found by the network with separations between 0.15″ and 0.45″. The number of objects in this separation range exceeds the number expected from foreground objects and false positives caused by clumpy galaxy structure, making these candidates more reliable than those at larger separations. The size of each cutout is 3″ × 3″, and the flux is shown in logarithmic scale.

Photometry and PSF subtraction

Euclid obtains images in four bands as described in Sect. 5.1, and the colours can in principle be used to study the nature of the sources. For systems with multiple entries in the MER catalogue, we can use MER fluxes to study the photometry with different apertures. To ensure reliable colour measurements, we implemented our own photometric pipeline, as accurate PSF subtraction is essential when analysing closely separated sources. While the MER catalogue provides photometric measurements using a range of aperture sizes, these are often affected by flux contamination of close sources, which is the case for our candidates. To perform the photometry on the candidate sample, we implemented a customized PSF-fitting algorithm for measuring the photometry of the blended sources. We first used `FittableImageModel` of `photutils.psf` on the VIS PSF of the MER catalogue mosaic at the source position. Then we used `IRAFStarFinder` on the VIS stamp, which has higher resolution, to search for point sources. Once we found the positions of the two sources, we measured the fluxes in the VIS and NISP bands by using the appropriate PSF (from MER) and fixing the positions to within 1 pixel. We also included in the fit a Sérsic component convolved with the PSF of the corresponding band to model the host galaxy. The effective radius ($r_{\rm eff}$) was allowed to vary between 2 and 3 pixels, the Sérsic index (n) between 2 and 4, the ellipticity in the range 0 and 1, and the position within a radius of 1 pixel from the center. We then summed the fluxes of each pixel in the model and using the ZERO MAG, we computed the magnitude of the two sources and of the host galaxy in each band.

Colours of the companion candidates

Figure 5.15 shows a colour-colour diagram (($J_{\rm E}$ - $H_{\rm E}$) vs. ($I_{\rm E}$ - $Y_{\rm E}$)) used to analyze the photometric properties of dual AGN candidates. The coloured points represent simulated AGN generated using the `qsogen` package from Temple et al. [2021], with redshift varying between 0.7 and 5 and extinction $E(B-V)$ ranging from 0 to 0.1. Black points correspond to stellar templates from the `XSL_DR3_release` catalogue [Verro et al., 2022], included to trace the stellar region in colour space. The green dashed box

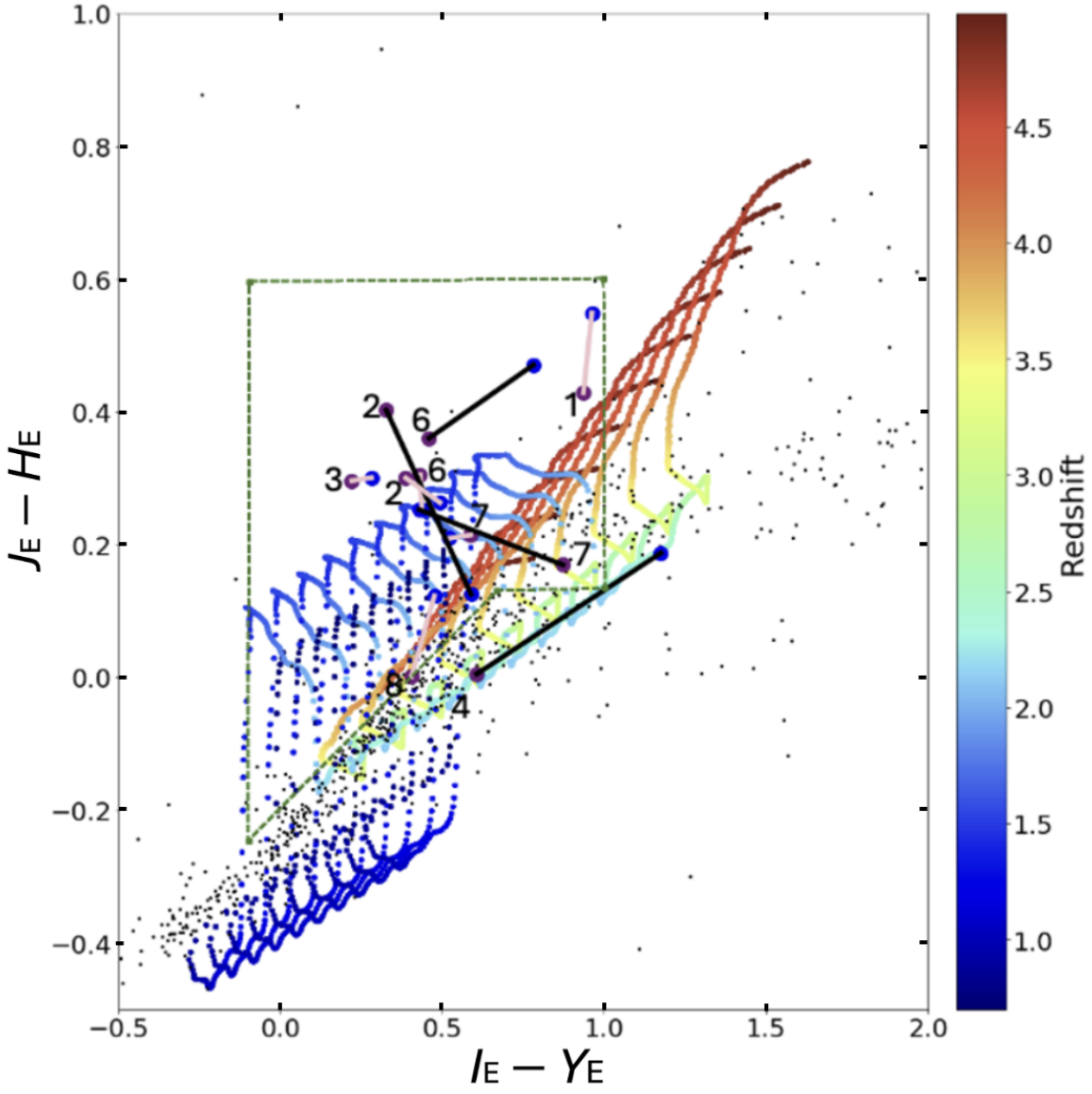

Figure 5.15: Colour-colour diagram of dual AGN candidates in Fig. 5.16 overlayed with simulated AGN colour coded with redshift [Temple et al., 2021] and stars (black dots). The numbers correspond to the sources shown in Fig. 5.16. Each line connects the primary (purple dots) to the secondary (blue dot) source in a dual AGN candidate. Pink lines indicate photometry derived from MER catalogue using a 1 FWHM aperture, while black lines correspond to photometry obtained after PSF subtraction. The green dashed box indicates the AGN selection region defined in Euclid Collaboration: Matamoro Zatarain et al. [2025].

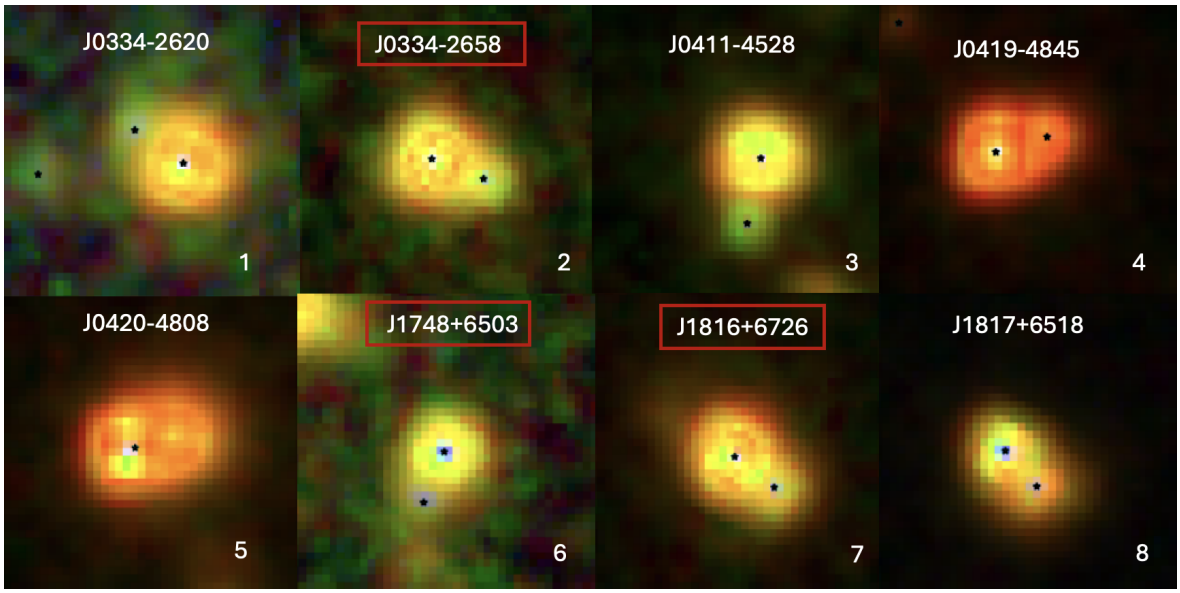

Figure 5.16: Three-colour composite images (I_E, J_E, H_E) of dual AGN candidates derived from MER photometry or PSF subtraction. Systems enclosed in red boxes are those where both sources lie within the AGN region in both photometric methods. The black stars mark the positions of the input sources from the MER catalogue. The size of each cutout is $3'' \times 3''$.

indicates the AGN selection region defined in Euclid Collaboration: Matamoro Zatarain et al. [2025], which is used to separate AGN from stars. For each dual AGN candidate pair, we compute and plot the colours of both the primary and secondary components. We measured the colours of all source pairs for which reliable photometry could be performed for all bands. In general, for dual sources with separations $> 0.5''$, we obtain good fits with errors on the flux of the two sources about 20%, which corresponds to an error on the magnitude of ~ 0.2 mag. To assess the consistency of our photometric method, we compared the colours derived from our PSF subtraction technique with those listed in the MER catalogue, where the two sources are recorded as distinct entries. Figure 5.16 presents seven source pairs in which both components fall within the AGN colour region in at least one of the two photometric methods (PSF subtraction or MER catalogue) and one source ($J0420 - 4808$) where the colours of both sources are consistent with being at the same redshift ($z \sim 2.5$). Such a comparison is only feasible for pairs with angular separations larger than $0.5''$. Only three dual systems exhibit both components within the AGN region (red box in Fig. 5.16), consistent with previous findings suggesting that most widely separated pairs are likely due to line of sight (LOS) contaminations rather than physically associated AGN.

Visual inspection

We conducted a visual inspection of the QSO sample input to the network, categorising objects as follow:

0. Clear dual objects: These are well-separated pairs where both components are distinctly visible and compatible with being point sources.

1. Possible duals at low separations: Objects that could be dual sources but are at

low separation ($< 0.25''$) or with asymmetric morphology, making identification less certain.

2. Contaminated objects: These include secondary sources that are not point-like sources or that are point-like but have a separation greater than $0.8''$.

3. Possible lens-like structures: Sources that exhibit morphological features like gravitational lensing effects such as arcs.

4. Single objects: Sources with no secondary components visible.

5. Objects with a bright host: QSOs where the presence of a luminous host galaxy that could affect the classification.

Out of the 5993 target in the input sample, we found 51 clear dual objects (class 0), 40 possible dual objects at low separation (class 1), about 340 classified as contaminations, 8 possible lenses, 5208 singles, and 336 associated with bright hosts. We compared the dual AGN candidates found by the CNN with the visual inspection. Thirty-two candidates belong to class 0 or 1, 8 belong to class 2, two are possible lenses, and 7 belong to class 4 or 5. We note that visual inspection was carried out in log scale on images normalized between 0 and 1, so we classified as dual objects with a very weak secondary when the network was trained to detect secondaries as faint as $I_{\rm E} = 25$. Table 5.2 shows the number of TPs and FPs based on visual inspection identified by the CNN across different threshold values. TPs and FPs refer to the class identified during the visual inspection (P: class 0, 1; N: other classes). The configuration adopted in this work is the first one which, as suggested by simulations, maximizes the difference between the TPs and FPs. For comparison, the other two configurations maximize TP/FP and the number of TPs but significantly increasing the number of FPs. We also applied visual inspection to simulations, finding that we were able to correctly classify only 4% of simulated dual objects between $0.15''$ and $0.2''$, while between $0.25''$ and $0.3''$ we classify correctly 60% of objects.

Additional space-based imaging To test our results, we searched for higher resolution images of our dual AGN candidates obtained with facilities such as JWST and HST. In this case, we applied the network without using any threshold in `ISOAREA` and we defined as dual candidates all the objects for which the sum of the predicted probabilities for labels 1 and 2 is higher than 0.5 (lower than the threshold we used in Sect. 5.2.4). This approach allows us to identify cases that may represent true positives which were excluded by the CNN due to a too conservative threshold. Moreover, it provides a way to investigate potential FPs and understand the sources of misclassification and to assess whether the observed number of FPs is consistent with expectations from simulations. However, this comparison relies on the assumption that the simulated distributions of separations and the magnitudes of the primary, secondary, and host components accurately reflect the underlying real distributions, which may not always be the case. We confirm that when the thresholds are not applied the network does not always select sources with point-like secondary components in the data, as expected. Two sources with high resolution images were excluded from the initial selection due to ISOAREA values higher than 450 (both having known redshifts below 0.6) though they show clear indications of dual morphology (a and e in Fig. 5.17). In one case, we identify an arc-like feature that could be both a foreground lensed galaxy or a tidal feature (b). In two other cases, the network misclassifies the sources, since it is confused

Table 5.2: Performance metrics for different threshold configurations which maximise TP–FP (first row), TP/FP (second row) and TP (third row). TP and FP refer to the class identified during the visual inspection (P: class 0, 1; N: other classes).

Thres	Sep	$\Delta I_{\mathrm{E,21}}$	$\Delta I_{\mathrm{E,H1}}$	TP	FP	TP-FP	TP/FP	TPR (%)	FPR (%)
>0.90	$>$ $0.15''$	<4	>-2	32	7	25	4.5	35	0.12
>0.80	$>$ $0.20''$	<4	>1	20	3	17	6.7	22	0.05
>0.5	$>0.0''$	<5	>-2	48	141	-93	0.34	53	2.5

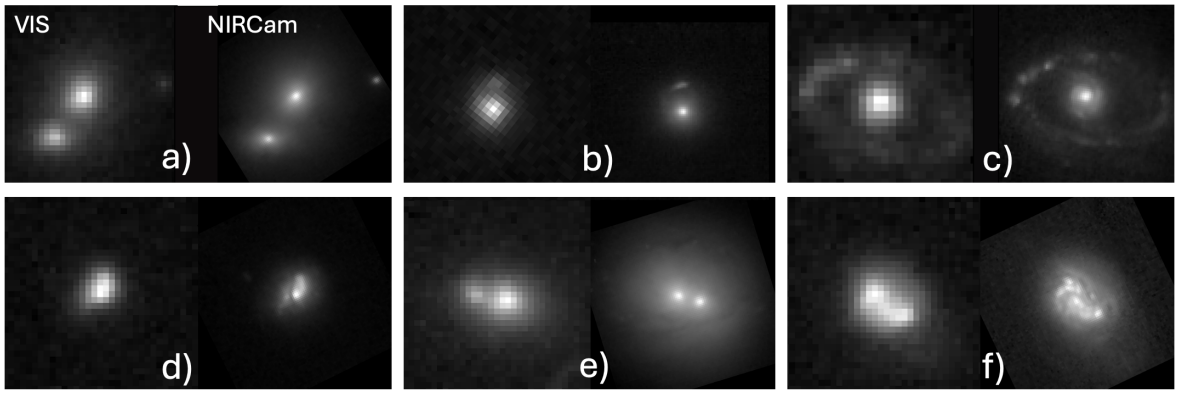

Figure 5.17: VIS and NIRCam/JWST images of objects predicted dual without considering thresholds.

by the clumpiness and the irregular structure of the host galaxy (c, f). Another object presents a more ambiguous scenario (d, shown either in Fig. 5.14): it may be a dual AGN with a separation of $\sim 0.2''$, or alternatively a single AGN whose nuclear emission is covered by a dust lane, creating two distinct components. These examples illustrate some of the limitations of the network when dealing with complex morphologies and highlight the importance of high-resolution imaging for proper classification.

5.3.3 MER catalogue

Working directly on images and building a network made specifically for the dual AGN search is of paramount importance because in many cases the MER catalogue merges two objects with small separation into a single catalogue entry. It is interesting to understand which is the minimum distance between two point sources that allows the MER catalogue to distinguish the two objects and thus list them as two separate entries. To answer this, we calculated for each source in the catalogue the distance to the nearest source and studied in detail the pairs of sources with separations less than $0.8''$. In particular, we studied the minimum distance as a function of the I_{E} and Kron radius. We found that the MER catalogue is not effective for binary sources at distances less than $0.8''$ and with flux ratios > 2. We checked which dual candidates predicted by the neural network are associated with two different entries in the MER catalogue. Of the 32 dual visual inspected sources of class 0 or 1, only one third have double entries in the MER catalogue.

5.3.4 Summary of the CNN appliacation to real data

We found 265 candidates classified as dual systems by the CNN. Using the threshold defined in the previous Section, we identified a sample of 49 objects that fulfil the selection criteria, representing 0.8% of the initial sample. Of these 49 objects, 32 were classified according to the visual inspection as class 0 or 1, eight as class 2, two as class 3, and seven as class 4 or 5, as defined in Sect. 5.3.2. We showed that most systems with projected separations larger than 0.5″ are likely to be LOS contaminants. However, *Euclid*-band photometry allows us to further investigate the nature of these systems. Among the objects with separations greater than 0.5″ and available MER photometry, seven systems have both the primary and the secondary components falling within the AGN selection region defined by Euclid Collaboration: Matamoro Zatarain et al. [2025]. After performing PSF subtraction and adding a host galaxy component when required, we found that only three of these systems lie within the AGN region. In addition to these three, the most reliable candidates are those with smaller separations. These selected systems are reported in Fig. 5.14. All the dual candidates we have found, once we excluded foreground contaminants, represent around the 0.25% of the initial sample.

Table 5.3: Sample Selection

Category	**Number of objects**
QSO catalogue	15317
Selection and avoiding repetition	5993
D/L AGN (CNN w/o threshold)	265
D/L AGN (CNN w/ threshold)	49
" foreground contamination	$\sim$35
" D/L AGN cand. $> 0.45''$ (phot)	3
" D/L AGN cand. $< 0.45''$	$\sim$12
" lens cand.	2

5.4 Discussion

Estimating the true fraction of dual AGN systems remains highly challenging, even when follow-up observations are available. Providing a robust estimate of the dual fraction is beyond the scope of this work. We note that the definition of dual fraction is not always the same in all works, and different definitions may lead to underestimation or overestimation. In this section, we explore how our results compare with cosmological simulations, particularly the Horizon-AGN simulation [Volonteri et al., 2022], and with previous studies.

5.4.1 Comparison with simulation

The dual fraction, i.e., the number of multiple AGN over the total number of AGN, is one of the main predictions of the models of SMBH formation and BH-galaxy coevolu-

tion. Our results are still too preliminary to test these predictions, but it is interesting to compare the number of candidates we select with the results of these predictions.

The Horizon-AGN simulation [Volonteri et al., 2022] predicts a dual fraction of 5% when considering AGN with bolometric luminosities $L_{\rm bol} > 10^{44}$ erg s^{-1} and projected separations less than 30 kpc. From this we can obtain an order-of-magnitude estimate of the expected number of dual AGN in our sample by assuming that the dual fraction does not depend on redshift and bolometric luminosity. This assumption is very simplistic and known not to be true in most cases [Comerford et al., 2015, De Rosa et al., 2019], but can be used to obtain a rough estimate of the expected numbers. Given our parent sample of $\sim$6000 AGN, this implies an expected number of $\sim$300 dual AGN systems with the same selections. In this study, we focused on small projected separation ($< 0.8''$). This threshold excludes about 80% of the dual AGN population predicted by simulations, significantly reducing our expected number of detections. Moreover, our selection requires optical magnitude $I_{\rm E} < 25$, which limits our sample to $L_{\rm bol} > 10^{44}$ erg s^{-1} at $z = 1$ and $L_{\rm bol} > 10^{45}$ erg s^{-1} at $z = 3$. This corresponds to only $\sim$1.8% of the dual AGN population found in Volonteri et al. [2022]. As a result, we expect to identify $5 - 6$ dual AGN within our sample, at redshifts up to $z \sim 3$. It is important to note, however, that the Horizon-AGN simulations do not resolve dual AGN at physical separations below $\sim$4 kpc, corresponding to $0.5''$. This limitation implies that our estimate is a lower bound, particularly at small separations where the majority of dual AGN are likely to reside. In fact, the most reliable candidates found in this work are at separations between $0.2''$ and $0.45''$.

This range of separations is sampled by ROMULUS25 simulations [Tremmel et al., 2017, 2019] presented in Saeedzadeh et al. [2024, Fig. 7], Chen et al. [2023, Astrid], and Steinborn et al. [2016, Magneticum], which show that dual AGN dominate at small separations. Rosas-Guevara et al. [2019] showed that there is not a clear trend in the distribution at small distances (< 15 kpc), while the dual AGN fraction increases around 20 and 25 kpc.

5.4.2 Comparison with other works

Numerous studies have searched for dual AGNs using different selection techniques, including imaging and optical spectroscopy [Hennawi et al., 2006, More et al., 2016, Eftekharzadeh et al., 2017, Mannucci et al., 2022, Scialpi et al., 2023, Jiang et al., 2025], X-ray observations [Koss et al., 2012, Gross et al., 2019, Guainazzi et al., 2021, Sandoval et al., 2023] and radio surveys [Fu et al., 2015, Rubinur et al., 2018, Gross et al., 2019]. Each of these approaches, however, is subject to selection biases. A major observational bias arises from the fact that dual AGNs in the late stages of galaxy mergers are often heavily obscured by dust [Ricci et al., 2017, Koss et al., 2018, Barrows et al., 2023]. Another important limitation is due to the sensitivity and the angular resolution of the instruments employed, which probe different dual AGN populations and different physical scales. As shown in Fig. 24 of Pfeifle et al. [2024], dual AGN candidates reported in the literature are scarce at both high redshift ($z > 0.5$) and small separations (< 5 kpc). These unexplored regions of parameter space can be effectively probed thanks to the capabilities of *Euclid*. The dual AGN fractions reported in previous works are not directly comparable to our estimation, as they depend strongly on the adopted selection criteria as well as on the properties of the systems (e.g., separation, luminosity), but a comparison can still be instructive.

Barrows et al. [2023] reported a dual AGN fractions between 0.2% and 1%, depending on bolometric luminosity and separation, within the redshift range $0.08 < z < 0.58$ and projected separations ranging between 10 and 70 kpc. These values correspond to angular separations between $\sim$ 1″ and $\sim$ 0.6″, i.e. an order of magnitude larger than the physical scales probed in the present work. Li et al. [2024] estimated that the pair fraction increases with redshift, starting at approximately 4.5% at $z \sim 0.5$ and reaching around 22.9% at $z \sim 4.5$. This fraction drops to below 1% when considering only objects with projected separations smaller than 0.8″ as in this work. They found the distribution of projected separations to be relatively flat, but did not identify any pairs with separations smaller than $\sim$2 kpc.

Recently Silverman et al. [2020] found a dual QSO fraction of (0.26 ± 0.18)% from $z = 3$ to $z = 1.5$ with separations of 0.6″ and 4″. Yu et al. [2011] found that 0.02%–0.06% of AGN are dual AGN with double-peaked narrow line features at redshifts of $z \sim$ 0.5–1.2. Rosario et al. [2011] estimated a dual fraction between 0.32% and 0.5%, similar to Fu et al. [2011]. Koss et al. [2012] estimated that, among AGN in the *Swift* BAT sample, the fraction of dual AGN at projected separations of less than 15 kpc is approximately 5% (8 out of 167 systems). In contrast, the corresponding dual AGN fraction among Seyfert galaxies in the SDSS is significantly lower, at only 0.25%. These estimates are all broadly comparable with our results.

5.4.3 Other architectures

We explored the use of Domain-Adversarial Neural Networks (DANN) for domain adaptation, a technique designed to help models generalize when the target domain data (i.e. the real data) is entirely unlabeled, as in our case [Ganin et al., 2015]. The goal of DANN is to learn a mapping between domains such that the features extracted by the network are both discriminative for the task and invariant to domain shifts. This means that the features should have similar distributions in both the source (simulations) and target (data) domains, allowing the model to generalise well to the target domain [Ajakan et al., 2014, Huertas-Company et al., 2024, Belfiore et al., 2025, Ginolfi et al., 2025]. However, our attempt did not provide any improvement on the real data, though the network was able to generalize the features of data and simulations. Minimising the discriminator, we found no improvement in terms of reducing FPs labelled with the visual inspection.

We also used one of the most popular architectures, Resnet18 [He et al., 2016], by adding the last layers for the prediction of system properties as described in Sect. 5.1.4. Although it achieved a training set accuracy of 99%, which was not achieved by the other networks, its performance on the test set and on the real data was worse than the network we used, producing an order of magnitude more FPs compared to our CNN, probably due to overfitting.

We also tried combining different simulations, increasing the size of the training set, but the performance remained similar.

5.5 Conclusion

In this chapter, we applied a CNN to the Euclid Q1 data release to search for close pairs of AGN, a population expected from cosmological models as a consequence of galaxy

mergers. Taking advantage of Euclid's wide-field coverage, high resolution, and sensitivity, we trained the network on realistic image simulations to identify dual or lensed AGN at sub-arcsecond separations (<0.8"). The CNN performs better than traditional detection methods, especially at the smallest separations, achieving high completeness while keeping false positives low. When applied to a sample of around 6,000 quasars, the network revealed a first set of promising dual or lensed AGN candidates. After accounting for statistical uncertainties and possible foreground contamination, we estimated a dual AGN fraction of roughly 0.25%, with an excess of systems at separations below 0.45", where contamination is less. These results demonstrate the potential of ML approaches in future *Euclid* releases to identify dual or lensed AGNs, which should then be confirmed with resolved spectroscopy using JWST.

Chapter 6

Final Remarks

6.1 Summary

In this thesis, we explored the main processes that shape how galaxies grow and evolve. Our focus was on the most active phase of a galaxy, the AGN phase, during which a lot amounts of energy are released from the central black hole and injected into the host galaxy. These so-called feedback phenomena, such as energetic outflows and radio jets, are common in AGN and play a crucial role in regulating galaxy evolution. By studying them, we can understand how galaxies form stars, destroy dust, remove gas, and shape their overall structure. Another major driver of galactic evolution is the merging of galaxies, which can supply new gas, trigger bursts of star formation, fuel black hole activity, or even form additional AGN within the same system.
The thesis is divided into three main parts, in which we analyze these phenomena in detail: starting with radio jets, then outflows, and finally the search for dual AGN.

In the first original chapter, we presented a study of four luminous type 2 AGN (J1000+1242, J1010+1413, J1010+0612, and J1100+0846) with optical observations obtained using the integral field spectrograph MUSE at the VLT. These luminous AGN ($L_{bol} \sim 10^{46}$ erg/s) are classified as radio-quiet, although they host moderate-power ($\sim 10^{44}$ erg/s) radio emission. To study the relationship between the radio emission and the properties of the ionized gas, we combined our optical analysis with the radio analysis carried out by Jarvis et al. [2019] using VLA and e-MERLIN observations. We investigated the kinematics of the ionized gas through the emission line profiles of [OIII]5007 and Hα. We identified the outflowing gas by decoupling a narrow emission component tracing the disk or tidal tails from a broad emission component tracing outflows and turbulent gas in all four targets. We detected extended outflows (up to 15 kpc) with high bulk velocities (up to 1000 km/s) aligned with the jet and AGN ionization cones in the two targets with extended radio emission (J1000+1242 and J1010+1413). The main result of our work is the detection of a strong (up to W70 $\sim$ 1000 km/s) and extended (up to 20 kpc) enhancement in the velocity width of the emission lines perpendicular to the direction of the radio jets and AGN ionization cones in at least two targets of the sample. Other recent works (e.g., Venturi et al. 2021, Girdhar et al. 2022) observed the same phenomenon in other AGN hosting jets with low kinetic power ($P_{jet} < 10^{44}$ erg/s), interpreted as an interaction between the jet and the ISM in the host galaxy disk. Combining our results with those of Venturi et al. [2021], we found a correlation between the kinetic power of the radio emission

and the mass and energy of the ionized gas involved, consistent with the scenario of jet–ISM interaction. The jets are powerful enough to inject the observed kinetic energy into the ISM, suggesting that even low-power jets can represent an important channel of AGN feedback.

In the second original chapter, we present an integral field study resolving the inner kiloparsec of Arp 220 and Mrk231, two ULIRGs undergoing a merger. Using the exceptional capabilities of JWST/NIRSpec, we spatially resolved the ionized (Paα) and hot molecular (H_2 2.12 μm) gas in the nuclear region, allowing us to identify multiple high-velocity, multiphase outflows associated with its two nuclei of Arp220. Modeling these outflows with a new tool for clumpy gas kinematics, MOKA^{3D}, we constrained their intrinsic geometry and kinematics, finding good agreement with standard methods. We detected several distinct outflow components: an hourglass-shaped hot molecular and ionized outflow from the W nucleus extending to ∼600 pc with velocities up to 500 km/s; a compact nuclear ionized outflow in the W nucleus reaching 550 km/s; a conical multiphase outflow from the E nucleus extending at least 400 pc with velocities up to 600 km/s; and a large-scale (∼1 kpc) blueshifted bubble with velocities up to 1100 km/s, aligned with the ∼10 kpc outflow seen in MUSE data. Combining NIRSpec and ALMA results, we derived a hot-to-cold molecular gas ratio of $\sim 10^{-4}$, with the majority of the outflow mass in cold molecular gas (∼20 $M_\odot$ yr^{-1}), followed by ionized (∼10 $M_\odot$ yr^{-1}) and hot molecular gas (∼0.003 $M_\odot$ yr^{-1}). Both star formation and AGN activity could drive these outflows, given the observed SFRs (∼100 $M_\odot$ yr^{-1}), AGN luminosities ($\sim 10^{43} - 10^{44}$ erg/s), mass loading factors (∼ 0.1), and kinetic powers ($\sim 10^{42}$ erg/s). The multidirectional nature of the outflows indicates that each nucleus can significantly impact the host galaxy's ISM, potentially contributing to widespread regulation of star formation. These results demonstrate the unprecedented power of JWST/NIRSpec to disentangle complex nuclear kinematics in ULIRGs and probe the interplay of multiphase outflows during merger-driven galaxy evolution, providing key insights into feedback mechanisms in extreme environments.

We also studied the kinematics of Mrk231 using NIRSpec in the infrared band and MEGARA in the optical band. We first subtracted the stellar continuum emission and the AGN contribution, and then fitted all the recombination lines originating from the BLR using a nuclear integrated spectrum. We then decoupled the contribution of a narrow component tracing a disk surrounding the nucleus, which is also observed in the stellar kinematic study. Despite the high level of nuclear activity in Mrk231, but also in Arp220, the nuclear disk is not destroyed. We also identified two nuclear clumps: one brighter and more compact, located at approximately 860pc east of the nucleus, and one fainter and more elongated located north of the nucleus. Finally, we detected two high-velocity blueshifted clumps further from the nucleus, with velocities of −420 and −900,km,s^{-1}, possibly representing clouds in outflow.

We also detected a prominent nuclear outflow traced by the [O,II] doublet, which extends over ∼1.4,kpc and reaches velocities of ∼2000,km,s^{-1}, with a mass outflow rate of 0.15,$M_\odot$ yr^{-1}, lower than the SFR in the nuclear region of Mrk231. As observed in Arp220, also in Mrk231 the main contribution to the overall mass outflow rate comes from the molecular gas. The ionized component is spatially more extended than the molecular gas, suggesting that it may impact the ISM at larger distances. We also found a possible signature of positive feedback due to the cospatiality between the

[O,II] outflow and a region of enhanced UV continuum. Alternative interpretations are also possible, as the UV continuum could instead arise from AGN light scattered by the outflowing region rather than from local star formation. Given the high complexity of the SED of Mrk231, we attempted to propose a new binary model capable of explaining several observational constraints across multiple wavelength bands, including the radio and FUV regimes. This is particularly relevant because ULIRGs are interacting systems and are therefore suitable environments for hosting dual AGN or binary SMBHs.

In the third chapter, we took advantage of imaging data from Euclid, whose wide area, high sensitivity, and high resolution provide a unique opportunity to identify close AGN pairs predicted by cosmological simulations as a consequence of merging activity. We developed a Convolutional Neural Network (CNN) trained on realistic simulations to search for dual or lensed AGN at sub-arcsec separations (<0.8"). The CNN performs significantly better than classical detection methods, especially at small separations, maintaining high completeness while minimizing false positives. Applying our model to a sample of ∼6000 QSOs, we identified a first set of promising dual/lensed AGN candidates. After estimating foreground contamination and expected false positives, we found a dual AGN fraction of ∼0.25%, with an overdensity at low separations (< 0.45") where contamination is lower. For sources at larger separations (> 0.45"), photometric analysis suggested that three objects could be dual AGN, while most systems are likely foreground contaminants. While our CNN demonstrates promising performance for future Euclid releases, further improvements require refining the simulated training set, including the use of all four Euclid bands. Spectroscopic follow-up and higher-resolution imaging will be critical to confirm candidates, especially at sub-arcsec separations.

The presented work thus provides new insights into the interplay between SMBH and their host galaxies across different evolutionary stages and different phenomena. By combining high-resolution observations and multiwavelength analyses, we have shown that AGN feedback, even in systems with relatively low-power radio jets, can have a significant impact on the surrounding interstellar medium. We also show the morphology of multiphase outflows in ULIRGs and merging galaxies such as Arp 220 and Mrk231, which can potentially influence the nuclear regions across all ISM phases. Moreover, we propose a new binary black hole model for Mrk 231 that could, in principle, be applied to other sources to identify binary candidates. Finally, the development and application of machine learning tools on Euclid data open a promising path toward the systematic discovery of dual AGN, an important population of AGN to understand the black hole co-evolution and the final stages of galaxy merging. Future Euclid releases, complemented by data from JWST, LSST, and Roman, will be key to building a statistical census of dual AGN and constraining models of SMBH growth and galaxy evolution.

6.2 Future Perspectives

One of the fundamental questions in astrophysics is understanding the numerous processes that shape galaxies and drive their evolution. To do this, we need to understand the role and relative importance of each mechanism, from the small-scale physics of star formation and feedback to larger cosmic events such as mergers and interactions.

Studying these processes both individually, within a single galaxy, and collectively, in large sample with similar properties, allows us to build a coherent picture of galaxy evolve over cosmic time.

To conclude this thesis, as we began with a metaphor for life, one could imagine writing the biography of every astrophysical object (as if it were a person), understanding which events shape its behavior, identity, and relationships with others. Mergers could be seen as new friendships or external impulses, while the surrounding environment influences growth, changes, and destiny, just as society shapes a person and the humanity. As important as each of us is, it remains essential to look at the bigger picture, the direction in which humanity, society, technological progress, and our rights are moving. Similarly, as of crucial importance is studying a single galaxy, it is equally important to understand the collective evolution of galaxies. In this thesis, we have tried to address both aspects, starting with the study of a phenomenon in galaxies with similar properties, then we analyzed in depth two galaxies, and finally we use the Euclid survey to quest dual AGN.

What comes next? The combination of VLT/MUSE and JWST/NIRSpec IFS has opened up the possibility of extending current analyses to larger and statistically more significant samples, allowing for a detailed comparison of the kinematic and ionization properties of AGN-driven winds, jets at different evolutionary stages. In particular, future studies could exploit the unprecedented spatial of JWST to resolve the few hundred parsecs inside nearby AGNs, tracing the coupling between outflowing gas, radio jets, star formation, molecular gas reservoirs. It will be possible to study Polycyclic Aromatic Hydrocarbon (PAHs), which provide information on the star formation process on timescales comparable to those of galactic flows, playing a key role in determining whether recent star formation is suppressed or triggered by outflows, or whether both processes can occur simultaneously. The use of MIRI will also be fundamental for tracing PAHs in the mid-IR in order to study their ratios that are indicative of dust distribution and dust grain properties. Moreover, it will be possible to study the faintest coronal lines to better understand their formation, whether due to ionization by the AGN or due to shocks created by the outflow. Finally, in the context of our last project involving Euclid, JWST is the only telescope capable of confirming and characterizing the discovered dual AGN candidates. Unlike the brighter systems identified by Gaia, these sources are significantly fainter and not accessible to observations with ground-based facilities. Thanks to its exceptional sensitivity, JWST can unveil their true nature and provide the crucial link between observations and cosmological models.

These goals clearly belong to the near future. Looking further ahead, the LISA mission will allow us to detect the gravitational waves produced by merging SMBHs, the same systems that we are now starting to identify.

Bibliography

S. Aalto, S. Garcia-Burillo, S. Muller, J. M. Winters, E. Gonzalez-Alfonso, P. van der Werf, C. Henkel, F. Costagliola, and R. Neri. High resolution observations of HCN and HCO^+J = 3-2 in the disk and outflow of Mrk 231. Detection of vibrationally excited HCN in the warped nucleus. , 574:A85, February 2015. doi: 10.1051/0004-6361/201423987.

Sandro Ackermann, Kevin Schawinski, Ce Zhang, Anna K. Weigel, and M. Dennis Turp. Using transfer learning to detect galaxy mergers. , 479(1):415–425, September 2018. doi: 10.1093/mnras/sty1398.

Gabriella Agazie, Akash Anumarlapudi, Anne M. Archibald, Zaven Arzoumanian, Paul T. Baker, Bence Bécsy, Laura Blecha, Adam Brazier, Paul R. Brook, Sarah Burke-Spolaor, J. Andrew Casey-Clyde, Maria Charisi, Shami Chatterjee, Tyler Cohen, James M. Cordes, Neil J. Cornish, Fronefield Crawford, H. Thankful Cromartie, Kathryn Crowter, Megan E. DeCesar, Paul B. Demorest, Timothy Dolch, Brendan Drachler, Elizabeth C. Ferrara, William Fiore, Emmanuel Fonseca, Gabriel E. Freedman, Emiko Gardiner, Nate Garver-Daniels, Peter A. Gentile, Joseph Glaser, Deborah C. Good, Kayhan Gültekin, Jeffrey S. Hazboun, Ross J. Jennings, Aaron D. Johnson, Megan L. Jones, Andrew R. Kaiser, David L. Kaplan, Luke Zoltan Kelley, Matthew Kerr, Joey S. Key, Nima Laal, Michael T. Lam, William G. Lamb, T. Joseph W. Lazio, Natalia Lewandowska, Tingting Liu, Duncan R. Lorimer, Jing Luo, Ryan S. Lynch, Chung-Pei Ma, Dustin R. Madison, Alexander McEwen, James W. McKee, Maura A. McLaughlin, Natasha McMann, Bradley W. Meyers, Chiara M. F. Mingarelli, Andrea Mitridate, Cherry Ng, David J. Nice, Stella Koch Ocker, Ken D. Olum, Timothy T. Pennucci, Benetge B. P. Perera, Nihan S. Pol, Henri A. Radovan, Scott M. Ransom, Paul S. Ray, Joseph D. Romano, Shashwat C. Sardesai, Ann Schmiedekamp, Carl Schmiedekamp, Kai Schmitz, Levi Schult, Brent J. Shapiro-Albert, Xavier Siemens, Joseph Simon, Magdalena S. Siwek, Ingrid H. Stairs, Daniel R. Stinebring, Kevin Stovall, Abhimanyu Susobhanan, Joseph K. Swiggum, Stephen R. Taylor, Jacob E. Turner, Caner Unal, Michele Vallisneri, Sarah J. Vigeland, Haley M. Wahl, Caitlin A. Witt, and Olivia Young. The NANOGrav 15 yr Data Set: Search for Anisotropy in the Gravitational-wave Background. , 956(1):L3, October 2023. doi: 10.3847/2041-8213/acf4fd.

J. Aird, D. M. Alexander, D. R. Ballantyne, F. Civano, A. Del-Moro, R. C. Hickox, G. B. Lansbury, J. R. Mullaney, F. E. Bauer, W. N. Brandt, A. Comastri, A. C. Fabian, P. Gandhi, F. A. Harrison, B. Luo, D. Stern, E. Treister, L. Zappacosta, M. Ajello, R. Assef, M. Baloković, S. E. Boggs, M. Brightman, F. E. Christensen, W. W. Craig, M. Elvis, K. Forster, B. W. Grefenstette, C. J. Hailey, M. Koss, S. M. LaMassa, K. K. Madsen, S. Puccetti, C. Saez, C. M. Urry, D. R. Wik, and W. Zhang.

The NuSTAR Extragalactic Survey: First Direct Measurements of the $\gtrsim$10 KeV X-Ray Luminosity Function for Active Galactic Nuclei at z>0.1. , 815(1):66, December 2015. doi: 10.1088/0004-637X/815/1/66.

Hana Ajakan, Pascal Germain, Hugo Larochelle, François Laviolette, and Mario Marchand. Domain-Adversarial Neural Networks. *arXiv e-prints*, art. arXiv:1412.4446, December 2014. doi: 10.48550/arXiv.1412.4446.

Hollis B. Akins, Caitlin M. Casey, Natalie Allen, Micaela B. Bagley, Mark Dickinson, Steven L. Finkelstein, Maximilien Franco, Santosh Harish, Pablo Arrabal Haro, Olivier Ilbert, Jeyhan S. Kartaltepe, Anton M. Koekemoer, Daizhong Liu, Arianna S. Long, Henry Joy McCracken, Louise Paquereau, Casey Papovich, Nor Pirzkal, Jason Rhodes, Brant E. Robertson, Marko Shuntov, Sune Toft, Guang Yang, Guillermo Barro, Laura Bisigello, Véronique Buat, Jaclyn B. Champagne, Olivia Cooper, Luca Costantin, Alexander de La Vega, Nicole E. Drakos, Andreas Faisst, Adriano Fontana, Seiji Fujimoto, Steven Gillman, Carlos Gómez-Guijarro, Ghassem Gozaliasl, Nimish P. Hathi, Christopher C. Hayward, Michaela Hirschmann, Benne W. Holwerda, Shuowen Jin, Dale D. Kocevski, Vasily Kokorev, Erini Lambrides, Ray A. Lucas, Georgios E. Magdis, Benjamin Magnelli, Jed McKinney, Bahram Mobasher, Pablo G. Pérez-González, R. Michael Rich, Lise-Marie Seillé, Margherita Talia, C. Megan Urry, Francesco Valentino, Katherine E. Whitaker, L. Y. Aaron Yung, Jorge Zavala, Cosmos-Web Team, and Ceers Team. Two Massive, Compact, and Dust-obscured Candidate z 8 Galaxies Discovered by JWST. , 956(1):61, October 2023. doi: 10.3847/1538-4357/acef21.

K. Alatalo, P. N. Appleton, U. Lisenfeld, T. Bitsakis, L. Lanz, M. Lacy, V. Charmandaris, M. Cluver, M. A. Dopita, P. Guillard, T. Jarrett, L. J. Kewley, K. Nyland, P. M. Ogle, J. Rasmussen, J. A. Rich, L. Verdes-Montenegro, C. K. Xu, and M. Yun. Star Formation Suppression in Compact Group Galaxies: A New Path to Quenching? , 812(2):117, October 2015. doi: 10.1088/0004-637X/812/2/117.

A. Alonso Herrero, L. Hermosa Muñoz, A. Labiano, P. Guillard, V. A. Buiten, D. Dicken, P. van der Werf, J. Álvarez-Márquez, T. Böker, L. Colina, A. Eckart, M. García-Marín, O. C. Jones, L. Pantoni, P. G. Pérez-González, D. Rouan, M. J. Ward, M. Baes, G. Östlin, P. Royer, G. S. Wright, M. Güdel, Th. Henning, P.-O. Lagage, and E. F. van Dishoeck. MICONIC: JWST/MIRI MRS observations of the nuclear and circumnuclear regions of Mrk 231. , 690:A95, October 2024. doi: 10.1051/0004-6361/202450071.

Pau Amaro-Seoane, Jeff Andrews, Manuel Arca Sedda, Abbas Askar, Quentin Baghi, Razvan Balasov, Imre Bartos, Simone S. Bavera, Jillian Bellovary, Christopher P. L. Berry, Emanuele Berti, Stefano Bianchi, Laura Blecha, Stéphane Blondin, Tamara Bogdanović, Samuel Boissier, Matteo Bonetti, Silvia Bonoli, Elisa Bortolas, Katelyn Breivik, Pedro R. Capelo, Laurentiu Caramete, Federico Cattorini, Maria Charisi, Sylvain Chaty, Xian Chen, Martyna Chruślińska, Alvin J. K. Chua, Ross Church, Monica Colpi, Daniel D'Orazio, Camilla Danielski, Melvyn B. Davies, Pratika Dayal, Alessandra De Rosa, Andrea Derdzinski, Kyriakos Destounis, Massimo Dotti, Ioana Duţan, Irina Dvorkin, Gaia Fabj, Thierry Foglizzo, Saavik Ford, Jean-Baptiste Fouvry, Alessia Franchini, Tassos Fragos, Chris Fryer, Massimo Gaspari, Davide Gerosa, Luca Graziani, Paul Groot, Melanie Habouzit, Daryl Haggard, Zoltan Haiman,

Wen-Biao Han, Alina Istrate, Peter H. Johansson, Fazeel Mahmood Khan, Tomas Kimpson, Kostas Kokkotas, Albert Kong, Valeriya Korol, Kyle Kremer, Thomas Kupfer, Astrid Lamberts, Shane Larson, Mike Lau, Dongliang Liu, Nicole Lloyd-Ronning, Giuseppe Lodato, Alessandro Lupi, Chung-Pei Ma, Tomas Maccarone, Ilya Mandel, Alberto Mangiagli, Michela Mapelli, Stéphane Mathis, Lucio Mayer, Sean McGee, Berry McKernan, M. Coleman Miller, David F. Mota, Matthew Mumpower, Syeda S. Nasim, Gijs Nelemans, Scott Noble, Fabio Pacucci, Francesca Panessa, Vasileios Paschalidis, Hugo Pfister, Delphine Porquet, John Quenby, Angelo Ricarte, Friedrich K. Röpke, John Regan, Stephan Rosswog, Ashley Ruiter, Milton Ruiz, Jessie Runnoe, Raffaella Schneider, Jeremy Schnittman, Amy Secunda, Alberto Sesana, Naoki Seto, Lijing Shao, Stuart Shapiro, Carlos Sopuerta, Nicholas C. Stone, Arthur Suvorov, Nicola Tamanini, Tomas Tamfal, Thomas Tauris, Karel Temmink, John Tomsick, Silvia Toonen, Alejandro Torres-Orjuela, Martina Toscani, Antonios Tsokaros, Caner Unal, Verónica Vázquez-Aceves, Rosa Valiante, Maurice van Putten, Jan van Roestel, Christian Vignali, Marta Volonteri, Kinwah Wu, Ziri Younsi, Shenghua Yu, Silvia Zane, Lorenz Zwick, Fabio Antonini, Vishal Baibhav, Enrico Barausse, Alexander Bonilla Rivera, Marica Branchesi, Graziella Branduardi-Raymont, Kevin Burdge, Srija Chakraborty, Jorge Cuadra, Kristen Dage, Benjamin Davis, Selma E. de Mink, Roberto Decarli, Daniela Doneva, Stephanie Escoffier, Poshak Gandhi, Francesco Haardt, Carlos O. Lousto, Samaya Nissanke, Jason Nordhaus, Richard O'Shaughnessy, Simon Portegies Zwart, Adam Pound, Fabian Schussler, Olga Sergijenko, Alessandro Spallicci, Daniele Vernieri, and Alejandro Vigna-Gómez. Astrophysics with the Laser Interferometer Space Antenna. *Living Reviews in Relativity*, 26(1):2, December 2023. doi: 10.1007/s41114-022-00041-y.

R. R. J. Antonucci and J. S. Miller. Spectropolarimetry and the nature of NGC 1068. , 297:621–632, October 1985. doi: 10.1086/163559.

L. Armus, V. Charmandaris, J. Bernard-Salas, H. W. W. Spoon, J. A. Marshall, S. J. U. Higdon, V. Desai, H. I. Teplitz, L. Hao, D. Devost, B. R. Brandl, Y. Wu, G. C. Sloan, B. T. Soifer, J. R. Houck, and T. L. Herter. Observations of Ultraluminous Infrared Galaxies with the Infrared Spectrograph on the Spitzer Space Telescope. II. The IRAS Bright Galaxy Sample. , 656(1):148–167, February 2007. doi: 10.1086/510107.

L. Armus, T. Lai, V. U, K. L. Larson, T. Diaz-Santos, A. S. Evans, M. A. Malkan, J. Rich, A. M. Medling, D. R. Law, H. Inami, F. Muller-Sanchez, V. Charmandaris, P. van der Werf, S. Stierwalt, S. Linden, G. C. Privon, L. Barcos-Muñoz, C. Hayward, Y. Song, P. Appleton, S. Aalto, T. Bohn, T. Böker, M. J. I. Brown, L. Finnerty, J. Howell, K. Iwasawa, F. Kemper, J. Marshall, J. M. Mazzarella, J. McKinney, E. J. Murphy, D. Sanders, and J. Surace. GOALS-JWST: Mid-infrared Spectroscopy of the Nucleus of NGC 7469. , 942(2):L37, January 2023. doi: 10.3847/2041-8213/acac66.

S. Arribas, L. Colina, A. Alonso-Herrero, F. F. Rosales-Ortega, A. Monreal-Ibero, M. García-Marín, S. García-Burillo, and J. Rodríguez-Zaurín. Integral field spectroscopy based Hα sizes of local luminous and ultraluminous infrared galaxies. A direct comparison with high-z massive star-forming galaxies. , 541:A20, May 2012. doi: 10.1051/0004-6361/201118007.

S. Arribas, L. Colina, E. Bellocchi, R. Maiolino, and M. Villar-Martín. Ionized gas

outflows and global kinematics of low-z luminous star-forming galaxies. , 568:A14, August 2014. doi: 10.1051/0004-6361/201323324.

Santiago Arribas, Luis Colina, and David Clements. Two-dimensional Kinematical and Ionization Structure of the Warm Gas in the Nuclear Regions of Arp 220. , 560(1): 160–167, October 2001. doi: 10.1086/322768.

R. J. Assef, D. Stern, G. Noirot, H. D. Jun, R. M. Cutri, and P. R. M. Eisenhardt. The WISE AGN Catalog. , 234(2):23, February 2018. doi: 10.3847/1538-4365/aaa00a.

Astropy Collaboration, Thomas P. Robitaille, Erik J. Tollerud, Perry Greenfield, Michael Droettboom, Erik Bray, Tom Aldcroft, Matt Davis, Adam Ginsburg, Adrian M. Price-Whelan, Wolfgang E. Kerzendorf, Alexander Conley, Neil Crighton, Kyle Barbary, Demitri Muna, Henry Ferguson, Frédéric Grollier, Madhura M. Parikh, Prasanth H. Nair, Hans M. Günther, Christoph Deil, Julien Woillez, Simon Conseil, Roban Kramer, James E. H. Turner, Leo Singer, Ryan Fox, Benjamin A. Weaver, Victor Zabalza, Zachary I. Edwards, K. Azalee Bostroem, D. J. Burke, Andrew R. Casey, Steven M. Crawford, Nadia Dencheva, Justin Ely, Tim Jenness, Kathleen Labrie, Pey Lian Lim, Francesco Pierfederici, Andrew Pontzen, Andy Ptak, Brian Refsdal, Mathieu Servillat, and Ole Streicher. Astropy: A community python package for astronomy. *A&A*, 558:A33, sep 2013. doi: 10.1051/0004-6361/201322068.

Hyun-Jin Bae and Jong-Hak Woo. A Census of Gas Outflows in Type 2 Active Galactic Nuclei. , 795(1):30, November 2014. doi: 10.1088/0004-637X/795/1/30.

J. A. Baldwin, M. M. Phillips, and R. Terlevich. Classification parameters for the emission-line spectra of extragalactic objects. , 93:5–19, February 1981a. doi: 10.1086/130766.

J. A. Baldwin, M. M. Phillips, and R. Terlevich. Classification parameters for the emission-line spectra of extragalactic objects. , 93:5–19, February 1981b.

B. Balmaverde, A. Marconi, M. Brusa, S. Carniani, G. Cresci, E. Lusso, R. Maiolino, F. Mannucci, and T. Nagao. Is there any evidence that ionized outflows quench star formation in type 1 quasars at z $<$ 1? , 585:A148, January 2016. doi: 10.1051/0004-6361/201526694.

L. Barcos-Muñoz, A. K. Leroy, A. S. Evans, G. C. Privon, L. Armus, J. Condon, J. M. Mazzarella, D. S. Meier, E. Momjian, E. J. Murphy, J. Ott, A. Reichardt, K. Sakamoto, D. B. Sanders, E. Schinnerer, S. Stierwalt, J. A. Surace, T. A. Thompson, and F. Walter. High-resolution Radio Continuum Measurements of the Nuclear Disks of Arp 220. , 799(1):10, January 2015. doi: 10.1088/0004-637X/799/1/10.

Loreto Barcos-Muñoz, Susanne Aalto, Todd A. Thompson, Kazushi Sakamoto, Sergio Martín, Adam K. Leroy, George C. Privon, Aaron S. Evans, and Amanda Kepley. Fast, Collimated Outflow in the Western Nucleus of Arp 220. , 853(2):L28, February 2018a. doi: 10.3847/2041-8213/aaa28d.

Loreto Barcos-Muñoz, Susanne Aalto, Todd A. Thompson, Kazushi Sakamoto, Sergio Martín, Adam K. Leroy, George C. Privon, Aaron S. Evans, and Amanda Kepley. Fast, Collimated Outflow in the Western Nucleus of Arp 220. , 853(2):L28, February 2018b. doi: 10.3847/2041-8213/aaa28d.

Guillermo Barro, Pablo G. Perez-Gonzalez, Dale D. Kocevski, Elizabeth J. McGrath, Gene C. K. Leung, Fergus Cullen, James S. Dunlop, Richard S. Ellis, Steven L. Finkelstein, Norman A. Grogin, Garth Illingworth, Jeyhan S. Kartaltepe, Anton M. Koekemoer, Ray A. Lucas, Ross J. McLure, and Guang Yang. A Comprehensive Photometric Selection of 'Little Red Dots' in MIRI Fields: An IR-Bright LRD at $z = 3.1386$ with Warm Dust Emission. *arXiv e-prints*, art. arXiv:2412.01887, December 2024. doi: 10.48550/arXiv.2412.01887.

R. Scott Barrows, Claud H. Sandberg Lacy, Julia Kennefick, Julia M. Comerford, Daniel Kennefick, and Joel C. Berrier. Identification of Outflows and Candidate Dual Active Galactic Nuclei in SDSS Quasars at z = 0.8-1.6. , 769(2):95, June 2013. doi: 10.1088/0004-637X/769/2/95.

R. Scott Barrows, Julia M. Comerford, Daniel Stern, and Roberto J. Assef. A Census of WISE-selected Dual and Offset AGNs Across the Sky: New Constraints on Merger-driven Triggering of Obscured AGNs. , 951(2):92, July 2023. doi: 10.3847/1538-4357/acd2d3.

Manuel A. Bautista and Anil K. Pradhan. Ionization Structure and Spectra of Iron in Gaseous Nebulae. , 492(2):650–676, January 1998. doi: 10.1086/305061.

M. C. Begelman, R. D. Blandford, and M. J. Rees. Massive black hole binaries in active galactic nuclei. , 287(5780):307–309, September 1980. doi: 10.1038/287307a0.

Mitchell C. Begelman, Roger D. Blandford, and Martin J. Rees. Theory of extragalactic radio sources. *Reviews of Modern Physics*, 56(2):255–351, April 1984. doi: 10.1103/RevModPhys.56.255.

Francesco Belfiore, Kyle B. Westfall, Adam Schaefer, Michele Cappellari, Xihan Ji, Matthew A. Bershady, Christy Tremonti, David R. Law, Renbin Yan, Kevin Bundy, Shravan Shetty, Niv Drory, Daniel Thomas, Eric Emsellem, and Sebastián F. Sánchez. The Data Analysis Pipeline for the SDSS-IV MaNGA IFU Galaxy Survey: Emission-line Modeling. , 158(4):160, October 2019. doi: 10.3847/1538-3881/ab3e4e.

Francesco Belfiore, Michele Ginolfi, Guillermo Blanc, Mederic Boquien, Melanie Chevance, Enrico Congiu, Simon C. O. Glover, Brent Groves, Ralf S. Klessen, J. Eduardo Méndez-Delgado, and Thomas G. Williams. Machine learning the gap between real and simulated nebulae: A domain-adaptation approach to classify ionised nebulae in nearby galaxies. , 694:A212, February 2025. doi: 10.1051/0004-6361/202451934.

Eric F. Bell, Daniel H. McIntosh, Neal Katz, and Martin D. Weinberg. The Optical and Near-Infrared Properties of Galaxies. I. Luminosity and Stellar Mass Functions. , 149(2):289–312, December 2003. doi: 10.1086/378847.

E. Bellocchi, M. Pereira-Santaella, L. Colina, A. Labiano, M. Sánchez-García, A. Alonso-Herrero, S. Arribas, S. García-Burillo, M. Villar-Martín, D. Rigopoulou, F. Valentino, A. Puglisi, T. Díaz-Santos, S. Cazzoli, and A. Usero. Compact molecular gas emission in local LIRGs among low- and high-z galaxies. , 664:A60, August 2022. doi: 10.1051/0004-6361/202142802.

Enrica Bellocchi, Santiago Arribas, Luis Colina, and Daniel Miralles-Caballero. VLT/VIMOS integral field spectroscopy of luminous and ultraluminous infrared galaxies: 2D kinematic properties. , 557:A59, September 2013. doi: 10.1051/0004-6361/201221019.

C. L. Bennett, D. Larson, J. L. Weiland, and G. Hinshaw. The 1% Concordance Hubble Constant. , 794(2):135, October 2014. doi: 10.1088/0004-637X/794/2/135.

E. Bertin and S. Arnouts. SExtractor: Software for source extraction. , 117:393–404, June 1996. doi: 10.1051/aas:1996164.

P. N. Best and T. M. Heckman. On the fundamental dichotomy in the local radio-AGN population: accretion, evolution and host galaxy properties. , 421(2):1569–1582, April 2012. doi: 10.1111/j.1365-2966.2012.20414.x.

M. Bianchin, R. A. Riffel, T. Storchi-Bergmann, R. Riffel, D. Ruschel-Dutra, C. M. Harrison, L. G. Dahmer-Hahn, V. Mainieri, A. J. Schönell, and N. Z. Dametto. Gemini NIFS survey of feeding and feedback in nearby active galaxies - V. Molecular and ionized gas kinematics. , 510(1):639–657, February 2022. doi: 10.1093/mnras/stab3468.

J. Biedermann, F. Marin, and T. Barnouin. Polarimetric insights into a potential binary supermassive black hole system in Mrk 231. , 698:A107, June 2025. doi: 10.1051/0004-6361/202553694.

L. Bîrzan, D. A. Rafferty, B. R. McNamara, M. W. Wise, and P. E. J. Nulsen. A Systematic Study of Radio-induced X-Ray Cavities in Clusters, Groups, and Galaxies. , 607(2):800–809, June 2004. doi: 10.1086/383519.

L. Bîrzan, B. R. McNamara, P. E. J. Nulsen, C. L. Carilli, and M. W. Wise. Radiative Efficiency and Content of Extragalactic Radio Sources: Toward a Universal Scaling Relation between Jet Power and Radio Power. , 686(2):859–880, October 2008. doi: 10.1086/591416.

M. Bischetti, E. Piconcelli, G. Vietri, A. Bongiorno, F. Fiore, E. Sani, A. Marconi, F. Duras, L. Zappacosta, M. Brusa, A. Comastri, G. Cresci, C. Feruglio, E. Giallongo, F. La Franca, V. Mainieri, F. Mannucci, S. Martocchia, F. Ricci, R. Schneider, V. Testa, and C. Vignali. The WISSH quasars project. I. Powerful ionised outflows in hyper-luminous quasars. , 598:A122, February 2017. doi: 10.1051/0004-6361/201629301.

M. Bischetti, R. Maiolino, S. Carniani, F. Fiore, E. Piconcelli, and A. Fluetsch. Widespread QSO-driven outflows in the early Universe. , 630:A59, October 2019. doi: 10.1051/0004-6361/201833557.

M. Bischetti, C. Feruglio, E. Piconcelli, F. Duras, M. Pérez-Torres, R. Herrero, G. Venturi, S. Carniani, G. Bruni, I. Gavignaud, V. Testa, A. Bongiorno, M. Brusa, C. Circosta, G. Cresci, V. D'Odorico, R. Maiolino, A. Marconi, M. Mingozzi, C. Pappalardo, M. Perna, E. Traianou, A. Travascio, G. Vietri, L. Zappacosta, and F. Fiore. The WISSH quasars project. IX. Cold gas content and environment of luminous QSOs at z $\sim$ 2.4-4.7. , 645:A33, January 2021. doi: 10.1051/0004-6361/202039057.

Laura E Blecha. Modeling Dual Active Galactic Nuclei in Mergers: Unique Probes of Black Hole Inspiral and Growth. NSF Award Number 1715413. Directorate for Mathematical and Physical Sciences, Division Of Astronomical Sciences. 2017., September 2017.

J. S. Bloom, J. W. Richards, P. E. Nugent, R. M. Quimby, M. M. Kasliwal, D. L. Starr, D. Poznanski, E. O. Ofek, S. B. Cenko, N. R. Butler, S. R. Kulkarni, A. Gal-Yam, and N. Law. Automating Discovery and Classification of Transients and Variable Stars in the Synoptic Survey Era. , 124(921):1175, November 2012. doi: 10.1086/668468.

Katherine M. Blundell and Steve Rawlings. The Spectra and Energies of Classical Double Radio Lobes. , 119(3):1111–1122, March 2000. doi: 10.1086/301254.

J. J. Bock, G. Neugebauer, K. Matthews, B. T. Soifer, E. E. Becklin, M. Ressler, K. Marsh, M. W. Werner, E. Egami, and R. Blandford. High Spatial Resolution Imaging of NGC 1068 in the Mid-Infrared. , 120(6):2904–2919, December 2000. doi: 10.1086/316871.

Thomas Bohn, Hanae Inami, Aditya Togi, Lee Armus, Thomas S. Y. Lai, Loreto Barcos-Munoz, Yiqing Song, Sean T. Linden, Jason Surace, Marina Bianchin, Vivian U, Aaron S. Evans, Torsten Böker, Matthew A. Malkan, Kirsten L. Larson, Sabrina Stierwalt, Victorine A. Buiten, Vassilis Charmandaris, Tanio Diaz-Santos, Justin H. Howell, George C. Privon, Claudio Ricci, Paul P. van der Werf, Susanne Aalto, Christopher C. Hayward, Justin A. Kader, Joseph M. Mazzarella, Francisco Muller-Sanchez, and David B. Sanders. GOALS-JWST: The Warm Molecular Outflows of the Merging Starburst Galaxy NGC 3256. *arXiv e-prints*, art. arXiv:2403.14751, March 2024. doi: 10.48550/arXiv.2403.14751.

T. Böker, S. Arribas, N. Lützgendorf, C. Alves de Oliveira, T. L. Beck, S. Birkmann, A. J. Bunker, S. Charlot, G. de Marchi, P. Ferruit, G. Giardino, P. Jakobsen, N. Kumari, M. López-Caniego, R. Maiolino, E. Manjavacas, A. Marston, S. H. Moseley, J. Muzerolle, P. Ogle, N. Pirzkal, B. Rauscher, T. Rawle, H.-W. Rix, E. Sabbi, B. Sargent, M. Sirianni, M. te Plate, J. Valenti, C. J. Willott, and P. Zeidler. The near-infrared spectrograph (NIRSpec) on the ijames webb/i space telescope. *A&A*, 661:A82, may 2022. doi: 10.1051/0004-6361/202142589.

F. Bournaud and F. Combes. Gas accretion on spiral galaxies: Bar formation and renewal. , 392:83–102, September 2002. doi: 10.1051/0004-6361:20020920.

R. G. Bower, A. J. Benson, and Robert A. Crain. What shapes the galaxy mass function? Exploring the roles of supernova-driven winds and active galactic nuclei. , 422(4):2816–2840, June 2012. doi: 10.1111/j.1365-2966.2012.20516.x.

Andrew P. Bradley. The use of the area under the ROC curve in the evaluation of machine learning algorithms. *Pattern Recognition*, 30(7):1145–1159, January 1997. doi: 10.1016/S0031-3203(96)00142-2.

Larry Bradley, Brigitta Sipőcz, Thomas Robitaille, Erik Tollerud, Zé Vinícius, Christoph Deil, Kyle Barbary, Tom J Wilson, Ivo Busko, Axel Donath, Hans Moritz Günther, Mihai Cara, Krachyon, Simon Conseil, Azalee Bostroem, Michael Droettboom, E. M. Bray, P. L. Lim, Lars Andersen Bratholm, Geert Barentsen, Matt

Craig, Shivangee Rathi, Sergio Pascual, Gabriel Perren, Iskren Y. Georgiev, Miguel De Val-Borro, Wolfgang Kerzendorf, Yoonsoo P. Bach, Bruno Quint, and Harrison Souchereau. astropy/photutils: 1.3.0, December 2021.

M. Brusa, A. Bongiorno, G. Cresci, M. Perna, A. Marconi, V. Mainieri, R. Maiolino, M. Salvato, E. Lusso, P. Santini, A. Comastri, F. Fiore, R. Gilli, F. La Franca, G. Lanzuisi, D. Lutz, A. Merloni, M. Mignoli, F. Onori, E. Piconcelli, D. Rosario, C. Vignali, and G. Zamorani. X-shooter reveals powerful outflows in z $\sim$ 1.5 X-ray selected obscured quasi-stellar objects. , 446(3):2394–2417, January 2015a. doi: 10.1093/mnras/stu2117.

M. Brusa, C. Feruglio, G. Cresci, V. Mainieri, M. T. Sargent, M. Perna, P. Santini, F. Vito, A. Marconi, A. Merloni, D. Lutz, E. Piconcelli, G. Lanzuisi, R. Maiolino, D. Rosario, E. Daddi, A. Bongiorno, F. Fiore, and E. Lusso. Evidence for feedback in action from the molecular gas content in the z ~1.6 outflowing QSO XID2028. , 578:A11, June 2015b. doi: 10.1051/0004-6361/201425491.

M. Brusa, G. Cresci, E. Daddi, R. Paladino, M. Perna, A. Bongiorno, E. Lusso, M. T. Sargent, V. Casasola, C. Feruglio, F. Fraternali, I. Georgiev, V. Mainieri, S. Carniani, A. Comastri, F. Duras, F. Fiore, F. Mannucci, A. Marconi, E. Piconcelli, G. Zamorani, R. Gilli, F. La Franca, G. Lanzuisi, D. Lutz, P. Santini, N. Z. Scoville, C. Vignali, F. Vito, S. Rabien, L. Busoni, and M. Bonaglia. Molecular outflow and feedback in the obscured quasar XID2028 revealed by ALMA. , 612:A29, April 2018. doi: 10.1051/0004-6361/201731641.

Daniela Calzetti, Lee Armus, Ralph C. Bohlin, Anne L. Kinney, Jan Koornneef, and Thaisa Storchi-Bergmann. The Dust Content and Opacity of Actively Star-forming Galaxies. , 533(2):682–695, April 2000. doi: 10.1086/308692.

Pedro R. Capelo, Marta Volonteri, Massimo Dotti, Jillian M. Bellovary, Lucio Mayer, and Fabio Governato. Growth and activity of black holes in galaxy mergers with varying mass ratios. , 447(3):2123–2143, March 2015. doi: 10.1093/mnras/stu2500.

Pedro R. Capelo, Massimo Dotti, Marta Volonteri, Lucio Mayer, Jillian M. Bellovary, and Sijing Shen. A survey of dual active galactic nuclei in simulations of galaxy mergers: frequency and properties. , 469(4):4437–4454, August 2017. doi: 10.1093/mnras/stx1067.

Michele Cappellari. Improving the full spectrum fitting method: accurate convolution with Gauss-Hermite functions. , 466(1):798–811, April 2017. doi: 10.1093/mnras/stw3020.

Michele Cappellari and Yannick Copin. Adaptive spatial binning of integral-field spectroscopic data using Voronoi tessellations. , 342(2):345–354, June 2003. doi: 10.1046/j.1365-8711.2003.06541.x.

Michele Cappellari and Eric Emsellem. Parametric Recovery of Line-of-Sight Velocity Distributions from Absorption-Line Spectra of Galaxies via Penalized Likelihood. , 116(816):138–147, February 2004. doi: 10.1086/381875.

Michele Cappellari, Eric Emsellem, R. Bacon, M. Bureau, Roger L. Davies, P. T. de Zeeuw, Jesús Falcón-Barroso, Davor Krajnović, Harald Kuntschner, Richard M. McDermid, Reynier F. Peletier, Marc Sarzi, Remco C. E. van den Bosch, and Glenn van de Ven. The SAURON project - X. The orbital anisotropy of elliptical and lenticular galaxies: revisiting the (V/σ,) diagram with integral-field stellar kinematics. , 379 (2):418–444, August 2007. doi: 10.1111/j.1365-2966.2007.11963.x.

Michele Cappellari, N. Neumayer, J. Reunanen, P. P. van der Werf, P. T. de Zeeuw, and H. W. Rix. The mass of the black hole in Centaurus A from SINFONI AO-assisted integral-field observations of stellar kinematics. , 394(2):660–674, April 2009. doi: 10.1111/j.1365-2966.2008.14377.x.

Jason A. Cardelli, Geoffrey C. Clayton, and John S. Mathis. The Relationship between Infrared, Optical, and Ultraviolet Extinction. , 345:245, October 1989. doi: 10.1086/167900.

S. Carniani, A. Marconi, R. Maiolino, B. Balmaverde, M. Brusa, M. Cano-Díaz, C. Cicone, A. Comastri, G. Cresci, F. Fiore, C. Feruglio, F. La Franca, V. Mainieri, F. Mannucci, T. Nagao, H. Netzer, E. Piconcelli, G. Risaliti, R. Schneider, and O. Shemmer. Ionised outflows in z ~2.4 quasar host galaxies. , 580:A102, August 2015. doi: 10.1051/0004-6361/201526557.

Caitlin M. Casey, Desika Narayanan, and Asantha Cooray. Dusty star-forming galaxies at high redshift. *Phy. Reports*, 541(2):45–161, August 2014. ISSN 03701573. doi: 10.1016/j.physrep.2014.02.009. URL `http://linkinghub.elsevier.com/retrieve/pii/S0370157314000477`.

K. W. Cavagnolo, B. R. McNamara, P. E. J. Nulsen, C. L. Carilli, C. Jones, and L. Bîrzan. A Relationship Between AGN Jet Power and Radio Power. , 720(2):1066–1072, September 2010. doi: 10.1088/0004-637X/720/2/1066.

S. Cazzoli, S. Arribas, R. Maiolino, and L. Colina. Neutral gas outflows in nearby [U]LIRGs via optical NaD feature. , 590:A125, May 2016. doi: 10.1051/0004-6361/201526788.

Rupali Chandar, Miranda Caputo, Sean Linden, Angus Mok, Bradley C. Whitmore, Daniela Calzetti, Debra M. Elmegreen, Janice C. Lee, Leonardo Ubeda, Richard White, and David O. Cook. Arp 220: A Post-starburst Galaxy with Little Current Star Formation outside of Its Nuclear Disks. , 943(2):142, February 2023. doi: 10.3847/1538-4357/acac96.

M. Charisi, I. Bartos, Z. Haiman, A. M. Price-Whelan, M. J. Graham, E. C. Bellm, R. R. Laher, and S. Márka. A population of short-period variable quasars from PTF as supermassive black hole binary candidates. , 463(2):2145–2171, December 2016. doi: 10.1093/mnras/stw1838.

Edmond Chaussidon, Christophe Yèche, Nathalie Palanque-Delabrouille, David M. Alexander, Jinyi Yang, Steven Ahlen, Stephen Bailey, David Brooks, Zheng Cai, Solène Chabanier, Tamara M. Davis, Kyle Dawson, Axel de laMacorra, Arjun Dey, Biprateep Dey, Sarah Eftekharzadeh, Daniel J. Eisenstein, Kevin Fanning, Andreu Font-Ribera, Enrique Gaztañaga, Satya Gontcho A Gontcho, Alma X. Gonzalez-Morales, Julien Guy, Hiram K. Herrera-Alcantar, Klaus Honscheid, Mustapha Ishak,

Linhua Jiang, Stephanie Juneau, Robert Kehoe, Theodore Kisner, Andras Kovács, Anthony Kremin, Ting-Wen Lan, Martin Landriau, Laurent Le Guillou, Michael E. Levi, Christophe Magneville, Paul Martini, Aaron M. Meisner, John Moustakas, Andrea Muñoz-Gutiérrez, Adam D. Myers, Jeffrey A. Newman, Jundan Nie, Will J. Percival, Claire Poppett, Francisco Prada, Anand Raichoor, Corentin Ravoux, Ashley J. Ross, Edward Schlafly, David Schlegel, Ting Tan, Gregory Tarlé, Rongpu Zhou, Zhimin Zhou, and Hu Zou. Target Selection and Validation of DESI Quasars. , 944(1):107, February 2023. doi: 10.3847/1538-4357/acb3c2.

Nianyi Chen, Tiziana Di Matteo, Yueying Ni, Michael Tremmel, Colin DeGraf, Yue Shen, A. Miguel Holgado, Simeon Bird, Rupert Croft, and Yu Feng. Properties and evolution of dual and offset AGN in the ASTRID simulation at z 2. , 522(2): 1895–1913, June 2023. doi: 10.1093/mnras/stad834.

Zuyi Chen, Daniel P. Stark, Charlotte Mason, Michael W. Topping, Lily Whitler, Mengtao Tang, Ryan Endsley, and Stéphane Charlot. JWST spectroscopy of z 5-8 UV-selected galaxies: new constraints on the evolution of the Ly α escape fraction in the reionization era. , 528(4):7052–7075, March 2024. doi: 10.1093/mnras/stae455.

John Chisholm, Christy A. Tremonti, Claus Leitherer, and Yanmei Chen. The mass and momentum outflow rates of photoionized galactic outflows. , 469(4):4831–4849, August 2017. doi: 10.1093/mnras/stx1164.

C. Cicone, C. Feruglio, R. Maiolino, F. Fiore, E. Piconcelli, N. Menci, H. Aussel, and E. Sturm. The physics and the structure of the quasar-driven outflow in Mrk 231. , 543:A99, July 2012. doi: 10.1051/0004-6361/201218793.

C. Cicone, R. Maiolino, E. Sturm, J. Graciá-Carpio, C. Feruglio, R. Neri, S. Aalto, R. Davies, F. Fiore, J. Fischer, S. García-Burillo, E. González-Alfonso, S. Hailey-Dunsheath, E. Piconcelli, and S. Veilleux. Massive molecular outflows and evidence for AGN feedback from CO observations. , 562:A21, February 2014. doi: 10.1051/0004-6361/201322464.

Claudia Cicone, Marcella Brusa, Cristina Ramos Almeida, Giovanni Cresci, Bernd Husemann, and Vincenzo Mainieri. The largely unconstrained multiphase nature of outflows in AGN host galaxies. *Nature Astronomy*, 2:176–178, February 2018. doi: 10.1038/s41550-018-0406-3.

Luis Colina, Santiago Arribas, and David Clements. INTEGRAL Field Spectroscopy of the Extended Ionized Gas in Arp 220. , 602(1):181–189, February 2004. doi: 10.1086/380958.

Adrian A. Collister and Ofer Lahav. ANNz: Estimating Photometric Redshifts Using Artificial Neural Networks. , 116(818):345–351, April 2004. doi: 10.1086/383254.

F. Combes, S. García-Burillo, V. Casasola, L. Hunt, M. Krips, A. J. Baker, F. Boone, A. Eckart, I. Marquez, R. Neri, E. Schinnerer, and L. J. Tacconi. ALMA observations of feeding and feedback in nearby Seyfert galaxies: an AGN-driven outflow in NGC 1433. , 558:A124, October 2013. doi: 10.1051/0004-6361/201322288.

F. Combes, A. Audibert, S. Garcia-Burillo, L. Hunt, S. Aalto, V. Casasola, K. Dasyra, A. Eckart, M. Krips, S. Martin, S. Muller, K. Sakamoto, P. van der Werf, and S. Viti. High resolution mapping of molecular tori with ALMA. *arXiv e-prints*, art. arXiv:2509.08635, September 2025. doi: 10.48550/arXiv.2509.08635.

Julia M. Comerford, Brian F. Gerke, Daniel Stern, Michael C. Cooper, Benjamin J. Weiner, Jeffrey A. Newman, Kristin Madsen, and R. Scott Barrows. Kiloparsec-scale Spatial Offsets in Double-peaked Narrow-line Active Galactic Nuclei. I. Markers for Selection of Compelling Dual Active Galactic Nucleus Candidates. , 753(1):42, July 2012. doi: 10.1088/0004-637X/753/1/42.

Julia M. Comerford, David Pooley, R. Scott Barrows, Jenny E. Greene, Nadia L. Zakamska, Greg M. Madejski, and Michael C. Cooper. Merger-driven Fueling of Active Galactic Nuclei: Six Dual and Offset AGNs Discovered with Chandra and Hubble Space Telescope Observations. , 806(2):219, June 2015. doi: 10.1088/0004-637X/806/2/219.

A. Concas, P. Popesso, M. Brusa, V. Mainieri, and D. Thomas. Two-face(s): ionized and neutral gas winds in the local Universe. , 622:A188, February 2019. doi: 10.1051/0004-6361/201732152.

Alice Concas, Roberto Maiolino, Mirko Curti, Connor Hayden-Pawson, Michele Cirasuolo, Gareth C. Jones, Amata Mercurio, Francesco Belfiore, Giovanni Cresci, Fergus Cullen, Filippo Mannucci, Alessandro Marconi, Michele Cappellari, Claudia Cicone, Yingjie Peng, and Paulina Troncoso. Being KLEVER at cosmic noon: Ionized gas outflows are inconspicuous in low-mass star-forming galaxies but prominent in massive AGN hosts. , 513(2):2535–2562, June 2022. doi: 10.1093/mnras/stac1026.

A. J. Connolly, I. Csabai, A. S. Szalay, D. C. Koo, R. G. Kron, and J. A. Munn. Slicing Through Multicolor Space: Galaxy Redshifts from Broadband Photometry. , 110:2655, December 1995. doi: 10.1086/117720.

Christopher J. Conselice. The relationship between stellar light distributions of galaxies and their formation histories. *ApJS*, 147(1):1–28, jul 2003. doi: 10.1086/375001.

Tiago Costa, Debora Sijacki, and Martin G. Haehnelt. Feedback from active galactic nuclei: energy- versus momentum-driving. *MNRAS*, 444(3):2355–2376, sep 2014. doi: 10.1093/mnras/stu1632.

Tiago Costa, Joakim Rosdahl, Debora Sijacki, and Martin G. Haehnelt. Quenching star formation with quasar outflows launched by trapped IR radiation. , 479(2):2079–2111, September 2018. doi: 10.1093/mnras/sty1514.

G. S. Couto, T. Storchi-Bergmann, D. J. Axon, A. Robinson, P. Kharb, and R. A. Riffel. Kinematics and excitation of the nuclear spiral in the active galaxy Arp 102B. In *Revista Mexicana de Astronomia y Astrofisica Conference Series*, volume 44 of *Revista Mexicana de Astronomia y Astrofisica Conference Series*, pages 191–192, October 2014.

Guilherme S. Couto, Thaisa Storchi-Bergmann, David J. Axon, Andrew Robinson, Preeti Kharb, and Rogemar A. Riffel. Kinematics and excitation of the nuclear

spiral in the active galaxy Arp 102B. , 435(4):2982–3000, November 2013. doi: 10.1093/mnras/stt1491.

Michael Crawshaw. Multi-Task Learning with Deep Neural Networks: A Survey. *arXiv e-prints*, art. arXiv:2009.09796, September 2020. doi: 10.48550/arXiv.2009.09796.

G. Cresci, G. Tozzi, M. Perna, M. Brusa, C. Marconcini, A. Marconi, S. Carniani, M. Brienza, M. Giroletti, F. Belfiore, M. Ginolfi, F. Mannucci, L. Ulivi, J. Scholtz, G. Venturi, S. Arribas, H. Übler, F. D'Eugenio, M. Mingozzi, B. Balmaverde, A. Capetti, E. Parlanti, and T. Zana. Bubbles and outflows: The novel JWST/NIRSpec view of the z = 1.59 obscured quasar XID2028. , 672:A128, April 2023a. doi: 10.1051/0004-6361/202346001.

G. Cresci, G. Tozzi, M. Perna, M. Brusa, C. Marconcini, A. Marconi, S. Carniani, M. Brienza, M. Giroletti, F. Belfiore, M. Ginolfi, F. Mannucci, L. Ulivi, J. Scholtz, G. Venturi, S. Arribas, H. Übler, F. D'Eugenio, M. Mingozzi, B. Balmaverde, A. Capetti, E. Parlanti, and T. Zana. Bubbles and outflows: The novel JWST/NIRSpec view of the z = 1.59 obscured quasar XID2028. , 672:A128, April 2023b. doi: 10.1051/0004-6361/202346001.

A. Crespo Gómez, J. Piqueras López, S. Arribas, M. Pereira-Santaella, L. Colina, and B. Rodríguez del Pino. Stellar kinematics in the nuclear regions of nearby LIRGs with VLT-SINFONI. Comparison with gas phases and implications for dynamical mass estimations. , 650:A149, June 2021. doi: 10.1051/0004-6361/202039472.

S. M. Croom, R. J. Smith, B. J. Boyle, T. Shanks, L. Miller, P. J. Outram, and N. S. Loaring. The 2dF QSO Redshift Survey - XII. The spectroscopic catalogue and luminosity function. , 349(4):1397–1418, April 2004. doi: 10.1111/j.1365-2966.2004.07619.x.

Scott F. Daniel, Andrew Connolly, Jeff Schneider, Jake Vanderplas, and Liang Xiong. Classification of Stellar Spectra with Local Linear Embedding. , 142(6):203, December 2011. doi: 10.1088/0004-6256/142/6/203.

C. J. Davis, B. Cervantes, B. Nisini, T. Giannini, M. Takami, E. Whelan, M. D. Smith, T. P. Ray, A. Chrysostomou, and T. S. Pyo. VLT integral field spectroscopy of embedded protostars: using near-infrared emission lines as tracers of accretion and outflow. , 528:A3, April 2011. doi: 10.1051/0004-6361/201015897.

Timothy A. Davis, Kate Rowlands, James R. Allison, Stanislav S. Shabala, Yuan-Sen Ting, Claudia del P. Lagos, Sugata Kaviraj, Nathan Bourne, Loretta Dunne, Steve Eales, Rob. J. Ivison, Steve Maddox, Daniel J. B. Smith, Matthew W. L. Smith, and Pasquale Temi. Molecular and atomic gas in dust lane early-type galaxies - I. Low star formation efficiencies in minor merger remnants. , 449(4):3503–3516, June 2015. doi: 10.1093/mnras/stv597.

Alessandra De Rosa, Cristian Vignali, Tamara Bogdanović, Pedro R. Capelo, Maria Charisi, Massimo Dotti, Bernd Husemann, Elisabeta Lusso, Lucio Mayer, Zsolt Paragi, Jessie Runnoe, Alberto Sesana, Lisa Steinborn, Stefano Bianchi, Monica Colpi, Luciano del Valle, Sándor Frey, Krisztina É. Gabányi, Margherita Giustini, Matteo Guainazzi, Zoltan Haiman, Noelia Herrera Ruiz, Rubén Herrero-Illana,

Kazushi Iwasawa, S. Komossa, Davide Lena, Nora Loiseau, Miguel Perez-Torres, Enrico Piconcelli, and Marta Volonteri. The quest for dual and binary supermassive black holes: A multi-messenger view. , 86:101525, December 2019. doi: 10.1016/j.newar.2020.101525.

Roberto Decarli, Fabian Walter, Bram P. Venemans, Eduardo Bañados, Frank Bertoldi, Chris Carilli, Xiaohui Fan, Emanuele Paolo Farina, Chiara Mazzucchelli, Dominik Riechers, Hans-Walter Rix, Michael A. Strauss, Ran Wang, and Yujin Yang. An ALMA [c ii] survey of 27 quasars atz 5.94. *ApJ*, 854(2):97, feb 2018. doi: 10.3847/1538-4357/aaa5aa.

A. Dekel and J. Silk. The Origin of Dwarf Galaxies, Cold Dark Matter, and Biased Galaxy Formation. , 303:39, April 1986. doi: 10.1086/164050.

A. Del Moro, D. M. Alexander, J. R. Mullaney, E. Daddi, M. Pannella, F. E. Bauer, A. Pope, M. Dickinson, D. Elbaz, P. D. Barthel, M. A. Garrett, W. N. Brandt, V. Charmandaris, R. R. Chary, K. Dasyra, R. Gilli, R. C. Hickox, H. S. Hwang, R. J. Ivison, S. Juneau, E. Le Floc'h, B. Luo, G. E. Morrison, E. Rovilos, M. T. Sargent, and Y. Q. Xue. GOODS-Herschel: radio-excess signature of hidden AGN activity in distant star-forming galaxies. , 549:A59, January 2013. doi: 10.1051/0004-6361/201219880.

M. Delli Veneri, S. Cavuoti, M. Brescia, G. Longo, and G. Riccio. Star formation rates for photometric samples of galaxies using machine learning methods. , 486(1): 1377–1391, June 2019. doi: 10.1093/mnras/stz856.

Francesco D'Eugenio, Pablo Perez-Gonzalez, Roberto Maiolino, Jan Scholtz, Michele Perna, Chiara Circosta, Hannah Uebler, Santiago Arribas, Torsten Boeker, Andrew Bunker, Stefano Carniani, Stephane Charlot, Jacopo Chevallard, Giovanni Cresci, Emma Curtis-Lake, Gareth Jones, Nimisha Kumari, Isabella Lamperti, Tobias Looser, Eleonora Parlanti, Hans-Walter Rix, Brant Robertson, Bruno Rodriguez Del Pino, Sandro Tacchella, Giacomo Venturi, and Chris Willott. A fast-rotator post-starburst galaxy quenched by supermassive black-hole feedback at z=3. *arXiv e-prints*, art. arXiv:2308.06317, August 2023. doi: 10.48550/arXiv.2308.06317.

Tiziana Di Matteo, Volker Springel, and Lars Hernquist. Energy input from quasars regulates the growth and activity of black holes and their host galaxies. , 433(7026): 604–607, February 2005. doi: 10.1038/nature03335.

M. A. DiPompeo, R. C. Hickox, C. M. Carroll, J. C. Runnoe, J. R. Mullaney, and T. C. Fischer. The [O III] Profiles of Infrared-selected Active Galactic Nuclei: More Powerful Outflows in the Obscured Population. , 856(1):76, March 2018. doi: 10.3847/1538-4357/aab365.

A. D'Isanto and K. L. Polsterer. Photometric redshift estimation via deep learning. Generalized and pre-classification-less, image based, fully probabilistic redshifts. , 609:A111, January 2018. doi: 10.1051/0004-6361/201731326.

A. Domínguez, B. Siana, A. L. Henry, C. Scarlata, A. G. Bedregal, M. Malkan, H. Atek, N. R. Ross, J. W. Colbert, H. I. Teplitz, M. Rafelski, P. McCarthy, A. Bunker, N. P. Hathi, A. Dressler, C. L. Martin, and D. Masters. Dust Extinction from Balmer Decrements of Star-forming Galaxies at 0.75 <= z <=

1.5 with Hubble Space Telescope/Wide-Field-Camera 3 Spectroscopy from the WFC3 Infrared Spectroscopic Parallel Survey. , 763(2):145, February 2013. doi: 10.1088/0004-637X/763/2/145.

Qiao Duan, Qiong Li, Christopher J. Conselice, Thomas Harvey, Duncan Austin, Nathan J. Adams, Leonardo Ferreira, Kenneth J. Duncan, James Trussler, Robert G. Pascalau, Rogier A. Windhorst, Benne W. Holwerda, Thomas J. Broadhurst, Dan Coe, Seth H. Cohen, Xiaojing Du, Simon P. Driver, Brenda Frye, Norman A. Grogin, Nimish P. Hathi, Rolf A. Jansen, Anton M. Koekemoer, Madeline A. Marshall, Mario Nonino, Rafael Ortiz, III, Nor Pirzkal, Aaron Robotham, Russell E. Ryan, Jr, Jake Summers, Jordan C. J. D'Silva, Christopher N. A. Willmer, and Haojing Yan. Galaxy Mergers in the Epoch of Reionization II: Major Merger-Triggered Star Formation and AGN Activities at $z = 4.5$-8.5. *arXiv e-prints*, art. arXiv:2411.04944, November 2024. doi: 10.48550/arXiv.2411.04944.

Antoine Dumont, Nadine Neumayer, Anil C. Seth, Torsten Böker, Michael Eracleous, Kameron Goold, Jenny E. Greene, Kayhan Gültekin, Luis C. Ho, Jonelle L. Walsh, and Nora Lützgendorf. WIggle Corrector Kit for NIRSpEc Data: WICKED. *arXiv e-prints*, art. arXiv:2503.09697, March 2025. doi: 10.48550/arXiv.2503.09697.

Kenneth Duncan, Christopher J. Conselice, Carl Mundy, Eric Bell, Jennifer Donley, Audrey Galametz, Yicheng Guo, Norman A. Grogin, Nimish Hathi, Jeyhan Kartaltepe, Dale Kocevski, Anton M. Koekemoer, Pablo G. Pérez-González, Kameswara B. Mantha, Gregory F. Snyder, and Mauro Stefanon. Observational Constraints on the Merger History of Galaxies since z $\approx$ 6: Probabilistic Galaxy Pair Counts in the CANDELS Fields. , 876(2):110, May 2019. doi: 10.3847/1538-4357/ab148a.

Mark Durré and Jeremy Mould. The AGN Ionization Cones of NGC 5728. II. Kinematics. , 870(1):37, January 2019. doi: 10.3847/1538-4357/aaf000.

S. Eftekharzadeh, A. D. Myers, J. F. Hennawi, S. G. Djorgovski, G. T. Richards, A. A. Mahabal, and M. J. Graham. Clustering on very small scales from a large sample of confirmed quasar pairs: does quasar clustering track from Mpc to kpc scales? , 468 (1):77–90, June 2017. doi: 10.1093/mnras/stx412.

Sara L. Ellison, David R. Patton, Luc Simard, Alan W. McConnachie, Ivan K. Baldry, and J. Trevor Mendel. Galaxy pairs in the Sloan Digital Sky Survey - II. The effect of environment on interactions. , 407(3):1514–1528, September 2010. doi: 10.1111/j.1365-2966.2010.17076.x.

Sara L. Ellison, David R. Patton, J. Trevor Mendel, and Jillian M. Scudder. Galaxy pairs in the sloan digital sky survey - IV. interactions trigger active galactic nuclei. *MNRAS*, 418(3):2043–2053, sep 2011. doi: 10.1111/j.1365-2966.2011.19624.x.

Sara L. Ellison, Scott Wilkinson, Joanna Woo, Ho-Hin Leung, Vivienne Wild, Robert W. Bickley, David R. Patton, Salvatore Quai, and Stephen Gwyn. Galaxy mergers can rapidly shut down star formation. , 517(1):L92–L96, November 2022. doi: 10.1093/mnrasl/slac109.

B. H. C. Emonts, L. Colina, J. Piqueras-López, S. Garcia-Burillo, M. Pereira-Santaella, S. Arribas, A. Labiano, and A. Alonso-Herrero. Outflows of hot molecular gas in

ultra-luminous infrared galaxies mapped with VLT-SINFONI. , 607:A116, November 2017. doi: 10.1051/0004-6361/201731508.

H. Engel, R. I. Davies, R. Genzel, L. J. Tacconi, E. Sturm, and D. Downes. Arp 220: Extinction and Merger-induced Star Formation. , 729(1):58, March 2011a. doi: 10.1088/0004-637X/729/1/58.

H. Engel, R. I. Davies, R. Genzel, L. J. Tacconi, E. Sturm, and D. Downes. Arp 220: Extinction and Merger-induced Star Formation. , 729(1):58, March 2011b. doi: 10.1088/0004-637X/729/1/58.

Michael Eracleous, Todd A. Boroson, Jules P. Halpern, and Jia Liu. A Large Systematic Search for Close Supermassive Binary and Rapidly Recoiling Black Holes. , 201(2): 23, August 2012. doi: 10.1088/0067-0049/201/2/23.

H. Euclid Collaboration: Aussel, I. Tereno, M. Schirmer, et al. Euclid Quick Data Release (Q1) - Data release overview. *A&A, submitted (Euclid Q1 SI)*, art. arXiv:2503.15302, March 2025.

M. Euclid Collaboration: Cropper, A. Al-Bahlawan, J. Amiaux, et al. Euclid - ii. the vis instrument. *A&A*, 697:A2, 2025. doi: 10.1051/0004-6361/202450996. URL `https://doi.org/10.1051/0004-6361/202450996`.

K. Euclid Collaboration: Jahnke, W. Gillard, M. Schirmer, et al. Euclid - iii. the nisp instrument. *A&A*, 697:A3, 2025. doi: 10.1051/0004-6361/202450786. URL `https://doi.org/10.1051/0004-6361/202450786`.

T. Euclid Collaboration: Matamoro Zatarain, S. Fotopoulou, F. Ricci, et al. Euclid Quick Data Release (Q1). The active galaxies of Euclid. *A&A, submitted (Euclid Q1 SI)*, art. arXiv:2503.15320, March 2025.

E. Euclid Collaboration: Romelli, M. Kümmel, H. Dole, et al. Euclid Quick Data Release (Q1). From images to multiwavelength catalogues: the Euclid MERge Processing Function. *A&A, in press (Euclid Q1 SI), https://doi.org/10.1051/0004-6361/202554586*, art. arXiv:2503.15305, March 2025.

R. Euclid Collaboration: Scaramella, J. Amiaux, Y. Mellier, et al. Euclid preparation. I. The Euclid Wide Survey. , 662:A112, June 2022. doi: 10.1051/0004-6361/202141938.

Euclid Quick Release Q1. `https://doi.org/10.57780/esa-2853f3b`, 2025.

A. C. Fabian. Observational Evidence of Active Galactic Nuclei Feedback. , 50:455–489, September 2012. doi: 10.1146/annurev-astro-081811-125521.

A. C. Fabian, J. S. Sanders, C. S. Crawford, C. J. Conselice, J. S. Gallagher, and R. F. G. Wyse. The relationship between the optical Hα filaments and the X-ray emission in the core of the Perseus cluster. , 344(3):L48–L52, September 2003. doi: 10.1046/j.1365-8711.2003.06856.x.

A. C. Fabian, A. Lohfink, E. Kara, M. L. Parker, R. Vasudevan, and C. S. Reynolds. Properties of AGN coronae in the NuSTAR era. , 451(4):4375–4383, August 2015. doi: 10.1093/mnras/stv1218.

J. Falcón-Barroso, P. Sánchez-Blázquez, A. Vazdekis, E. Ricciardelli, N. Cardiel, A. J. Cenarro, J. Gorgas, and R. F. Peletier. An updated MILES stellar library and stellar population models. , 532:A95, August 2011. doi: 10.1051/0004-6361/201116842.

E. A. Fath. Bulletin Number 149 - The spectra of some spiral nebulae and globular star clusters. *Lick Observatory Bulletin*, 5:71–77, 1908.

G. J. Ferland, M. Chatzikos, F. Guzmán, M. L. Lykins, P. A. M. van Hoof, R. J. R. Williams, N. P. Abel, N. R. Badnell, F. P. Keenan, R. L. Porter, and P. C. Stancil. The 2017 release of cloudy. *Revista Mexicana de Astronomía y Astrofísica*, 53:385–438, 2017.

Antonia Fernández-Figueroa, Glenn G. Kacprzak, Tania M. Barone, Nikole M. Nielsen, Kate H. R. Rubin, Andrew J. Pitts, and Barbara Mazzilli Ciraulo. Ultra-strong Mg II absorbers trace both inflowing and outflowing gas: insights from dual down-the-barrel and quasar sightlines. , October 2025. doi: 10.1093/mnras/staf1712.

Laura Ferrarese and David Merritt. A Fundamental Relation between Supermassive Black Holes and Their Host Galaxies. , 539(1):L9–L12, August 2000. doi: 10.1086/312838.

Leonardo Ferreira, Christopher J. Conselice, Kenneth Duncan, Ting-Yun Cheng, Alex Griffiths, and Amy Whitney. Galaxy Merger Rates up to z $\sim$ 3 Using a Bayesian Deep Learning Model: A Major-merger Classifier Using IllustrisTNG Simulation Data. , 895(2):115, June 2020. doi: 10.3847/1538-4357/ab8f9b.

Leonardo Ferreira, Christopher J. Conselice, Elizaveta Sazonova, Fabricio Ferrari, Joseph Caruana, Clár-Bríd Tohill, Geferson Lucatelli, Nathan Adams, Dimitrios Irodotou, Madeline A. Marshall, Will J. Roper, Christopher C. Lovell, Aprajita Verma, Duncan Austin, James Trussler, and Stephen M. Wilkins. The JWST Hubble Sequence: The Rest-frame Optical Evolution of Galaxy Structure at $1.5 < z < 6.5$. , 955(2):94, October 2023. doi: 10.3847/1538-4357/acec76.

C. Feruglio, R. Maiolino, E. Piconcelli, N. Menci, H. Aussel, A. Lamastra, and F. Fiore. Quasar feedback revealed by giant molecular outflows. , 518:L155, July 2010. doi: 10.1051/0004-6361/201015164.

C. Feruglio, F. Fiore, S. Carniani, E. Piconcelli, L. Zappacosta, A. Bongiorno, C. Cicone, R. Maiolino, A. Marconi, N. Menci, S. Puccetti, and S. Veilleux. The multiphase winds of Markarian 231: from the hot, nuclear, ultra-fast wind to the galaxy-scale, molecular outflow. , 583:A99, November 2015. doi: 10.1051/0004-6361/201526020.

Kristian Finlator and Romeel Davé. The origin of the galaxy mass-metallicity relation and implications for galactic outflows. , 385(4):2181–2204, April 2008. doi: 10.1111/j.1365-2966.2008.12991.x.

Carolina Finlez, Neil M. Nagar, Thaisa Storchi-Bergmann, Allan Schnorr-Müller, Rogemar A. Riffel, Davide Lena, C. G. Mundell, and Martin S. Elvis. The complex jet- and bar-perturbed kinematics in NGC 3393 as revealed with ALMA and GEMINI-GMOS/IFU. , 479(3):3892–3908, September 2018. doi: 10.1093/mnras/sty1555.

F. Fiore, C. Feruglio, F. Shankar, M. Bischetti, A. Bongiorno, M. Brusa, S. Carniani, C. Cicone, F. Duras, A. Lamastra, V. Mainieri, A. Marconi, N. Menci, R. Maiolino, E. Piconcelli, G. Vietri, and L. Zappacosta. AGN wind scaling relations and the co-evolution of black holes and galaxies. , 601:A143, May 2017. doi: 10.1051/0004-6361/201629478.

J. Fischer, E. Sturm, E. González-Alfonso, J. Graciá-Carpio, S. Hailey-Dunsheath, A. Poglitsch, A. Contursi, D. Lutz, R. Genzel, A. Sternberg, A. Verma, and L. Tacconi. Herschel-PACS spectroscopic diagnostics of local ULIRGs: Conditions and kinematics in Markarian 231. , 518:L41, July 2010. doi: 10.1051/0004-6361/201014676.

Eric Wim Flesch. The Million Quasars (Milliquas) Catalogue, v8. *The Open Journal of Astrophysics*, 6:49, December 2023. doi: 10.21105/astro.2308.01505.

A. Fluetsch, R. Maiolino, S. Carniani, A. Marconi, C. Cicone, M. A. Bourne, T. Costa, A. C. Fabian, W. Ishibashi, and G. Venturi. Cold molecular outflows in the local Universe and their feedback effect on galaxies. , 483(4):4586–4614, March 2019. doi: 10.1093/mnras/sty3449.

A. Fluetsch, R. Maiolino, S. Carniani, S. Arribas, F. Belfiore, E. Bellocchi, S. Cazzoli, C. Cicone, G. Cresci, A. C. Fabian, R. Gallagher, W. Ishibashi, F. Mannucci, A. Marconi, M. Perna, E. Sturm, and G. Venturi. Properties of the multiphase outflows in local (ultra)luminous infrared galaxies. , 505(4):5753–5783, August 2021. doi: 10.1093/mnras/stab1666.

Adi Foord, Nico Cappelluti, Tingting Liu, Marta Volonteri, Melanie Habouzit, Fabio Pacucci, Stefano Marchesi, Nianyi Chen, Tiziana Di Matteo, Labani Mallick, and Michael Koss. Tracking Supermassive Black Hole Mergers from kpc to sub-pc Scales with AXIS. *Universe*, 10(6):237, May 2024. doi: 10.3390/universe10060237.

N. M. Förster Schreiber, H. Übler, R. L. Davies, R. Genzel, E. Wisnioski, S. Belli, T. Shimizu, D. Lutz, M. Fossati, R. Herrera-Camus, J. T. Mendel, L. J. Tacconi, D. Wilman, A. Beifiori, G. B. Brammer, A. Burkert, C. M. Carollo, R. I. Davies, F. Eisenhauer, M. Fabricius, S. J. Lilly, I. Momcheva, T. Naab, E. J. Nelson, S. H. Price, A. Renzini, R. Saglia, A. Sternberg, P. van Dokkum, and S. Wuyts. The KMOS^{3D} Survey: Demographics and Properties of Galactic Outflows at z = 0.6-2.7. , 875(1):21, April 2019. doi: 10.3847/1538-4357/ab0ca2.

J. Frank and M. J. Rees. Effects of massive black holes on dense stellar systems. , 176: 633–647, September 1976. doi: 10.1093/mnras/176.3.633.

I. C. Freitas, R. A. Riffel, T. Storchi-Bergmann, M. Elvis, A. Robinson, D. M. Crenshaw, N. M. Nagar, D. Lena, H. R. Schmitt, and S. B. Kraemer. Outflows in the narrow-line region of bright Seyfert galaxies - I. GMOS-IFU data. , 476(2):2760–2778, May 2018. doi: 10.1093/mnras/sty303.

H. Fu, L. Yan, A. D. Myers, A. Stockton, S. G. Djorgovski, G. Aldering, and J. A. Rich. The Nature of Double-peaked [O III] Active Galactic Nuclei. , 745:67, January 2012. doi: 10.1088/0004-637X/745/1/67.

Hai Fu, Adam D. Myers, S. G. Djorgovski, and Lin Yan. Mergers in Double-peaked [O III] Active Galactic Nuclei. , 733(2):103, June 2011. doi: 10.1088/0004-637X/733/2/103.

Hai Fu, A. D. Myers, S. G. Djorgovski, Lin Yan, J. M. Wrobel, and A. Stockton. Radio-selected Binary Active Galactic Nuclei from the Very Large Array Stripe 82 Survey. , 799(1):72, January 2015. doi: 10.1088/0004-637X/799/1/72.

Lukas J. Furtak, Ivo Labbé, Adi Zitrin, Jenny E. Greene, Pratika Dayal, Iryna Chemerynska, Vasily Kokorev, Tim B. Miller, Andy D. Goulding, Anna de Graaff, Rachel Bezanson, Gabriel B. Brammer, Sam E. Cutler, Joel Leja, Richard Pan, Sedona H. Price, Bingjie Wang, John R. Weaver, Katherine E. Whitaker, Hakim Atek, Ákos Bogdán, Stéphane Charlot, Emma Curtis-Lake, Pieter van Dokkum, Ryan Endsley, Robert Feldmann, Yoshinobu Fudamoto, Seiji Fujimoto, Karl Glazebrook, Stéphanie Juneau, Danilo Marchesini, Micheal V. Maseda, Erica Nelson, Pascal A. Oesch, Adèle Plat, David J. Setton, Daniel P. Stark, and Christina C. Williams. A high black-hole-to-host mass ratio in a lensed AGN in the early Universe. , 628 (8006):57–61, April 2024. doi: 10.1038/s41586-024-07184-8.

J. M. Gabor, R. Davé, B. D. Oppenheimer, and K. Finlator. Quenching massive galaxies with on-the-fly feedback in cosmological hydrodynamic simulations. , 417 (4):2676–2695, November 2011. doi: 10.1111/j.1365-2966.2011.19430.x.

Gaia Collaboration, T. Prusti, J. H. J. de Bruijne, A. G. A. Brown, A. Vallenari, C. Babusiaux, C. A. L. Bailer-Jones, U. Bastian, M. Biermann, D. W. Evans, L. Eyer, F. Jansen, C. Jordi, S. A. Klioner, U. Lammers, L. Lindegren, X. Luri, F. Mignard, D. J. Milligan, C. Panem, V. Poinsignon, D. Pourbaix, S. Randich, G. Sarri, P. Sartoretti, H. I. Siddiqui, C. Soubiran, V. Valette, F. van Leeuwen, N. A. Walton, C. Aerts, F. Arenou, M. Cropper, R. Drimmel, E. Høg, D. Katz, M. G. Lattanzi, W. O'Mullane, E. K. Grebel, A. D. Holland, C. Huc, X. Passot, L. Bramante, C. Cacciari, J. Castañeda, L. Chaoul, N. Cheek, F. De Angeli, C. Fabricius, R. Guerra, J. Hernández, A. Jean-Antoine-Piccolo, E. Masana, R. Messineo, N. Mowlavi, K. Nienartowicz, D. Ordóñez-Blanco, P. Panuzzo, J. Portell, P. J. Richards, M. Riello, G. M. Seabroke, P. Tanga, F. Thévenin, J. Torra, S. G. Els, G. Gracia-Abril, G. Comoretto, M. Garcia-Reinaldos, T. Lock, E. Mercier, M. Altmann, R. Andrae, T. L. Astraatmadja, I. Bellas-Velidis, K. Benson, J. Berthier, R. Blomme, G. Busso, B. Carry, A. Cellino, G. Clementini, S. Cowell, O. Creevey, J. Cuypers, M. Davidson, J. De Ridder, A. de Torres, L. Delchambre, A. Dell'Oro, C. Ducourant, Y. Frémat, M. García-Torres, E. Gosset, J. L. Halbwachs, N. C. Hambly, D. L. Harrison, M. Hauser, D. Hestroffer, S. T. Hodgkin, H. E. Huckle, A. Hutton, G. Jasniewicz, S. Jordan, M. Kontizas, A. J. Korn, A. C. Lanzafame, M. Manteiga, A. Moitinho, K. Muinonen, J. Osinde, E. Pancino, T. Pauwels, J. M. Petit, A. Recio-Blanco, A. C. Robin, L. M. Sarro, C. Siopis, M. Smith, K. W. Smith, A. Sozzetti, W. Thuillot, W. van Reeven, Y. Viala, U. Abbas, A. Abreu Aramburu, S. Accart, J. J. Aguado, P. M. Allan, W. Allasia, G. Altavilla, M. A. Álvarez, J. Alves, R. I. Anderson, A. H. Andrei, E. Anglada Varela, E. Antiche, T. Antoja, S. Antón, B. Arcay, A. Atzei, L. Ayache, N. Bach, S. G. Baker, L. Balaguer-Núñez, C. Barache, C. Barata, A. Barbier, F. Barblan, M. Baroni, D. Barrado y Navascués, M. Barros, M. A. Barstow, U. Becciani, M. Bellazzini, G. Bellei, A. Bello García, V. Belokurov,

P. Bendjoya, A. Berihuete, L. Bianchi, O. Bienaymé, F. Billebaud, N. Blagorodnova, S. Blanco-Cuaresma, T. Boch, A. Bombrun, R. Borrachero, S. Bouquillon, G. Bourda, H. Bouy, A. Bragaglia, M. A. Breddels, N. Brouillet, T. Brüsemeister, B. Bucciarelli, F. Budnik, P. Burgess, R. Burgon, A. Burlacu, D. Busonero, R. Buzzi, E. Caffau, J. Cambras, H. Campbell, R. Cancelliere, T. Cantat-Gaudin, T. Carlucci, J. M. Carrasco, M. Castellani, P. Charlot, J. Charnas, P. Charvet, F. Chassat, A. Chiavassa, M. Clotet, G. Cocozza, R. S. Collins, P. Collins, and G. Costigan. The Gaia mission. , 595:A1, November 2016. doi: 10.1051/0004-6361/201629272.

Gaia Collaboration, A. Vallenari, A. G. A. Brown, T. Prusti, J. H. J. de Bruijne, F. Arenou, C. Babusiaux, M. Biermann, O. L. Creevey, C. Ducourant, D. W. Evans, L. Eyer, R. Guerra, A. Hutton, C. Jordi, S. A. Klioner, U. L. Lammers, L. Lindegren, X. Luri, F. Mignard, C. Panem, D. Pourbaix, S. Randich, P. Sartoretti, C. Soubiran, P. Tanga, N. A. Walton, C. A. L. Bailer-Jones, U. Bastian, R. Drimmel, F. Jansen, D. Katz, M. G. Lattanzi, F. van Leeuwen, J. Bakker, C. Cacciari, J. Castañeda, F. De Angeli, C. Fabricius, M. Fouesneau, Y. Frémat, L. Galluccio, A. Guerrier, U. Heiter, E. Masana, R. Messineo, N. Mowlavi, C. Nicolas, K. Nienartowicz, F. Pailler, P. Panuzzo, F. Riclet, W. Roux, G. M. Seabroke, R. Sordo, F. Thévenin, G. Gracia-Abril, J. Portell, D. Teyssier, M. Altmann, R. Andrae, M. Audard, I. Bellas-Velidis, K. Benson, J. Berthier, R. Blomme, P. W. Burgess, D. Busonero, G. Busso, H. Cánovas, B. Carry, A. Cellino, N. Cheek, G. Clementini, Y. Damerdji, M. Davidson, P. de Teodoro, M. Nuñez Campos, L. Delchambre, A. Dell'Oro, P. Esquej, J. Fernández-Hernández, E. Fraile, D. Garabato, P. García-Lario, E. Gosset, R. Haigron, J. L. Halbwachs, N. C. Hambly, D. L. Harrison, J. Hernández, D. Hestroffer, S. T. Hodgkin, B. Holl, K. Janßen, G. Jevardat de Fombelle, S. Jordan, A. Krone-Martins, A. C. Lanzafame, W. Löffler, O. Marchal, P. M. Marrese, A. Moitinho, K. Muinonen, P. Osborne, E. Pancino, T. Pauwels, A. Recio-Blanco, C. Reylé, M. Riello, L. Rimoldini, T. Roegiers, J. Rybizki, L. M. Sarro, C. Siopis, M. Smith, A. Sozzetti, E. Utrilla, M. van Leeuwen, U. Abbas, P. Ábrahám, A. Abreu Aramburu, C. Aerts, J. J. Aguado, M. Ajaj, F. Aldea-Montero, G. Altavilla, M. A. Álvarez, J. Alves, F. Anders, R. I. Anderson, E. Anglada Varela, T. Antoja, D. Baines, S. G. Baker, L. Balaguer-Núñez, E. Balbinot, Z. Balog, C. Barache, D. Barbato, M. Barros, M. A. Barstow, S. Bartolomé, J. L. Bassilana, N. Bauchet, U. Becciani, M. Bellazzini, A. Berihuete, M. Bernet, S. Bertone, L. Bianchi, A. Binnenfeld, S. Blanco-Cuaresma, A. Blazere, T. Boch, A. Bombrun, D. Bossini, S. Bouquillon, A. Bragaglia, L. Bramante, E. Breedt, A. Bressan, N. Brouillet, E. Brugaletta, B. Bucciarelli, A. Burlacu, A. G. Butkevich, R. Buzzi, E. Caffau, R. Cancelliere, T. Cantat-Gaudin, R. Carballo, T. Carlucci, M. I. Carnerero, J. M. Carrasco, L. Casamiquela, M. Castellani, A. Castro-Ginard, L. Chaoul, P. Charlot, L. Chemin, V. Chiaramida, A. Chiavassa, N. Chornay, G. Comoretto, G. Contursi, W. J. Cooper, T. Cornez, S. Cowell, F. Crifo, M. Cropper, M. Crosta, C. Crowley, C. Dafonte, A. Dapergolas, M. David, P. David, P. de Laverny, F. De Luise, and R. De March. Gaia Data Release 3. Summary of the content and survey properties. , 674:A1, June 2023. doi: 10.1051/0004-6361/202243940.

Yaroslav Ganin, Evgeniya Ustinova, Hana Ajakan, Pascal Germain, Hugo Larochelle, François Laviolette, Mario Marchand, and Victor Lempitsky. Domain-Adversarial Training of Neural Networks. *arXiv e-prints*, art. arXiv:1505.07818, May 2015. doi: 10.48550/arXiv.1505.07818.

F Gao, L Wang, W J Pearson, Y A Gordon, B W Holwerda, A M Hopkins, M J I Brown, J Bland-Hawthorn, and M S Owers. Mergers trigger active galactic nuclei out to z 0.6.

S. García-Burillo, F. Combes, A. Usero, S. Aalto, M. Krips, S. Viti, A. Alonso-Herrero, L. K. Hunt, E. Schinnerer, A. J. Baker, F. Boone, V. Casasola, L. Colina, F. Costagliola, A. Eckart, A. Fuente, C. Henkel, A. Labiano, S. Martín, I. Márquez, S. Muller, P. Planesas, C. Ramos Almeida, M. Spaans, L. J. Tacconi, and P. P. van der Werf. Molecular line emission in NGC 1068 imaged with ALMA. I. An AGN-driven outflow in the dense molecular gas. , 567:A125, July 2014. doi: 10.1051/0004-6361/201423843.

S. García-Burillo, F. Combes, A. Usero, S. Aalto, L. Colina, A. Alonso-Herrero, L. K. Hunt, S. Arribas, F. Costagliola, A. Labiano, R. Neri, M. Pereira-Santaella, L. J. Tacconi, and P. P. van der Werf. High-resolution imaging of the molecular outflows in two mergers: <ASTROBJ>IRAS 17208-0014</ASTROBJ> and <ASTROBJ>NGC 1614</ASTROBJ>. , 580:A35, August 2015. doi: 10.1051/0004-6361/201526133.

Jun-Qiang Ge, Chen Hu, Jian-Min Wang, Jin-Ming Bai, and Shu Zhang. Double-peaked Narrow Emission-line Galaxies from the Sloan Digital Sky Survey. I. Sample and Basic Properties. , 201(2):31, August 2012. doi: 10.1088/0067-0049/201/2/31.

Karl Gebhardt, Ralf Bender, Gary Bower, Alan Dressler, S. M. Faber, Alexei V. Filippenko, Richard Green, Carl Grillmair, Luis C. Ho, John Kormendy, Tod R. Lauer, John Magorrian, Jason Pinkney, Douglas Richstone, and Scott Tremaine. A Relationship between Nuclear Black Hole Mass and Galaxy Velocity Dispersion. , 539 (1):L13–L16, August 2000. doi: 10.1086/312840.

R. Genzel, S. Newman, T. Jones, N. M. Förster Schreiber, K. Shapiro, S. Genel, S. J. Lilly, A. Renzini, L. J. Tacconi, N. Bouché, A. Burkert, G. Cresci, P. Buschkamp, C. M. Carollo, D. Ceverino, R. Davies, A. Dekel, F. Eisenhauer, E. Hicks, J. Kurk, D. Lutz, C. Mancini, T. Naab, Y. Peng, A. Sternberg, D. Vergani, and G. Zamorani. The Sins Survey of z ~2 Galaxy Kinematics: Properties of the Giant Star-forming Clumps. , 733(2):101, June 2011. doi: 10.1088/0004-637X/733/2/101.

R. Genzel, N. M. Förster Schreiber, D. Rosario, P. Lang, D. Lutz, E. Wisnioski, E. Wuyts, S. Wuyts, K. Bandara, R. Bender, S. Berta, J. Kurk, T. Mendel, L. J. Tacconi, D. Wilman, A. Beifiori, G. Brammer, A. Burkert, P. Buschkamp, J. Chan, C. M. Carollo, R. Davies, F. Eisenhauer, M. Fabricius, M. Fossati, M. Kriek, S. Kulkarni, S. J. Lilly, C. Mancini, I. Momcheva, T. Naab, E. J. Nelson, A. Renzini, R. Saglia, R. M. Sharples, A. Sternberg, S. Tacchella, and P. van Dokkum. Evidence for Wide-Spread AGN Driven Outflows in the Most Massive z˜1-2 Star Forming Galaxies. *ArXiv e-prints*, June 2014.

Clara Giménez-Arteaga, Gabriel B. Brammer, Danilo Marchesini, Luis Colina, Varun Bajaj, Malte Brinch, Daniela Calzetti, Daniel Lange-Vagle, Eric J. Murphy, Michele Perna, Javier Piqueras-López, and Gregory F. Snyder. High-resolution Hubble Space Telescope Imaging Survey of Local Star-forming Galaxies. I. Spatially Resolved Obscured Star Formation with Hα and Paschen-β Recombination Lines. , 263(1):17, November 2022. doi: 10.3847/1538-4365/ac958c.

M Ginolfi, R Maiolino, S Carniani, F Arrigoni Battaia, S Cantalupo, and R Schneider. Extended and broad ly emission around a BAL quasar at z $\sim$ 5. *MNRAS*, 476(2): 2421–2431, feb 2018. doi: 10.1093/mnras/sty364.

Michele Ginolfi, Filippo Mannucci, Francesco Belfiore, Alessandro Marconi, Nicholas Boardman, Lucia Pozzetti, Micol Bolzonella, Enrico Di Teodoro, Giovanni Cresci, Vivienne Wild, Myriam Rodrigues, Roberto Maiolino, Michele Cirasuolo, and Ernesto Oliva. Inferring redshift and galaxy properties via a multi-task neural net with probabilistic outputs: An application to simulated MOONS spectra. , 693:A73, January 2025. doi: 10.1051/0004-6361/202452799.

A. Girdhar, C. M. Harrison, V. Mainieri, A. Bittner, T. Costa, P. Kharb, D. Mukherjee, F. Arrigoni Battaia, D. M. Alexander, G. Calistro Rivera, C. Circosta, C. De Breuck, A. C. Edge, E. P. Farina, D. Kakkad, G. B. Lansbury, S. J. Molyneux, J. R. Mullaney, Silpa S, A. P. Thomson, and S. R. Ward. Quasar feedback survey: multiphase outflows, turbulence, and evidence for feedback caused by low power radio jets inclined into the galaxy disc. , 512(2):1608–1628, May 2022. doi: 10.1093/mnras/stac073.

Marcello Giroletti and Francesca Panessa. The Faintest Seyfert Radio Cores Revealed by VLBI. , 706(2):L260–L264, December 2009. doi: 10.1088/0004-637X/706/2/L260.

M. Gitti, M. Giroletti, G. Giovannini, L. Feretti, and E. Liuzzo. A candidate supermassive binary black hole system in the brightest cluster galaxy of RBS 797. , 557: L14, September 2013. doi: 10.1051/0004-6361/201322401.

S. Gonzaga, W. Hack, A. Fruchter, and J. Mack. *The DrizzlePac Handbook*. 2012.

E. González-Alfonso, J. Fischer, J. Graciá-Carpio, E. Sturm, S. Hailey-Dunsheath, D. Lutz, A. Poglitsch, A. Contursi, H. Feuchtgruber, S. Veilleux, H. W. W. Spoon, A. Verma, N. Christopher, R. Davies, A. Sternberg, R. Genzel, and L. Tacconi. Herschel/PACS spectroscopy of NGC 4418 and Arp 220: H_2O, $H_2{}^{18}O$, OH, ^{18}OH, O I, HCN, and NH_3. , 541:A4, May 2012. doi: 10.1051/0004-6361/201118029.

E. González-Alfonso, J. Fischer, J. Graciá-Carpio, N. Falstad, E. Sturm, M. Meléndez, H. W. W. Spoon, A. Verma, R. I. Davies, D. Lutz, S. Aalto, E. Polisensky, A. Poglitsch, S. Veilleux, and A. Contursi. The Mrk 231 molecular outflow as seen in OH. , 561:A27, January 2014. doi: 10.1051/0004-6361/201321709.

E. González-Alfonso, L. Armus, F. J. Carrera, V. Charmandaris, A. Efstathiou, E. Egami, J. A. Fernández-Ontiveros, J. Fischer, G. L. Granato, C. Gruppioni, E. Hatziminaoglou, M. Imanishi, N. Isobe, H. Kaneda, D. Koziel-Wierzbowska, M. A. Malkan, J. Martín-Pintado, S. Mateos, H. Matsuhara, G. Miniutti, T. Nakagawa, F. Pozzi, F. Rico-Villas, G. Rodighiero, P. Roelfsema, L. Spinoglio, H. W. W. Spoon, E. Sturm, F. van der Tak, C. Vignali, and L. Wang. Feedback and Feeding in the Context of Galaxy Evolution with SPICA: Direct Characterisation of Molecular Outflows and Inflows. , 34:e054, November 2017. doi: 10.1017/pasa.2017.46.

Andy D. Goulding, Kris Pardo, Jenny E. Greene, Chiara M. F. Mingarelli, Kristina Nyland, and Michael A. Strauss. Discovery of a Close-separation Binary Quasar at the Heart of a z $\sim$ 0.2 Merging Galaxy and Its Implications for Low-frequency Gravitational Waves. , 879(2):L21, July 2019. doi: 10.3847/2041-8213/ab2a14.

Matthew J. Graham, S. G. Djorgovski, Daniel Stern, Andrew J. Drake, Ashish A. Mahabal, Ciro Donalek, Eilat Glikman, Steve Larson, and Eric Christensen. A systematic search for close supermassive black hole binaries in the Catalina Real-time Transient Survey. , 453(2):1562–1576, October 2015a. doi: 10.1093/mnras/stv1726.

Matthew J. Graham, S. G. Djorgovski, Daniel Stern, Eilat Glikman, Andrew J. Drake, Ashish A. Mahabal, Ciro Donalek, Steve Larson, and Eric Christensen. A possible close supermassive black-hole binary in a quasar with optical periodicity. , 518(7537): 74–76, February 2015b. doi: 10.1038/nature14143.

Jenny E. Greene, Ivo Labbe, Andy D. Goulding, Lukas J. Furtak, Iryna Chemerynska, Vasily Kokorev, Pratika Dayal, Marta Volonteri, Christina C. Williams, Bingjie Wang, David J. Setton, Adam J. Burgasser, Rachel Bezanson, Hakim Atek, Gabriel Brammer, Sam E. Cutler, Robert Feldmann, Seiji Fujimoto, Karl Glazebrook, Anna de Graaff, Gourav Khullar, Joel Leja, Danilo Marchesini, Michael V. Maseda, Jorryt Matthee, Tim B. Miller, Rohan P. Naidu, Themiya Nanayakkara, Pascal A. Oesch, Richard Pan, Casey Papovich, Sedona H. Price, Pieter van Dokkum, John R. Weaver, Katherine E. Whitaker, and Adi Zitrin. UNCOVER Spectroscopy Confirms the Surprising Ubiquity of Active Galactic Nuclei in Red Sources at z $>$ 5. , 964(1): 39, March 2024. doi: 10.3847/1538-4357/ad1e5f.

Arran Gross, Hai Fu, S. G. Djorgovski, Adam D. Myers, Dylan Paré, Joshua L. Steffen, and J. M. Wrobel. Chandra X-ray Observations of Radio-Selected Dual AGNs. In *American Astronomical Society Meeting Abstracts #233*, volume 233 of *American Astronomical Society Meeting Abstracts*, page 243.26, January 2019.

Matteo Guainazzi, Alessandra De Rosa, Stefano Bianchi, Bernd Husemann, Tamara Bogdanovic, Stefanie Komossa, Nora Loiseau, Zsolt Paragi, Miguel Pérez-Torres, Enrico Piconcelli, and Cristian Vignali. An XMM-Newton study of active-inactive galaxy pairs. , 504(1):393–405, June 2021. doi: 10.1093/mnras/stab808.

Siddhartha Gurung-López, Álvaro A. Orsi, Silvia Bonoli, Nelson Padilla, Cedric G. Lacey, and Carlton M. Baugh. Ly α emitters in a cosmological volume II: the impact of the intergalactic medium. , 491(3):3266–3289, January 2020. doi: 10.1093/mnras/stz3204.

B. Gustafsson, B. Edvardsson, K. Eriksson, U. G. Jørgensen, Å. Nordlund, and B. Plez. A grid of MARCS model atmospheres for late-type stars. I. Methods and general properties. , 486(3):951–970, August 2008. doi: 10.1051/0004-6361:200809724.

Yuichi Harikane, Yechi Zhang, Kimihiko Nakajima, Masami Ouchi, Yuki Isobe, Yoshiaki Ono, Shun Hatano, Yi Xu, and Hiroya Umeda. A JWST/NIRSpec First Census of Broad-line AGNs at z = 4-7: Detection of 10 Faint AGNs with M $_{BH}$ 10^6-10^8 M $_\odot$ and Their Host Galaxy Properties. , 959(1):39, December 2023. doi: 10.3847/1538-4357/ad029e.

Nadine Häring and Hans-Walter Rix. On the Black Hole Mass-Bulge Mass Relation. , 604(2):L89–L92, April 2004. doi: 10.1086/383567.

C. M. Harrison, D. M. Alexander, J. R. Mullaney, and A. M. Swinbank. Kiloparsec-scale outflows are prevalent among luminous AGN: outflows and feedback in the

context of the overall AGN population. , 441(4):3306–3347, July 2014. doi: 10.1093/mnras/stu515.

C. M. Harrison, T. Costa, C. N. Tadhunter, A. Flütsch, D. Kakkad, M. Perna, and G. Vietri. AGN outflows and feedback twenty years on. *Nature Astronomy*, 2:198–205, February 2018a. doi: 10.1038/s41550-018-0403-6.

C. M. Harrison, T. Costa, C. N. Tadhunter, A. Flütsch, D. Kakkad, M. Perna, and G. Vietri. AGN outflows and feedback twenty years on. *Nature Astronomy*, 2:198–205, February 2018b. doi: 10.1038/s41550-018-0403-6.

Kaiming He, Xiangyu Zhang, Shaoqing Ren, and Jian Sun. Deep Residual Learning for Image Recognition. In *2016 IEEE Conference on Computer Vision and Pattern Recognition (CVPR)*, page 1, June 2016. doi: 10.1109/CVPR.2016.90.

T. M. Heckman. An Optical and Radio Survey of the Nuclei of Bright Galaxies - Activity in the Normal Galactic Nuclei. , 87:152, July 1980.

Timothy M. Heckman and Philip N. Best. The Coevolution of Galaxies and Supermassive Black Holes: Insights from Surveys of the Contemporary Universe. , 52:589–660, August 2014. doi: 10.1146/annurev-astro-081913-035722.

Timothy M. Heckman, Rachel M. Alexandroff, Sanchayeeta Borthakur, Roderik Overzier, and Claus Leitherer. The Systematic Properties of the Warm Phase of Starburst-Driven Galactic Winds. , 809(2):147, August 2015. doi: 10.1088/0004-637X/809/2/147.

G. Helou, B. T. Soifer, and M. Rowan-Robinson. Thermal infrared and nonthermal radio : remarkable correlation in disks of galaxies. , 298:L7–L11, November 1985. doi: 10.1086/184556.

Joseph F. Hennawi, Michael A. Strauss, Masamune Oguri, Naohisa Inada, Gordon T. Richards, Bartosz Pindor, Donald P. Schneider, Robert H. Becker, Michael D. Gregg, Patrick B. Hall, David E. Johnston, Xiaohui Fan, Scott Burles, David J. Schlegel, James E. Gunn, Robert H. Lupton, Neta A. Bahcall, Robert J. Brunner, and Jon Brinkmann. Binary Quasars in the Sloan Digital Sky Survey: Evidence for Excess Clustering on Small Scales. , 131(1):1–23, January 2006. doi: 10.1086/498235.

Lars Hernquist. Tidal triggering of starbursts and nuclear activity in galaxies. , 340(6236):687–691, August 1989. doi: 10.1038/340687a0.

Ryan C. Hickox and David M. Alexander. Obscured Active Galactic Nuclei. , 56:625–671, September 2018. doi: 10.1146/annurev-astro-081817-051803.

G. Hinshaw, D. Larson, E. Komatsu, D. N. Spergel, C. L. Bennett, J. Dunkley, M. R. Nolta, M. Halpern, R. S. Hill, N. Odegard, L. Page, K. M. Smith, J. L. Weiland, B. Gold, N. Jarosik, A. Kogut, M. Limon, S. S. Meyer, G. S. Tucker, E. Wollack, and E. L. Wright. Nine-year Wilkinson Microwave Anisotropy Probe (WMAP) Observations: Cosmological Parameter Results. *ApJS*, 208:19, October 2013. doi: 10.1088/0067-0049/208/2/19.

Luke R. Holden, Clive Tadhunter, Anelise Audibert, Tom Oosterloo, Cristina Ramos Almeida, Raffaella Morganti, Miguel Pereira-Santaella, and Isabella Lamperti. ALMA reveals a compact and massive molecular outflow driven by the young AGN in a nearby ULIRG. , 530(1):446–456, May 2024. doi: 10.1093/mnras/stae810.

S. F. Hönig and M. Kishimoto. The dusty heart of nearby active galaxies. II. From clumpy torus models to physical properties of dust around AGN. , 523:A27, November 2010. doi: 10.1051/0004-6361/200912676.

Sebastian F. Hönig. Redefining the Torus: A Unifying View of AGNs in the Infrared and Submillimeter. , 884(2):171, October 2019. doi: 10.3847/1538-4357/ab4591.

Philip F. Hopkins and Eliot Quataert. How do massive black holes get their gas? *MNRAS*, 407(3):1529–1564, jul 2010. doi: 10.1111/j.1365-2966.2010.17064.x.

Philip F. Hopkins, Lars Hernquist, Thomas J. Cox, and Dušan Kereš. A Cosmological Framework for the Co-Evolution of Quasars, Supermassive Black Holes, and Elliptical Galaxies. I. Galaxy Mergers and Quasar Activity. , 175(2):356–389, April 2008. doi: 10.1086/524362.

M. Huertas-Company, K. G. Iyer, E. Angeloudi, M. B. Bagley, S. L. Finkelstein, J. Kartaltepe, E. J. McGrath, R. Sarmiento, J. Vega-Ferrero, P. Arrabal Haro, P. Behroozi, F. Buitrago, Y. Cheng, L. Costantin, A. Dekel, M. Dickinson, D. Elbaz, N. A. Grogin, N. P. Hathi, B. W. Holwerda, A. M. Koekemoer, R. A. Lucas, C. Papovich, P. G. Pérez-González, N. Pirzkal, L. M. Seillé, A. de la Vega, S. Wuyts, G. Yang, and L. Y. A. Yung. Galaxy morphology from z $\sim$ 6 through the lens of JWST. , 685:A48, May 2024. doi: 10.1051/0004-6361/202346800.

D. G. Hummer and P. J. Storey. Recombination-line intensities for hydrogenic ions - I. Case B calculations for H I and He II. , 224:801–820, February 1987. doi: 10.1093/mnras/224.3.801.

Chao-Ling Hung, D. B. Sanders, Caitlin M. Casey, Michael Koss, Kirsten L. Larson, Nicholas Lee, Yanxia Li, Kelly Lockhart, Hsin-Yi Shih, Joshua E. Barnes, Jeyhan S. Kartaltepe, and Howard A. Smith. A Comparison of the Morphological Properties between Local and z ~1 Infrared Luminous Galaxies: Are Local and High-z (U)LIRGs Different? , 791(1):63, August 2014. doi: 10.1088/0004-637X/791/1/63.

J. W. Isbell, S. Ertel, J. U. Pott, G. Weigelt, M. Stalevski, J. Leftley, W. Jaffe, R. G. Petrov, N. Moszczynski, P. Vermot, P. Hinz, L. Burtscher, V. Gámez Rosas, A. Becker, J. Carlson, V. Faramaz-Gorka, W. F. Hoffmann, J. Leisenring, J. Power, and K. Wagner. Direct imaging of active galactic nucleus outflows and their origin with the 23 m Large Binocular Telescope. *Nature Astronomy*, 9:417–427, March 2025. doi: 10.1038/s41550-024-02461-y.

W. Ishibashi, A. C. Fabian, and R. Maiolino. The energetics of AGN radiation pressure-driven outflows. , 476(1):512–519, May 2018. doi: 10.1093/mnras/sty236.

E. E. O. Ishida, R. Beck, S. González-Gaitán, R. S. de Souza, A. Krone-Martins, J. W. Barrett, N. Kennamer, R. Vilalta, J. M. Burgess, B. Quint, A. Z. Vitorelli,

A. Mahabal, E. Gangler, and COIN Collaboration. Optimizing spectroscopic follow-up strategies for supernova photometric classification with active learning. , 483(1): 2–18, February 2019. doi: 10.1093/mnras/sty3015.

Yuki Isobe, Masami Ouchi, Kimihiko Nakajima, Yuichi Harikane, Yoshiaki Ono, Yi Xu, Yechi Zhang, and Hiroya Umeda. Redshift Evolution of Electron Density in the Interstellar Medium at z 0-9 Uncovered with JWST/NIRSpec Spectra and Line-spread Function Determinations. , 956(2):139, October 2023. doi: 10.3847/1538-4357/acf376.

R. J. Ivison, B. Magnelli, E. Ibar, P. Andreani, D. Elbaz, B. Altieri, A. Amblard, V. Arumugam, R. Auld, H. Aussel, T. Babbedge, S. Berta, A. Blain, J. Bock, A. Bongiovanni, A. Boselli, V. Buat, D. Burgarella, N. Castro-Rodríguez, A. Cava, J. Cepa, P. Chanial, A. Cimatti, M. Cirasuolo, D. L. Clements, A. Conley, L. Conversi, A. Cooray, E. Daddi, H. Dominguez, C. D. Dowell, E. Dwek, S. Eales, D. Farrah, N. Förster Schreiber, M. Fox, A. Franceschini, W. Gear, R. Genzel, J. Glenn, M. Griffin, C. Gruppioni, M. Halpern, E. Hatziminaoglou, K. Isaak, G. Lagache, L. Levenson, N. Lu, D. Lutz, S. Madden, B. Maffei, G. Magdis, G. Mainetti, R. Maiolino, L. Marchetti, G. E. Morrison, A. M. J. Mortier, H. T. Nguyen, R. Nordon, B. O'Halloran, S. J. Oliver, A. Omont, F. N. Owen, M. J. Page, P. Panuzzo, A. Papageorgiou, C. P. Pearson, I. Pérez-Fournon, A. M. Pérez García, A. Poglitsch, M. Pohlen, P. Popesso, F. Pozzi, J. I. Rawlings, G. Raymond, D. Rigopoulou, L. Riguccini, D. Rizzo, G. Rodighiero, I. G. Roseboom, M. Rowan-Robinson, A. Saintonge, M. Sanchez Portal, P. Santini, B. Schulz, D. Scott, N. Seymour, L. Shao, D. L. Shupe, A. J. Smith, J. A. Stevens, E. Sturm, M. Symeonidis, L. Tacconi, M. Trichas, K. E. Tugwell, M. Vaccari, I. Valtchanov, J. Vieira, L. Vigroux, L. Wang, R. Ward, G. Wright, C. K. Xu, and M. Zemcov. The far-infrared/radio correlation as probed by Herschel. , 518:L31, July 2010. doi: 10.1051/0004-6361/201014552.

K. Iwasawa, G. Matt, M. Guainazzi, and A. C. Fabian. A hard X-ray constraint on the presence of an AGN in the ultraluminous infrared galaxy Arp 220. , 326(3):894–900, September 2001. doi: 10.1046/j.1365-8711.2001.04478.x.

W. Jaffe, K. Meisenheimer, H. J. A. Röttgering, C. Leinert, A. Richichi, O. Chesneau, D. Fraix-Burnet, A. Glazenborg-Kluttig, G.-L. Granato, U. Graser, B. Heijligers, R. Köhler, F. Malbet, G. K. Miley, F. Paresce, J.-W. Pel, G. Perrin, F. Przygodda, M. Schoeller, H. Sol, L. B. F. M. Waters, G. Weigelt, J. Woillez, and P. T. de Zeeuw. The central dusty torus in the active nucleus of NGC 1068. , 429:47–49, May 2004. doi: 10.1038/nature02531.

P. Jakobsen, P. Ferruit, C. Alves de Oliveira, S. Arribas, G. Bagnasco, R. Barho, T. L. Beck, S. Birkmann, T. Böker, A. J. Bunker, S. Charlot, P. de Jong, G. de Marchi, R. Ehrenwinkler, M. Falcolini, R. Fels, M. Franx, D. Franz, M. Funke, G. Giardino, X. Gnata, W. Holota, K. Honnen, P. L. Jensen, M. Jentsch, T. Johnson, D. Jollet, H. Karl, G. Kling, J. Köhler, M.-G. Kolm, N. Kumari, M. E. Lander, R. Lemke, M. López-Caniego, N. Lützgendorf, R. Maiolino, E. Manjavacas, A. Marston, M. Maschmann, R. Maurer, B. Messerschmidt, S. H. Moseley, P. Mosner, D. B. Mott, J. Muzerolle, N. Pirzkal, J.-F. Pittet, A. Plitzke, W. Posselt, B. Rapp, B. J. Rauscher, T. Rawle, H.-W. Rix, A. Rödel, P. Rumler, E. Sabbi, J.-C. Salvignol, T. Schmid, M. Sirianni, C. Smith, P. Strada, M. te Plate, J. Valenti, T. Wettemann,

T. Wiehe, M. Wiesmayer, C. J. Willott, R. Wright, P. Zeidler, and C. Zincke. The near-infrared spectrograph (NIRSpec) on the ijames webb/i space telescope. *A&A*, 661:A80, may 2022. doi: 10.1051/0004-6361/202142663.

M. E. Jarvis, C. M. Harrison, A. P. Thomson, C. Circosta, V. Mainieri, D. M. Alexander, A. C. Edge, G. B. Lansbury, S. J. Molyneux, and J. R. Mullaney. Prevalence of radio jets associated with galactic outflows and feedback from quasars. , 485(2): 2710–2730, May 2019. doi: 10.1093/mnras/stz556.

M. E. Jarvis, C. M. Harrison, V. Mainieri, D. M. Alexander, F. Arrigoni Battaia, G. Calistro Rivera, C. Circosta, T. Costa, C. De Breuck, A. C. Edge, A. Girdhar, D. Kakkad, P. Kharb, G. B. Lansbury, S. J. Molyneux, D. Mukherjee, J. R. Mullaney, E. P. Farina, S. Silpa, A. P. Thomson, and S. R. Ward. The quasar feedback survey: discovering hidden Radio-AGN and their connection to the host galaxy ionized gas. , 503(2):1780–1797, May 2021. doi: 10.1093/mnras/stab549.

Yuanzhe Jiang, Yue Shen, Xin Liu, Nadia Zakamska, Ming-yang Zhuang, Arran C. Gross, Junyao Li, Yu-ching Chen, and Yuzo Ishikawa. Galactic-scale Quasar Pairs from the Sloan Digital Sky Survey and Gaia DR3. *arXiv e-prints*, art. arXiv:2504.06415, April 2025. doi: 10.48550/arXiv.2504.06415.

Jun-Jie Jin, Xue-Bing Wu, Yuming Fu, Su Yao, Yan-Li Ai, Xiao-Tong Feng, Zi-Qi He, Qin-Chun Ma, Yu-Xuan Pang, Rui Zhu, Yan-xia Zhang, Hai-long Yuan, and Zhi-Ying Huo. The Large Sky Area Multi-Object Fiber Spectroscopic Telescope (LAMOST) Quasar Survey: Quasar Properties from Data Releases 6 to 9. , 265(1): 25, March 2023. doi: 10.3847/1538-4365/acaf89.

Wenhua Ju, Jenny E. Greene, Roman R. Rafikov, Steven J. Bickerton, and Carles Badenes. Search for Supermassive Black Hole Binaries in the Sloan Digital Sky Survey Spectroscopic Sample. , 777(1):44, November 2013. doi: 10.1088/0004-637X/777/1/44.

D. Kakkad, V. Mainieri, G. Vietri, S. Carniani, C. M. Harrison, M. Perna, J. Scholtz, C. Circosta, G. Cresci, B. Husemann, M. Bischetti, C. Feruglio, F. Fiore, A. Marconi, P. Padovani, M. Brusa, C. Cicone, A. Comastri, G. Lanzuisi, F. Mannucci, N. Menci, H. Netzer, E. Piconcelli, A. Puglisi, M. Salvato, M. Schramm, J. Silverman, C. Vignali, G. Zamorani, and L. Zappacosta. SUPER. II. Spatially resolved ionised gas kinematics and scaling relations in z $\sim$ 2 AGN host galaxies. , 642:A147, October 2020. doi: 10.1051/0004-6361/202038551.

Guinevere Kauffmann, Timothy M. Heckman, Christy Tremonti, Jarle Brinchmann, Stéphane Charlot, Simon D. M. White, Susan E. Ridgway, Jon Brinkmann, Masataka Fukugita, Patrick B. Hall, Željko Ivezić, Gordon T. Richards, and Donald P. Schneider. The host galaxies of active galactic nuclei. , 346(4):1055–1077, December 2003. doi: 10.1111/j.1365-2966.2003.07154.x.

Emily Kehoe, Alice E. Shapley, Ryan L. Sanders, Naveen A. Reddy, Michael W. Topping, Natalie Lam, Leonardo Clarke, Fergus Cullen, Richard S. Ellis, N. M. Forster Schreiber, Tucker Jones, Ali Ahmad Khostovan, Derek J. McLeod, Ross J. McLure, Desika Narayanan, Pascal Oesch, and Anthony J. Pahl. The AURORA Survey: Tracing Galactic Outflows at $zrsim2.5$ with JWST/NIRSpec NUV Absorption Lines. *arXiv e-prints*, art. arXiv:2506.17381, June 2025. doi: 10.48550/arXiv.2506.17381.

K. I. Kellermann, R. Sramek, M. Schmidt, D. B. Shaffer, and R. Green. VLA observations of objects in the Palomar Bright Quasar Survey. , 98:1195–1207, October 1989. doi: 10.1086/115207.

Luke Zoltan Kelley, Laura Blecha, and Lars Hernquist. Massive black hole binary mergers in dynamical galactic environments. , 464(3):3131–3157, January 2017. doi: 10.1093/mnras/stw2452.

Robert C. Kennicutt and Neal J. Evans. Star Formation in the Milky Way and Nearby Galaxies. , 50:531–608, September 2012. doi: 10.1146/annurev-astro-081811-125610.

L. J. Kewley, C. A. Heisler, M. A. Dopita, and S. Lumsden. Optical Classification of Southern Warm Infrared Galaxies. , 132(1):37–71, January 2001. doi: 10.1086/318944.

Lisa J. Kewley, Brent Groves, Guinevere Kauffmann, and Tim Heckman. The host galaxies and classification of active galactic nuclei. , 372(3):961–976, November 2006. doi: 10.1111/j.1365-2966.2006.10859.x.

E. Y. Khachikian and D. W. Weedman. An atlas of Seyfert galaxies. , 192:581–589, September 1974. doi: 10.1086/153093.

Fazeel Mahmood Khan, Miguel Preto, Peter Berczik, Ingo Berentzen, Andreas Just, and Rainer Spurzem. Mergers of Unequal-mass Galaxies: Supermassive Black Hole Binary Evolution and Structure of Merger Remnants. , 749(2):147, April 2012. doi: 10.1088/0004-637X/749/2/147.

P. Kharb, D. V. Lal, and D. Merritt. A candidate sub-parsec binary black hole in the Seyfert galaxy NGC 7674. *Nature Astronomy*, 1:727–733, September 2017. doi: 10.1038/s41550-017-0256-4.

A. King. The AGN-Starburst Connection, Galactic Superwinds, and $M_{BH} - \sigma$. , 635: L121–L123, December 2005. doi: 10.1086/499430.

A. R. King, J. E. Pringle, and J. A. Hofmann. The evolution of black hole mass and spin in active galactic nuclei. , 385(3):1621–1627, April 2008. doi: 10.1111/j.1365-2966.2008.12943.x.

Andrew King. Black Holes, Galaxy Formation, and the M_{BH}-σ Relation. , 596(1): L27–L29, October 2003. doi: 10.1086/379143.

Andrew King and Ken Pounds. Powerful Outflows and Feedback from Active Galactic Nuclei. , 53:115–154, August 2015a. doi: 10.1146/annurev-astro-082214-122316.

Andrew King and Ken Pounds. Powerful Outflows and Feedback from Active Galactic Nuclei. , 53:115–154, August 2015b. doi: 10.1146/annurev-astro-082214-122316.

Diederik P. Kingma and Jimmy Ba. Adam: A Method for Stochastic Optimization. *arXiv e-prints*, art. arXiv:1412.6980, December 2014. doi: 10.48550/arXiv.1412.6980.

M. Kishimoto, S. F. Hönig, R. Antonucci, T. Kotani, R. Barvainis, K. R. W. Tristram, and G. Weigelt. Exploring the inner region of type 1 AGNs with the Keck interferometer. , 507(3):L57–L60, December 2009. doi: 10.1051/0004-6361/200913512.

Makoto Kishimoto, Matthew Anderson, Theo ten Brummelaar, Christopher Farrington, Robert Antonucci, Sebastian Hönig, Florentin Millour, Konrad R. W. Tristram, Gerd Weigelt, Laszlo Sturmann, Judit Sturmann, Gail Schaefer, and Nic Scott. The Dust Sublimation Region of the Type 1 AGN NGC 4151 at a Hundred Microarcsecond Scale as Resolved by the CHARA Array Interferometer. , 940(1):28, November 2022. doi: 10.3847/1538-4357/ac91c4.

Dale D. Kocevski, Masafusa Onoue, Kohei Inayoshi, Jonathan R. Trump, Pablo Arrabal Haro, Andrea Grazian, Mark Dickinson, Steven L. Finkelstein, Jeyhan S. Kartaltepe, Michaela Hirschmann, James Aird, Benne W. Holwerda, Seiji Fujimoto, Stéphanie Juneau, Ricardo O. Amorín, Bren E. Backhaus, Micaela B. Bagley, Guillermo Barro, Eric F. Bell, Laura Bisigello, Antonello Calabrò, Nikko J. Cleri, M. C. Cooper, Xuheng Ding, Norman A. Grogin, Luis C. Ho, Taylor A. Hutchison, Akio K. Inoue, Linhua Jiang, Brenda Jones, Anton M. Koekemoer, Wenxiu Li, Zhengrong Li, Elizabeth J. McGrath, Juan Molina, Casey Papovich, Pablo G. Pérez-González, Nor Pirzkal, Stephen M. Wilkins, Guang Yang, and L. Y. Aaron Yung. Hidden Little Monsters: Spectroscopic Identification of Low-mass, Broad-line AGNs at z $>$ 5 with CEERS. , 954(1):L4, September 2023. doi: 10.3847/2041-8213/ace5a0.

Vasily Kokorev, Seiji Fujimoto, Ivo Labbe, Jenny E. Greene, Rachel Bezanson, Pratika Dayal, Erica J. Nelson, Hakim Atek, Gabriel Brammer, Karina I. Caputi, Iryna Chemerynska, Sam E. Cutler, Robert Feldmann, Yoshinobu Fudamoto, Lukas J. Furtak, Andy D. Goulding, Anna de Graaff, Joel Leja, Danilo Marchesini, Tim B. Miller, Themiya Nanayakkara, Pascal A. Oesch, Richard Pan, Sedona H. Price, David J. Setton, Renske Smit, Mauro Stefanon, Bingjie Wang, John R. Weaver, Katherine E. Whitaker, Christina C. Williams, and Adi Zitrin. UNCOVER: A NIRSpec Identification of a Broad-line AGN at z = 8.50. , 957(1):L7, November 2023. doi: 10.3847/2041-8213/ad037a.

Bon-Chul Koo, John C. Raymond, and Hyun-Jeong Kim. Infrared [FE II] Emission Lines from Radiative Atomic Shocks. *Journal of Korean Astronomical Society*, 49 (3):109–122, June 2016. doi: 10.5303/JKAS.2016.49.3.109.

John Kormendy and Luis C. Ho. Coevolution (Or Not) of Supermassive Black Holes and Host Galaxies. , 51(1):511–653, August 2013. doi: 10.1146/annurev-astro-082708-101811.

John Kormendy and Douglas Richstone. Inward Bound—The Search For Supermassive Black Holes In Galactic Nuclei. , 33:581, January 1995. doi: 10.1146/annurev.aa.33.090195.003053.

Michael Koss, Richard Mushotzky, Ezequiel Treister, Sylvain Veilleux, Ranjan Vasudevan, and Margaret Trippe. Understanding Dual Active Galactic Nucleus Activation in the nearby Universe. , 746(2):L22, February 2012. doi: 10.1088/2041-8205/746/2/L22.

Michael J. Koss, Laura Blecha, Phillip Bernhard, Chao-Ling Hung, Jessica R. Lu, Benny Trakhtenbrot, Ezequiel Treister, Anna Weigel, Lia F. Sartori, Richard Mushotzky, Kevin Schawinski, Claudio Ricci, Sylvain Veilleux, and David B. Sanders. A population of luminous accreting black holes with hidden mergers. , 563(7730):214–216, November 2018. doi: 10.1038/s41586-018-0652-7.

Jelena Kovacevic, Luka C. Popovic, and Milan S. Dimitrijevic. Analysis of optical fe ii emission in a sample of agn spectra. *ApJS*, 189(1):15–36, April 2010. doi: 10.1088/0067-0049/189/1/15.

Davor Krajnović, Eric Emsellem, Michele Cappellari, Katherine Alatalo, Leo Blitz, Maxime Bois, Frédéric Bournaud, Martin Bureau, Roger L. Davies, Timothy A. Davis, P. T. de Zeeuw, Sadegh Khochfar, Harald Kuntschner, Pierre-Yves Lablanche, Richard M. McDermid, Raffaella Morganti, Thorsten Naab, Tom Oosterloo, Marc Sarzi, Nicholas Scott, Paolo Serra, Anne-Marie Weijmans, and Lisa M. Young. The ATLAS^{3D} project - II. Morphologies, kinemetric features and alignment between photometric and kinematic axes of early-type galaxies. , 414(4):2923–2949, July 2011. doi: 10.1111/j.1365-2966.2011.18560.x.

A. Kramida, Reader J. Ralchenko, Yu., and NIST ASD Team. NIST Atomic Spectra Database (version 5.11). Available: https://physics.nist.gov/asd, 2023. URL `https://physics.nist.gov/asd`.

L. E. Kristensen, B. Godard, P. Guillard, A. Gusdorf, and G. Pineau des Forêts. Shock excitation of H_2 in the James Webb Space Telescope era. , 675:A86, July 2023. doi: 10.1051/0004-6361/202346254.

A. Krone-Martins and A. Moitinho. UPMASK: unsupervised photometric membership assignment in stellar clusters. , 561:A57, January 2014. doi: 10.1051/0004-6361/201321143.

A. Krone-Martins, L. Delchambre, O. Wertz, C. Ducourant, F. Mignard, R. Teixeira, J. Klüter, J.-F. Le Campion, L. Galluccio, J. Surdej, U. Bastian, J. Wambsganss, M. J. Graham, S. G. Djorgovski, and E. Slezak. Gaia GraL: Gaia DR2 gravitational lens systems. I. New quadruply imaged quasar candidates around known quasars. , 616:L11, August 2018. doi: 10.1051/0004-6361/201833337.

Ivo Labbe, Jenny E. Greene, Rachel Bezanson, Seiji Fujimoto, Lukas J. Furtak, Andy D. Goulding, Jorryt Matthee, Rohan P. Naidu, Pascal A. Oesch, Hakim Atek, Gabriel Brammer, Iryna Chemerynska, Dan Coe, Sam E. Cutler, Pratika Dayal, Robert Feldmann, Marijn Franx, Karl Glazebrook, Joel Leja, Michael Maseda, Danilo Marchesini, Themiya Nanayakkara, Erica J. Nelson, Richard Pan, Casey Papovich, Sedona H. Price, Katherine A. Suess, Bingjie Wang, John R. Weaver, Katherine E. Whitaker, Christina C. Williams, and Adi Zitrin. UNCOVER: Candidate Red Active Galactic Nuclei at $3 < z < 7$ with JWST and ALMA. , 978(1):92, January 2025. doi: 10.3847/1538-4357/ad3551.

Thomas S. Y. Lai, Lee Armus, Vivian U, Tanio Díaz-Santos, Kirsten L. Larson, Aaron Evans, Matthew A. Malkan, Philip Appleton, Jeff Rich, Francisco Müller-Sánchez, Hanae Inami, Thomas Bohn, Jed McKinney, Luke Finnerty, David R. Law, Sean T. Linden, Anne M. Medling, George C. Privon, Yiqing Song, Sabrina Stierwalt, Paul P. van der Werf, Loreto Barcos-Muñoz, J. D. T. Smith, Aditya Togi, Susanne Aalto, Torsten Böker, Vassilis Charmandaris, Justin Howell, Kazushi Iwasawa, Francisca Kemper, Joseph M. Mazzarella, Eric J. Murphy, Michael J. I. Brown, Christopher C. Hayward, Jason Marshall, David Sanders, and Jason Surace. GOALS-JWST: Tracing AGN Feedback on the Star-forming Interstellar Medium in NGC 7469. , 941(2):L36, December 2022. doi: 10.3847/2041-8213/ac9ebf.

Dharam Vir Lal and A. Pramesh Rao. Giant Metrewave Radio Telescope observations of X-shaped radio sources. , 374(3):1085–1102, January 2007. doi: 10.1111/j.1365-2966.2006.11225.x.

F. Lamareille. Spectral classification of emission-line galaxies from the Sloan Digital Sky Survey. I. An improved classification for high-redshift galaxies. , 509:A53, January 2010. doi: 10.1051/0004-6361/200913168.

I. Lamperti, M. Pereira-Santaella, M. Perna, L. Colina, S. Arribas, S. García-Burillo, E. González-Alfonso, S. Aalto, A. Alonso-Herrero, F. Combes, A. Labiano, J. Piqueras-López, D. Rigopoulou, and P. van der Werf. Physics of ULIRGs with MUSE and ALMA: The PUMA project. IV. No tight relation between cold molecular outflow rates and AGN luminosities. , 668:A45, December 2022. doi: 10.1051/0004-6361/202244054.

Lauranne Lanz, Andreas Zezas, Nicola Brassington, Howard A. Smith, Matthew L. N. Ashby, Elisabete da Cunha, Giovanni G. Fazio, Christopher C. Hayward, Lars Hernquist, and Patrik Jonsson. Global Star Formation Rates and Dust Emission over the Galaxy Interaction Sequence. , 768(1):90, May 2013. doi: 10.1088/0004-637X/768/1/90.

O. Laurino, R. D'Abrusco, G. Longo, and G. Riccio. Astroinformatics of galaxies and quasars: a new general method for photometric redshifts estimation. , 418(4): 2165–2195, December 2011. doi: 10.1111/j.1365-2966.2011.19416.x.

David D. Law, Jane E. Morrison, Ioannis Argyriou, Polychronis Patapis, J. Álvarez-Márquez, Alvaro Labiano, and Bart Vandenbussche. A 3D Drizzle Algorithm for JWST and Practical Application to the MIRI Medium Resolution Spectrometer. , 166(2):45, August 2023. doi: 10.3847/1538-3881/acdddc.

David R. Law, Xihan Ji, Francesco Belfiore, Matthew A. Bershady, Michele Cappellari, Kyle B. Westfall, Renbin Yan, Dmitry Bizyaev, Joel R. Brownstein, Niv Drory, and Brett H. Andrews. SDSS-IV MaNGA: Refining Strong Line Diagnostic Classifications Using Spatially Resolved Gas Dynamics. , 915(1):35, July 2021. doi: 10.3847/1538-4357/abfe0a.

Karen M. Leighly, Donald M. Terndrup, Eddie Baron, Adrian B. Lucy, Matthias Dietrich, and Sarah C. Gallagher. Evidence for Active Galactic Nucleus Feedback in the Broad Absorption Lines and Reddening of Mrk 231. , 788(2):123, June 2014. doi: 10.1088/0004-637X/788/2/123.

Karen M. Leighly, Donald M. Terndrup, Sarah C. Gallagher, and Adrian B. Lucy. The Binary Black Hole Model for Mrk 231 Bites the Dust. , 829(1):4, September 2016. doi: 10.3847/0004-637X/829/1/4.

Karen M. Leighly, Sarah C. Gallagher, Hyunseop Choi, Donald M. Terndrup, Julianna R. Voelker, Gordon T. Richards, and Leah K. Morabito. Balmer Absorption in Iron Low-Ionization Broad Absorption Line Quasars. *arXiv e-prints*, art. arXiv:2509.07611, September 2025. doi: 10.48550/arXiv.2509.07611.

Junyao Li, Ming-Yang Zhuang, Yue Shen, Marta Volonteri, Nianyi Chen, and Tiziana Di Matteo. Active Galactic Nuclei and Host Galaxies in COSMOS-Web. II. First Look at the Kpc-scale Dual and Offset AGN Population. *arXiv e-prints*, art. arXiv:2405.14980, May 2024. doi: 10.48550/arXiv.2405.14980.

G. Liu, N. L. Zakamska, J. E. Greene, N. P. H. Nesvadba, and X. Liu. Observations of feedback from radio-quiet quasars - II. Kinematics of ionized gas nebulae. , 436: 2576–2597, December 2013. doi: 10.1093/mnras/stt1755.

G. Liu, N. L. Zakamska, and J. E. Greene. Similarity of ionized gas nebulae around unobscured and obscured quasars. *ArXiv e-prints*, January 2014.

Jia Liu, Michael Eracleous, and Jules P. Halpern. A Radial Velocity Test for Supermassive Black Hole Binaries as an Explanation for Broad, Double-peaked Emission Lines in Active Galactic Nuclei. , 817(1):42, January 2016. doi: 10.3847/0004-637X/817/1/42.

T. Liu, S. Gezari, M. Ayers, W. Burgett, K. Chambers, K. Hodapp, M. E. Huber, R.-P. Kudritzki, N. Metcalfe, J. Tonry, R. Wainscoat, and C. Waters. Supermassive Black Hole Binary Candidates from the Pan-STARRS1 Medium Deep Survey. , 884(1):36, October 2019. doi: 10.3847/1538-4357/ab40cb.

X. Liu, Y. Shen, M. A. Strauss, and J. E. Greene. Type 2 Active Galactic Nuclei with Double-Peaked [O III] Lines: Narrow-Line Region Kinematics or Merging Supermassive Black Hole Pairs? , 708:427–434, January 2010. doi: 10.1088/0004-637X/708/1/427.

Kelly E. Lockhart, Lisa J. Kewley, Jessica R. Lu, Mark G. Allen, David Rupke, Daniela Calzetti, Richard I. Davies, Michael A. Dopita, Hauke Engel, Timothy M. Heckman, Claus Leitherer, and David B. Sanders. HST/WFC3 Observations of an Off-nuclear Superbubble in Arp 220. , 810(2):149, September 2015. doi: 10.1088/0004-637X/810/2/149.

C. J. Lonsdale, D. Farrah, and H. E. Smith. Ultraluminous Infrared Galaxies. In John W. Mason, editor, *Astrophysics Update 2*, page 285. 2006. doi: 10.1007/3-540-30313-8_9.

E. Lopez-Rodriguez, C. Packham, T. J. Jones, R. Siebenmorgen, P. F. Roche, N. A. Levenson, A. Alonso-Herrero, E. Perlman, K. Ichikawa, C. Ramos Almeida, O. González-Martín, R. Nikutta, M. Martinez-Paredez, D. Shenoy, M. S. Gordon, and C. M. Telesco. Infrared polarimetry of mrk 231: scattering off hot dust grains in the central core. *Monthly Notices of the Royal Astronomical Society*, 464(2): 1762–1770, September 2016. ISSN 1365-2966. doi: 10.1093/mnras/stw2491. URL `http://dx.doi.org/10.1093/mnras/stw2491`.

Enrique Lopez-Rodriguez, Joel Sanchez-Bermudez, Omaira Gonzalez-Martin, Robert Nikutta, Ryan M. Lau, Deepashri Thatte, Ismael Garcia-Bernete, Julien H. Girard, and Matthew J. Hankins. JWST interferometric imaging reveals the dusty disk obscuring the supermassive black hole of the Circinus galaxy. *arXiv e-prints*, art. arXiv:2506.08077, June 2025. doi: 10.48550/arXiv.2506.08077.

Geferson Lucatelli, Robert J. Beswick, Javier Moldón, Miguel A. Pérez-Torres, John E. Conway, Antxon Alberdi, Cristina Romero-Cañizales, Eskil Varenius, Hans-Rainer Klöckner, Loreto Barcos-Muñoz, Marco Bondi, Simon T. Garrington, Susanne Aalto, Willem A. Baan, and Ylva M. Pihlström. The PARADIGM project I: a multiscale radio morphological analysis of local U/LIRGS. , 529(4):4468–4499, April 2024. doi: 10.1093/mnras/stae744.

V. Luridiana, C. Morisset, and R. A. Shaw. PyNeb: a new tool for analyzing emission lines. I. Code description and validation of results. , 573:A42, January 2015. doi: 10.1051/0004-6361/201323152.

E. Lusso, A. Comastri, B. D. Simmons, M. Mignoli, G. Zamorani, C. Vignali, M. Brusa, F. Shankar, D. Lutz, J. R. Trump, R. Maiolino, R. Gilli, M. Bolzonella, S. Puccetti, M. Salvato, C. D. Impey, F. Civano, M. Elvis, V. Mainieri, J. D. Silverman, A. M. Koekemoer, A. Bongiorno, A. Merloni, S. Berta, E. Le Floc'h, B. Magnelli, F. Pozzi, and L. Riguccini. Bolometric luminosities and Eddington ratios of X-ray selected active galactic nuclei in the XMM-COSMOS survey. , 425:623–640, September 2012. doi: 10.1111/j.1365-2966.2012.21513.x.

D. Lutz, E. Sturm, A. Janssen, S. Veilleux, S. Aalto, C. Cicone, A. Contursi, R. I. Davies, C. Feruglio, J. Fischer, A. Fluetsch, S. Garcia-Burillo, R. Genzel, E. González-Alfonso, J. Graciá-Carpio, R. Herrera-Camus, R. Maiolino, A. Schruba, T. Shimizu, A. Sternberg, L. J. Tacconi, and A. Weiß. Molecular outflows in local galaxies: Method comparison and a role of intermittent AGN driving. *A&A*, 633: A134, jan 2020. doi: 10.1051/0004-6361/201936803.

Brad W. Lyke, Alexandra N. Higley, J. N. McLane, Danielle P. Schurhammer, Adam D. Myers, Ashley J. Ross, Kyle Dawson, Solène Chabanier, Paul Martini, Nicolás G. Busca, Hélion du Mas des Bourboux, Mara Salvato, Alina Streblyanska, Pauline Zarrouk, Etienne Burtin, Scott F. Anderson, Julian Bautista, Dmitry Bizyaev, W. N. Brandt, Jonathan Brinkmann, Joel R. Brownstein, Johan Comparat, Paul Green, Axel de la Macorra, Andrea Muñoz Gutiérrez, Jiamin Hou, Jeffrey A. Newman, Nathalie Palanque-Delabrouille, Isabelle Pâris, Will J. Percival, Patrick Petitjean, James Rich, Graziano Rossi, Donald P. Schneider, Alexander Smith, M. Vivek, and Benjamin Alan Weaver. The Sloan Digital Sky Survey Quasar Catalog: Sixteenth Data Release. , 250(1):8, September 2020. doi: 10.3847/1538-4365/aba623.

C. Macfarlane, P. N. Best, J. Sabater, G. Gürkan, M. J. Jarvis, H. J. A. Röttgering, R. D. Baldi, G. Calistro Rivera, K. J. Duncan, L. K. Morabito, I. Prandoni, and E. Retana-Montenegro. The radio loudness of SDSS quasars from the LOFAR Two-metre Sky Survey: ubiquitous jet activity and constraints on star formation. , 506 (4):5888–5907, October 2021. doi: 10.1093/mnras/stab1998.

Camilo Machuca, Matthew A. Bershady, Kate H. R. Rubin, and Eric Wilcots. SDSS-IV MaNGA: Spectroscopic Probes of Neutral Gas in Nearby Galaxies. , 982(2):108, April 2025. doi: 10.3847/1538-4357/adb72d.

Piero Madau and Mark Dickinson. Cosmic Star-Formation History. , 52:415–486, August 2014. doi: 10.1146/annurev-astro-081811-125615.

A. Mahabal, S. G. Djorgovski, M. Turmon, J. Jewell, R. R. Williams, A. J. Drake, M. G. Graham, C. Donalek, E. Glikman, and Palomar-QUEST Team. Automated probabilistic classification of transients and variables. *Astronomische Nachrichten*, 329(3):288–291, March 2008. doi: 10.1002/asna.200710943.

Ashish Mahabal, Umaa Rebbapragada, Richard Walters, Frank J. Masci, Nadejda Blagorodnova, Jan van Roestel, Quan-Zhi Ye, Rahul Biswas, Kevin Burdge, Chan-Kao Chang, Dmitry A. Duev, V. Zach Golkhou, Adam A. Miller, Jakob Nordin, Charlotte Ward, Scott Adams, Eric C. Bellm, Doug Branton, Brian Bue, Chris Cannella, Andrew Connolly, Richard Dekany, Ulrich Feindt, Tiara Hung, Lucy Fortson, Sara Frederick, C. Fremling, Suvi Gezari, Matthew Graham, Steven Groom, Mansi M. Kasliwal, Shrinivas Kulkarni, Thomas Kupfer, Hsing Wen Lin, Chris Lintott, Ragnhild Lunnan, John Parejko, Thomas A. Prince, Reed Riddle, Ben Rusholme, Nicholas Saunders, Nima Sedaghat, David L. Shupe, Leo P. Singer, Maayane T. Soumagnac, Paula Szkody, Yutaro Tachibana, Kushal Tirumala, Sjoert van Velzen, and Darryl Wright. Machine Learning for the Zwicky Transient Facility. , 131(997):038002, March 2019. doi: 10.1088/1538-3873/aaf3fa.

R. Maiolino, S. Gallerani, R. Neri, C. Cicone, A. Ferrara, R. Genzel, D. Lutz, E. Sturm, L. J. Tacconi, F. Walter, C. Feruglio, F. Fiore, and E. Piconcelli. Evidence of strong quasar feedback in the early universe. *MNRAS: Letters*, 425(1):L66–L70, jul 2012. doi: 10.1111/j.1745-3933.2012.01303.x.

Roberto Maiolino, Jan Scholtz, Emma Curtis-Lake, Stefano Carniani, William Baker, Anna de Graaff, Sandro Tacchella, Hannah Übler, Francesco D'Eugenio, Joris Witstok, Mirko Curti, Santiago Arribas, Andrew J. Bunker, Stéphane Charlot, Jacopo Chevallard, Daniel J. Eisenstein, Eiichi Egami, Zhiyuan Ji, Gareth C. Jones, Jianwei Lyu, Tim Rawle, Brant Robertson, Wiphu Rujopakarn, Michele Perna, Fengwu Sun, Giacomo Venturi, Christina C. Williams, and Chris Willott. JADES: The diverse population of infant black holes at $4 < z < 11$: Merging, tiny, poor, but mighty. , 691:A145, November 2024a. doi: 10.1051/0004-6361/202347640.

Roberto Maiolino, Jan Scholtz, Emma Curtis-Lake, Stefano Carniani, William Baker, Anna de Graaff, Sandro Tacchella, Hannah Übler, Francesco D'Eugenio, Joris Witstok, Mirko Curti, Santiago Arribas, Andrew J. Bunker, Stéphane Charlot, Jacopo Chevallard, Daniel J. Eisenstein, Eiichi Egami, Zhiyuan Ji, Gareth C. Jones, Jianwei Lyu, Tim Rawle, Brant Robertson, Wiphu Rujopakarn, Michele Perna, Fengwu Sun, Giacomo Venturi, Christina C. Williams, and Chris Willott. JADES: The diverse population of infant black holes at $4 < z < 11$: Merging, tiny, poor, but mighty. , 691:A145, November 2024b. doi: 10.1051/0004-6361/202347640.

Ankush Mandal, Dipanjan Mukherjee, Christoph Federrath, Nicole P. H. Nesvadba, Geoffrey V. Bicknell, Alexander Y. Wagner, and Moun Meenakshi. Impact of relativistic jets on the star formation rate: a turbulence-regulated framework. , 508(4): 4738–4757, December 2021. doi: 10.1093/mnras/stab2822.

F. Mannucci, E. Pancino, F. Belfiore, C. Cicone, A. Ciurlo, G. Cresci, E. Lusso, A. Marasco, A. Marconi, E. Nardini, E. Pinna, P. Severgnini, P. Saracco, G. Tozzi, and S. Yeh. Unveiling the population of dual and lensed active galactic nuclei at sub-arcsec separations. *Nature Astronomy*, 6:1185–1192, August 2022. doi: 10.1038/s41550-022-01761-5.

A. Marasco, G. Cresci, E. Nardini, F. Mannucci, A. Marconi, P. Tozzi, G. Tozzi, A. Amiri, G. Venturi, E. Piconcelli, G. Lanzuisi, F. Tombesi, M. Mingozzi, M. Perna, S. Carniani, M. Brusa, and S. di Serego Alighieri. Galaxy-scale ionised winds driven by ultra-fast outflows in two nearby quasars. , 644:A15, December 2020. doi: 10.1051/0004-6361/202038889.

C. Marconcini, A. Marconi, G. Cresci, G. Venturi, L. Ulivi, F. Mannucci, F. Belfiore, G. Tozzi, M. Ginolfi, A. Marasco, S. Carniani, A. Amiri, E. Di Teodoro, M. Scialpi, N. Tomicic, M. Mingozzi, M. Brazzini, and B. Moreschini. MOKA^{3D}: An innovative approach to 3D gas kinematic modelling. I. Application to AGN ionised outflows. , 677:A58, September 2023. doi: 10.1051/0004-6361/202346821.

Cosimo Marconcini, Alessandro Marconi, Giovanni Cresci, Filippo Mannucci, Lorenzo Ulivi, Giacomo Venturi, Martina Scialpi, Giulia Tozzi, Francesco Belfiore, Elena Bertola, Stefano Carniani, Elisa Cataldi, Avinanda Chakraborty, Quirino D'Amato, Enrico Di Teodoro, Anna Feltre, Michele Ginolfi, Bianca Moreschini, Nicole Orientale, Bartolomeo Trefoloni, and Andrew King. Evidence of the fast acceleration of AGN-driven winds at kiloparsec scales. *Nature Astronomy*, March 2025. doi: 10.1038/s41550-025-02518-6.

A. Marconi, G. Risaliti, R. Gilli, L. K. Hunt, R. Maiolino, and M. Salvati. Local supermassive black holes, relics of active galactic nuclei and the X-ray background. , 351(1):169–185, June 2004. doi: 10.1111/j.1365-2966.2004.07765.x.

S. Martín, S. Aalto, K. Sakamoto, E. González-Alfonso, S. Muller, C. Henkel, S. García-Burillo, R. Aladro, F. Costagliola, N. Harada, M. Krips, J. Martín-Pintado, S. Mühle, P. van der Werf, and S. Viti. The unbearable opaqueness of Arp220. , 590:A25, May 2016. doi: 10.1051/0004-6361/201528064.

Frank J. Masci, Douglas I. Hoffman, Carl J. Grillmair, and Roc M. Cutri. Automated Classification of Periodic Variable Stars Detected by the Wide-field Infrared Survey Explorer. , 148(1):21, July 2014. doi: 10.1088/0004-6256/148/1/21.

Jorryt Matthee, Rohan P. Naidu, Gabriel Brammer, John Chisholm, Anna-Christina Eilers, Andy Goulding, Jenny Greene, Daichi Kashino, Ivo Labbe, Simon J. Lilly, Ruari Mackenzie, Pascal A. Oesch, Andrea Weibel, Stijn Wuyts, Mengyuan Xiao, Rongmon Bordoloi, Rychard Bouwens, Pieter van Dokkum, Garth Illingworth, Ivan Kramarenko, Michael V. Maseda, Charlotte Mason, Romain A. Meyer, Erica J. Nelson, Naveen A. Reddy, Irene Shivaei, Robert A. Simcoe, and Minghao Yue. Little Red Dots: An Abundant Population of Faint Active Galactic Nuclei at z $\sim$ 5 Revealed by the EIGER and FRESCO JWST Surveys. , 963(2):129, March 2024. doi: 10.3847/1538-4357/ad2345.

D. May and J. E. Steiner. A two-stage outflow in NGC 1068. , 469(1):994–1025, July 2017. doi: 10.1093/mnras/stx886.

D. May, A. Rodríguez-Ardila, M. A. Prieto, J. A. Fernández-Ontiveros, Y. Diaz, and X. Mazzalay. Powerful mechanical-driven outflows in the central parsecs of the low-luminosity active galactic nucleus ESO 428-G14. , 481(1):L105–L109, November 2018. doi: 10.1093/mnrasl/sly155.

D. May, J. E. Steiner, R. B. Menezes, D. R. A. Williams, and J. Wang. The nuclear architecture of NGC 4151: on the path toward a universal outflow mechanism in light of NGC 1068. , 496(2):1488–1516, August 2020. doi: 10.1093/mnras/staa1545.

X. Mazzalay, R. P. Saglia, Peter Erwin, M. H. Fabricius, S. P. Rusli, J. Thomas, R. Bender, M. Opitsch, N. Nowak, and Michael J. Williams. Molecular gas in the centre of nearby galaxies from VLT/SINFONI integral field spectroscopy - I. Morphology and mass inventory. , 428(3):2389–2406, January 2013. doi: 10.1093/mnras/sts204.

J. C. McDowell, D. L. Clements, S. A. Lamb, S. Shaked, N. C. Hearn, L. Colina, C. Mundell, K. Borne, A. C. Baker, and S. Arribas. Chandra Observations of Extended X-Ray Emission in Arp 220. , 591(1):154–166, July 2003. doi: 10.1086/375289.

R. C. McGurk, C. E. Max, A. M. Medling, G. A. Shields, and J. M. Comerford. Spatially Resolved Imaging and Spectroscopy of Candidate Dual Active Galactic Nuclei. , 811(1):14, September 2015. doi: 10.1088/0004-637X/811/1/14.

Rosalie C. McGurk, D. J. Rosario, C. E. Max, G. A. Shields, and K. L. Smith. Keck LGS AO Imaging of QSOs with Double-Peaked or Offset Narrow Lines: Are They Signs of Potential Black Hole Mergers? In *American Astronomical Society Meeting Abstracts #217*, volume 217 of *American Astronomical Society Meeting Abstracts*, page 310.05, January 2011.

Jed McKinney, Alexandra Pope, Allison Kirkpatrick, Lee Armus, Tanio Díaz-Santos, Carlos Gómez-Guijarro, Maximilien Franco, David Elbaz, Christopher C. Hayward, Hanae Inami, Gergö Popping, and Mengyuan Xiao. The IR Compactness of Dusty Galaxies Sets Star Formation and Dust Properties at z 0-2. , 955(2):136, October 2023. doi: 10.3847/1538-4357/ace25c.

B. R. McNamara, P. E. J. Nulsen, M. W. Wise, D. A. Rafferty, C. Carilli, C. L. Sarazin, and E. L. Blanton. The heating of gas in a galaxy cluster by X-ray cavities and large-scale shock fronts. , 433(7021):45–47, January 2005. doi: 10.1038/nature03202.

B. R. McNamara, F. Kazemzadeh, D. A. Rafferty, L. Bîrzan, P. E. J. Nulsen, C. C. Kirkpatrick, and M. W. Wise. An Energetic AGN Outburst Powered by a Rapidly Spinning Supermassive Black Hole or an Accreting Ultramassive Black Hole. , 698 (1):594–605, June 2009. doi: 10.1088/0004-637X/698/1/594.

Moun Meenakshi, Dipanjan Mukherjee, Alexander Y. Wagner, Nicole P. H. Nesvadba, Geoffrey V. Bicknell, Raffaella Morganti, Reinier M. J. Janssen, Ralph S. Sutherland, and Ankush Mandal. Modelling observable signatures of jet-ISM interaction: thermal emission and gas kinematics. , 516(1):766–786, October 2022. doi: 10.1093/mnras/stac2251.

A. Merloni, G. Lamer, T. Liu, M. E. Ramos-Ceja, H. Brunner, E. Bulbul, K. Dennerl, V. Doroshenko, M. J. Freyberg, S. Friedrich, E. Gatuzz, A. Georgakakis, F. Haberl, Z. Igo, I. Kreykenbohm, A. Liu, C. Maitra, A. Malyali, M. G. F. Mayer, K. Nandra, P. Predehl, J. Robrade, M. Salvato, J. S. Sanders, I. Stewart, D. Tubín-Arenas, P. Weber, J. Wilms, R. Arcodia, E. Artis, J. Aschersleben, A. Avakyan, C. Aydar, Y. E. Bahar, F. Balzer, W. Becker, K. Berger, T. Boller, W. Bornemann,

M. Brüggen, M. Brusa, J. Buchner, V. Burwitz, F. Camilloni, N. Clerc, J. Comparat, D. Coutinho, S. Czesla, S. M. Dannhauer, L. Dauner, T. Dauser, J. Dietl, K. Dolag, T. Dwelly, K. Egg, E. Ehl, S. Freund, P. Friedrich, R. Gaida, C. Garrel, V. Ghirardini, A. Gokus, G. Grünwald, S. Grandis, I. Grotova, D. Gruen, A. Gueguen, S. Hämmerich, N. Hamaus, G. Hasinger, K. Haubner, D. Homan, J. Ider Chitham, W. M. Joseph, A. Joyce, O. König, D. M. Kaltenbrunner, A. Khokhriakova, W. Kink, C. Kirsch, M. Kluge, J. Knies, S. Krippendorf, M. Krumpe, J. Kurpas, P. Li, Z. Liu, N. Locatelli, M. Lorenz, S. Müller, E. Magaudda, C. Mannes, H. McCall, N. Meidinger, M. Michailidis, K. Migkas, D. Muñoz-Giraldo, B. Musiimenta, N. T. Nguyen-Dang, Q. Ni, A. Olechowska, N. Ota, F. Pacaud, T. Pasini, E. Perinati, A. M. Pires, C. Pommranz, G. Ponti, K. Poppenhaeger, G. Pühlhofer, A. Rau, M. Reh, T. H. Reiprich, W. Roster, S. Saeedi, A. Santangelo, M. Sasaki, J. Schmitt, P. C. Schneider, T. Schrabback, N. Schuster, A. Schwope, R. Seppi, M. M. Serim, S. Shreeram, E. Sokolova-Lapa, H. Starck, B. Stelzer, J. Stierhof, V. Suleimanov, C. Tenzer, I. Traulsen, J. Trümper, K. Tsuge, T. Urrutia, A. Veronica, S. G. H. Waddell, R. Willer, J. Wolf, M. C. H. Yeung, A. Zainab, F. Zangrandi, X. Zhang, Y. Zhang, and X. Zheng. The SRG/eROSITA all-sky survey. First X-ray catalogues and data release of the western Galactic hemisphere. , 682:A34, February 2024. doi: 10.1051/0004-6361/202347165.

E. Middelberg, A. L. Roy, N. M. Nagar, T. P. Krichbaum, R. P. Norris, A. S. Wilson, H. Falcke, E. J. M. Colbert, A. Witzel, and K. J. Fricke. Motion and properties of nuclear radio components in Seyfert galaxies seen with VLBI. , 417:925–944, April 2004. doi: 10.1051/0004-6361:20040019.

M. Mingozzi, G. Venturi, F. Mannucci, A. Marconi, and G. Cresci. The MAGNUM survey: a high-resolution study of the complex nuclear environment of local Seyfert galaxies. *Communications of the Byurakan Astrophysical Observatory*, 66(2):159–172, December 2019. doi: 10.52526/25792776-2019.66.2-159.

Matilde Mingozzi, Bethan L. James, Danielle A. Berg, Karla Z. Arellano-Córdova, Adele Plat, Claudia Scarlata, Alessandra Aloisi, Ricardo O. Amorín, Jarle Brinchmann, Stéphane Charlot, John Chisholm, Anna Feltre, Simon Gazagnes, Matthew Hayes, Timothy Heckman, Svea Hernandez, Lisa J. Kewley, Nimisha Kumari, Claus Leitherer, Crystal L. Martin, Michael Maseda, Themiya Nanayakkara, Swara Ravindranath, Jane R. Rigby, Peter Senchyna, Evan D. Skillman, Yuma Sugahara, Stephen M. Wilkins, Aida Wofford, and Xinfeng Xu. CLASSY. VIII. Exploring the Source of Ionization with UV Interstellar Medium Diagnostics in Local High-z Analogs. , 962(1):95, February 2024. doi: 10.3847/1538-4357/ad1033.

Persis Misquitta, Benita Dünnebier, Andreas Eckart, and Harshitha Bhat. The peculiar optical spectrum of Mrk 231. , 690:A155, October 2024. doi: 10.1051/0004-6361/202347589.

Anupreeta More, Masamune Oguri, Issha Kayo, Joel Zinn, Michael A. Strauss, Basilio X. Santiago, Ana M. Mosquera, Naohisa Inada, Christopher S. Kochanek, Cristian E. Rusu, Joel R. Brownstein, Luiz N. da Costa, Jean-Paul Kneib, Marcio A. G. Maia, Robert M. Quimby, Donald P. Schneider, Alina Streblyanska, and Donald G. York. The SDSS-III BOSS quasar lens survey: discovery of 13 gravitationally lensed quasars. , 456(2):1595–1606, February 2016. doi: 10.1093/mnras/stv2813.

Jorge Moreno, Paul Torrey, Sara L. Ellison, David R. Patton, Asa F. L. Bluck, Gunjan Bansal, and Lars Hernquist. Mapping galaxy encounters in numerical simulations: the spatial extent of induced star formation. , 448(2):1107–1117, April 2015. doi: 10.1093/mnras/stv094.

Jorge Moreno, Paul Torrey, Sara L. Ellison, David R. Patton, Philip F. Hopkins, Michael Bueno, Christopher C. Hayward, Desika Narayanan, Dušan Kereš, Asa F. L. Bluck, and Lars Hernquist. Interacting galaxies on FIRE-2: the connection between enhanced star formation and interstellar gas content. , 485(1):1320–1338, May 2019. doi: 10.1093/mnras/stz417.

Raffaella Morganti, Tom Oosterloo, J. B. Raymond Oonk, Wilfred Frieswijk, and Clive Tadhunter. The fast molecular outflow in the Seyfert galaxy IC 5063 as seen by ALMA. , 580:A1, August 2015. doi: 10.1051/0004-6361/201525860.

Raffaella Morganti, Sylvain Veilleux, Tom Oosterloo, Stacy H. Teng, and David Rupke. Another piece of the puzzle: The fast H I outflow in Mrk 231. , 593:A30, September 2016. doi: 10.1051/0004-6361/201628978.

Dipanjan Mukherjee, Geoffrey V. Bicknell, Ralph Sutherland, and Alex Wagner. Relativistic jet feedback in high-redshift galaxies - I. Dynamics. , 461(1):967–983, September 2016. doi: 10.1093/mnras/stw1368.

Dipanjan Mukherjee, Geoffrey V. Bicknell, Alexander Y. Wagner, Ralph S. Sutherland, and Joseph Silk. Relativistic jet feedback - III. Feedback on gas discs. , 479(4):5544–5566, October 2018a. doi: 10.1093/mnras/sty1776.

Dipanjan Mukherjee, Alexander Y. Wagner, Geoffrey V. Bicknell, Raffaella Morganti, Tom Oosterloo, Nicole Nesvadba, and Ralph S. Sutherland. The jet-ISM interactions in IC 5063. , 476(1):80–95, May 2018b. doi: 10.1093/mnras/sty067.

F. Müller-Sánchez, J. M. Comerford, R. Nevin, R. S. Barrows, M. C. Cooper, and J. E. Greene. The Origin of Double-peaked Narrow Lines in Active Galactic Nuclei. I. Very Large Array Detections of Dual AGNs and AGN Outflows. , 813(2):103, November 2015. doi: 10.1088/0004-637X/813/2/103.

B. Musiimenta, G. Speranza, T. Urrutia, M. Brusa, C. Ramos Almeida, M. Perna, I. E. López, D. Alexander, B. Laloux, F. Shankar, A. Lapi, M. Salvato, Y. Toba, C. Andonie, and I. M. Rodríguez. Ionised AGN outflows in the Goldfish galaxy: The illuminating and interacting red quasar eFEDSJ091157.4+014327 at z $\sim$ 0.6. , 687: A111, July 2024. doi: 10.1051/0004-6361/202449283.

E. Nardini, G. Risaliti, Y. Watabe, M. Salvati, and E. Sani. The role of nuclear activity as the power source of ultraluminous infrared galaxies. , 405(4):2505–2520, July 2010. doi: 10.1111/j.1365-2966.2010.16618.x.

E. Nardini, J. N. Reeves, J. Gofford, F. A. Harrison, G. Risaliti, V. Braito, M. T. Costa, G. A. Matzeu, D. J. Walton, E. Behar, S. E. Boggs, F. E. Christensen, W. W. Craig, C. J. Hailey, G. Matt, J. M. Miller, P. T. O'Brien, D. Stern, T. J. Turner, and M. J. Ward. Black hole feedback in the luminous quasar PDS 456. *Science*, 347(6224): 860–863, February 2015. doi: 10.1126/science.1259202.

Brett Naul, Joshua S. Bloom, Fernando Pérez, and Stéfan van der Walt. A recurrent neural network for classification of unevenly sampled variable stars. *Nature Astronomy*, 2:151–155, November 2018. doi: 10.1038/s41550-017-0321-z.

Dylan Nelson, Volker Springel, Annalisa Pillepich, Vicente Rodriguez-Gomez, Paul Torrey, Shy Genel, Mark Vogelsberger, Ruediger Pakmor, Federico Marinacci, Rainer Weinberger, Luke Kelley, Mark Lovell, Benedikt Diemer, and Lars Hernquist. The IllustrisTNG simulations: public data release. *CompAC*, 6(1), may 2019. doi: 10.1186/s40668-019-0028-x.

Erica J. Nelson, Katherine A. Suess, Rachel Bezanson, Sedona H. Price, Pieter van Dokkum, Joel Leja, Bingjie Wang, Katherine E. Whitaker, Ivo Labbé, Laia Barrufet, Gabriel Brammer, Daniel J. Eisenstein, Justus Gibson, Abigail I. Hartley, Benjamin D. Johnson, Kasper E. Heintz, Elijah Mathews, Tim B. Miller, Pascal A. Oesch, Lester Sandles, David J. Setton, Joshua S. Speagle, Sandro Tacchella, Kenichi Tadaki, Hannah Übler, and John. R. Weaver. JWST Reveals a Population of Ultrared, Flattened Galaxies at $2 \lesssim z \lesssim 6$ Previously Missed by HST. , 948(2):L18, May 2023. doi: 10.3847/2041-8213/acc1e1.

N. P. H. Nesvadba, M. D. Lehnert, F. Eisenhauer, A. Gilbert, M. Tecza, and R. Abuter. Extreme Gas Kinematics in the z=2.2 Powerful Radio Galaxy MRC 1138-262: Evidence for Efficient Active Galactic Nucleus Feedback in the Early Universe? , 650 (2):693–705, October 2006. doi: 10.1086/507266.

N. P. H. Nesvadba, M. D. Lehnert, C. De Breuck, A. Gilbert, and W. van Breugel. Compact radio sources and jet-driven AGN feedback in the early universe: constraints from integral-field spectroscopy. , 475(1):145–153, November 2007. doi: 10.1051/0004-6361:20078175.

N. P. H. Nesvadba, M. D. Lehnert, C. De Breuck, A. M. Gilbert, and W. van Breugel. Evidence for powerful AGN winds at high redshift: dynamics of galactic outflows in radio galaxies during the "Quasar Era". , 491(2):407–424, November 2008. doi: 10.1051/0004-6361:200810346.

R. Nevin, J. Comerford, F. Müller-Sánchez, R. Barrows, and M. Cooper. The Origin of Double-peaked Narrow Lines in Active Galactic Nuclei. II. Kinematic Classifications for the Population at $z < 0.1$. , 832(1):67, November 2016. doi: 10.3847/0004-637X/832/1/67.

S. F. Newman, R. Genzel, N. M. Förster-Schreiber, K. Shapiro Griffin, C. Mancini, S. J. Lilly, A. Renzini, N. Bouché, A. Burkert, P. Buschkamp, C. M. Carollo, G. Cresci, R. Davies, F. Eisenhauer, S. Genel, E. K. S. Hicks, J. Kurk, D. Lutz, T. Naab, Y. Peng, A. Sternberg, L. J. Tacconi, D. Vergani, S. Wuyts, and G. Zamorani. The SINS/zC-SINF Survey of z ˜ 2 Galaxy Kinematics: Outflow Properties. , 761:43, December 2012. doi: 10.1088/0004-637X/761/1/43.

Ray P. Norris, M. Salvato, G. Longo, M. Brescia, T. Budavari, S. Carliles, S. Cavuoti, D. Farrah, J. Geach, K. Luken, A. Musaeva, K. Polsterer, G. Riccio, N. Seymour, V. Smolčić, M. Vaccari, and P. Zinn. A Comparison of Photometric Redshift Techniques for Large Radio Surveys. , 131(1004):108004, October 2019. doi: 10.1088/1538-3873/ab0f7b.

D. E. Osterbrock. Spectrophotometry of Seyfert 1 galaxies. , 215:733–745, August 1977. doi: 10.1086/155407.

Donald E. Osterbrock and Gary J. Ferland. *Astrophysics of gaseous nebulae and active galactic nuclei*. 2006.

Christopher Packham, James T. Radomski, Patrick F. Roche, David K. Aitken, Eric Perlman, Almudena Alonso-Herrero, Luis Colina, and Charles M. Telesco. The Extended Mid-Infrared Structure of the Circinus Galaxy. , 618(1):L17–L20, January 2005. doi: 10.1086/427691.

Fabio Pacucci, Bao Nguyen, Stefano Carniani, Roberto Maiolino, and Xiaohui Fan. JWST CEERS and JADES Active Galaxies at z = 4-7 Violate the Local M -M $_\star$ Relation at $>3\sigma$: Implications for Low-mass Black Holes and Seeding Models. , 957 (1):L3, November 2023. doi: 10.3847/2041-8213/ad0158.

Alessandro Paggi, Giuseppina Fabbiano, Guido Risaliti, Junfeng Wang, Margarita Karovska, Martin Elvis, W. Peter Maksym, Jonathan McDowell, and Jay Gallagher. X-Ray Emission from the Nuclear Region of Arp 220. , 841(1):44, May 2017. doi: 10.3847/1538-4357/aa713b.

Francesca Panessa and Marcello Giroletti. Sub-parsec radio cores in nearby Seyfert galaxies. , 432(2):1138–1143, June 2013. doi: 10.1093/mnras/stt547.

Adam Paszke, Sam Gross, Francisco Massa, Adam Lerer, James Bradbury, Gregory Chanan, Trevor Killeen, Zeming Lin, Natalia Gimelshein, Luca Antiga, Alban Desmaison, Andreas Köpf, Edward Yang, Zach DeVito, Martin Raison, Alykhan Tejani, Sasank Chilamkurthy, Benoit Steiner, Lu Fang, Junjie Bai, and Soumith Chintala. PyTorch: An Imperative Style, High-Performance Deep Learning Library. *arXiv e-prints*, art. arXiv:1912.01703, December 2019. doi: 10.48550/arXiv.1912.01703.

David R. Patton, Sara L. Ellison, Luc Simard, Alan W. McConnachie, and J. Trevor Mendel. Galaxy pairs in the Sloan Digital Sky Survey - III. Evidence of induced star formation from optical colours. , 412(1):591–606, March 2011. doi: 10.1111/j.1365-2966.2010.17932.x.

David R. Patton, Paul Torrey, Sara L. Ellison, J. Trevor Mendel, and Jillian M. Scudder. Galaxy pairs in the Sloan Digital Sky Survey - VI. The orbital extent of enhanced star formation in interacting galaxies. , 433(1):L59–L63, June 2013. doi: 10.1093/mnrasl/slt058.

David R Patton, Kieran D Wilson, Colin J Metrow, Sara L Ellison, Paul Torrey, Westley Brown, Maan H Hani, Stuart McAlpine, Jorge Moreno, and Joanna Woo. Interacting galaxies in the IllustrisTNG simulations - i: Triggered star formation in a cosmological context. *MNRAS*, 494(4):4969–4985, apr 2020. doi: 10.1093/mnras/staa913.

W. J. Pearson, L. Wang, M. Alpaslan, I. Baldry, M. Bilicki, M. J. I. Brown, M. W. Grootes, B. W. Holwerda, T. D. Kitching, S. Kruk, and F. F. S. van der Tak. Effect of galaxy mergers on star-formation rates. , 631:A51, November 2019. doi: 10.1051/0004-6361/201936337.

L. Peralta de Arriba, A. Alonso-Herrero, S. García-Burillo, I. García-Bernete, M. Villar-Martín, B. García-Lorenzo, R. Davies, D. J. Rosario, S. F. Hönig, N. A. Levenson, C. Packham, C. Ramos Almeida, M. Pereira-Santaella, A. Audibert, E. Bellocchi, E. K. S. Hicks, A. Labiano, C. Ricci, and D. Rigopoulou. A radio-jet driven outflow in the Seyfert 2 galaxy NGC 2110? *arXiv e-prints*, art. arXiv:2305.06366, May 2023. doi: 10.48550/arXiv.2305.06366.

M. Pereira-Santaella, L. Colina, S. García-Burillo, A. Alonso-Herrero, S. Arribas, S. Cazzoli, B. Emonts, J. Piqueras López, P. Planesas, T. Storchi Bergmann, A. Usero, and M. Villar-Martín. High-velocity extended molecular outflow in the star-formation dominated luminous infrared galaxy ESO 320-G030. , 594:A81, October 2016. doi: 10.1051/0004-6361/201628875.

M. Pereira-Santaella, L. Colina, S. García-Burillo, F. Combes, B. Emonts, S. Aalto, A. Alonso-Herrero, S. Arribas, C. Henkel, A. Labiano, S. Muller, J. Piqueras López, D. Rigopoulou, and P. van der Werf. Spatially resolved cold molecular outflows in ULIRGs. , 616:A171, August 2018. doi: 10.1051/0004-6361/201833089.

M. Pereira-Santaella, L. Colina, S. García-Burillo, I. Lamperti, E. González-Alfonso, M. Perna, S. Arribas, A. Alonso-Herrero, S. Aalto, F. Combes, A. Labiano, J. Piqueras-López, D. Rigopoulou, and P. van der Werf. Physics of ULIRGs with MUSE and ALMA: The PUMA project. II. Are local ULIRGs powered by AGN? The subkiloparsec view of the 220 GHz continuum. , 651:A42, July 2021. doi: 10.1051/0004-6361/202140955.

M. Perna, M. Brusa, G. Cresci, A. Comastri, G. Lanzuisi, E. Lusso, A. Marconi, M. Salvato, G. Zamorani, A. Bongiorno, V. Mainieri, R. Maiolino, and M. Mignoli. Galaxy-wide outflows in z ~1.5 luminous obscured quasars revealed through near-IR slit-resolved spectroscopy. , 574:A82, February 2015. doi: 10.1051/0004-6361/201425035.

M. Perna, G. Lanzuisi, M. Brusa, G. Cresci, and M. Mignoli. An X-ray/SDSS sample. II. AGN-driven outflowing gas plasma properties. , 606:A96, October 2017. doi: 10.1051/0004-6361/201730819.

M. Perna, M. T. Sargent, M. Brusa, E. Daddi, C. Feruglio, G. Cresci, G. Lanzuisi, E. Lusso, A. Comastri, R. T. Coogan, Q. D'Amato, R. Gilli, E. Piconcelli, and C. Vignali. Molecular gas content in obscured AGN at $z > 1$. , 619:A90, November 2018. doi: 10.1051/0004-6361/201833040.

M. Perna, S. Arribas, C. Catalán-Torrecilla, L. Colina, E. Bellocchi, A. Fluetsch, R. Maiolino, S. Cazzoli, A. Hernán Caballero, M. Pereira Santaella, J. Piqueras López, and B. Rodríguez del Pino. MUSE view of Arp220: Kpc-scale multi-phase outflow and evidence for positive feedback. , 643:A139, November 2020. doi: 10.1051/0004-6361/202038328.

M. Perna, S. Arribas, M. Pereira Santaella, L. Colina, E. Bellocchi, C. Catalán-Torrecilla, S. Cazzoli, A. Crespo Gómez, R. Maiolino, J. Piqueras López, and B. Rodríguez del Pino. Physics of ULIRGs with MUSE and ALMA: The PUMA project. I. Properties of the survey and first MUSE data results. , 646:A101, February 2021. doi: 10.1051/0004-6361/202039702.

M. Perna, S. Arribas, M. Marshall, F. D'Eugenio, H. Übler, A. Bunker, S. Charlot, S. Carniani, P. Jakobsen, R. Maiolino, B. Rodríguez Del Pino, C. J. Willott, T. Böker, C. Circosta, G. Cresci, M. Curti, B. Husemann, N. Kumari, I. Lamperti, P. G. Pérez-González, and J. Scholtz. GA-NIFS: The ultra-dense, interacting environment of a dual AGN at z $\sim$ 3.3 revealed by JWST/NIRSpec IFS. , 679:A89, November 2023. doi: 10.1051/0004-6361/202346649.

Michele Perna, Santiago Arribas, Isabella Lamperti, Miguel Pereira-Santaella, Lorenzo Ulivi, Torsten Böker, Roberto Maiolino, Andrew J. Bunker, Stéphane Charlot, Giovanni Cresci, Bruno Rodríguez Del Pino, Francesco D'Eugenio, Hannah Übler, Katja Fahrion, and Matteo Ceci. No evidence of agn features in the nuclei of arp 220 from jwst/nirspec ifs, 2024.

Michele Perna, Santiago Arribas, Isabella Lamperti, Chiara Circosta, Elena Bertola, Pablo G. Pérez-González, Francesco D'Eugenio, Hannah Übler, Giovanni Cresci, Marta Volonteri, Filippo Mannucci, Roberto Maiolino, Bruno Rodríguez Del Pino, Torsten Böker, Andrew J. Bunker, Stéphane Charlot, Chris J. Willott, Stefano Carniani, Mirko Curti, Gareth C. Jones, Nimisha Kumari, Madeline A. Marshall, Giacomo Venturi, Aayush Saxena, Jan Scholtz, and Joris Witstok. GA-NIFS: High number of dual active galactic nuclei at z $\sim$ 3. , 696:A59, April 2025. doi: 10.1051/0004-6361/202453430.

S. Perrotta, F. Hamann, N. L. Zakamska, R. M. Alexandroff, D. Rupke, and D. Wylezalek. ERQs are the BOSS of quasar samples: the highest velocity [O III] quasar outflows. , 488(3):4126–4148, September 2019. doi: 10.1093/mnras/stz1993.

Ismael Pessa, Lutz Wisotzki, Tanya Urrutia, John Pharo, Ramona Augustin, Nicolas F. Bouché, Anna Feltre, Yucheng Guo, Daria Kozlova, Davor Krajnovic, Haruka Kusakabe, Floriane Leclercq, Héctor Salas, Joop Schaye, and Anne Verhamme. A galactic outflow traced by its extended Mg II emission out to a $\sim$30 kpc radius in the Hubble Ultra Deep Field with MUSE. , 691:A5, November 2024. doi: 10.1051/0004-6361/202450547.

Ryan W. Pfeifle, Kimberly A. Weaver, Nathan J. Secrest, Barry Rothberg, and David R. Patton. Super-Size Me: The Big Multi-AGN Catalog (The Big MAC), Data Release 1: The Source Catalog. *arXiv e-prints*, art. arXiv:2411.12799, November 2024. doi: 10.48550/arXiv.2411.12799.

J. Piqueras López, L. Colina, S. Arribas, A. Alonso-Herrero, and A. G. Bedregal. VLT-SINFONI integral field spectroscopy of low-z luminous and ultraluminous infrared galaxies: I. Atlas of the 2d gas structureâ. *A&A*, 546:A64, October 2012. ISSN 0004-6361, 1432-0746. doi: 10.1051/0004-6361/201219372. URL `http://www.aanda.org/10.1051/0004-6361/201219372`.

Clara Puerto-Sánchez, Mélanie Habouzit, Marta Volonteri, Yueying Ni, Adi Foord, Daniel Anglés-Alcázar, Nianyi Chen, Paloma Guetzoyan, Romeel Davé, Tiziana Di Matteo, Yohan Dubois, Michael Koss, and Yetli Rosas-Guevara. Large-scale dual AGN in large-scale cosmological hydrodynamical simulations. , 536(3):3016–3040, January 2025. doi: 10.1093/mnras/stae2763.

M. Querejeta, E. Schinnerer, S. García-Burillo, F. Bigiel, G. A. Blanc, D. Colombo, A. Hughes, K. Kreckel, A. K. Leroy, S. E. Meidt, D. S. Meier, J. Pety, and K. Sliwa. AGN feedback in the nucleus of M 51. , 593:A118, October 2016. doi: 10.1051/0004-6361/201628674.

Suvendu Rakshit, C. S. Stalin, and Jari Kotilainen. Spectral Properties of Quasars from Sloan Digital Sky Survey Data Release 14: The Catalog. , 249(1):17, July 2020. doi: 10.3847/1538-4365/ab99c5.

C. Ramos Almeida, J. A. Acosta-Pulido, C. N. Tadhunter, C. González-Fernández, C. Cicone, and M. Fernández-Torreiro. A near-infrared study of the multiphase outflow in the type-2 quasar J1509+0434. , 487(1):L18–L23, July 2019. doi: 10.1093/mnrasl/slz072.

C. Ramos Almeida, M. Bischetti, S. García-Burillo, A. Alonso-Herrero, A. Audibert, C. Cicone, C. Feruglio, C. N. Tadhunter, J. C. S. Pierce, M. Pereira-Santaella, and P. S. Bessiere. The diverse cold molecular gas contents, morphologies, and kinematics of type-2 quasars as seen by ALMA. , 658:A155, February 2022. doi: 10.1051/0004-6361/202141906.

Bernard J. Rauscher, Richard G. Arendt, D. J. Fixsen, Matthew A. Greenhouse, Matthew Lander, Don Lindler, Markus Loose, S. H. Moseley, D. Brent Mott, Yiting Wen, Donna V. Wilson, and Christos Xenophontos. Improved Reference Sampling and Subtraction: A Technique for Reducing the Read Noise of Near-infrared Detector Systems. , 129(980):105003, October 2017. doi: 10.1088/1538-3873/aa83fd.

J. T. Rayner, D. W. Toomey, P. M. Onaka, A. J. Denault, W. E. Stahlberger, W. D. Vacca, M. C. Cushing, and S. Wang. SpeX: A Medium-Resolution 0.8-5.5 Micron Spectrograph and Imager for the NASA Infrared Telescope Facility. , 115(805):362–382, March 2003. doi: 10.1086/367745.

P. Re Fiorentin, C. A. L. Bailer-Jones, Y. S. Lee, T. C. Beers, T. Sivarani, R. Wilhelm, C. Allende Prieto, and J. E. Norris. Estimation of stellar atmospheric parameters from SDSS/SEGUE spectra. , 467(3):1373–1387, June 2007. doi: 10.1051/0004-6361:20077334.

J. I. Read and Neil Trentham. The baryonic mass function of galaxies. *Philosophical Transactions of the Royal Society of London Series A*, 363(1837):2693, December 2005. doi: 10.1098/rsta.2005.1648.

Naveen A. Reddy, Michael W. Topping, Ryan L. Sanders, Alice E. Shapley, and Gabriel Brammer. Paschen-line Constraints on Dust Attenuation and Star Formation at z 1-3 with JWST/NIRSpec. , 948(2):83, May 2023. doi: 10.3847/1538-4357/acc869.

Andrew M. M. Reeves and Michael J. Hudson. How many stars form in galaxy mergers? , 527(2):2037–2048, January 2024. doi: 10.1093/mnras/stad3211.

Itamar Reis, Dalya Baron, and Sahar Shahaf. Probabilistic Random Forest: A Machine Learning Algorithm for Noisy Data Sets. , 157(1):16, January 2019. doi: 10.3847/1538-3881/aaf101.

Florent Renaud, Álvaro Segovia Otero, and Oscar Agertz. The merger-starburst connection across cosmic times. , 516(4):4922–4931, November 2022. doi: 10.1093/mnras/stac2557.

J. Reunanen, M. A. Prieto, and R. Siebenmorgen. VLT diffraction-limited imaging at 11 and 18μm of the nearest active galactic nuclei. , 402(2):879–894, February 2010. doi: 10.1111/j.1365-2966.2009.15997.x.

Mitchell Revalski, D. Michael Crenshaw, Marc Rafelski, Steven B. Kraemer, Garrett E. Polack, Anna Trindade Falcão, Travis C. Fischer, Beena Meena, Francisco Martinez, Henrique R. Schmitt, Nicholas R. Collins, and Julia Falcone. Quantifying Feedback from Narrow Line Region Outflows in Nearby Active Galaxies. IV. The Effects of Different Density Estimates on the Ionized Gas Masses and Outflow Rates. , 930(1):14, May 2022. doi: 10.3847/1538-4357/ac5f3d.

Cormac Reynolds, Brian Punsly, Christopher P. O'Dea, and Natasha Hurley-Walker. A Blazar-like Radio Flare in Mrk 231. , 776(2):L21, October 2013. doi: 10.1088/2041-8205/776/2/L21.

C. Ricci, F. E. Bauer, E. Treister, K. Schawinski, G. C. Privon, L. Blecha, P. Arevalo, L. Armus, F. Harrison, L. C. Ho, K. Iwasawa, D. B. Sanders, and D. Stern. Growing supermassive black holes in the late stages of galaxy mergers are heavily obscured. , 468(2):1273–1299, June 2017. doi: 10.1093/mnras/stx173.

Joseph W. Richards, Darren Homrighausen, Peter E. Freeman, Chad M. Schafer, and Dovi Poznanski. Semi-supervised learning for photometric supernova classification. , 419(2):1121–1135, January 2012. doi: 10.1111/j.1365-2966.2011.19768.x.

Marcia J. Rieke, Douglas Kelly, and Scott Horner. Overview of James Webb Space Telescope and NIRCam's Role. In James B. Heaney and Lawrence G. Burriesci, editors, *Cryogenic Optical Systems and Instruments XI*, volume 5904 of *Society of Photo-Optical Instrumentation Engineers (SPIE) Conference Series*, pages 1–8, August 2005. doi: 10.1117/12.615554.

Rogemar A. Riffel, Thaisa Storchi-Bergmann, and Rogério Riffel. An Outflow Perpendicular to the Radio Jet in the Seyfert Nucleus of NGC 5929. , 780(2):L24, January 2014. doi: 10.1088/2041-8205/780/2/L24.

Rogemar A. Riffel, Thaisa Storchi-Bergmann, and Rogério Riffel. Feeding versus feedback in active galactic nuclei from near-infrared integral field spectroscopy - X. NGC 5929. , 451(4):3587–3605, August 2015. doi: 10.1093/mnras/stv1129.

Rogemar A. Riffel, Nadia L. Zakamska, and Rogério Riffel. Active galactic nuclei winds as the origin of the H_2 emission excess in nearby galaxies. , 491(1):1518–1529, January 2020. doi: 10.1093/mnras/stz3137.

G. W. Roberts-Borsani, A. Saintonge, K. L. Masters, and D. V. Stark. Outflows in star-forming galaxies: Stacking analyses of resolved winds and the relation to their hosts' properties. , 493(3):3081–3097, April 2020. doi: 10.1093/mnras/staa464.

Brant E. Robertson, Sandro Tacchella, Benjamin D. Johnson, Ryan Hausen, Adebusola B. Alabi, Kristan Boyett, Andrew J. Bunker, Stefano Carniani, Eiichi Egami, Daniel J. Eisenstein, Kevin N. Hainline, Jakob M. Helton, Zhiyuan Ji, Nimisha Kumari, Jianwei Lyu, Roberto Maiolino, Erica J. Nelson, Marcia J. Rieke, Irene Shivaei, Fengwu Sun, Hannah Übler, Christina C. Williams, Christopher N. A. Willmer, and Joris Witstok. Morpheus Reveals Distant Disk Galaxy Morphologies with JWST: The First AI/ML Analysis of JWST Images. , 942(2):L42, January 2023. doi: 10.3847/2041-8213/aca086.

Carlos Rodrigo, Enrique Solano, and Amelia Bayo. SVO Filter Profile Service Version 1.0. IVOA Working Draft 15 October 2012, October 2012.

C. Rodriguez, G. B. Taylor, R. T. Zavala, A. B. Peck, L. K. Pollack, and R. W. Romani. A Compact Supermassive Binary Black Hole System. , 646(1):49–60, July 2006. doi: 10.1086/504825.

A. Rodríguez-Ardila, M. A. Prieto, X. Mazzalay, J. A. Fernández-Ontiveros, R. Luque, and F. Müller-Sánchez. Powerful outflows in the central parsecs of the low-luminosity active galactic nucleus NGC 1386. , 470(3):2845–2860, September 2017. doi: 10.1093/mnras/stx1401.

Vicente Rodriguez-Gomez, Shy Genel, Mark Vogelsberger, Debora Sijacki, Annalisa Pillepich, Laura V. Sales, Paul Torrey, Greg Snyder, Dylan Nelson, Volker Springel, Chung-Pei Ma, and Lars Hernquist. The merger rate of galaxies in the Illustris simulation: a comparison with observations and semi-empirical models. , 449(1):49–64, May 2015. doi: 10.1093/mnras/stv264.

D. J. Rosario, R. C. McGurk, C. E. Max, G. A. Shields, K. L. Smith, and S. M. Ammons. Adaptive Optics Imaging of Quasi-stellar Objects with Double-peaked Narrow Lines: Are They Dual Active Galactic Nuclei? , 739(1):44, September 2011. doi: 10.1088/0004-637X/739/1/44.

Yetli M. Rosas-Guevara, Richard G. Bower, Stuart McAlpine, Silvia Bonoli, and Patricia B. Tissera. The abundances and properties of Dual AGN and their host galaxies in the EAGLE simulations. , 483(2):2712–2720, February 2019. doi: 10.1093/mnras/sty3251.

Murray Rosenblatt. A multi-dimensional prediction problem. *Arkiv for Matematik*, 3 (5):407–424, January 1958. doi: 10.1007/BF02589495.

Laurence S. Rothman. History of the HITRAN Database. *Nature Reviews Physics*, 3 (5):302–304, January 2021. doi: 10.1038/s42254-021-00309-2.

K. Rubinur, M. Das, and P. Kharb. Searching for dual active galactic nuclei. *Journal of Astrophysics and Astronomy*, 39(1):8, February 2018. doi: 10.1007/s12036-018-9512-y.

Sebastian Ruder. An Overview of Multi-Task Learning in Deep Neural Networks. *arXiv e-prints*, art. arXiv:1706.05098, June 2017. doi: 10.48550/arXiv.1706.05098.

Jessie C. Runnoe, Michael Eracleous, Gavin Mathes, Alison Pennell, Todd Boroson, Steinn Sigurðsson, Tamara Bogdanović, Jules P. Halpern, and Jia Liu. A Large Systematic Search for Close Supermassive Binary and Rapidly Recoiling Black Holes. II. Continued Spectroscopic Monitoring and Optical Flux Variability. , 221(1):7, November 2015. doi: 10.1088/0067-0049/221/1/7.

David S. Rupke, Sylvain Veilleux, and D. B. Sanders. Keck Absorption-Line Spectroscopy of Galactic Winds in Ultraluminous Infrared Galaxies. , 570(2):588–609, May 2002. doi: 10.1086/339789.

David S. N. Rupke and Sylvain Veilleux. Integral Field Spectroscopy of Massive, Kiloparsec-scale Outflows in the Infrared-luminous QSO Mrk 231. , 729(2):L27, March 2011. doi: 10.1088/2041-8205/729/2/L27.

David S. N. Rupke and Sylvain Veilleux. The Multiphase Structure and Power Sources of Galactic Winds in Major Mergers. , 768(1):75, May 2013a. doi: 10.1088/0004-637X/768/1/75.

David S. N. Rupke and Sylvain Veilleux. Breaking the Obscuring Screen: A Resolved Molecular Outflow in a Buried QSO. , 775(1):L15, September 2013b. doi: 10.1088/2041-8205/775/1/L15.

D. Ruschel-Dutra, T. Storchi-Bergmann, A. Schnorr-Müller, R. A. Riffel, B. Dall'Agnol de Oliveira, D. Lena, A. Robinson, N. Nagar, and M. Elvis. AGNIFS survey of local AGN: GMOS-IFU data and outflows in 30 sources. , 507(1):74–89, October 2021. doi: 10.1093/mnras/stab2058.

Vida Saeedzadeh, Arif Babul, Suvodip Mukherjee, Michael Tremmel, Thomas R. Quinn, and Lucio Mayer. Dual Active Galactic Nuclei: Precursors of Binary Supermassive Black Hole Formation and Mergers. , 975(2):265, November 2024. doi: 10.3847/1538-4357/ad7a6f.

K. Sakamoto, N. Z. Scoville, M. S. Yun, M. Crosas, R. Genzel, and L. J. Tacconi. Counterrotating Nuclear Disks in ARP 220. , 514(1):68–76, March 1999. doi: 10.1086/306951.

Kazushi Sakamoto, Susanne Aalto, David J. Wilner, John H. Black, John E. Conway, Francesco Costagliola, Alison B. Peck, Marco Spaans, Junzhi Wang, and Martina C. Wiedner. P Cygni Profiles of Molecular Lines Toward Arp 220 Nuclei. , 700(2):L104–L108, August 2009. doi: 10.1088/0004-637X/700/2/L104.

Dragan Salak, Naomasa Nakai, Kazuo Sorai, and Yusuke Miyamoto. Molecular Gas Outflow in the Starburst Galaxy NGC 1482. , 901(2):151, October 2020. doi: 10.3847/1538-4357/abb134.

P. Sánchez-Blázquez, R. F. Peletier, J. Jiménez-Vicente, N. Cardiel, A. J. Cenarro, J. Falcón-Barroso, J. Gorgas, S. Selam, and A. Vazdekis. Medium-resolution Isaac Newton Telescope library of empirical spectra. , 371(2):703–718, September 2006. doi: 10.1111/j.1365-2966.2006.10699.x.

D. B. Sanders and I. F. Mirabel. Luminous Infrared Galaxies. , 34:749–+, 1996. doi: 10.1146/annurev.astro.34.1.749.

D. B. Sanders, B. T. Soifer, J. H. Elias, B. F. Madore, K. Matthews, G. Neugebauer, and N. Z. Scoville. Ultraluminous infrared galaxies and the origin of quasars. *ApJ*, 325:74, February 1988. ISSN 0004-637X, 1538-4357. doi: 10.1086/165983. URL `http://adsabs.harvard.edu/doi/10.1086/165983`.

J. S. Sanders and A. C. Fabian. A deeper X-ray study of the core of the Perseus galaxy cluster: the power of sound waves and the distribution of metals and cosmic rays. , 381(4):1381–1399, November 2007. doi: 10.1111/j.1365-2966.2007.12347.x.

Brandon Sandoval, Adi Foord, Steven W. Allen, Marta Volonteri, Aaron Stemo, Nianyi Chen, Tiziana Di Matteo, Kayhan Gultekin, Melanie Habouzit, Clara Puerto-Sanchez, Edmund Hodges-Kluck, and Yohan Dubois. Searching for the Highest-z Dual AGN in the Deepest Chandra Surveys. *arXiv e-prints*, art. arXiv:2312.02311, December 2023. doi: 10.48550/arXiv.2312.02311.

Shobita Satyapal, Sara L. Ellison, William McAlpine, Ryan C. Hickox, David R. Patton, and J. Trevor Mendel. Galaxy pairs in the Sloan Digital Sky Survey - IX. Merger-induced AGN activity as traced by the Wide-field Infrared Survey Explorer. , 441(2):1297–1304, June 2014. doi: 10.1093/mnras/stu650.

Shobita Satyapal, Nathan J. Secrest, Claudio Ricci, Sara L. Ellison, Barry Rothberg, Laura Blecha, Anca Constantin, Mario Gliozzi, Paul McNulty, and Jason Ferguson. Buried AGNs in Advanced Mergers: Mid-infrared Color Selection as a Dual AGN Candidate Finder. , 848(2):126, October 2017. doi: 10.3847/1538-4357/aa88ca.

Kevin Schawinski, C. Megan Urry, Brooke D. Simmons, Lucy Fortson, Sugata Kaviraj, William C. Keel, Chris J. Lintott, Karen L. Masters, Robert C. Nichol, Marc Sarzi, Ramin Skibba, Ezequiel Treister, Kyle W. Willett, O. Ivy Wong, and Sukyoung K. Yi. The green valley is a red herring: Galaxy Zoo reveals two evolutionary pathways towards quenching of star formation in early- and late-type galaxies. , 440(1):889–907, May 2014. doi: 10.1093/mnras/stu327.

P. Schechter. An analytic expression for the luminosity function for galaxies. , 203: 297–306, January 1976.

Astor J. Schönell, Thaisa Storchi-Bergmann, Rogemar A. Riffel, Rogério Riffel, Marina Bianchin, Luis G. Dahmer-Hahn, Marlon R. Diniz, and Natacha Z. Dametto. Gemini NIFS survey of feeding and feedback in nearby active galaxies - III. Ionized versus warm molecular gas masses and distributions. , 485(2):2054–2070, May 2019. doi: 10.1093/mnras/stz523.

Malte Schramm and John D. Silverman. The Black Hole-Bulge Mass Relation of Active Galactic Nuclei in the Extended Chandra Deep Field-South Survey. , 767(1):13, April 2013. doi: 10.1088/0004-637X/767/1/13.

M. Scialpi, F. Mannucci, C. Marconcini, G. Venturi, E. Pancino, A. Marconi, G. Cresci, F. Belfiore, A. Amiri, E. Bertola, S. Carniani, C. Cicone, A. Ciurlo, Q. D'Amato, M. Ginolfi, E. Lusso, A. Marasco, E. Nardini, K. Rubinur, P. Severgnini, G. Tozzi, L. Ulivi, C. Vignali, and M. Volonteri. MUSE AO spectroscopy confirms five dual AGNs and two strongly lensed QSOs at sub-arcsec separation. *arXiv e-prints*, art. arXiv:2305.11850, May 2023. doi: 10.48550/arXiv.2305.11850.

N. Scoville, H. Aussel, M. Brusa, P. Capak, C. M. Carollo, M. Elvis, M. Giavalisco, L. Guzzo, G. Hasinger, C. Impey, J.-P. Kneib, O. LeFevre, S. J. Lilly, B. Mobasher, A. Renzini, R. M. Rich, D. B. Sanders, E. Schinnerer, D. Schminovich, P. Shopbell, Y. Taniguchi, and N. D. Tyson. The cosmic evolution survey (COSMOS): Overview. *ApJS*, 172(1):1–8, sep 2007. doi: 10.1086/516585.

N. Z. Scoville, D. N. B. Hall, S. T. Ridgway, and S. G. Kleinmann. Velocity, reddening, and temperature structure of the H2 emission in Orion. , 253:136–148, February 1982. doi: 10.1086/159618.

Nick Scoville, Lena Murchikova, Fabian Walter, Catherine Vlahakis, Jin Koda, Paul Vanden Bout, Joshua Barnes, Lars Hernquist, Kartik Sheth, Min Yun, David Sanders, Lee Armus, Pierre Cox, Todd Thompson, Brant Robertson, Laura Zschaechner, Linda Tacconi, Paul Torrey, Christopher C. Hayward, Reinhard Genzel, Phil Hopkins, Paul van der Werf, and Roberto Decarli. ALMA Resolves the Nuclear Disks of Arp 220. , 836(1):66, February 2017. doi: 10.3847/1538-4357/836/1/66.

Jillian M. Scudder, Sara L. Ellison, Paul Torrey, David R. Patton, and J. Trevor Mendel. Galaxy pairs in the Sloan Digital Sky Survey - V. Tracing changes in star formation rate and metallicity out to separations of 80 kpc. , 426(1):549–565, October 2012. doi: 10.1111/j.1365-2966.2012.21749.x.

C. K. Seyfert. Nuclear Emission in Spiral Nebulae. , 97:28–+, January 1943.

N. I. Shakura and R. A. Sunyaev. Black holes in binary systems. Observational appearance. , 24:337–355, January 1973.

Francesco Shankar, David H. Weinberg, and Jordi Miralda-Escudé. SELF-CONSISTENT MODELS OF THE AGN AND BLACK HOLE POPULATIONS: DUTY CYCLES, ACCRETION RATES, AND THE MEAN RADIATIVE EFFICIENCY. *ApJ*, 690(1):20–41, dec 2009. doi: 10.1088/0004-637x/690/1/20.

Ray S. Sharma, Ena Choi, Rachel S. Somerville, Gregory F. Snyder, Hannah Jhee, Dale D. Kocevski, Michaela Hirschmann, Benjamin P. Moster, Thorsten Naab, Desika Narayanan, Jeremiah P. Ostriker, and David J. Rosario. The connection between mergers and AGN activity in simulated and observed massive galaxies. , 527 (3):9461–9479, January 2024. doi: 10.1093/mnras/stad3836.

Y. Shen. The mass of quasars. *Bull. Astron. Soc. India*, 41:61–115, March 2013. URL `http://adsabs.harvard.edu/abs/2013BASI...41...61S`.

Yue Shen, Gordon T. Richards, Michael A. Strauss, Patrick B. Hall, Donald P. Schneider, Stephanie Snedden, Dmitry Bizyaev, Howard Brewington, Viktor Malanushenko, Elena Malanushenko, Dan Oravetz, Kaike Pan, and Audrey Simmons. A CATALOG OF QUASAR PROPERTIES FROM SLOAN DIGITAL SKY SURVEY DATA RELEASE 7. *ApJS*, 194(2):45, June 2011. ISSN 0067-0049, 1538-4365. doi: 10.1088/0067-0049/194/2/45. URL `http://stacks.iop.org/0067-0049/194/i=2/a=45?key=crossref.54d679edfa91473a01062d70aa6bb013`.

T. Taro Shimizu, R. I. Davies, D. Lutz, L. Burtscher, M. Lin, D. Baron, R. L. Davies, R. Genzel, E. K. S. Hicks, M. Koss, W. Maciejewski, F. Müller-Sánchez, G. Orban de Xivry, S. H. Price, C. Ricci, R. Riffel, R. A. Riffel, D. Rosario, M. Schartmann,

A. Schnorr-Müller, A. Sternberg, E. Sturm, T. Storchi-Bergmann, L. Tacconi, and S. Veilleux. The multiphase gas structure and kinematics in the circumnuclear region of NGC 5728. , 490(4):5860–5887, December 2019. doi: 10.1093/mnras/stz2802.

Jaejin Shin, Jong-Hak Woo, Aeree Chung, Junhyun Baek, Kyuhyoun Cho, Daeun Kang, and Hyun-Jin Bae. Positive and Negative Feedback of AGN Outflows in NGC 5728. , 881(2):147, August 2019. doi: 10.3847/1538-4357/ab2e72.

Yiping Shu, Sergey E. Koposov, N. Wyn Evans, Vasily Belokurov, Richard G. McMahon, Matthew W. Auger, and Cameron A. Lemon. Catalogues of active galactic nuclei from Gaia and unWISE data. , 489(4):4741–4759, November 2019. doi: 10.1093/mnras/stz2487.

Joseph Silk. Unleashing Positive Feedback: Linking the Rates of Star Formation, Supermassive Black Hole Accretion, and Outflows in Distant Galaxies. , 772(2):112, August 2013. doi: 10.1088/0004-637X/772/2/112.

Joseph Silk and Martin J. Rees. Quasars and galaxy formation. , 331:L1–L4, March 1998. doi: 10.48550/arXiv.astro-ph/9801013.

S. Silpa, P. Kharb, C. P. O'Dea, S. A. Baum, B. Sebastian, D. Mukherjee, and C. M. Harrison. AGN jets and winds in polarized light: the case of Mrk 231. , 507(2): 2550–2561, October 2021. doi: 10.1093/mnras/stab2110.

John D. Silverman, Shenli Tang, Khee-Gan Lee, Tilman Hartwig, Andy Goulding, Michael A. Strauss, Malte Schramm, Xuheng Ding, Rogemar A. Riffel, Seiji Fujimoto, Chiaki Hikage, Masatoshi Imanishi, Kazushi Iwasawa, Knud Jahnke, Issha Kayo, Nobunari Kashikawa, Toshihiro Kawaguchi, Kotaro Kohno, Wentao Luo, Yoshiki Matsuoka, Yuichi Matsuda, Tohru Nagao, Masamune Oguri, Yoshiaki Ono, Masafusa Onoue, Masami Ouchi, Kazuhiro Shimasaku, Hyewon Suh, Nao Suzuki, Yoshiaki Taniguchi, Yoshiki Toba, Yoshihiro Ueda, and Naoki Yasuda. Dual Supermassive Black Holes at Close Separation Revealed by the Hyper Suprime-Cam Subaru Strategic Program. , 899(2):154, August 2020. doi: 10.3847/1538-4357/aba4a3.

K. L. Smith, G. A. Shields, E. W. Bonning, C. C. McMullen, D. J. Rosario, and S. Salviander. A Search for Binary Active Galactic Nuclei: Double-peaked [O III] AGNs in the Sloan Digital Sky Survey. , 716(1):866–877, June 2010. doi: 10.1088/0004-637X/716/1/866.

B. T. Soifer, M. Rowan-Robinson, J. R. Houck, T. de Jong, G. Neugebauer, H. H. Aumann, C. A. Beichman, N. Boggess, P. E. Clegg, J. P. Emerson, F. C. Gillett, H. J. Habing, M. G. Hauser, F. J. Low, G. Miley, and E. Young. Infrared galaxies in the IRAS minisurvey. *ApJ*, 278:L71, March 1984. ISSN 0004-637X, 1538-4357. doi: 10.1086/184226. URL `http://adsabs.harvard.edu/doi/10.1086/184226`.

G. Speranza, C. Ramos Almeida, J. A. Acosta-Pulido, R. A. Riffel, C. Tadhunter, J. C. S. Pierce, A. Rodríguez-Ardila, M. Coloma Puga, M. Brusa, B. Musiimenta, D. M. Alexander, A. Lapi, F. Shankar, and C. Villforth. Warm molecular and ionized gas kinematics in the type-2 quasar J0945+1737. , 665:A55, September 2022. doi: 10.1051/0004-6361/202243585.

G. Speranza, C. Ramos Almeida, J. A. Acosta-Pulido, A. Audibert, L. R. Holden, C. N. Tadhunter, A. Lapi, O. González-Martín, M. Brusa, I. E. López, B. Musiimenta, and F. Shankar. Multiphase characterization of AGN winds in five local type-2 quasars. , 681:A63, January 2024. doi: 10.1051/0004-6361/202347715.

H. W. W. Spoon, D. Farrah, V. Lebouteiller, E. González-Alfonso, J. Bernard-Salas, T. Urrutia, D. Rigopoulou, M. S. Westmoquette, H. A. Smith, J. Afonso, C. Pearson, D. Cormier, A. Efstathiou, C. Borys, A. Verma, M. Etxaluze, and D. L. Clements. Diagnostics of AGN-Driven Molecular Outflows in ULIRGs from Herschel-PACS Observations of OH at 119 μm. , 775(2):127, October 2013. doi: 10.1088/0004-637X/775/2/127.

Marko Stalevski, Jacopo Fritz, Maarten Baes, Theodoros Nakos, and Luka Č. Popović. 3D radiative transfer modelling of the dusty tori around active galactic nuclei as a clumpy two-phase medium. , 420(4):2756–2772, March 2012. doi: 10.1111/j.1365-2966.2011.19775.x.

Marko Stalevski, Claudio Ricci, Yoshihiro Ueda, Paulina Lira, Jacopo Fritz, and Maarten Baes. The dust covering factor in active galactic nuclei. , 458(3):2288–2302, May 2016. doi: 10.1093/mnras/stw444.

Lisa K. Steinborn, Klaus Dolag, Julia M. Comerford, Michaela Hirschmann, Rhea-Silvia Remus, and Adelheid F. Teklu. Origin and properties of dual and offset active galactic nuclei in a cosmological simulation at z=2. , 458(1):1013–1028, May 2016. doi: 10.1093/mnras/stw316.

Daniel Stern, Roberto J. Assef, Dominic J. Benford, Andrew Blain, Roc Cutri, Arjun Dey, Peter Eisenhardt, Roger L. Griffith, T. H. Jarrett, Sean Lake, Frank Masci, Sara Petty, S. A. Stanford, Chao-Wei Tsai, E. L. Wright, Lin Yan, Fiona Harrison, and Kristin Madsen. Mid-infrared Selection of Active Galactic Nuclei with the Wide-Field Infrared Survey Explorer. I. Characterizing WISE-selected Active Galactic Nuclei in COSMOS. , 753(1):30, July 2012. doi: 10.1088/0004-637X/753/1/30.

Meredith A. Stone, Jianwei Lyu, George H. Rieke, and Stacey Alberts. Detection of the Low-stellar-mass Host Galaxy of a z 6.25 Quasar with JWST. , 953(2):180, August 2023. doi: 10.3847/1538-4357/acebe0.

T. Storchi-Bergmann, R. D. Simões Lopes, P. J. McGregor, Rogemar A. Riffel, T. Beck, and P. Martini. Feeding versus feedback in NGC4151 probed with Gemini NIFS - II. Kinematics. , 402(2):819–835, February 2010. doi: 10.1111/j.1365-2966.2009.15962.x.

Kate Storey-Fisher, David W. Hogg, Hans-Walter Rix, Anna-Christina Eilers, Giulio Fabbian, Michael R. Blanton, and David Alonso. Quaia, the Gaia-unWISE Quasar Catalog: An All-sky Spectroscopic Quasar Sample. , 964(1):69, March 2024. doi: 10.3847/1538-4357/ad1328.

E. Sturm, E. González-Alfonso, S. Veilleux, J. Fischer, J. Graciá-Carpio, S. Hailey-Dunsheath, A. Contursi, A. Poglitsch, A. Sternberg, R. Davies, R. Genzel, D. Lutz, L. Tacconi, A. Verma, R. Maiolino, and J. A. de Jong. Massive Molecular Outflows and Negative Feedback in ULIRGs Observed by Herschel-PACS. , 733(1):L16, May 2011. doi: 10.1088/2041-8205/733/1/L16.

M. Talia, M. Brusa, A. Cimatti, B. C. Lemaux, R. Amorin, S. Bardelli, L. P. Cassarà, O. Cucciati, B. Garilli, A. Grazian, L. Guaita, N. P. Hathi, A. Koekemoer, O. Le Fèvre, D. Maccagni, K. Nakajima, L. Pentericci, J. Pforr, D. Schaerer, E. Vanzella, D. Vergani, G. Zamorani, and E. Zucca. AGN-enhanced outflows of low-ionization gas in star-forming galaxies at $1.7 < z < 4.6$*. , 471(4):4527–4540, November 2017. doi: 10.1093/mnras/stx1788.

Matthew J. Temple, Paul C. Hewett, and Manda Banerji. Modelling type 1 quasar colours in the era of Rubin and Euclid. , 508(1):737–754, November 2021. doi: 10.1093/mnras/stab2586.

Stacy H. Teng, Jane R. Rigby, Daniel Stern, Andrew Ptak, D. M. Alexander, Franz E. Bauer, Stephen E. Boggs, W. Niel Brandt, Finn E. Christensen, Andrea Comastri, William W. Craig, Duncan Farrah, Poshak Gandhi, Charles J. Hailey, Fiona A. Harrison, Ryan C. Hickox, Michael Koss, Bin Luo, Ezequiel Treister, and William W. Zhang. A NuSTAR Survey of Nearby Ultraluminous Infrared Galaxies. , 814(1):56, November 2015. doi: 10.1088/0004-637X/814/1/56.

Yuichi Terashima, Naoko Iyomoto, Luis C. Ho, and Andrew F. Ptak. X-Ray Properties of LINERs and Low-Luminosity Seyfert Galaxies Observed with ASCA. I. Observations and Results. , 139(1):1–36, March 2002. doi: 10.1086/324373.

Mallory D. Thorp, Sara L. Ellison, Hsi-An Pan, Lihwai Lin, David R. Patton, Asa F. L. Bluck, Dan Walters, and Jillian M. Scudder. The ALMaQUEST Survey X: what powers merger induced star formation? , 516(1):1462–1480, October 2022. doi: 10.1093/mnras/stac2288.

F. Tombesi, M. Cappi, J. N. Reeves, G. G. C. Palumbo, V. Braito, and M. Dadina. Evidence for Ultra-fast Outflows in Radio-quiet Active Galactic Nuclei. II. Detailed Photoionization Modeling of Fe K-shell Absorption Lines. , 742(1):44, November 2011. doi: 10.1088/0004-637X/742/1/44.

Paul Torrey, Mark Vogelsberger, Debora Sijacki, Volker Springel, and Lars Hernquist. Moving-mesh cosmology: properties of gas discs. , 427(3):2224–2238, December 2012. doi: 10.1111/j.1365-2966.2012.22082.x.

G. Tozzi, G. Cresci, A. Marasco, E. Nardini, A. Marconi, F. Mannucci, G. Chartas, F. Rizzo, A. Amiri, M. Brusa, A. Comastri, M. Dadina, G. Lanzuisi, V. Mainieri, M. Mingozzi, M. Perna, G. Venturi, and C. Vignali. Connecting X-ray nuclear winds with galaxy-scale ionised outflows in two $z \sim 1.5$ lensed quasars. , 648:A99, April 2021. doi: 10.1051/0004-6361/202040190.

G. Tozzi, G. Cresci, M. Perna, V. Mainieri, F. Mannucci, A. Marconi, D. Kakkad, A. Marasco, M. Brusa, E. Bertola, M. Bischetti, S. Carniani, C. Cicone, C. Circosta, F. Fiore, C. Feruglio, C. M. Harrison, I. Lamperti, H. Netzer, E. Piconcelli, A. Puglisi, J. Scholtz, G. Vietri, C. Vignali, and G. Zamorani. SUPER: VIII. Fast and furious at $z \sim 2$: Obscured type-2 active nuclei host faster ionised winds than type-1 systems. , 690:A141, October 2024. doi: 10.1051/0004-6361/202450162.

M. Tremmel, M. Karcher, F. Governato, M. Volonteri, T. R. Quinn, A. Pontzen, L. Anderson, and J. Bellovary. The Romulus cosmological simulations: a physical approach

to the formation, dynamics and accretion models of SMBHs. , 470(1):1121–1139, September 2017. doi: 10.1093/mnras/stx1160.

M. Tremmel, T. R. Quinn, A. Ricarte, A. Babul, U. Chadayammuri, P. Natarajan, D. Nagai, A. Pontzen, and M. Volonteri. Introducing ROMULUSC: a cosmological simulation of a galaxy cluster with an unprecedented resolution. , 483(3):3336–3362, March 2019. doi: 10.1093/mnras/sty3336.

R. Tunnard, T. R. Greve, S. Garcia-Burillo, J. Graciá Carpio, J. Fischer, A. Fuente, E. González-Alfonso, S. Hailey-Dunsheath, R. Neri, E. Sturm, A. Usero, and P. Planesas. Chemically Distinct Nuclei and Outflowing Shocked Molecular Gas in Arp 220. , 800(1):25, February 2015. doi: 10.1088/0004-637X/800/1/25.

Vivian U, D. B. Sanders, J. M. Mazzarella, A. S. Evans, J. H. Howell, J. A. Surace, L. Armus, K. Iwasawa, D. C. Kim, C. M. Casey, T. Vavilkin, M. Dufault, K. L. Larson, J. E. Barnes, B. H. P. Chan, D. T. Frayer, S. Haan, H. Inami, C. M. Ishida, J. S. Kartaltepe, J. L. Melbourne, and A. O. Petric. Spectral Energy Distributions of Local Luminous and Ultraluminous Infrared Galaxies. , 203(1):9, November 2012. doi: 10.1088/0067-0049/203/1/9.

Vivian U, Anne M. Medling, Hanae Inami, Lee Armus, Tanio Díaz-Santos, Vassilis Charmandaris, Justin Howell, Sabrina Stierwalt, George C. Privon, Sean T. Linden, David B. Sanders, Claire E. Max, Aaron S. Evans, Loreto Barcos-Muñoz, Charleston W. K. Chiang, Phil Appleton, Gabriela Canalizo, Giovanni Fazio, Kazushi Iwasawa, Kirsten Larson, Joseph Mazzarella, Eric Murphy, Jeffrey Rich, and Jason Surace. Keck OSIRIS AO LIRG Analysis (KOALA): Feedback in the Nuclei of Luminous Infrared Galaxies. , 871(2):166, February 2019. doi: 10.3847/1538-4357/aaf1c2.

Junko Ueda, Tomonari Michiyama, Daisuke Iono, Yusuke Miyamoto, and Toshiki Saito. Spatially-resolved relation between [C I] $^3P_1$-$^3P_0$ and ^{12}CO (1-0) in Arp 220. , 74(2): 407–420, April 2022. doi: 10.1093/pasj/psac004.

J. S. Ulvestad, J. M. Wrobel, and C. L. Carilli. Radio Continuum Evidence for Outflow and Absorption in the Seyfert 1 Galaxy Markarian 231. , 516(1):127–140, May 1999. doi: 10.1086/307111.

Mauri J. Valtonen, Lankeswar Dey, Staszek Zola, Alok C. Gupta, Shubham Kishore, Achamveedu Gopakumar, Paul J. Wiita, Minfeng Gu, Kari Nilsson, Zhongli Zhang, Rene Hudec, Katsura Matsumoto, Marek Drozdz, Waldemar Ogloza, Andrei V. Berdyugin, Daniel E. Reichart, Markus Mugrauer, Tapio Pursimo, Stefano Ciprini, Tatsuya Nakaoka, Makoto Uemura, Ryo Imazawa, Michal Zejmo, Vladimir V. Kouprianov, James W. Davidson, Jr., Alberto Sadun, Jan Štrobl, Martin Jelínek, and Abhimanyu Susobhanan. Identifying the Secondary Jet in the RadioAstron Image of OJ 287. , 992(1):110, October 2025. doi: 10.3847/1538-4357/ae057e.

Sandor Van Wassenhove, Marta Volonteri, Lucio Mayer, Massimo Dotti, Jillian Bellovary, and Simone Callegari. Observability of Dual Active Galactic Nuclei in Merging Galaxies. , 748(1):L7, March 2012. doi: 10.1088/2041-8205/748/1/L7.

E. Varenius, J. E. Conway, I. Martí-Vidal, S. Aalto, L. Barcos-Muñoz, S. König, M. A. Pérez-Torres, A. T. Deller, J. Moldón, J. S. Gallagher, T. M. Yoast-Hull, C. Horellou,

L. K. Morabito, A. Alberdi, N. Jackson, R. Beswick, T. D. Carozzi, O. Wucknitz, and N. Ramírez-Olivencia. Subarcsecond international LOFAR radio images of Arp 220 at 150 MHz. A kpc-scale star forming disk surrounding nuclei with shocked outflows. , 593:A86, September 2016. doi: 10.1051/0004-6361/201628702.

E. Varenius, J. E. Conway, F. Batejat, I. Martí-Vidal, M. A. Pérez-Torres, S. Aalto, A. Alberdi, C. J. Lonsdale, and P. Diamond. The population of SNe/SNRs in the starburst galaxy Arp 220. A self-consistent analysis of 20 years of VLBI monitoring. , 623:A173, March 2019. doi: 10.1051/0004-6361/201730631.

S. Veilleux, D. C. Kim, D. B. Sanders, J. M. Mazzarella, and B. T. Soifer. Optical Spectroscopy of Luminous Infrared Galaxies. II. Analysis of the Nuclear and Long-Slit Data. , 98:171, May 1995. doi: 10.1086/192158.

S. Veilleux, G. Cecil, and J. Bland-Hawthorn. Galactic Winds. , 43:769–826, September 2005. doi: 10.1146/annurev.astro.43.072103.150610.

S. Veilleux, M. Meléndez, E. Sturm, J. Gracia-Carpio, J. Fischer, E. González-Alfonso, A. Contursi, D. Lutz, A. Poglitsch, R. Davies, R. Genzel, L. Tacconi, J. A. de Jong, A. Sternberg, H. Netzer, S. Hailey-Dunsheath, A. Verma, D. S. N. Rupke, R. Maiolino, S. H. Teng, and E. Polisensky. Fast Molecular Outflows in Luminous Galaxy Mergers: Evidence for Quasar Feedback from Herschel. , 776(1):27, October 2013a. doi: 10.1088/0004-637X/776/1/27.

S. Veilleux, M. Meléndez, E. Sturm, J. Gracia-Carpio, J. Fischer, E. González-Alfonso, A. Contursi, D. Lutz, A. Poglitsch, R. Davies, R. Genzel, L. Tacconi, J. A. de Jong, A. Sternberg, H. Netzer, S. Hailey-Dunsheath, A. Verma, D. S. N. Rupke, R. Maiolino, S. H. Teng, and E. Polisensky. Fast Molecular Outflows in Luminous Galaxy Mergers: Evidence for Quasar Feedback from Herschel. , 776(1):27, October 2013b. doi: 10.1088/0004-637X/776/1/27.

S. Veilleux, M. Meléndez, T. M. Tripp, F. Hamann, and D. S. N. Rupke. The Complete Ultraviolet Spectrum of the Archetypal "Wind-dominated" Quasar Mrk 231: Absorption and Emission from a High-speed Dusty Nuclear Outflow. , 825(1):42, July 2016. doi: 10.3847/0004-637X/825/1/42.

Sylvain Veilleux and Donald E. Osterbrock. Spectral Classification of Emission-Line Galaxies. In Carol J. Lonsdale Persson, editor, *NASA Conference Publication*, volume 2466 of *NASA Conference Publication*, pages 737–740, May 1987.

Sylvain Veilleux, Roberto Maiolino, Alberto D. Bolatto, and Susanne Aalto. Cool outflows in galaxies and their implications. , 28(1):2, April 2020. doi: 10.1007/s00159-019-0121-9.

G. Venturi, G. Cresci, A. Marconi, M. Mingozzi, E. Nardini, S. Carniani, F. Mannucci, A. Marasco, R. Maiolino, M. Perna, E. Treister, J. Bland-Hawthorn, and J. Gallimore. MAGNUM survey: Compact jets causing large turmoil in galaxies. Enhanced line widths perpendicular to radio jets as tracers of jet-ISM interaction. , 648:A17, April 2021. doi: 10.1051/0004-6361/202039869.

G. Venturi, E. Treister, C. Finlez, G. D'Ago, F. Bauer, C. M. Harrison, C. Ramos Almeida, M. Revalski, F. Ricci, L. F. Sartori, A. Girdhar, W. C. Keel, and D. Tubín. Complex AGN feedback in the Teacup galaxy. A powerful ionised galactic outflow, jet-ISM interaction, and evidence for AGN-triggered star formation in a giant bubble. , 678:A127, October 2023. doi: 10.1051/0004-6361/202347375.

Giacomo Venturi, Emanuele Nardini, Alessandro Marconi, Stefano Carniani, Matilde Mingozzi, Giovanni Cresci, Filippo Mannucci, Guido Risaliti, Roberto Maiolino, Barbara Balmaverde, Angela Bongiorno, Marcella Brusa, Alessandro Capetti, Claudia Cicone, Stefano Ciroi, Chiara Feruglio, Fabrizio Fiore, Anna Gallazzi, Fabio La Franca, Vincenzo Mainieri, Kenta Matsuoka, Tohru Nagao, Michele Perna, Enrico Piconcelli, Eleonora Sani, Paolo Tozzi, and Stefano Zibetti. MAGNUM survey: A MUSE-Chandra resolved view on ionized outflows and photoionization in the Seyfert galaxy NGC1365. , 619:A74, November 2018. doi: 10.1051/0004-6361/201833668.

K. Verro, S. C. Trager, R. F. Peletier, A. Lançon, A. Gonneau, A. Vazdekis, P. Prugniel, Y. P. Chen, P. R. T. Coelho, P. Sánchez-Blázquez, L. Martins, A. Arentsen, M. Lyubenova, J. Falcón-Barroso, and M. Dries. The X-shooter Spectral Library (XSL): Data Release 3. , 660:A34, April 2022. doi: 10.1051/0004-6361/202142388.

M. Villar Martín, B. Emonts, A. Humphrey, A. Cabrera Lavers, and L. Binette. The triggering mechanism and properties of ionized outflows in the nearest obscured quasars. , 440:3202–3219, June 2014. doi: 10.1093/mnras/stu448.

M. Volonteri, F. Haardt, and P. Madau. The Assembly and Merging History of Supermassive Black Holes in Hierarchical Models of Galaxy Formation. , 582:559–573, January 2003. doi: 10.1086/344675.

Marta Volonteri, Hugo Pfister, Ricarda Beckmann, Massimo Dotti, Yohan Dubois, Warren Massonneau, Gibwa Musoke, and Michael Tremmel. Dual AGN in the Horizon-AGN simulation and their link to galaxy and massive black hole mergers, with an excursus on multiple AGN. , 514(1):640–656, July 2022. doi: 10.1093/mnras/stac1217.

A. Y. Wagner, G. V. Bicknell, and M. Umemura. Driving Outflows with Relativistic Jets and the Dependence of Active Galactic Nucleus Feedback Efficiency on Interstellar Medium Inhomogeneity. , 757(2):136, October 2012. doi: 10.1088/0004-637X/757/2/136.

Ailing Wang, Tao An, Sumit Jaiswal, Prashanth Mohan, Yuchan Wang, Willem A. Baan, Yingkang Zhang, and Xiaolong Yang. The obstructed jet in Mrk 231. , 504 (3):3823–3830, July 2021. doi: 10.1093/mnras/stab587.

Jian-Guo Wang, Xiao-Bo Dong, Ting-Gui Wang, Luis C. Ho, Weimin Yuan, Huiyuan Wang, Kai Zhang, Shaohua Zhang, and Hongyan Zhou. ESTIMATING BLACK HOLE MASSES IN ACTIVE GALACTIC NUCLEI USING THE Mg II Î»2800 EMISSION LINE. *ApJ*, 707(2):1334–1346, December 2009. ISSN 0004-637X, 1538-4357. doi: 10.1088/0004-637X/707/2/1334. URL http://stacks.iop.org/0004-637X/707/i=2/a=1334?key=crossref.b4fb9e9f1c089606a9478f173d083ad1.

Peter M. Weilbacher, Ralf Palsa, Ole Streicher, Roland Bacon, Tanya Urrutia, Lutz Wisotzki, Simon Conseil, Bernd Husemann, Aurélien Jarno, Andreas Kelz, Arlette Pécontal-Rousset, Johan Richard, Martin M. Roth, Fernando Selman, and Joël Vernet. The data processing pipeline for the MUSE instrument. , 641:A28, September 2020. doi: 10.1051/0004-6361/202037855.

B. J. Weiner, A. L. Coil, J. X. Prochaska, J. A. Newman, M. C. Cooper, K. Bundy, C. J. Conselice, A. A. Dutton, S. M. Faber, D. C. Koo, J. M. Lotz, G. H. Rieke, and K. H. R. Rubin. Ubiquitous Outflows in DEEP2 Spectra of Star-Forming Galaxies at z = 1.4. , 692:187–211, February 2009. doi: 10.1088/0004-637X/692/1/187.

M. S. Westmoquette, D. L. Clements, G. J. Bendo, and S. A. Khan. Spatially resolved observations of warm ionized gas and feedback in local ULIRGs. , 424:416–456, July 2012. doi: 10.1111/j.1365-2966.2012.21214.x.

Jordan Wheeler, Jason Glenn, Naseem Rangwala, and Adalyn Fyhrie. Arp 220: New Observational Insights into the Structure and Kinematics of the Nuclear Molecular Disks and Surrounding Gas. , 896(1):43, June 2020. doi: 10.3847/1538-4357/ab8f32.

S. D. M. White and M. J. Rees. Core condensation in heavy halos: a two-stage theory for galaxy formation and clustering. , 183:341–358, May 1978. doi: 10.1093/mnras/183.3.341.

A. S. Wilson and E. J. M. Colbert. The Difference between Radio-loud and Radio-quiet Active Galaxies. , 438:62, January 1995. doi: 10.1086/175054.

Christine D. Wilson, William E. Harris, Rebecca Longden, and N. Z. Scoville. Two Populations of Young Massive Star Clusters in Arp 220. , 641(2):763–772, April 2006. doi: 10.1086/500577.

Jong-Hak Woo, Hyun-Jin Bae, Donghoon Son, and Marios Karouzos. The Prevalence of Gas Outflows in Type 2 AGNs. , 817(2):108, February 2016. doi: 10.3847/0004-637X/817/2/108.

Jong-Hak Woo, Donghoon Son, and Hyun-Jin Bae. Delayed or No Feedback? Gas Outflows in Type 2 AGNs. III. , 839(2):120, April 2017. doi: 10.3847/1538-4357/aa6894.

Xin Xiang, Jon M. Miller, Ehud Behar, Rozenn Boissay-Malaquin, Laura Brenneman, Margaret Buhariwalla, Doyee Byun, Chris Done, Luigi Gallo, Dimitra Gerolymatou, Scott Hagen, Jelle Kaastra, Stephane Paltani, Frederick S. Porter, Richard Mushotzky, Hirofumi Noda, Missagh Mehdipour, Takeo Minezaki, Makoto Tashiro, and Abderahmen Zoghbi. XRISM Spectroscopy of Accretion-driven Wind Feedback in NGC 4151. , 988(2):L54, August 2025. doi: 10.3847/2041-8213/adee9b.

Chun Xu, Mario Livio, and Stefi Baum. Radio-loud and Radio-quiet Active Galactic Nuclei. , 118(3):1169–1176, September 1999. doi: 10.1086/301007.

Chang-Shuo Yan, Youjun Lu, Xinyu Dai, and Qingjuan Yu. A Probable Milli-parsec Supermassive Binary Black Hole in the Nearest Quasar Mrk 231. , 809(2):117, August 2015. doi: 10.1088/0004-637X/809/2/117.

Tova M. Yoast-Hull and Norman Murray. Breaking the radio - gamma-ray connection in Arp 220. , 484(3):3665–3680, April 2019. doi: 10.1093/mnras/stz223.

Qingjuan Yu, Youjun Lu, Roya Mohayaee, and Jacques Colin. The Low Frequency of Dual Active Galactic Nuclei versus the High Merger Rate of Galaxies: A Phenomenological Model. , 738(1):92, September 2011. doi: 10.1088/0004-637X/738/1/92.

Fang-Ting Yuan, Zhen-Ya Zheng, Chunyan Jiang, Shuairu Zhu, Ruqiu Lin, and Cheng Cheng. Merging Signatures in an Offset Lyman Continuum Emitter at Redshift 3.8. , 975(1):53, November 2024. doi: 10.3847/1538-4357/ad75ff.

Minghao Yue, Anna-Christina Eilers, Tonima Tasnim Ananna, Christos Panagiotou, Erin Kara, and Takamitsu Miyaji. Stacking X-Ray Observations of "Little Red Dots": Implications for Their Active Galactic Nucleus Properties. , 974(2):L26, October 2024. doi: 10.3847/2041-8213/ad7eba.

Nadia L. Zakamska, Fred Hamann, Isabelle Pâris, W. N. Brandt, Jenny E. Greene, Michael A. Strauss, Carolin Villforth, Dominika Wylezalek, Rachael M. Alexandroff, and Nicholas P. Ross. Discovery of extreme [O III] λ5007 Å outflows in high-redshift red quasars. , 459(3):3144–3160, July 2016. doi: 10.1093/mnras/stw718.

Laura K. Zschaechner, Jürgen Ott, Fabian Walter, David S. Meier, Emmanuel Momjian, and Nick Scoville. High-resolution Observations of Molecular Lines in Arp 220: Kinematics, Morphology, and Limits on the Applicability of the Ammonia Thermometer. , 833(1):41, December 2016. doi: 10.3847/1538-4357/833/1/41.

Kastytis Zubovas and Andrew King. Clearing Out a Galaxy. , 745(2):L34, February 2012. doi: 10.1088/2041-8205/745/2/L34.

Kastytis Zubovas and Andrew R. King. Galaxy-wide outflows: cold gas and star formation at high speeds. , 439(1):400–406, March 2014. doi: 10.1093/mnras/stt2472.

Acknowledgments

This article was produced while attending the PhD program in Space Science and Technology at the University of Trento, Cycle XXXVIII, with the support of a scholarship financed by the Ministerial Decree no. 351 of 9th April 2022, based on the NRRP - funded by the European Union - NextGenerationEU - Mission 4 "Education and Research", Component 1 "Enhancement of the offer of educational services: from nurseries to universities" - Investment 4.1 "Extension of the number of research doctorates and innovative doctorates for public administration and cultural heritage" - E63C22001340001.